

EXPERIMENTELLE PHYSIK

**Small Animal Positron Emission
Tomography with Gas Detectors**
Simulations, Prototyping, and Quantitative Image
Reconstruction.

Inauguraldissertation
zur Erlangung des Doktorgrades
der Naturwissenschaften im Fachbereich Physik
der Mathematisch-Naturwissenschaftlichen Fakultät
der Westfälischen Wilhelms-Universität Münster

vorgelegt von
Don Vernekohl
aus Lünen

— April 2014 —

Dekan: Prof. Dr. M. Donath
Erster Gutachter: Prof. Dr. J. P. Wessels
Zweiter Gutachter: Prof. Dr. K. Schäfers

Tag der Disputation:

Tag der Promotion:

Contents

I	Introduction	1
II	Basics	3
II.1	Radioactive Decay	3
II.2	Principle of PET	4
II.3	Interactions of Positrons, Electrons, and Photons	4
II.3.1	Positrons and Electrons	4
II.3.2	Photons	6
II.4	Radiotracers	7
II.4.1	Isotope Production	8
II.4.2	Tracer Production	9
II.4.3	Used Isotopes and Tracers	10
II.5	Positron Range and Positronium Annihilation	10
II.6	Event Types	12
II.7	Partial Volume Effect	13
III	quadHIDAC	15
III.1	Detector Concept	15
III.1.1	MWPC	16
III.1.2	HIDAC Principle	17
III.2	Detection Concept	19
III.3	Electronic Readout	20
III.4	Gas Support	22
III.5	Other Small Animal PET Scanners	24
III.5.1	Spatial Resolution	25
III.5.2	Sensitivity	28
III.5.3	Comparison to the HIDAC Performance	30

IV	Monte-Carlo Simulations and Geant4	33
IV.1	Monte-Carlo Methods	33
IV.1.1	Pseudorandom Number Generation Methods	34
IV.1.2	Sampling of Probability Distributions	36
IV.2	Geant4	38
IV.2.1	The Geant4 Framework	38
IV.2.2	Implementation of the quadHIDAC Geometry	41
V	Converter Optimization	47
V.1	The quadHIDAC Converters	47
V.2	Simulations for Performance Enhancement	49
V.2.1	Optimization of Conversion Probability	49
V.2.2	Ionization Induced by Electrons and Their Drift in Gaseous Holes	56
V.2.3	Simulation of the Electron Detection Probability	61
V.2.4	Implication on the Overall Coincidence Sensitivity	64
V.3	Photon Converter Manufacturing	67
V.3.1	Mechanical Perforation	67
V.3.2	Drilling	68
V.3.3	Etching	69
V.3.4	Laser Perforation	71
V.3.5	Powder Metallic Screen Print	75
V.3.6	Further Production Techniques	78
V.4	Discussion	78
VI	Converter Test-Bench	81
VI.1	Setup	81
VI.2	SPADIC	83
VI.3	Validation of the Test-Bench	85
VI.4	Simulation	89
VI.5	Drilled Converter Results	90
VI.6	Results from Measurements with a Drift Layer	94
VI.7	Cone Shaped Structured Single Layer Design Results	95
VI.8	External Trigger	97
VI.9	Discussion	100
VII	Micro Pattern Gas Detector Prototypes	103
VII.1	Detector Concepts	103

VII.2	Simulation	105
VII.2.1	Environment and Setup	105
VII.2.2	Sensitivity Predictions for Different Conversion Materials	106
VII.2.3	MPGD based Scanner Simulations	107
VII.3	Experimental Evaluation	110
VII.3.1	Prototype Manufacturing	110
VII.3.2	Prototype Measurements	113
VII.3.3	Discussion	117
VIII	Image Reconstruction	119
VIII.1	Reconstruction Methods	119
VIII.2	The EM Image Reconstruction Algorithm for Emission Tomography	122
VIII.2.1	Generic Concept	122
VIII.2.2	Discrete Realization	123
VIII.3	EMrecon Reconstruction for quadHIDAC Data	125
VIII.3.1	List-Mode Reconstruction	125
VIII.3.2	System Matrix	126
VIII.3.3	OS-EM	127
VIII.3.4	Geometrical Correction	128
VIII.3.5	Randoms and Scatter Correction Implementation	128
IX	Randoms and Scatter Correction	129
IX.1	Quantitative Image Reconstruction	129
IX.2	Reconstruction including Randoms and Scatter Corrections	131
IX.3	Randoms Correction	133
IX.3.1	Estimation of the Spatial Distribution from Random Co- incidences	133
IX.3.2	Influence of Random Events in Reconstructed Images	134
IX.3.3	Shortcomings of the Shuffled Half-Coincidence (SHC) Estimation Method	138
IX.3.4	Randoms Correction for Two Simulated Small Spherical Sources	140
IX.4	Scatter Correction for a Simulated Mouse Phantom	142
IX.5	Randoms and Scatter Correction on Simulated and Measured Mouse Data	143
IX.6	Statistical Analysis	148
IX.7	Discussion	151

X	Non-collinearity and Spatial Resolution	153
X.1	Simulation Setup	153
X.2	Analysis Method	154
X.3	Non-collinearity Model	158
X.4	Analysis Results	161
X.4.1	Scanner Geometry Variations on the Example of the Ze- brafish	163
X.5	Discussion	165
XI	Summary	167
XI.1	Outlook	169
XI	Zusammenfassung	171
XI.1	Ausblick	174
A	Appendix	181
	Bibliography	186

CHAPTER I

Introduction

In the exploration of biological processes, especially in Molecular Imaging, it is often important to visualize specific interactions of molecules in the living organism. Here, positron emission tomography (PET) is one of the major modalities. PET allows one to investigate the spatial distribution and the kinetics of tracer molecules with high precision and to access the functionality of these molecules and their recipients within the organism. Its unique molar sensitivity is unsurpassed compared to all other *in vivo* imaging techniques, but constraints in life-time and chemical characteristics of the signal-inducing isotopes explain why other molecular imaging technologies are sometimes preferred. In the last decades, technical progress has allowed a constant improvement of PET instrumentation and still offers opportunities to optimize the systems. Especially the combination with devices providing morphological information received a lot of enhancements in recent years.

Because human patients should not be endangered, preclinical evaluations of new approaches with animal disease models in research are unavoidable. The requirements for small animal PET systems differ from clinical machines as the reduction in object size significantly changes the physical conditions. In the case of mice, the volume of organs is approximately a factor of 1000 smaller than in humans and unfortunately, it is currently not possible to improve the spatial resolution by the same factor for preclinical scanners, which would correspond to values of around 500 μm FWHM. The first commercial small animal PET scanner which was able to reach the sub-millimeter regime in spatial resolution was the quadHIDAC which consists of high-density avalanche chambers (HIDAC). This scanner offers a large field of view (FOV) with a homogeneous spatial resolution by using large panel detectors based on

gaseous particle tracking detectors. The conventional scanner developments based on inorganic scintillators, in contrast, reached the sub-millimeter domain several years later, yet all of these systems still suffer on spatial resolution degradation along the radial direction. However, due to a decreased photon detection efficiency, the coincidence sensitivity of the HIDAC is around 2-3 times lower than for state-of-the-art crystal based systems. This, in combination with the necessity of profound experience to handle the device and its supply systems, makes the HIDAC uncomfortable for daily use in preclinical imaging laboratories. The university hospital of Münster is well-experienced in HIDAC handling by operating two devices in daily service and maintaining two additional devices for research and backup tasks. The scanner applies several multi-wire proportional chambers each combined with two complex photon-electron converters. Motivated by the advantages of the scanner, it was anticipated to figure out how these converters should be designed and manufactured for a next generation HIDAC, as well as to test whether compact and modern readout electronics can be used to improve the HIDAC performance.

The dependence on geometrical effects on the photon conversion efficiency of the method employed by the HIDAC system are investigated further here; on the one hand with a simulation model of the scanner established by *Gottschlag* [Got10], and on the other hand, by a simulation framework which is set up to study the charge transport within the photon converters. Both frameworks are used to predict performance parameters for a future system. Additionally, it is examined whether manufacturing techniques are currently able to produce those optimized converter geometries. In a further step, an experimental test-bench was established to examine differently produced converter prototypes and to verify the feasibility of modern readout electronics (SPADIC), developed for the CBM experiment [FHK⁺11], for a new scanner system. Because of the difficult production of complex converters, an alternative detector concept with simpler single-lead-layer-converters is also proposed and studied in first prototypes.

Another shortcoming of gas detector-based PET is the missing energy information on the measured photon interaction, which prohibits obtaining quantitative activity concentrations in reconstructed images. A strategy to overcome this limitation by corrections based on Monte-Carlo simulations is provided and validated in this thesis.

In a last step, the presented methods are also used to compare kinematic models of positronium annihilation to measurements and to study its impact on spatial resolution in analytic and algebraic image reconstruction, which will pronounce the unparalleled spatial resolution potential of the HIDAC technology.

CHAPTER II

Basics

II.1 Radioactive Decay

The principle of emission tomography (ET) comprises the use of tracer molecules, which include at least one atom with an unstable nucleus. Unstable nuclei emit either α -, β -, and γ -radiation when they decay. Here, high energetic helium nuclei (α) or electrons/positrons (β) are emitted. In many cases, the daughter nucleus is in an excited state after one of the two former decays and is de-excited under the emission of electro-magnetic photons (γ).

The relevant decay for PET is the β^+ -decay, where a positron e^+ (the antiparticle to the electron) and an electron-neutrino ν_e are emitted. The β^+ -decay can be written as:



where ${}^A_Z X$ is the mother nucleus, ${}^A_{Z-1} Y$ is the daughter nucleus, and Q is the difference in binding energy of the two nucleus states. A proton within the nucleus is converted into a neutron in this decay. Hence, the element is changing during the decay. For free protons, the decay is not possible since an energy of at least two times the electron mass is needed. Therefore, the decay is only possible for atoms offering this energy in the binding energy change. A more detailed description of the overall β -decay is given in [Leo87] or with a quantum mechanical discussion in [MK79].

II.2 Principle of PET

The β^+ -emitters used for PET are usually light elements which are chemically well processable for the fusion with physiological interesting molecules to so-called “tracer” molecules. After the creation of tracer molecules, they can be administered to a patient or a subject of interest. During metabolism, some of the tracer molecules connect to their specific target molecules, enter target structures, or are processed by target objects. Dependent on the decay probability of the added β^+ -emitter, positrons are emitted somewhere on the tracers pathway through the living organism. In general, the positrons are high energetic and decelerate rapidly within the biological tissue. After thermalization, the positron combines with a surrounding electron to the so-called positronium, which subsequently annihilates primarily into two photons. The two 511 keV photons are emitted nearly back to back, and if both can be measured by detectors, a line is known to which the position of the tracer molecule has been very close. Therefore, a PET examination accumulates snapshots of traces of the molecules of interest within the scanned object. The sketch in Fig. II.1 summarizes some of the described steps. When some millions of these positronium annihilations are measured, sophisticated reconstruction techniques are able to calculate reasonable estimations of the original spatial distribution of these tracer molecules.

II.3 Interactions of Positrons, Electrons, and Photons

Since the energy loss of positrons in matter plays an important role for the positronium creation, the interactions from photons and electrons are essential to understand the detection principles of electromagnetic radiation. The processes are well described in nearly every basic nuclear physics textbook. Hence, this section only briefly touches on the most important points.

II.3.1 Positrons and Electrons

Electrons and positrons lose their kinetic energy mainly by electro-magnetic inelastic scatter interactions with shell electrons which lead to ionized and excited atoms

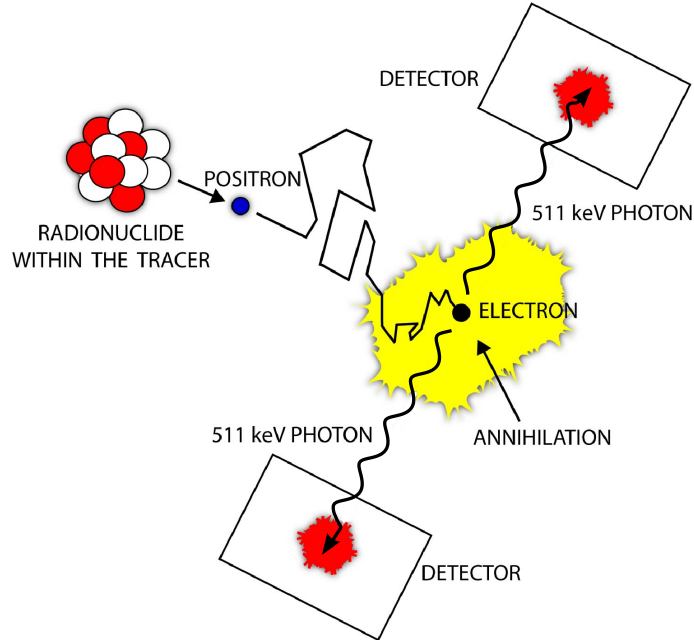


Fig. II.1: Scheme of the PET principle that shows the process of positron emission with subsequent positron-electron annihilation. The two 511 keV annihilation photons are registered by detector elements of a PET scanner.

in the absorbing material. The formula for this energy loss can be derived using relativistic quantum mechanical calculations and is described in [Leo87] as:

$$-\frac{dE}{dx} = 2\pi N_a r_e^2 m_e c^2 \rho \frac{Z}{A} \frac{1}{\beta^2} \left[\ln \frac{\tau^2(\tau+2)}{2(I/m_e c^2)^2} + F(\tau) \right] \quad (\text{II.2})$$

where τ is the kinetic energy of the incoming particle in units of $m_e c^2$. $F(\tau)$ differs for electrons and positrons:

$$F(\tau) = 1 - \beta^2 + \frac{\frac{\tau^2}{8} - (2r+1) \ln 2}{(\tau+1)^2} \quad \text{for } e^-$$

$$F(\tau) = 2 \ln 2 - \frac{\beta^2}{12} \left(23 + \frac{14}{\tau+2} + \frac{10}{(\tau+2)^2} + \frac{4}{(\tau+2)^3} \right) \quad \text{for } e^+$$

with

r_e :	classical electron radius	N_a :	Avogadro's number
Z :	atomic number of absorbing material	ρ :	density of absorbing material
A :	atomic weight of absorbing material	m_e :	electron mass
I :	mean excitation potential varying for each element	$\beta = v/c$:	of the incident particle

It should be mentioned that the formulation in (II.2) neither includes the influence of *Bremsstrahlung* nor shell- or density-corrections.

Regarding the term in front of the brackets in (II.2), the energy loss decreases for higher velocities of the particle as the time for interaction with a single electron is shortened. The term in the brackets increases with the particle velocity accounting for the growth of the transverse electric field for faster particles, causing higher interaction probabilities, whereas the longitudinal electric field of a relativistic particle experiences length contraction. Regarding both principles, a minimum energy loss is given for all particles at a kinetic energy of approximately $\beta\gamma \approx 3$ [Ams07]. Therefore, the positrons and electrons which occur in PET are commonly close to the energy range of minimal ionizing particles. Due to their low mass, they already move with relativistic velocities in this energy range, which can also cause energy losses due to *Cherenkov* radiation dependent of the transversed material. Furthermore, electrons and positrons lose energy while being deflected in the electric field of the atom nucleus by emitting photons known as *Bremsstrahlung*, but the contribution to the overall energy loss is very small for electrons with energies of a few MeV [Leo87]. Additionally, electron capture reactions can cause absorptions of low energetic electrons.

II.3.2 Photons

The interaction of photons with matter can be subdivided into three processes where the photon releases energy into its environment. The first process is the photoelectric effect, where the photon dispenses all its energy to a shell electron of an atom. The kinetic energy of the liberated electron is then $E_{kin} = E_\gamma - B$, where B is the binding energy of the electron. The cross section for the K-shell with a non-relativistic approximation is [BWW01]:

$$\sigma_{ph}^K = \left(\frac{32}{\varepsilon^7}\right)^{\frac{1}{2}} \alpha^4 Z^5 \sigma_{Th}^e \quad (\text{II.3})$$

with $\varepsilon = E_\gamma/m_e c^2$ as reduced photon energy and $\alpha = 1/137$ as the fine structure constant. The Thomson cross section for elastic scattering is given by

$$\sigma_{Th}^e = \frac{8}{3} \pi r_e^2 \quad (\text{II.4})$$

where $r_e \approx 2.818$ fm is the classical electron radius.

The second process is the *Compton*-effect, where the photon transfers only a part of

its energy to the shell electron. Due to momentum conservation, the energy of the liberated electron and the deflection angle of the photon are in a direct relationship. The cross section for the *Compton*-effect is energy dependent and higher for smaller scatter angles. The differential cross section was theoretical derived by Klein and Nishina [NK29] as:

$$\frac{d\sigma}{d\Omega} = Zr_e^2 \left(\frac{1}{1 + \varepsilon(1 - \cos \Theta)} \right)^2 \left(\frac{1 + \cos^2 \Theta}{2} \right) \left(1 + \frac{\alpha^2(1 - \cos \Theta)^2}{(1 + \cos^2 \Theta)[1 + \varepsilon(1 - \cos \Theta)]} \right) \quad (\text{II.5})$$

with Θ as scatter angle and Ω as azimuthal angle, which is distributed isotropically. The third process is the pair production, where a photon converts by interaction with the electro-magnetic field of an atom into two leptons. For the production of an electron-positron pair, an energy of at least 1.022 MeV of the initial photon is necessary. The cross section for electron-positron production is proportional to Z^2 and the natural logarithm of the photon energy.

To summarize and emphasize which process is dominant for a specific energy range, the cross sections for the three processes in a broad energy domain for aluminum and for lead are shown in Fig. II.2. It should be pointed out that the 511 keV photons occurring in PET interact in low Z materials mainly by *Compton* scattering, whereas the contribution of the photo-electric-effect rises for heavier elements reaching a contribution of approximately fifty per cent for the heaviest stable elements like lead and bismuth.

Besides these interactions, further scattering processes are possible where the initial photon does not lose any energy, e.g., the coherent *Rayleigh* scattering which is more relevant for lower energetic photons. Nevertheless, also in this energy domain the probability for the photo-electric effect is commonly several magnitudes higher.

II.4 Radiotracers

Tracers in ET are generally a combination of a pharmacophor with a flag or a label which is able to send signals out of the living object. The functional principle of the pharmacophor or its binding on a molecular target (receptors, cells, reporter genes, antibodies etc.) gives insights into the physiology or patho-physiology of the imaged subject and is tailored to a specific scientific question. Following this principle, the pharmacophor for example could be a disease offending drug or a molecule able to prove the success of a treatment, whereby the accumulation amount of tracer in the

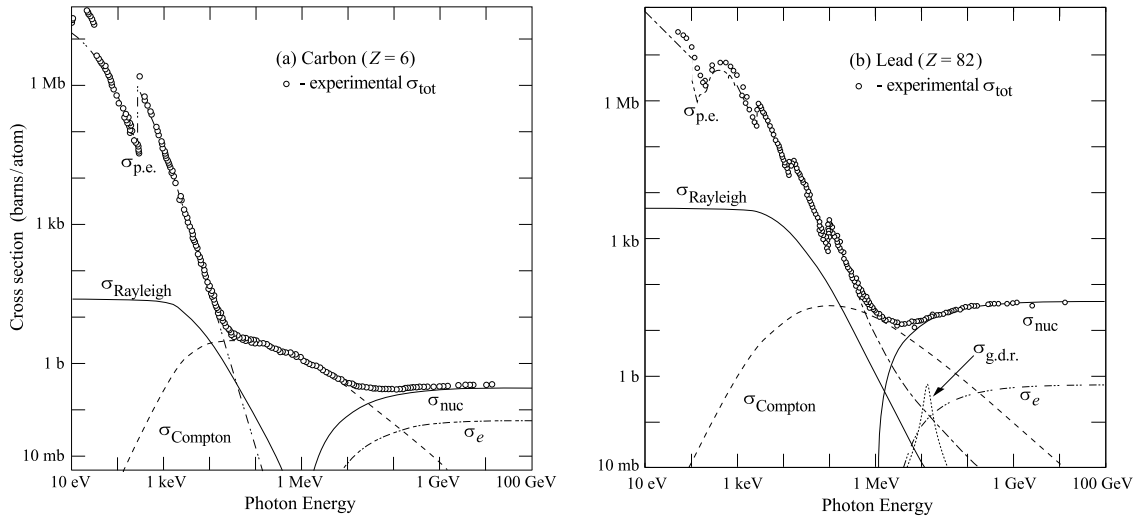


Fig. II.2: Comparison of the experimental total photon interaction cross sections to the theoretical values separated for the single photon interaction processes. Theoretical cross-sections are calculated for the photo-electric-effect $\sigma_{\text{p.e.}}$, coherent Rayleigh scattering σ_{Rayleigh} , incoherent *Compton* scattering σ_{Compton} , pair production in interaction with the nuclear electric field σ_{nuc} , pair production in interaction with the electric field of shell electrons σ_{e} , and nuclear photo absorption $\sigma_{\text{g.d.r.}}$ (i.e., giant dipole resonance). Figures are from [Hub99].

pathologic tissue indicates the treatment effectivity. As mentioned above, PET uses radioactive β^+ -emitters as the flags for these tracers.

II.4.1 Isotope Production

The interesting isotopes for PET are mainly short-lived and have no natural abundance. Hence a cyclotron, which is able to produce those isotopes, is necessary on site or at least in the local area of the scanner. A cyclotron accelerates ions within a homogeneous magnetic field of a large magnet on circular trajectories. In conventional cyclotrons, ions are accelerated n -times per orbit by applying an alternating current on n hollow so called D-electrodes (the name originates from the use of two electrodes given each a shape of a “D”). Thus, the circular trajectories of the ions increase with their kinetic energy. For PET isotopes, mainly negatively charged hydrogen ions are generated in the middle of the cyclotron. After acceleration, the ions are shot through thin metal foils where they strip off all their electrons and are pointed at target atoms.

The target nuclei have different cross sections for multiple possible nuclear reactions

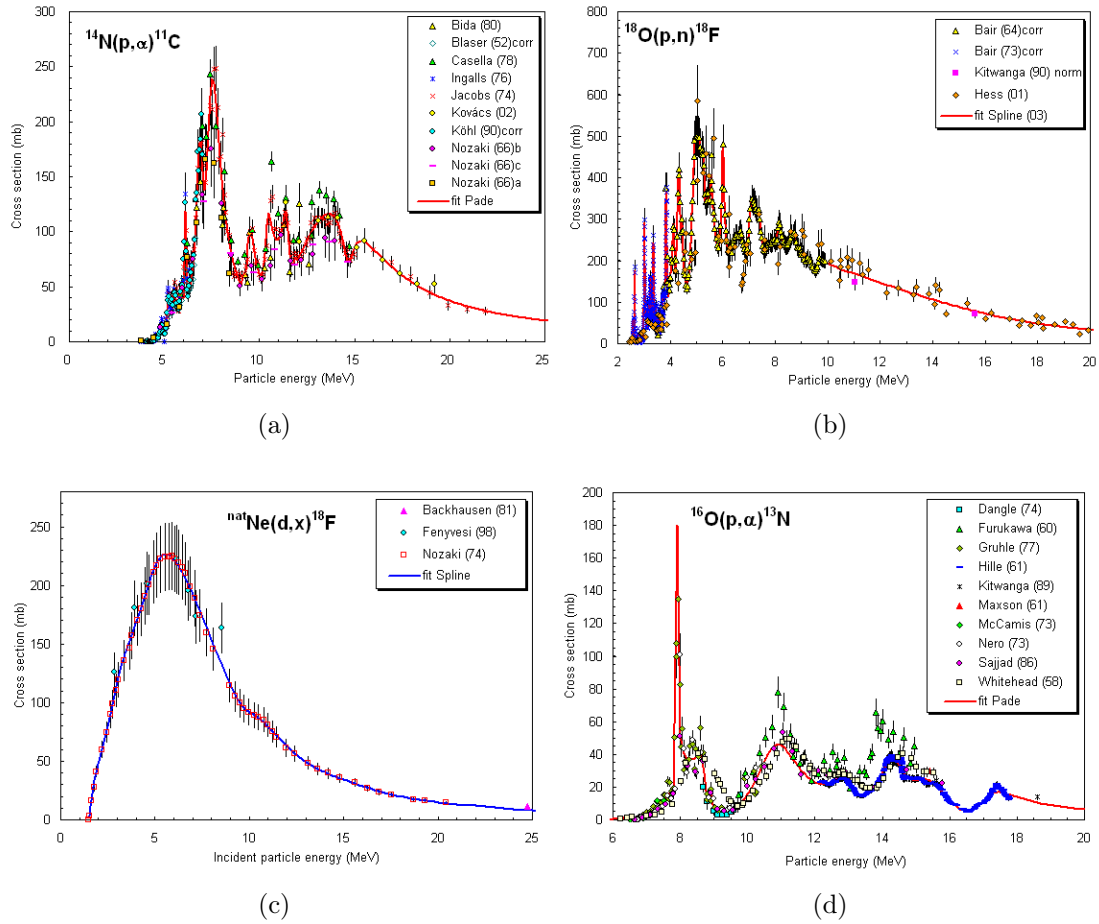


Fig. II.3: Examples for nuclear reaction cross sections for the production of ^{11}C (a), ^{18}F (b)(c), and ^{13}N (d) where different target nuclei are irradiated by protons (a),(b),(d) or deuterons (c) from [Obl01]

depending on the proton energy, where some dependencies are illustrated in Fig. II.3. The energy of protons can be set by extracting them on a specific radius by a kick-off magnet.

II.4.2 Tracer Production

Commonly, target nuclei are in a gaseous or liquid state as they are than more reactive in the further chemical treatment. Nevertheless, some isotopes are only producible in a solid state. Preferably, the isotopes are conducted automatically through pipelines to so called hot cells. The cells are shielded from their environment with lead and lead glass and are equipped internally with automatic synthesizers. The

synthesizers use precursors of the radiolabeled molecules or ions and the pharmaceutical compound as input. Several chemical reaction steps are performed with synthetization times from some minutes to some days depending on the complexity and reaction times of the single steps. Finally, the radiopharmaceutical has to be separated from all remaining solvents, catalysts, and side products mainly by high pressure liquid chromatography (HPLC) or gas chromatography (GC). After production, multiple tests are necessary to verify pH and osmolality, as well as to check the chemical-, radiochemical-, and radionuclide-purity [KP11].

II.4.3 Used Isotopes and Tracers

Important parameters for the production processes, the image acquisition, and the clinical routines are given by physical properties of the used isotopes. The maximum positron energy influences the obtainable spatial resolution in image acquisition, whereas the half-life time restricts the time for chemical reactions in the production and limits the observation of either slow or fast biological processes. It is also important that the half-life time is appropriate to the clinical infrastructure and permits passable scanning times. The reachable activity for a specific isotope is also dependent on the used cyclotron, dictating whether a complex tracer with long production steps is accessible with a reasonable tracer activity for clinical use. A list of all commonly used isotopes and some extraordinary isotopes with their specifications and some research and clinic tracer examples is given in Table II.1.

II.5 Positron Range and Positronium Annihilation

The principle of positron emission and positronium annihilation was already mentioned roughly in Section II.2, but the processes and their consequences should be discussed in more detail here.

Regarding (II.1), the β^+ -decay is a three body decay where the liberated binding energy is mainly transferred to the positron and the electron-neutrino. Therefore, the initial kinetic energy of the positron varies between zero and the maximum liberated energy. According to the deceleration processes of positrons in matter (section II.3.1), the energy loss is lowest directly after emission and increases when slowing down. Monte-Carlo simulations of the positron range [Got10] and [LH99] in water show that the annihilation position can vary substantially from the position of positron emission. Thus, in data space the position of the positron emitters is

TABLE II.1: Isotopes used in PET with their according half-life-time and maximum kinetic energy as well as examples for clinical and research tracers. Content collected from [Che01], [SH10], [Val03] and [KP11]. Missing values for positron ranges of ^{64}Cu , ^{76}Br , and ^{124}I in water obtained with linear regression.

Isotope	Half-Life	Max. Positron Energy	Mean Range in Water (mm)	Max. Range in Water (mm)	Tracer Examples
^{11}C	20.4 min	970 keV	1.1	4.1	$[^{11}\text{C}]\text{MET}$, $[^{11}\text{C}]\text{acetat}$, $[^{11}\text{C}]\text{choline}$, $[^{11}\text{C}]\text{raclopride}$, $[^{11}\text{C}]\text{HED}$
^{13}N	9.96 min	1.19 MeV	1.5	5.1	$[^{13}\text{N}]\text{Ammonia}$
^{15}O	124 s	1.72 MeV	2.5	7.3	$[^{15}\text{O}]\text{O}_2$, $[^{15}\text{O}]\text{H}_2\text{O}$, $[^{15}\text{O}]\text{CO}$, $[^{15}\text{O}]\text{butanol}$
^{18}F	109.7 min	635 keV	0.6	2.4	$[^{18}\text{F}]\text{FDG}$, $[^{18}\text{F}]\text{FDOPA}$, $[^{18}\text{F}]\text{FLT}$, $[^{18}\text{F}]\text{FMISO}$, $[^{18}\text{F}]\text{Fluoride}$, $[^{18}\text{F}]\text{FET}$, $[^{18}\text{F}]\text{FECH}$, $[^{18}\text{F}]\text{sodium fluoride}$
^{64}Cu	12.8 h	653 keV	0.7	2.7	$[^{64}\text{Cu}]\text{NOTA-HSA}$, $[^{64}\text{Cu}]\text{-ATSM}$, $[^{64}\text{Cu}]\text{-PTSM}$
^{68}Ga	68 min	1.9 MeV	2.9	8.2	$[^{68}\text{Ga}]\text{NOTA-HSA}$, $[^{68}\text{Ga}]\text{DOTATOC}$
^{76}Br	16.1 h	3.68 MeV	6.4	15.4	$[^{76}\text{Br}]\text{-BFU}$
^{82}Rb	75 s	3.4 MeV	5.9	14.1	$[^{82}\text{Rb}]\text{-chloride}$
^{124}I	100.32 h	1.54 MeV 2.15 MeV	2.3 3.4	6.5 9	$[^{124}\text{I}]\text{sodium iodide}$, $[^{124}\text{I}]\text{-FIAU}$

convolved with a “cusp-like” distribution due to the annihilation position [LH99]. A direct annihilation of a positron by interaction with an electron in flight is possible but very uncommon ($\sim 2\%$ [Hei53]) due to the small dimensions of the two leptons. Therefore, the majority of positrons decelerate down to kinetic energies of particles in the environment, called thermalization, until they reach the vicinity of the electric field of one of the numerous electrons existing in the environment. Both particles combine in the hydrogen like state of the positronium. Due to the spin of the leptons, they can combine in the singlet state (parapositronium) or triplet state (orthopositronium). Parapositronium has a significantly shorter half-life time (125 ps in vacuum) compared to orthopositronium (140 ns) [CD06]. As both states can convert into each other by spin flip interactions with the environment, the decay of parapositronium is far more likely ($\sim 99,7\%$ of all annihilations [CD06]) due to the half-life difference. This is particularly desired in PET as parapositronium annihilates into mainly two

(in every case into an even number) of photons. Orthopositronium however, with an overall spin of one, can therefore only annihilate in an uneven number of photons (at least three due to momentum conservation). These photons only produce erroneous events in the data acquisition.

Due to energy and momentum conservation in the two photon emission, the photons are emitted back to back carrying an energy of 511 keV each. Unfortunately, this is only true in the center of mass system. In the laboratory system of the scanner, the residual kinetic energy accounts for a deviation of the opening angle. The average kinetic energy of the positronium is dependent on the stopping material but is in the order of 10 eV [Mus95]. This leads to a Doppler broadening of the annihilation photons of around 2.5 keV [Mus95]. Thus, the opening angle of the two emission photons is 180° with a mean variance of 0.25° [CD06]. This effect is called “non-collinearity” and produces a convolution function for the position of positron emitters in data space which depends on the diameter of the scanner.

Up to this point, there are two physical phenomenons in the imaging process blurring the exact position of the positron emitters: namely the positron range and the non-collinearity.

II.6 Event Types

The majority of measurements are “single events”, where only one of the annihilation photons is recognized by the scanner and the other one is either absorbed by the examined object or the scanner support material or is scattered in a direction which is not covered by the scanners spatial acceptance. Furthermore, every photon always has a remaining probability to transverse the detection volume without an interaction. The type of event one is looking for is the case where two photons from one positronium annihilation are emitted back to back and both are measured within detector elements of a PET scanner without undergoing any scattering in advance. Thus, the detection system needs to define a time frame in which it recognizes two single events as a so-called “coincidence”. This time frame is called “coincidence window”, which dynamic range and constraints are given by the electronics and the detector type used in the PET scanner. The coincidences where the two annihilation photons are directly measured are called “true events”. In contrast, coincidences where both photons are measured within the scanner but one or both of them has undergone single or multiple elastic or inelastic scatter processes are called “scat-

tered events”.

Another erroneous event type is called “random event”, where two photons are measured by the scanner as a coincidence whereby each photon originates from different positronium annihilations. Furthermore, “multiple events” disturb the measurements if more than two photons are recognized within the coincidence window. The rate of random and multiple events is of course highly dependent on the overall activity within the scanners (FOV) and the coincidence window length. A good approximation for the random rate without knowledge about the activity, at least for scintillation based scanners, is given by [CEF⁺84], [CD06]:

$$c_R = 2 \cdot \Delta t_c \cdot s_A \cdot s_B. \quad (\text{II.6})$$

Here, $2 \cdot \Delta t_c$ is the coincidence window length and s_A, s_B are the singles rates for two individual detector elements. Multiple events are commonly rejected by the scanner electronics. For ease of understanding, all event types are summarized in Fig II.4.

II.7 Partial Volume Effect

In quantitative imaging, a problem of determining the exact local tracer uptake of an organ is given in the case that the dimension of the organ is close to the dimensions of the pixels or voxels of the reconstructed image. The two occurring misinterpretations of under- and overestimation of tracer uptake are summarized in the partial volume effect. The underestimation called “spill out” [DJS12] occurs if the surrounding tissue has a lower activity uptake than the organ of examination itself. If this is the case, the intensity in the pixel or voxel is lower than in the organ because the organ only fills a partial volume of the pixel or voxel. The other effect called “spill in” is quite the opposite. Here, the surrounding tissue has a higher activity than the organ itself, which leads to an overestimation of the local activity uptake.

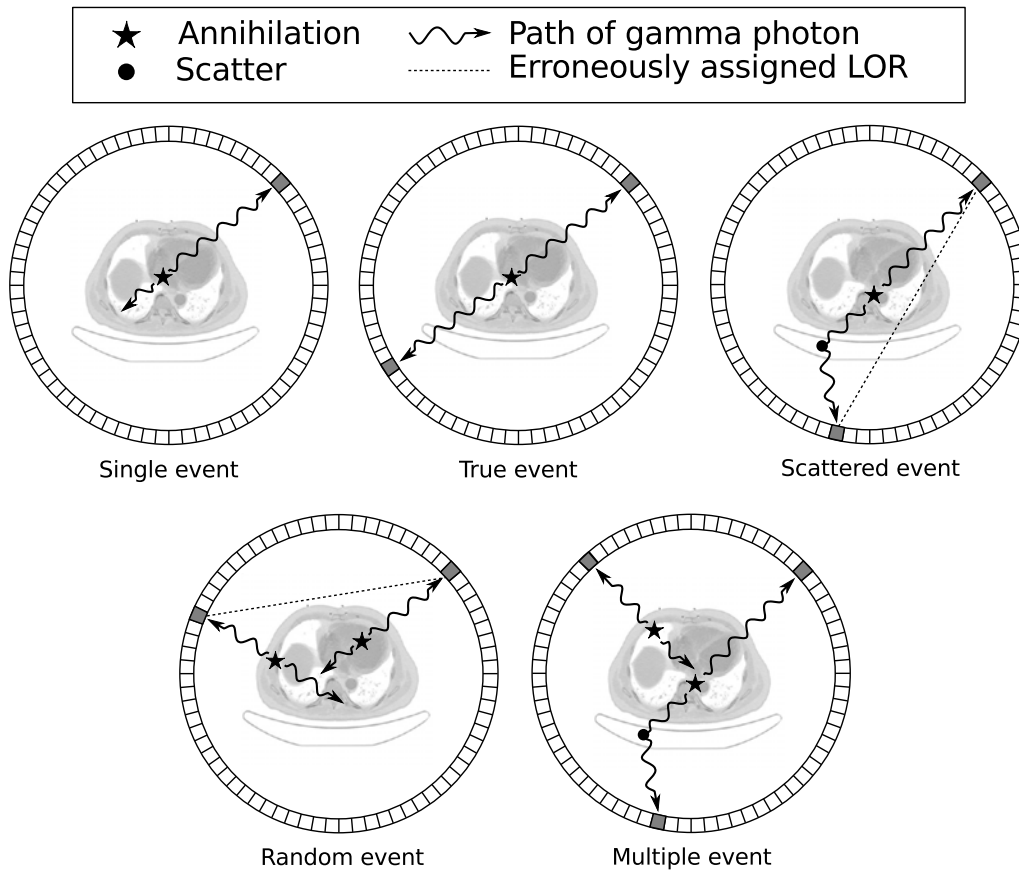


Fig. II.4: The different event types which occur in a PET examination. The differences of single, true, scattered, random, and multiple events are shown schematically in the sketches where the ring of detector elements registers the annihilation photons that are illustrated as wavy lines. The erroneous dotted lines are stored within the data set. The drawing is a modified version of [DJS12].

CHAPTER III

quadHIDAC

The quadHIDAC is a commercial PET scanner dedicated to small animal experiments developed by Oxford Positron Systems. Compared to other small animal scanners the quadHIDAC offers a larger FOV with an extent in diameter of 165 mm and in axial-length of 280 mm. This allows imaging of medium sized animals or one or more rodents at the same time. The large FOV is also profoundly beneficial if the imaging of awake moving mice [Fro12] is desired. The most powerful attribute of the quadHIDAC is its very high spatial resolution. The first version of the scanner, sold in 2000 [JB00], reached a spatial resolution of $1.08\text{ mm} \times 1.08\text{ mm} \times 1.04\text{ mm}$ [SRK⁺05], which was groundbreaking at the time. Even today, standard commercial PET scanners do not fully reach the same resolution, and only expensive research scanner developments were able exceed this value. Nevertheless, the sensitivity of the system is only moderate, which was sufficient in the past, but is not compatible with modern developments. This is most likely the reason why it is not manufactured anymore.

III.1 Detector Concept

The scanner consists of four detector heads, hence the name “quad”. In the versions of the scanner which are currently installed in the European Institute for Molecular Imaging (EIMI) and the Translational Research Imaging Center (TRIC) in Münster, each head has eight HIDAC modules resulting in an overall number of 32 single detector modules. The layout of a single detector module combines a simple multi-wire

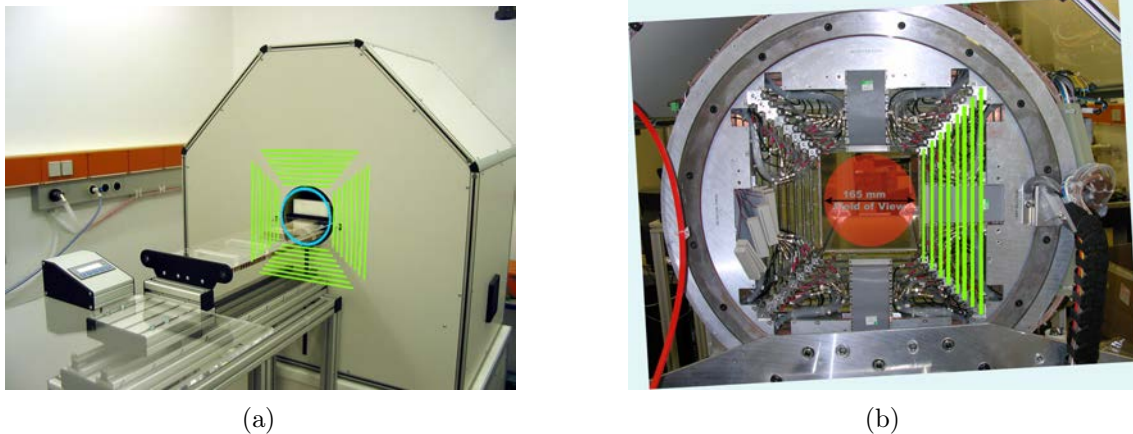


Fig. III.1: Photographs of the quadHIDAC PET System installed in the EIMI presented in a closed (a) and open (b) state. The position of the single detector modules is highlighted in green and the FOV in red. In (a), the scanner is shown together with a positioning system, which allows to move the examined subjects precisely in three dimensions [Sch13]. In (b), alongside the modules, the gas, high voltage, and cathode pad connectors as well as the surrounding rotatable gantry are also visible [Bol10].

proportional chamber (MWPC) with two photon-to-electron converters based on the HIDAC principle (Fig. III.3(a)). A photograph of the closed and opened scanner from the EIMI is illustrated in Fig. III.1. The sizes of the single modules together with their radial position and the covering solid angle of four related modules are given in Table III.1. The design of flat panel detectors is unusual in PET, where the most systems are designed in a ring setup. To overcome drawbacks which occur due to missing angles and varying efficiency depending on the impinging angle of the photon, the whole scanner can be rotated along the long-axis around 180° with a rotation speed of 6 s per half-rotation.

III.1.1 MWPC

The core of a single HIDAC detector module is a multi-wire proportional chamber. It is a successor of one of the first known radiation detectors, the *Geiger-Müller* counter. The extension to multiple wires combined with a segmented readout of cathode pads revolutionized particle tracking in the 70s [Leo87] as its development made it possible to follow and store charged particle tracks for the first time electronically. Two dimensional readout is possible either by collecting charge information on two cathode layers which are arranged perpendicular or by analyzing the signals on the

Detector Number	Module Size (mm ²)	Radial Distance to Center (mm)	Solid Angle Fraction $\frac{\Omega}{4\pi}$ (%)
1	135×280	94	64.4
2	155×280	108	61.1
3	173×280	122	57.4
4	195×280	136	54.9
5	213×280	150	51.7
6	232×280	164	48.9
7	251×280	178	46.4
8	271×280	192	44.1

TABLE III.1: Detector module sizes, positions and covered space angles. Space angle fractions were calculated with the method described in [Sch01].

wires itself and only one cathode layer, which is perpendicular to the wires. In the HIDAC, the two cathode layer solution is applied. A schematic illustration of the MWPC in the HIDAC is given in Fig. III.3(a). The 6 mm thick MWPC in the HIDAC uses 20 μm thin gold-plated tungsten-rhenium wires. At the edges, a thicker wire of 300 μm diameter is inserted on both sides which is a common method to obtain a more homogeneous electric field. The wires are spaced 1.5 mm apart. The cathode pads are 0.7 mm thick with a gap of 0.3 mm between two pads. The wires usually operate in a range of 2000-2200 V, while the cathode pads are grounded. A more detailed description about general concepts of MWPCs regarding electric fields, signal creation, operation and gas properties, and readout methods is given in [Ver10].

III.1.2 HIDAC Principle

A view of all the single components and their specifications of the HIDAC detector modules is given in the explosion drawing in Fig. III.2. A detailed description of the single components and their tasks is given in the following.

The point which distinguishes the high-density avalanche chamber from the classical MWPC is the photon-electron converter. The high density established by 60 μm thick lead sheets is necessary to achieve a high probability that at least a part of the energy of the 511 keV photon is transferred to an electron which is measurable by the MWPC. The thickness of 60 μm is optimized in such a way that electrons produced in the beginning of the sheet are able to exit it. This means that thicker foils would liberate the same amount of electrons, but the absorption of photons would be higher. This was evaluated experimentally by [Hün07], among others, and

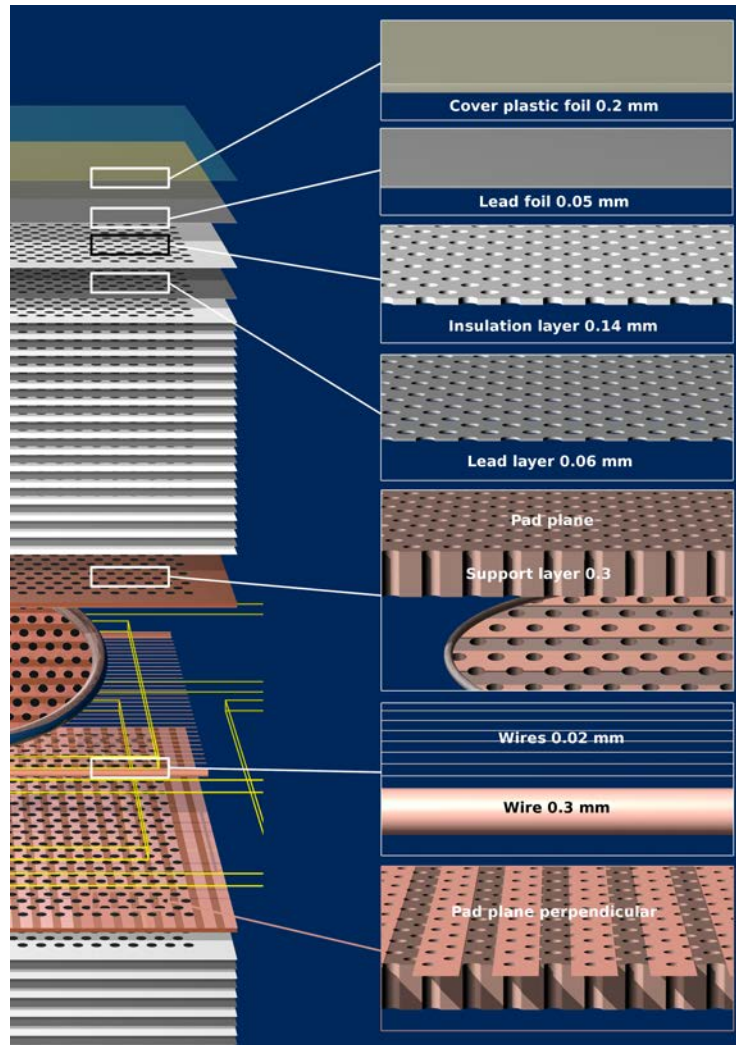


Fig. III.2: Explosion drawing that illustrates all the specifications of a HIDAC module with 32 layers of alternating perforated lead and insulation foils. The drawing was made with Cinema4D from Maxon by [Bol10].

in simulation by [Got10].

The trick of the HIDAC is to use 16 lead foils at the same time to reach an acceptable efficiency of a single detector module. Of course, the evolving electrons are not able to transverse multiple layers. Hence, the lead foils are perforated with holes which have a diameter of $400 \mu\text{m}$ and a hole to hole separation of $\sim 500 \mu\text{m}$. Since electrons which enter the gaseous holes would not be transferred naturally to the MWPC part of the detector, the lead sheets are interleaved with insulation foils which are $140 \mu\text{m}$ thick. Thus, a voltage cascade can be applied on the lead foils to form an electric field inside the holes that drifts upcoming electrons out of the holes. The

predecessor of the HIDAC was the high-density drift chamber (HDDC) [JCS75], where the difference to the HIDAC was that no insulator material was used. From an increased efficiency, it was concluded that there should be gas amplification in the holes; hence the name avalanche chamber. In the scanner version present in Münster, the first ten layers get $\sim 5\%$ potential difference between two layers and the last 6 layers $\sim 10\%$ of the overall applied negative voltage¹. A $50\ \mu\text{m}$ lead foil is used as the outermost layer, which is in direct contact with the first perforated lead sheet to get a further increase in sensitivity and a more efficient electric field. To enclose the gas volume, a $200\ \mu\text{m}$ thick plastic foil is set on top. This protects the gas inside the holes and the MWPC for impurities from the environment and keeps the valuable and unsafe counting gas inside the detector.

III.2 Detection Concept

While many of the crucial points of the detection procedure were mentioned in the last section, the focus was more on the technical side. In the following, the focus should lie on the evolution from the initial photon to the detected signal.

The initial $511\ \text{keV}$ photon most likely interacts within the converter with lead material, where the amount of photo electric and *Compton*-effects are approximately the same for this energy (Fig. II.2). Thus, single high energetic electrons are produced inside the lead. Depending on the position and the momentum direction within the lead, the single electron has a certain probability of reaching a gaseous hole. Depending on the path length inside the lead, the electron loses some of its kinetic energy but most often it is still high energetic. Hence, the electron usually moves along straight lines through the hole, since the electric field is too low to influence its track. On its way through the hole, the electron can ionize gas molecules, whereby ionization clusters with sizes from one to 20 electron-ion pairs are produced. In average the clusters contain four electrons, and the mean free path for ionization of minimum ionizing particles (MIPs) in argon is around $400\ \mu\text{m}$ [A⁺08]. Furthermore, secondary electrons from the energy loss of the primary electron inside the surface volumes of the lead or insulation material could reach the hole where they may also cause further ionization.

All low energetic electrons in the hole volume follow the electric field lines, which direct them into the MWPC region. In the lower region of the hole, the higher electric

¹The applied voltage to the converter is commonly in the range from -3000 to $-3300\ \text{V}$

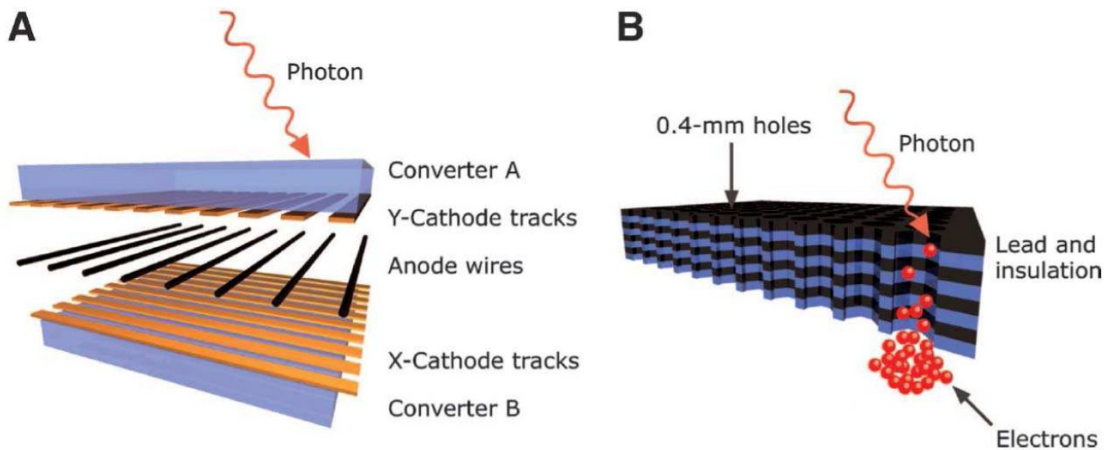


Fig. III.3: Schematic sketch that shows the principle concept of the HIDAC modules and describes its photon conversion and measurement process. A focus on MWPC with two photon converters is presented in (a) and a simplified zoom of the photon-to-electron converter with only four lead layers is shown in (b) [SRK⁺05].

field strength lead to a focus effect which guides the electrons to the central region of the hole. Maybe the electric field in the lower region also accelerates the electrons to kinetic energies able to ionize further gas molecules. Nevertheless, some of the electrons are lost as diffusion can cause that they hit the hole wall or are lost in attachment processes with gas molecules. This subject is maintained by simulations and will be discussed further in Section V.2.

The majority of electrons reaching the MWPC volume are drifted towards the vicinity of a wire. The electric field is inversely proportional to the distance from the wire. Hence, all electrons gain enough kinetic energy to ionize gas molecules approximately at the same wire distance. This results in an avalanche process, where in average the same amount of charged particles is generated for each incoming electron. The movement of the charge carriers inside this charge cloud induces a charge in the cathode pads, which can be registered electronically.

III.3 Electronic Readout

The readout cathodes are grouped in a smart pattern to multiplex the large number of readout pads to just a few readout channels. Each single pad is grouped alternating to a block or number set; the logic is illustrated in the sketch of Fig. III.4. The figure shows a multiplexing of 30 pads to eight channels whereby five even-numbered

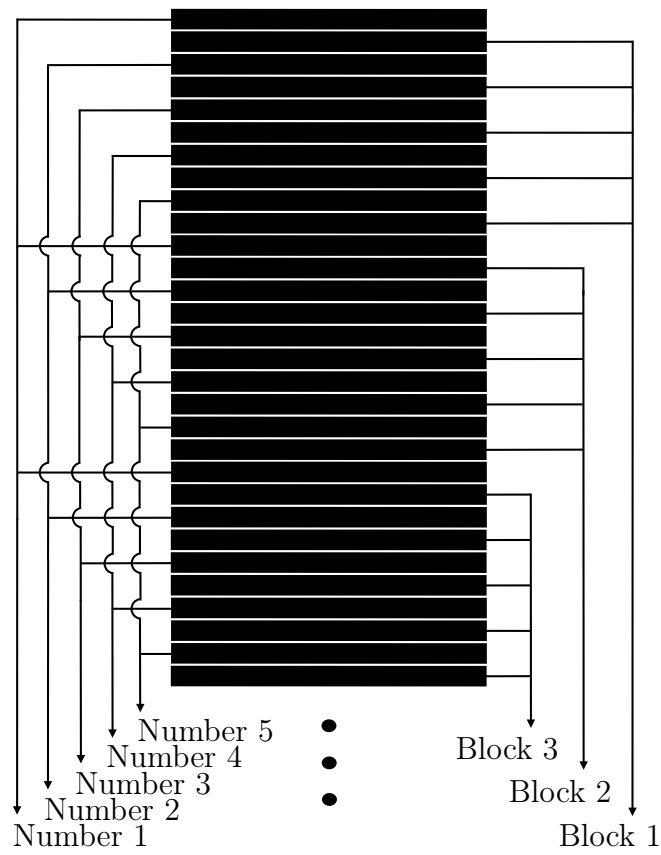


Fig. III.4: Simplified sketch of the readout pattern that is used to multiplex a large number of readout pads. The maximum charge on two neighbored pads gives a unique block-number pair. In the acquisition, the exact position is evaluated from the registered block-number pair. The conceptual idea of the drawing is taken from [Got10].

pads are addressed to one block set and three uneven-numbered pads to one channel number set. In the real setup, there are 24 channels for each readout plane of each module with twelve block sets and twelve channel number sets each. The modules are equally sized in z -direction and therefore always have 144 pads in this direction. Thus, there are twelve pads addressed to each set.

In the x, y -direction, the sizes of the modules vary leading to 70-140 pads per module. Here, twelve pads are still addressed to the block sets, but the number of pads addressed to the number sets is varying from 6-12 pads. The anode wire signal triggers the channel readout and the signals are amplified digitized and processed by a single electronic board for each module, which are all placed behind the single detector heads. The position determination is done with the center-of-cluster method [FHJ⁺76], where the 700 μm wide cathode strips with a 1 mm separation

combined with the block readout reaches sub-millimeter resolution². After each single hit, the readout processing causes a dead-time of 160 ns. The final data processing is done by a main board, which is placed on top of head 1 (Fig. IV.2). It is triggered when two module boards on opposite detector heads registered single hits. This process adds a further dead-time after coincidences of 400 ns. Furthermore, the main board streams the output onto a list-mode data file which is stored on a computer. The quadHIDAC list-mode file format consists of an ASCII header, where information about the date and system parameters like module number, converter size and position, angular and modular sample binning, and binning offsets are defined. Behind the header the coincidence information is listed event by event, hence the name list-mode data. The single coincidence is stored in a 10 byte segment, where the first two bytes give the detector gantry angle and each coordinate is stored in four byte segments. The gantry angle is constrained to 180° and encoded for the default setup in 3180 single steps. The following sequence of the four byte segments is as follows:

$$00\mathbf{d}\mathbf{d} \mathbf{y}\mathbf{y}\mathbf{y}\mathbf{y} \mathbf{y}\mathbf{y}\mathbf{y}\mathbf{y} \mathbf{y}\mathbf{y}\mathbf{y}\mathbf{y} \mathbf{c}\mathbf{c}\mathbf{c}\mathbf{c} \mathbf{x}\mathbf{x}\mathbf{x}\mathbf{x} \mathbf{x}\mathbf{x}\mathbf{x}\mathbf{x} \mathbf{x}\mathbf{x}\mathbf{x}\mathbf{x} \quad (\text{III.1})$$

where the detector head number \mathbf{d} is written in two bits, the \mathbf{x} and \mathbf{y} coordinate is written in 12 bit words where the position information is stored in 125 μm bins and the distinct converter number \mathbf{c} is stored in four bits. A detailed description and an example macro to read the file format is given in [Kae01]. Furthermore, every half a second a time tag is written to the file indicated by a negative one as angle value. Every two seconds, a list consisting of a single counter, a total counter, and a valid counter for each module as well as the overall coincidence and random number is written to the file, whereby each counter is indicated by a negative angle value ranging from -4047 to -4096.

III.4 Gas Support

The quadHIDAC system uses a mixture of argon and diisopropyl ether ($\text{C}_6\text{H}_{14}\text{O}$, DIPE) as counting gas. DIPE is used as an organic quenching gas which preserves the chamber against early discharge, since the large molecules are able to absorb de-excitation photons from the argon atoms, which would be able to liberate electrons from the electrode surfaces. It is a volatile organic compound. The gas mixture is

²More precise position determination algorithms like center of gravity or weighted displacement methods (explained in [Ber11] and [Ver10]) would reach higher resolutions, however, signal amplitudes of each channel must be determined.



Fig. III.5: Photograph of the cupboard located underneath the quadHIDAC. It contains a fridge with a vapor used for the gas supply and the high voltage power supplies (not shown here) [Bol10].

provided by flushing argon through a vapor which is filled with liquid DIPE. The vapor is stored in a fridge at a temperature of 10.2°C to assure a constant fraction of DIPE inside the counting gas. A photograph of the vapor in the fridge is illustrated in Fig. III.5.

Argon is bubbled through the vapor with a flow of around 200 sccm^3 and a pressure of 100 kPa . Behind the vapor, the gas supply line is split parallel with the use of gas impedances which assure an equally distribution on the different sized modules. Thus, each module is flushed with $\sim 6.25\text{ sccm}$. The benefit of using DIPE as quenching gas is that for the large molecules, the probability for ionization induced by the primary electrons is increased and that the reachable gain is increased, since more penning transfers are expected in DIPE compared to CO_2 . In the penning transfer, an excited argon atom ionizes a quencher molecule which should cause up to twice as many ionizations within the holes in the primary ionization process. The drawback of DIPE is that it is more difficult to handle, as it tends to build explosive peroxides, it is an anesthetic, and slightly toxic. Therefore, it was decided to omit the use of DIPE as quenching gas in test setup measurements (Chapter VI). Furthermore, the application of the gas leads to stronger aging effects of the detector modules since the molecules tend to form polymers which accumulate on the wires, cathode pads, and inside the holes. These aging effects made detector restoration work on single HIDAC modules necessary, which are presented in [Bol10].

³sccm $\hat{=}$ standard cubic centimeter per minute

III.5 Other Small Animal PET Scanners

Many different detector types are able to measure 511 keV photons. While in research most of them have been tested either for preclinical or clinical approaches, nowadays all commercial systems are based on inorganic scintillation crystals. At the moment, three main approaches for small animal imagers are on the market. The traditional way employs granulated crystal blocks, which are read out by photo multiplier tubes (PMTs) in anger logic⁴ (Siemens, Mediso). To stop the majority of annihilation photons, generally 2 cm thick crystals are necessary. However, in preclinical imaging, often only 1 cm thick crystals are used to constrain the so called depth-of-interaction (DOI) information to the crystal thickness to stay at acceptable image resolution.

The second long-time experienced concept for small animal PET obtains increased DOI information by the use of a double layer of crystals which reduces the negative influence of parallax errors⁵ (Sedecal). The third promising approach uses monolithic crystals with position sensitive photon sensors, where the spatial distribution of the light signal and the timing of each photon interaction is used to reconstruct the three dimensional position of the primary interaction of the 511 keV photon (Bruker). All these design concepts have their inherent advantages and drawbacks and are currently roughly head-to-head in terms of spatial resolution and coincidence sensitivity, which will be shown below. While a detailed comparison and description of the detection principles is beyond the scope of this chapter, it is intended to give an idea about the difficulties to compare the different scanner types and to get accustomed to some performance benchmarks.

The National Electrical Manufacturers Association (NEMA) develops measurement protocols which are suggested to fairly compare different electrical equipment and medical imaging products. The latest standard dedicated for small animal PET scanners is the NEMA NU 4-2008 protocol [NEM08]. In the following, results from several publications that report about spatial resolution and sensitivity measurements of current preclinical scanners will be presented and discussed.

⁴The anger logic reconstructs the 2D position of the photon interaction with at least four PMTs on a higher pixelated crystal array. From the weighted light signal sharing between the PMTs, the position can be easily calculated.

⁵The parallax error typically arises in ring geometries of PET scanners. For central placed sources, all lines of response (LOR) impinge edge on to the crystals and therefore the DOI position does not effect the measurement. For off-centered sources, this is not the case and the missing DOI information leads to errors in the LOR positioning.

III.5.1 Spatial Resolution

To compare the spatial resolution performance, the NEMA NU 4-2008 standard proposes to measure a ^{22}Na point source, embedded in a cube with an edge length of 1 cm, positioned at four different radial offsets for two different axial positions whereby one axial position is the center of the FOV and the other is one-fourth of the axial FOV from the center. In the next step, the data should be reconstructed with either 2D or 3D filtered backprojection (FBP) without any smoothing filters and tabulated values for the FWHM⁶ and FWTM⁷ of slice projections for the separate directions should be reported for each position. Even though the protocol already constrains a huge number of parameters, there are still some flexible settings like energy and timing windows, rebinning techniques or maximum ring difference (MRD)⁸. Furthermore, not all systems allow one to access the complete data necessary to produce the benchmarks suggested by this standard, e.g., if no list-mode or sinogram data is available.

A comparison between different modern and older scanners following the NEMA standard was done by *Goertzen et. al* [GBM⁺12]. Since the tabular with all calculated values for the examined scanners is quite difficult to compare, the authors also calculated the average FWHM_{ave} values as the geometric mean by [GBM⁺12]:

$$\text{FWHM}_{ave} = \sqrt{\left(\frac{\text{FWHM}_{rad.,center} + \text{FWHM}_{rad.,1/4}}{2}\right)\left(\frac{\text{FWHM}_{tan.,center} + \text{FWHM}_{tan.,1/4}}{2}\right)}, \quad (\text{III.2})$$

here $\text{FWHM}_{rad./tan.,center}$ are the according radial and tangential values at the axial center and $\text{FWHM}_{rad./tan.,1/4}$ are the respective values for the 1/4 axial position. With these definitions the plot illustrated in Fig. III.6 was derived. The averaged spatial resolution shows a strong increase in the case of larger radial source offsets due to the parallax error. The system performance for scanners developed before and after 2003 can be clearly distinguished, whereby systems after 2003 achieved averaged FWHMs from 1.5 to 2.1 mm and devices developed before 2003 values between 2.0 to 2.9 mm. In the comparison of the performance of the Inveon (Siemens without DOI) and the Argus (Sedecal with DOI), scanner it is presented that a system with DOI information leads to a less strong degradation of spatial resolution for larger source offsets than for systems without DOI.

⁶FWHM $\hat{=}$ full width at half maximum

⁷FWTM $\hat{=}$ full width at tenth maximum

⁸The maximum ring difference is the maximal allowed axial distance of the two single interaction positions of a LOR.

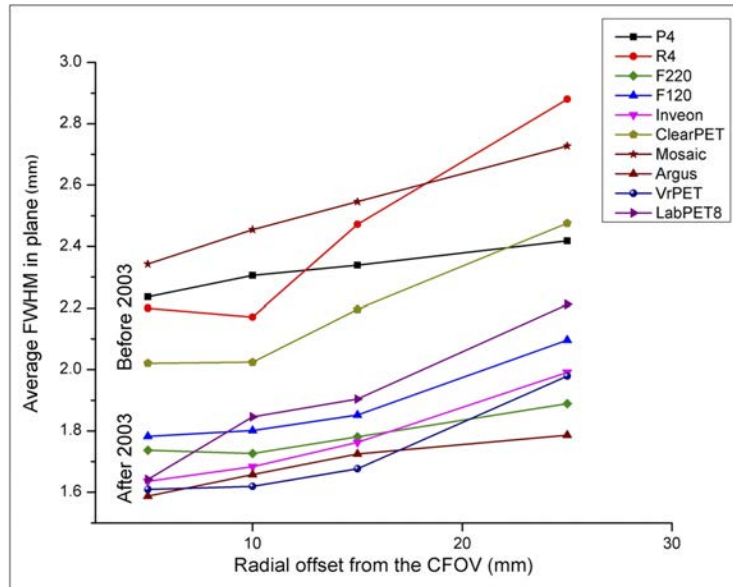


Fig. III.6: Spatial resolution performance measurements performed following the NEMA NU-2008 protocol. Average FWHM is calculated for preclinical scanners which have been developed before and after 2003. In the measurements a point source is measured at different radial positions where the degradation of spatial resolution for off-center sources is presented [GBM⁺12].

Plots for the separate radial and tangential performance for the central axial position of state-of-the-art preclinical scanners were edited by *Nagy et al.* [NTM⁺13], which is shown in Fig. III.7. Here, also the two newest systems from Mediso are compared whereby it has to be remarked that the authors are in a collaboration with the company. It is visible that along the radial direction the decline in spatial resolution for off-centered sources is much more pronounced than in the tangential direction. This is explained by that fact that, for the tangential direction, mainly the detector elements in the source-offset direction are responsible for the resolution. This is due to the fact that, for these crystal elements, the photon direction is nearly edge on to the crystals, which leads to a small parallax effect. Interestingly, the systems from Siemens and Sedecal provide constant or improved resolution for off-centered sources in the tangential direction.

Regarding the spatial resolution in the axial direction, the values were not determined for all systems presented in the two publications. The influence of the axial FOV of the scanner's spatial resolution will here be demonstrated by the example of the Inveon scanner which was examined in the work of *Visser et al.* [VDB⁺09]. In the study, 36 measurements of a ^{22}Na point source on transaxial

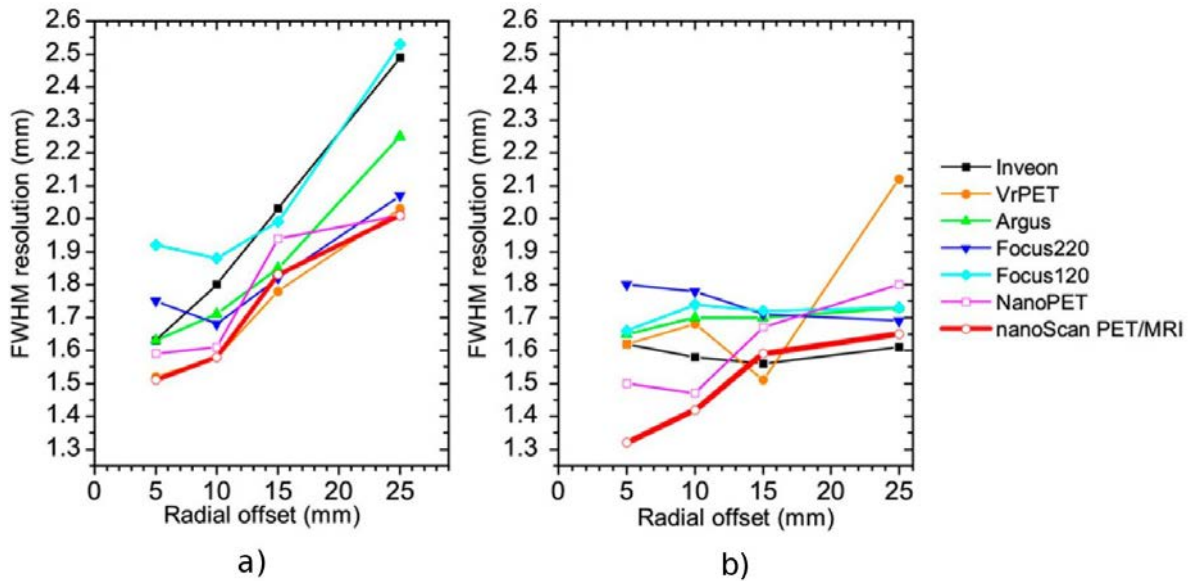


Fig. III.7: Spatial resolution measurements made for different modern small-animal PET scanners for sources on the central axial position with a radial offset from 5-25 mm [NTM⁺13]. The radial degradation of the spatial resolution is clearly visible for the FWHM along the radial direction (a) and also visible, but less pronounced, if determined for the tangential direction (b).

positions, ranging from -7 to 46 mm relative to the center of the FOV, were examined for the evaluation. The MRD is given in units of crystal rings whereby the maximal number of rings is 79 and the data was analyzed for five different MRD settings. The results of this study are illustrated for the different spatial directions in Fig. III.8. The spatial resolutions in the radial and tangential direction show no observable difference in regards to the MRD variation and, therefore, only the results for the full MRD are plotted. In the axial direction, instead, the degradation of spatial resolution for larger MRDs is quite strong, whereby the FWHM ranges from 1 to 2 mm for the central position and from 1.3 to 2.9 mm for a radial offset of 46 mm for variations from 1 to 79 MRD. The reason for the spatial resolution degradation in the axial direction is similar to the parallax error in the radial direction and therefore called axial parallax error, also induced by the missing DOI measurement. In this case, the error becomes larger in the case that the photon interaction position is further away from the annihilation position, as the impinging angle of the photon to the crystal surface increases. Another problem which causes the axial spatial resolution blurring is the limitation of binning methods necessary for the FBP reconstruction [VDB⁺09].

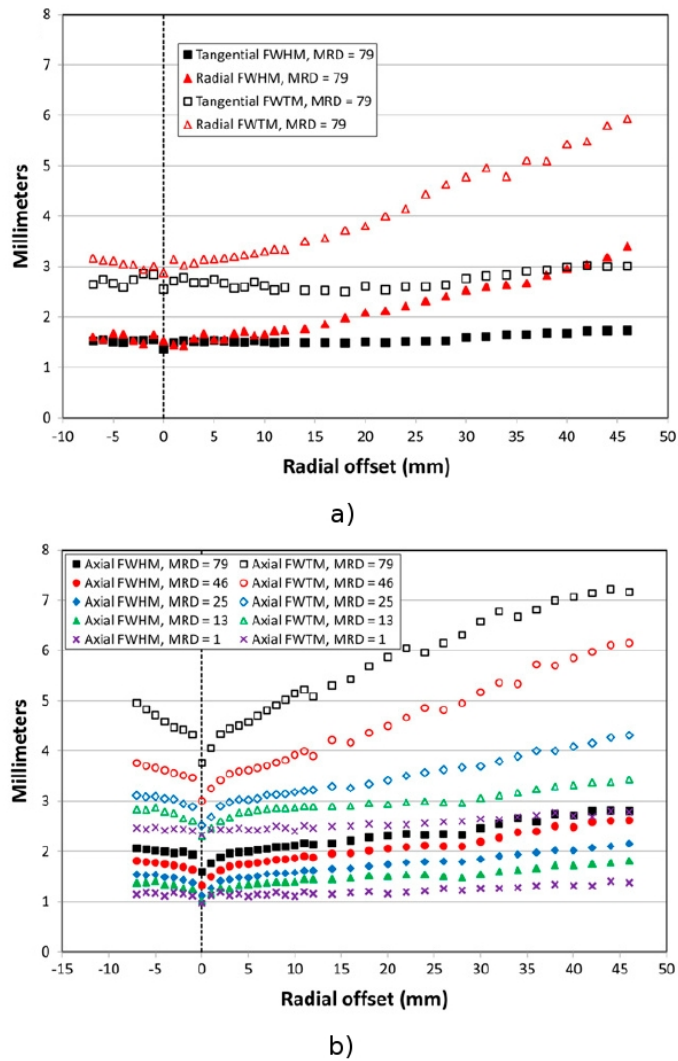


Fig. III.8: Spatial resolution measurements for the different direction orientations made on the example of the Inveon scanner from Siemens. In (a), the FWHM and FWTM are compared for the radial and tangential direction whereas in (b) the spatial resolution for the axial direction is presented. While the maximum ring difference (MRD) has a negligible influence on the radial and tangential direction, which is not shown here, it has a strong influence in the axial direction [VDB⁺09].

III.5.2 Sensitivity

For a comparison of the coincidence detection sensitivity for different small animal PET scanners, the NEMA NU 4-2008 suggests to step the same source which is used for the spatial resolution measurements on the transaxial center along the axial direction. The activity of the source should be low enough to constrain the amount of

TABLE III.2: Comparison of sensitivity performance measured for different small animal scanners. Sensitivity values were measured under different conditions and were taken mainly from [NTM⁺13].

Scanner	Peak absolute sensitivity (%)
nanoScan PET/MRI (Mediso)	8.4
NanoPET/CT (Mediso) [SMP11]	7.7
Inveon (Siemens) [VDB ⁺ 09]	10.1
microPET Focus220 (Siemens) [TRD ⁺ 05]	3.0
Argus (former Vista) (Sedecal) [WSB ⁺ 06]	4.0
Albira (Brucker) [SKLF14]	6.3

randoms to be below 5%. The measured coincidences shall be binned according to the slice in which the source is positioned. The step size between the single measurements should be the same as the bin size of the according sinogram binning. Besides a background correction for each slice on the basis of an empty measurement, the protocol requests to account for a part of random and scatter events by the application of a mask on the acquired sinogram, whereby only the events in a 2 cm range around the highest pixel of each sinogram row should be considered. While manufacturers commonly advertise their absolute peak sensitivity, the NEMA standard only demands the report of total and absolute sensitivity for defined mouse and rat axial lengths, as well as the total sensitivity for the whole FOV. Additionally, the sensitivity profile should be illustrated. Just as for the spatial resolution, no recommendations for the energy or time windows or MRD settings are given.

In the examined publications, it is not clearly stated whether the suggested sinogram masks were applied properly. However, calculated values for modern scanners are reported in [GBM⁺12] and [SMP11].

A comparison of the absolute peak sensitivity for different scanners is reported in [NTM⁺13] where the according values, combined with a value for the Albira system, which is the only commercial preclinical scanner based on the monolithic crystal approach, are presented in Table III.2. As stated above, the absolute peak sensitivity is not a benchmark recommended by the NEMA and all the values were acquired under different conditions (source, energy and time windows). The comparison, however, gives an idea of the different sensitivity performances. In a next step, the difficulty for the comparison with the absolute peak sensitivity will be demonstrated by the example of the Inveon scanner. Following [VDB⁺09], the man-

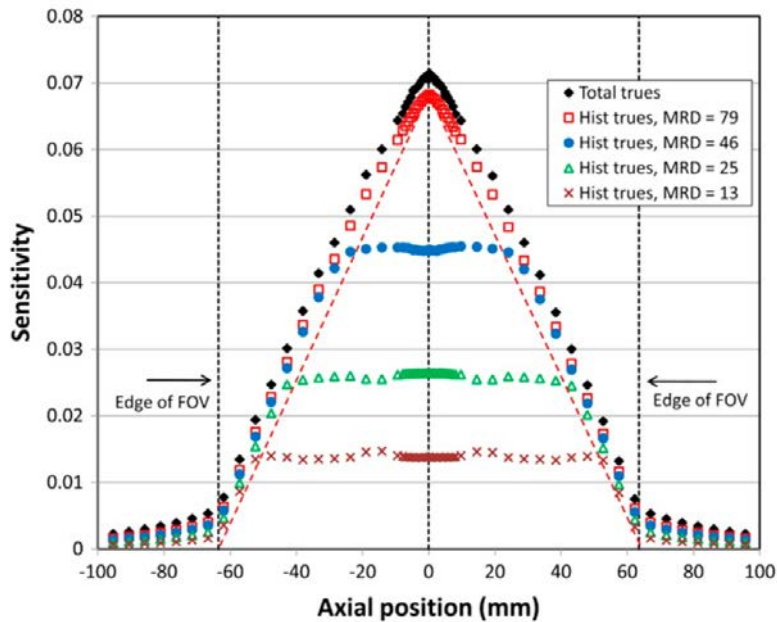


Fig. III.9: Sensitivity performance measured for the Inveon small animal PET scanner. Sensitivity measurements were taken for different positions of a point source along the axial axis and an energy window from 350-650 keV. A strong sensitivity decline is given for lower values of the maximum ring distance (MRD) [VDB⁺09].

manufacturer specified a sensitivity of greater than 10%, which was validated in the article for the largest energy window (250-750 keV) and direct coincidence counting. For a smaller energy window (350-650 keV) and binned data, the peak sensitivity already degrades to around 7%, as it can be seen in Fig. III.9.

Moreover, the peak sensitivity is most often calculated for a maximal setting for the MRD while for spatial resolution measurements a small value is chosen. Since the MRD has a strong influence on the spatial resolution in the axial direction, shown in Fig. III.8; this implies that the system cannot be operated in high resolution and high sensitivity mode at the same time. The strong decline in peak sensitivity for reduced MRD settings is also presented in Fig. III.9. For a moderate MRD of 13 rings, the peak sensitivity drops to only $\sim 1.5\%$ in the center of the FOV.

III.5.3 Comparison to the HIDAC Performance

In conclusion, it was presented that even with an elaborate standard, the comparison of different detector technologies cannot unambiguously taken out. In terms of spatial resolution, the HIDAC is still one of the best systems, considering the measurements from *Missimer et al.* [MZH⁺04] at the center of the the FOV and

especially the best system for off-centered positioned sources. In terms of absolute peak sensitivity, the HIDAC only reached a value of around 1.5% [SRK⁺05]. However, compared to the Inveon scanner, this is a head-to-head result in the case that the scanner is operated in high resolution mode. Of course, the HIDAC does not have the ability to increase sensitivity by reducing the spatial resolution. Nevertheless, in combination with the uniform spatial resolution within the large FOV, given by the precise DOI information of 3.2 mm (constrain of the photon interaction position to photon-converter level), this renders the quadHIDAC as the best choice for high resolution applications.

CHAPTER IV

Monte-Carlo Simulations and Geant4

IV.1 Monte-Carlo Methods

The use of Monte-Carlo methods proved its inalienability for many applications in scientific research as well as in financial, industrial, and many other sectors. Algorithms using the Monte-Carlo technique belong to the group of randomized algorithms (RA) which are defined by the use of one or multiple random number generators (RNG) within their processing. RAs themselves also include Las-Vegas algorithms, whereby the difference is given by the definition that Las-Vegas algorithms are forced to provide only true answers, whereas Monte-Carlo algorithms are not restricted by this constraint but have to give the correct output within a distinct probability. In contrast to the RAs, there are the deterministic algorithms which can only give correct output, since they are derived analytically and occupy all possible states in the phase space.

From these definitions, one can derive that Monte-Carlo methods would be the worst method to solve any given problem, but this is only true if an analytical solution exists or a correct solution is obtainable in finite time. Furthermore, if both are the case the application of a Monte-Carlo method can be much more efficient regarding the costs of the algorithms. Complexity can be reduced and usually handled more reliably in Monte-Carlo methods, whereas carelessly applied approximations often result in incorrect output for the other algorithms. Additionally, the method is extremely important if no analytical solution to a given problem exists.

In the case of simulations, we often regard systems where the theoretical or analytical treatment of the system is too complex. Hence, a model is built which should resemble the system insofar as that the model response is only allowed to deviate from the real system answer within a required precision.

Regarding experimental physics, various simulation packages, including Monte-Carlo methods, which are essential tool-kits especially in detector development are available. They consider relevant physical processes within the detection processes and offer great benefits for the detector developers because optimal parameter sets for specific applications can be retrieved before first experimental trials are taken out.

IV.1.1 Pseudorandom Number Generation Methods

It is time consuming and exhausting to derive random numbers from physical processes. Of course, lists of generated numbers can be stored, but using those lists is very inflexible as huge amounts of numbers are commonly needed, and it is hard to prove whether no errors occurred during number acquisition. Therefore pseudorandom numbers, which are derived by analytical methods, are used for most applications. These numbers only appear to be random. In reality, they are fully deterministic and reproducible and therefore only “pseudorandom”.

Simple Generators

The most common, very simple pseudorandom number generator (PRNG) is the multiplicative linear congruential generator (MLCG), which derives its numbers from the following recurrence relation:

$$X_{n+1} = (aX_n + c) \bmod m \quad (\text{IV.1})$$

where X gives the sequence of pseudorandom values, a and c are parameters, and m is the basis. The period length of such a generator is always smaller or equal to m . To obtain a full period length a, c , and m have to fulfill three simple requirements given by the Hull-Dobell Theorem. The sequence of pseudorandom numbers X needs an initial value X_0 named seed. Commonly the basis m is chosen to be as high as possible, resulting for 32-bit systems in period lengths of a little bit lower than 2^{32} . Hence, a fair period length can already reached with such a simple method,

which is sufficient for many daily problems. Nevertheless, many applications need longer period lengths and even more importantly, it was shown by Marsaglia that coordinates produced sequentially by those generators accumulate on hyperplanes if placed in a multidimensional space. This means that the subsequent elements of the sequence are correlated [Mar68].

Further important examples of simple PRNGs are the lagged Fibonacci¹ or Xorshift generators.

All simple PRNGs fail the majority of randomness tests² which have been developed to prove the quality of a random generator. Thus, more sophisticated PRNGs are needed for profound Monte-Carlo methods.

Very Long Period Generators

Since an incredible number of advanced PRNGs is used in high energy physics (HEP) [Dem11], we want to focus now on two important examples where the concepts of the RANMAR generator should be described in a concise systematic way as a model example. Also, the *Mersenne Twister* should be discussed roughly to clarify similarities and deviations of different very long period PRNGs. Higher level PRNGs are commonly established by carefully combining two or more simple PRNGs. Furthermore, they often need larger initialization arrays as seed, which can be filled by simple PRNGs or real physical RNGs. In the following, the RANMAR generator is presented. This is the default PRNG in CLHEP³ where a C++-Version is used from the former FORTRAN implementation introduced by F. James [Jam90]. The generator uses a lagged-Fibonacci generator

$$x_1, x_2, x_3, \dots, \text{ with } x_n = x_{n-r} \cdot x_{n-s} \quad (\text{IV.2})$$

with a binary operation $x \cdot y$, combined with a simple arithmetic sequence

$$I - k, I - 2k, I - 3k, \dots, \text{ mod } m \quad (\text{IV.3})$$

with initial integer I and decrement k . For software implementation the binary operation of the Fibonacci generator was chosen to

$$x \cdot y = \{\text{if } x \geq y \text{ then } x - y, \text{ else } x - y + 1\} \quad (\text{IV.4})$$

¹Lagged Fibonacci methods use two lagged elements of the sequence, whereas the original Fibonacci series only uses the direct two previous elements

²A set of elaborate randomness tests is summarized as BigCrush-Tests in the TestU01-Suite

³CLHEP $\hat{=}$ a class library for high energy physics

and the arithmetic sequence (IV.3) can be written in a similar way by

$$c \circ d = \{\text{if } c \geq d \text{ then } c - d, \text{ else } c - d + e\} \quad (\text{IV.5})$$

with parameter e , leading to the recurrence expression

$$c_n = c_{n-1} \circ f \quad (\text{IV.6})$$

with decrement f . The combination of the two generators can than be simply achieved by $U_n = x_n \bullet c_n$.

A point that was neglected so far is that the generator needs a seed array of 97 values. To make the generator user friendly, these seed values are generated once in the beginning by a further, slower generator. The used procedure involves one 3-lag Fibonacci and a MLCG generator. The explicit description is beyond the scope of this chapter, and the interested reader is referred to [MZT90].

Another very popular, very long period PRNG is the *Mersenne Twister*. It is the default generator of `Matlab`, `Python`, `Ruby`, `R`, `PHP` and an optional generator for `Geant4`, `ROOT`⁴, and `C++`. It heavily uses XOR and Shift operations, meaning that the generator somehow consists of multiple simple Xorshift generators. Compared to the RANMAR generator, it uses a significantly longer seed array with 624 elements, which needs more memory. However, this has the advantage that the elements can be chosen arbitrarily, meaning that in principle, every PRNG, including physical ones, can be used to initialize the seed array. However, with the recommended initialization PRNG for the seed array, the generator has an impressive period length of 2^{19937} .

Obviously, generators have many different properties which make unique ones preferable for specific applications. Properties like good distribution, long period, repeatability, long disjoint subsequences, portability, and efficiency [Jam90] should be optimized for a universal generator. Since no generator is superior in all properties at the same time, many different PRNGs exist.

IV.1.2 Sampling of Probability Distributions

The PRNGs presented above produce uniformly distributed random numbers in the range of $[0,1)$. This is sufficient as from this distribution, random variables following

⁴ROOT $\hat{=}$ rapid object-orientated technology. A data analysis software.

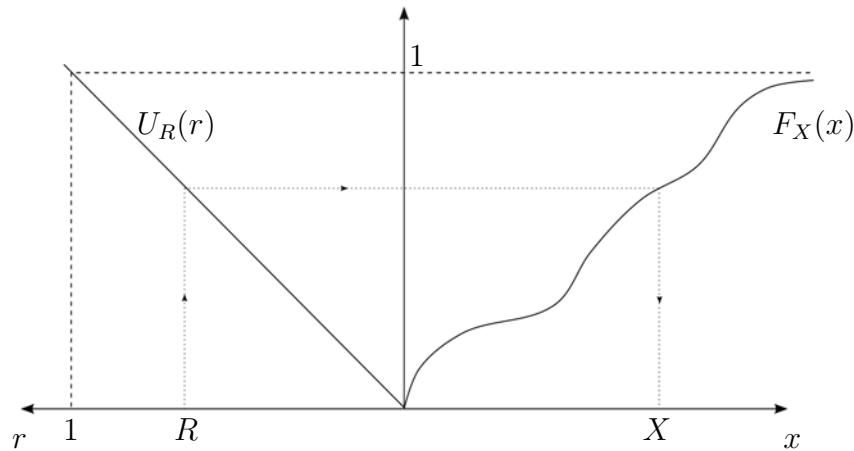


Fig. IV.1: Principal description how to sample a random variable X from an arbitrary pdf given the cdf of a uniform distribution $U_R(r)$. The conceptual idea of the drawing is taken from [MM02].

arbitrary probability distribution functions (pdf) can be produced by a technique from [MM02] which will be described in this section.

Let X be a random variable following any pdf $f_X(x)$ with

$$f_X(x) \geq 0 \quad ; \quad \int_{-\infty}^{\infty} f_X(x') dx' = 1 .$$

If $f_X(x)$ is integrable and continuous a corresponding cumulative distribution function (cdf) is existing giving the probability that X is below or equal its variable:

$$F_X(x) := \int_{-\infty}^x f(x) dx \hat{=} Prob\{X \leq x\} .$$

Following these definitions for a uniform distribution $U[0,1)$ which can be given from one of our PRNGs generating a random variable R one obtains for the cdf

$$U_R(r) = Prob\{R \leq r\} = r .$$

To derive now the random variable X of a desired pdf $f_X(x)$, its cdf $F_X(x)$ has to be invertible (this is often the case as $F_X(x)$ is per definition a non-decreasing function) by just calculating $X = F_X^{-1}(R)$ (Fig. IV.1). Thus, we get for the cdf:

$$F_X(x) = Prob\{X \leq x\} = Prob\{F_X^{-1}(R) \leq x\} .$$

Applying F_X on the right hand side leaves the disequality as F_X is an increasing function. Also $F_X(x) = r$ is given and we observe

$$F_X(x) = \text{Prob}\{R \leq F_X(x)\} = \text{Prob}\{R \leq r\}$$

which equates the fundamental relationship of the inverse transform:

$$F_X(x) = U_R(r) \quad \text{and} \quad R = \int_{-\infty}^x f_X(x') dx' . \quad (\text{IV.7})$$

This shows that one can derive random variables X from any pdf from a uniform distributed random variable R lying in $[0,1)$.

In the case that $F_X(x)$ is not invertible or the inversion is not known, a common method is to interpolate the cdf by an invertible polygonal function. Another possibility is the simple “rejection and composition method” [SV94], which discards inappropriate random values and is therefore less effective regarding computation time. This method is commonly used if a discrete pdf distribution is given.

IV.2 **Geant4**

IV.2.1 **The Geant4 Framework**

The geometry and tracking (**Geant4**) framework is a particle transport model platform making heavy use of Monte-Carlo techniques. The software package was primarily developed for HEP experiments to forecast the response of large and complex experimental setups and to design the geometrical dimensions of a detector layout able to reach required precisions. Nowadays, **Geant4** or one of its predecessor is used for nearly every HEP experiment and also shows an extensive use in many physics fields, as well as in medical and space science [AA⁺03]. Based on the object oriented programming language C++, its concept groups distinct models and processes into classes and objects. The modular class structure allows the user to establish experimental geometries and to control processes, models, and scorings on different levels. Relying on an open source code, the user is furthermore able to do even interventions beyond the established implementations or to modify implemented models.

Processes, Models, and Particle Transport

Here, a “process” means a distinct physical interaction. **Geant4** needs the total cross section for the distinct process to calculate which process (of the multiple available

ones for each particle) should occur. The unique interaction itself is implemented in the form of a “model” which can be derived from theoretical derivations, parameterizations on experimental results, or also semi-empirical models. Thus, different models can be assigned to a single process. Furthermore, the cross section necessary to determine the occurrence of a process is given by models.

The tracking inside **Geant4** is realized by the “differential approach to particle transport” [AA⁺13]. To calculate the distance from the origin to a specific process, the mean free path λ is calculated for a specific material by

$$\frac{1}{\lambda(E)} = \rho \sum_i \left(\frac{x_i \sigma_i(E, Z_i)}{m_i} \right), \quad (\text{IV.8})$$

where σ_i is the cross-section on isotope i of mass m_i that has the mass fraction x_i in the material with density ρ .

Assuming that the particle travels n_λ times the mean free path λ for a heterogeneous detector. Then it can be shown that for a random value n_r for the cdf follows:

$$\text{Prob}\{n_r \leq n_\lambda\} = 1 - e^{-n_\lambda}. \quad (\text{IV.9})$$

Following the inverse transform method from Section IV.1.2, the inversion is needed and one gets

$$n_\lambda = -\log(1 - \epsilon), \quad (\text{IV.10})$$

where ϵ is a random value from $U(0, 1]$. Due to the symmetry of U around 0.5 one can sample n_λ simply by $-\log(\epsilon)$. As the cross section is dependent on the particle energy and on the transversed medium n_λ , is updated after each step Δx by the relation:

$$n'_\lambda = n_\lambda - \frac{\Delta x}{\lambda(E)}. \quad (\text{IV.11})$$

Classes

Geant4 distinguishes between two classes. On the one hand there are the initialization classes, which are valid for the global simulation and must be set in advance. On the other hand there are the action classes, which are called on demand during event processing.

- **User Initialization Classes**

The initialization classes are mandatory for each application as no default classes are set.

- **Detector Construction**

The class defines the geometry and materials of detector elements as well as declaration of target objects and support infrastructures e.g., cooling systems or electric readout.

- **Physics List**

The different physical processes for every particle which should be considered by the simulation must be defined here. Hence, processes which are not subject to the foreseen analysis should not be selected to improve computation time and the user can select different models which are called by the focused processes.

- **User Action Classes**

The action classes handle the processing during the simulation. The user is able to control the processing in each step.

- **Primary Generator Action**

This is also a mandatory class which has to be set, since this class defines the set of particles which should be tracked by the simulation. Initial values for source distributions of particles, kinetic specifications, and momentum directions are selected in this class. All other action classes have default versions able to run the simulation directly. Nevertheless, they have to be modified to optimize processing and to control the simulation output.

- **Run Action**

This is the global control structure which conducts single events through space by calling and building geometries from the construction class. Furthermore, it calls the processes from the physics list and processes the events.

- **Event Action**

The event action is directly called at the beginning and end of each event. In the class, histograms for each event can be established and addressed before all primary particles are converted into track objects and sorted to their stacks.

- **Stacking Action**

All track objects initialized or produced during an event are pushed on

stacks with different priority and each track object is processed gradually following the initiated ordering.

– **Tracking Action**

The transport of particles through the simulation is recorded in track objects. The track information of each particle is updated after each step.

– **Stepping Action**

The stepping action invokes physical processes from the physics list and calculates the update information for the track. Single processes are handled either by `AtRestDoIt`, `AlongStepDoIt`, and `PostStepDoIt` actions or combinations of it. Therefore, a single step is completed if the probability for a `PostStepDoIt` call was calculated, the step reaches a volume boundary, or the particle lost all its kinetic energy on the track.

IV.2.2 Implementation of the quadHIDAC Geometry

The design of the quadHIDAC was presented in Chapter III. The first implementation of the quadHIDAC geometry in `Geant4` was done by *H. Gottschlag*, and for a more detailed description of the original version, the reader is referred to [Got10]. In this section, the general implementation will be roughly discussed, and then the extensions which were added to the existing code are presented in more detail.

General Concept of the Implementation

The detector geometry comprises four heads, shown in Fig. IV.2(left). Only two heads are implemented in the simulation, and the missing two heads are simulated by switching the x - y coordinates of the source volumes. The detector construction class of `Geant4` underlies the principle of placing daughter volumes in mother volumes to construct the detector setup. Thus, the heads and the source volumes are assigned to a global world volume. Each head consists of detectors called “layers”, each filled with two cover foils, encapsulation material, and so called “absorbers” building the two photon-electron converters and the gas volume of the MWPC. The absorbers themselves are subdivided in 16 layers, whereby each layer is split up into pixel elements containing a lead and insulation material box. Inside each box, a gaseous hole is placed at the central position. A visualization of a $5 \times 5 \times 12.4 \text{ mm}^3$ large piece of a layer is illustrated in Fig. IV.2(right). This detector construction design leads to approximately 460M individual detector elements for all four detector heads.

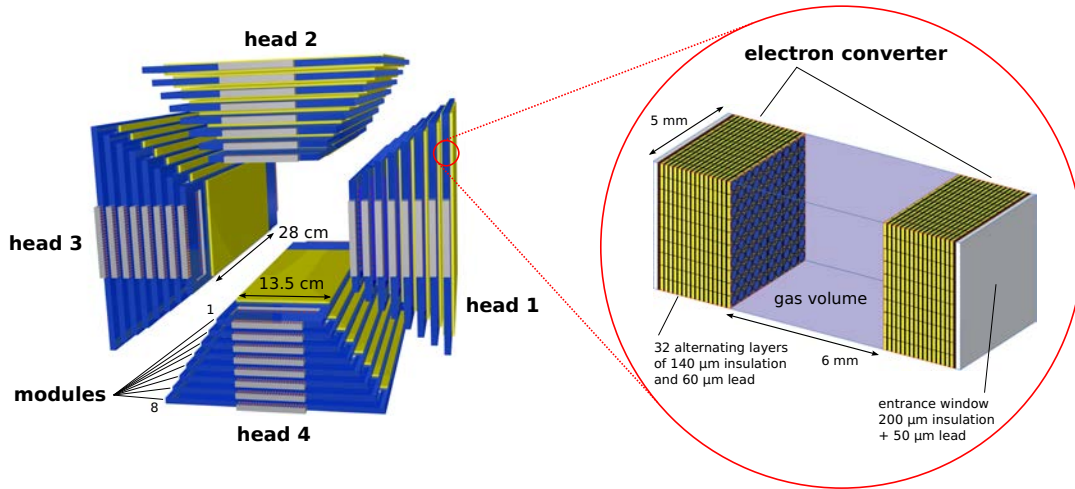


Fig. IV.2: Left: 3D CAD visualization of the quadHIDAC system showing 4 detector heads each containing 8 individual detector modules of different sizes made with Inventor [Bol13b]. Right: Enlarged piece of a small part of a single detector module where the gas volume of the MWPC is covered by two converters. The single implemented hole elements on 32 alternating layers of lead and insulation building the photon-to-electron converter [Got10].

A primary positron is positioned randomly inside the source volume at the beginning of each event. Its momentum direction is randomly and isotropically distributed. The positrons are liberated with a kinetic energy sampled from a distribution derived from the theoretical approximation from [Hol92] for the isotope ^{18}F , as it is the isotope with the lowest positron range.

The stepping action class was primarily modified to produce the output which stores the vertex position of each secondary electron reaching a gaseous element of the detector geometry. In addition, the information on event number, the layer number, converter number, kinetic energy, energy of the mother particle, the electrons creation process, the vertex coordinate of the mother particle, and the original annihilation photon directions are stored. The whole data output is stored in a ROOT [BR97] TTree. The distinct extraction of coincidence events are made post-simulation by analyzing the data file.

Event Definitions

The physical definitions of the different coincidence types were given in Section II.6. Since physical events and simulated event recognition cannot be translated one to one, the precise definitions are explained at this point.

Within the simulation, the gas amplification processes are not considered. Thus, a photon in the simulation is declared as detected when one of its following secondary electrons reaches a gaseous part (primarily holes) in the detector volume.

A coincidence is recognized as true if two annihilation photons originating from the same event do not undergo *Compton* or *Rayleigh* processes within the source volume or the detector material prior to the process initiating the detection process, i.e. each electron arriving in a gas volume coming from an unscattered photon is tagged as true.

The treatment of multiple events in the simulation is done in an information reduction style. If more than one electron reaches gaseous volumes within one detector head, the interaction point from the electron with the highest kinetic energy is taken as the one coordinate of the corresponding coincidence. However, for central positioned sources on the standard setup it was examined that the occurrence of this event type is far below 0.1%. Thereby, it should be remarked that this procedure does not account for random events in the multiple coincidence data, since the simulation only tracks photons from single annihilations.

Extensions to the Former Implementation

- **Hole Geometry**

In the former implementation, the realization of the hole pattern used a simpler geometry only approximating the real quadHIDAC geometry. The holes were only aligned in a rectangular structure Fig. IV.2(right), while the real geometry was designed in a pattern with displaced holes in every second row Fig. IV.3. To overcome design limitations occurring in the simple pattern and to have a realistic geometry, the heights of the lead and insulation boxes were doubled, and one hole and two half holes were assigned to each box. Furthermore, cone shape and hexagonal hole geometries were implemented to check their influence on the system sensitivity (Section V.2).

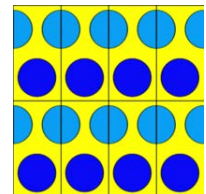


Fig. IV.3: New hole pattern

- **Adaption of Modules to Real quadHIDAC Dimensions**

The thickness of modules in the former simulation was thinner than in the real modules, which was addressed to unknown glue contributions. It turns out that the insulation layers which carry the cathode pads (thickness of $\sim 300 \mu\text{m}$ each) were not considered. As an approximation, the missing thickness was added by

enlarging the gas gap from 6 mm to 6.6 mm, to resemble the thick cathode layer, and the cover foil thickness from 0.2 mm to 0.45 mm, to address the module to module separation, leading to a perfect match for the radial position of the simulated modules to the quadHIDAC modules. Consequently, the remaining module dimensions could be set to the values of the real modules.

- **Voxelmap Source Generator**

A popular method to simulate complex source geometries, given from models which have no interface to the simulator or to generate input data from reconstructed images obtained from measurements, is to use a voxelized event generator. In the presented simulator, the voxelized event generator type established by the `GAMOS`⁵ collaboration [ARC⁺08] was adopted and incorporated in the `Geant4` code. Source geometries or images have to be converted into ASCII file format and read in at the beginning of a simulation run. Accordingly, positrons are liberated in the center of each voxel, whereby the number of positrons is proportional to the image voxel value. To assure that the positrons annihilate and no further object scattering occur, a source box with the size of the voxelized input FOV is initialized and filled with an artificial material with the characteristics of water and a very low density. Additionally, the positrons are generated with no kinetic energy.

- **Implementation of Non-Collinearity**

In a first approximation, the photons from positronium annihilation are emitted back to back. For a more realistic consideration of residual kinetic energy of the positronium, the annihilation model used in `GATE`⁶ [JSS⁺04] was taken and integrated into the source code. The model samples an energy deviation from the 511 keV annihilation photons with a *Gaussian* distribution with a mean energy of 0 keV and a standard deviation of 1.1 keV. This energy is subtracted from the 511 keV of the one photon and added to the other photon. Furthermore, the direction momentum of one of the photons is rotated proportional to the energy deviation with a mean rotation angle of $\sim 0.5^\circ$ (Appendix Source CodeA.1).

- **List-mode Data Output**

As mentioned above, the simulation output data gives a lot of information on

⁵`GAMOS` $\hat{=}$ `Geant4`-based architecture for medicine-oriented simulations

⁶`GATE` $\hat{=}$ `Geant4`-application toolkit for ET

each single event. This gives one the opportunity to study the system on an elementary level and to evaluate if the simulation response is reasonable on every level. Nevertheless, even after coincidence filtering, the data file format consumes a non-negligible amount of memory. Also, the interface to reconstruction tools is rather uncomfortable, as such tools commonly apply specific steps necessary to optimize quadHIDAC data reconstruction during processing only if the data file is given in the specific list-mode format. Hence, a converter macro was developed to bin the `ROOT TTree` data accordingly and write it in a binary list-mode file. The file format was presented in Section III.3. In the converter code, coordinates which do not match to the converter dimensions are discarded. The converter macro also fills timing and counter information to the according list-mode tags. However, it should also be mentioned that the time information can be set arbitrary, and only the overall coincidence and random counter are filled with reasonable values. Thus, the converter macro produces simulation output which is much more similar to the real quadHIDAC output. However, the binning of the x and y coordinate is more precise than the spatial resolution of the real modules, whereas the converter number binning in radial direction (DOI) is the same for simulation and measurement.

- **Rotation**

The quadHIDAC is able to measure in static mode or in rotational mode. In general, all examinations are made in rotational mode, in which the detector heads are rotated by 180° around the long axis of the scanner in 3180 angle steps to overcome drawbacks in image reconstruction due to missing angles in the data space. The former implementation of the simulation only modeled the static acquisition mode of the scanner. Since the demand to simulate measured source distributions to obtain estimations needed for correction methods in image reconstruction arose, it was also necessary to model the rotational mode. The direct rotation of the detector heads would make the current realizations of the coincidence filter, the list-mode conversion, and all the other analyzing macros useless. Thus, it was decided to rotate the source volume instead. The rotation is carried out by calling an extra class called `CreatePhi.cc`. The Primary Generator class calls the necessary angle from that class to rotate the source volume, while the Stepping Action class retrieves the value from the class to add it to the `TTree` output. All analyzing and readout macros were extended to handle the new `TBranch iangle`. In the presented results, the

simulation rotates the source in only 318 angle steps around the 180° , which is a sufficient precision for the studied examples.

- **Module Status**

The modules of the quadHIDAC scanner suffer from aging effects, which finally leads to full breakdowns of single modules. Hence, it is necessary that distinct modules have to be switched off in the simulation to be comparable with measurements. If a complete module would be removed in the simulation code, the missing absorption and scattering of the passive material would lead to incorrect data. Therefore, only the gas component in the module is exchanged, whereby the new gas component is not considered by the data extraction of the Stepping Action class. In contrast to post-processing filtering, this approach has the advantage of reduced disk space consumption and slightly increased processing speed.

- **Extension to four Detector Heads**

The simulation of two times two detector heads with coordinate switched source geometries for one simulation has no direct drawback, but makes the whole post-processing steps much more extensive. Thus, a simulation where the geometry of all four heads was modeled at the same time was implemented and all post-processing steps were adapted. It was shown that the computation time is slightly reduced compared to two single simulations. Unfortunately, it was later observed that the produced data output is slightly different from the old implementation. These differences result in rotational unsymmetrical images even for symmetric sources most probably induced by a bug in the source code or the post-processing macros. The differences only have a minor influence on the resulting data, and the problem was therefore not investigated further. However, to have no erroneous bias in the data, the presented simulations were all done with the old two detector head solution.

Hardware for the Geant4 Simulations

The Geant4 simulations performed for this thesis needed relatively large computing resources, since sufficient statistics were necessary. The simulations were performed on a computer cluster called “Münster Analyzing Facility” (MAF) located at the Institut für Kernphysik in Münster, where each simulation tracks the trace of all photons and conversion electrons induced by the β^+ -emitter. The cluster consists of 200 processors with CPU frequencies ranging from 1.99 GHz to 2.4 GHz.

Converter Optimization

The design geometry of the detector modules *Jeavons et al.* chose for the latest commercial scanner was a trade-off of drilling limitations, system spatial resolution, gas ionization probability, and cost reduction. The following chapter explains why the quadHIDAC converter geometry was chosen and shows which parameters would theoretically improve the system performance on the basis of simulations. Furthermore, updated limitations for drilling are discussed and the advantage and drawbacks of multiple alternative manufacturing techniques are presented and discussed.

V.1 The quadHIDAC Converters

The geometry of the detector modules concerning the specifications of the MWPC and converter dimensions were discussed in Section III.1. In the following, it will be explained how the modules are manufactured. Since most of the process steps are not precisely documented, some of the descriptions are just assumptions relying on profound expertise in gas detector manufacturing or are, at least, statements from Oxford Positron Systems.

In the initial step, the stack of 16 lead layers and 16 insulation fiberglass sheets is merged in a heated press. The cathode pad geometry is etched into 300 μm thick copper-cladded PCBs¹, which are commonly made of FR4 or G11. Each converter stack is laminated to one of the cathode pads PCBs. Consequently, the holes

¹PCB $\hat{=}$ Printed circuit board

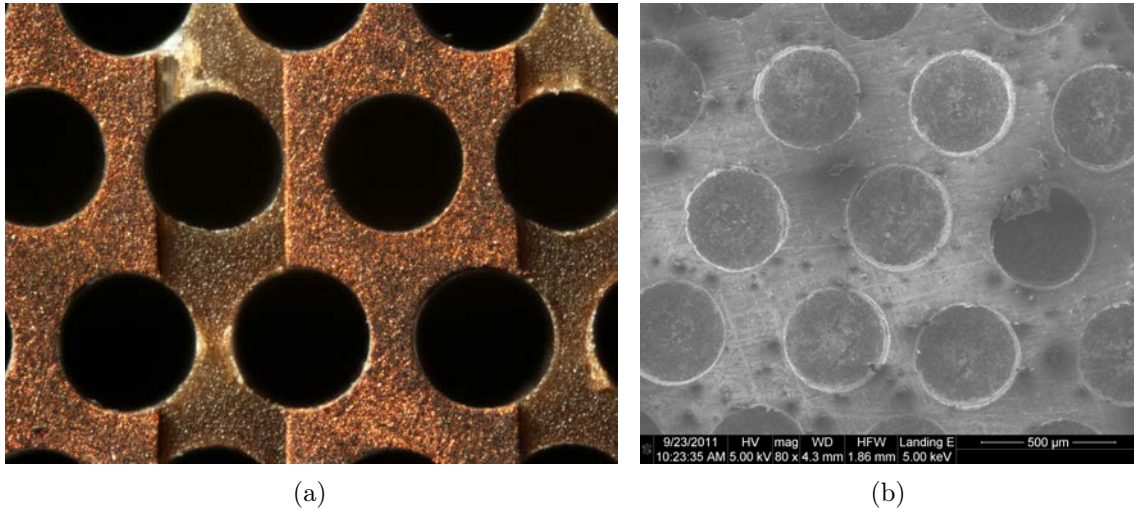


Fig. V.1: Microscopic and REM images recorded from converter samples to show the hole geometry of the HIDAC. The optical image (a) of the pad plane shows the good quality of the drilled converter holes and the precise width of the readout pads. The REM image (b) of a lead layer shows imperfections in the surface which may come from the roller production of the lead foils or the assembling of the detector modules.

with a diameter of $400 \mu\text{m}$ are drilled sequentially into the sandwich with an automated PCB drilling machine in an oil environment. Due to the large amount of holes ($\sim 300,000$ for the large modules), this step can take up to two days. During the drilling process, the drill tip has to be automatically exchanged after approximately 1000 holes, since the probability that the drill tip cracks and irreversibly clogs or destroys the converter is too high otherwise. Afterwards, the holes are polished chemically to reject remaining impurities and to improve the hole quality. The finished converter is then laminated to the outer foils, and two converters are assembled with the wire layer to build a whole detector module. A microscopic and a raster electron microscopic (REM) image of the drilled converter is shown in Fig. V.1. It is obvious that the production process is able to obtain high quality and regular hole shapes. Even though the illustration also shows a good hole-to-hole separation, this does not count for the overall converter. When looking for defects, one observes errors up to $50 \mu\text{m}$ in the hole-to-hole separation precision, which is only moderate. Indeed, the hole-to-hole separation does not influence the functionality of the converter. However, it will be presented later on that a precise reduction of the hole-to-hole separation is able to improve the converter efficiency. Furthermore, the figures show that the hole pattern has no equilaterally triangular geometry. In detail, the machine

parameters were set to obtain a hole-to-hole separation of $500 \mu\text{m}$ in the x-direction. In the y-direction, only the row distance was set to $500 \mu\text{m}$, which is maybe due to machine limitations or to remain on an equal distributed cathode pad surface. This results in a pattern that is not equilaterally triangular and leads to a mean hole-to-hole separation of $\sim 559 \mu\text{m}$ in the y-direction. The hole-to-hole separation and hole diameter are chosen by machine limitations given at that time. Also, the insulation material and its selected thickness may only have been addressed to establish a reasonable electric field instead of efficiency considerations. Therefore, these parameters are varied in simulations and discussed in Section V.2.1. The improvement potential of state of the art drilling machines will be the topic of Section V.3.2, and the dependence of hole size and the overall number of foils per converter on electron drift will be discussed on the basis of simulations in Section V.2.2.

V.2 Simulations for Performance Enhancement

To improve the converter performances in terms of coincidence sensitivity and spatial resolution, two main aspects must be considered from the theoretical point of view. On the one hand, the scanner geometry must be chosen in the way that the conversion probability should be as high as possible and the scanner should cover the largest possible solid angle. On the other hand, the efficiency of detecting the conversion electrons has to be optimized. The conversion probability is analyzed using **Geant4** simulations and the detection efficiency is studied following **Garfield** simulations.

V.2.1 Optimization of Conversion Probability

The conversion probability is simply optimized by increasing the amount of lead inside the converter. However, here we instead want to find out which parameters would be optimal to reach the highest yield of detected photons for quadHIDAC scanner dimensions. The described implementation of the quadHIDAC scanner in **Geant4** was used to study the influence of several geometric factors on the overall system coincidence sensitivity. Here, we define the sensitivity as the amount of extracted coincidences divided by the number of liberated positrons. The simulation results, that will be presented in the following, rely on the statistics of 5M positron annihilations which was adopted from the setups from the older implementation. A short statistical test with thirty simulations of the standard setup was made to find

out whether errors have to be indicated in the results. The test showed a relative error of only 0.3%. Thus, no error indication was applied to the final results.

The positrons were liberated in an infinitesimal point source surrounded by a small two centimeter thick water sphere with no kinetic energy in the center of the FOV of the scanner. The dimensions of the single scanner modules and the number of layers and the lead thickness were fixed while the hole geometry, dimensions, and the insulation thickness were varied.

IV.2.1.1 Hole-to-Hole Separation

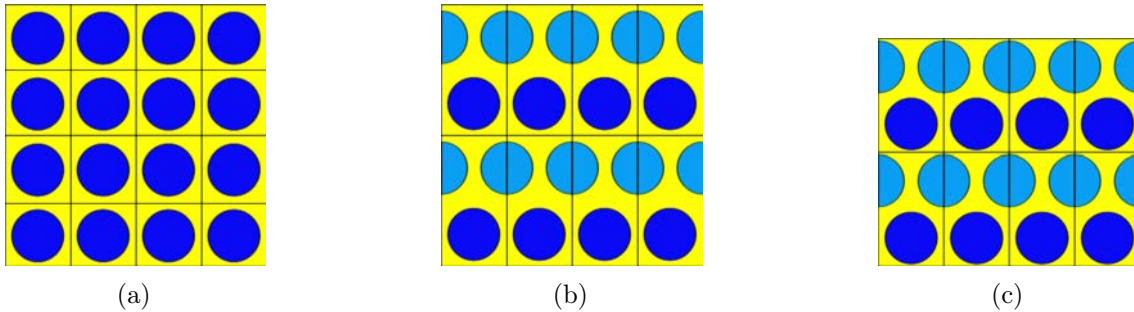


Fig. V.2: Different hole patterns used within the `Geant4` simulations. (a) Parallel hole pattern, (b) displaced HIDAC hole pattern, and (c) equilaterally triangular hole pattern are displayed.

In the first examination, the parallel hole design of the old implementation was compared to the realistically displaced hole pattern that is used in the quadHIDAC design presented in Section IV.2.2 and an equilaterally triangular hole pattern (Fig. V.2). Furthermore, hole-to-hole pitches leading to minimum wall thicknesses in the range from 0 to $100 \mu\text{m}^2$ were tested. In all simulations, the HIDAC hole diameter of $400 \mu\text{m}$ was used. The results are presented in Fig. V.3.

In comparison to the old implementation, the HIDAC hole pattern shows a slight increase in sensitivity of only 2.7% for the implemented $500 \mu\text{m}$ hole-to-hole separation. A substantial sensitivity increase of 21.6% compared to the HIDAC geometry can be obtained for the equilaterally triangular hole pattern. Furthermore, a remarkable coincidence sensitivity increase is given for smaller hole-to-hole separations for all hole patterns. The increase is most likely due to the fact that for smaller wall thicknesses, the probability for electrons to escape into the holes increases. In fact, this accounts in particular for electrons which are produced close to the lead surface

²Of course, a minimum wall thickness of $0 \mu\text{m}$ is impractical but possible in the simulation.

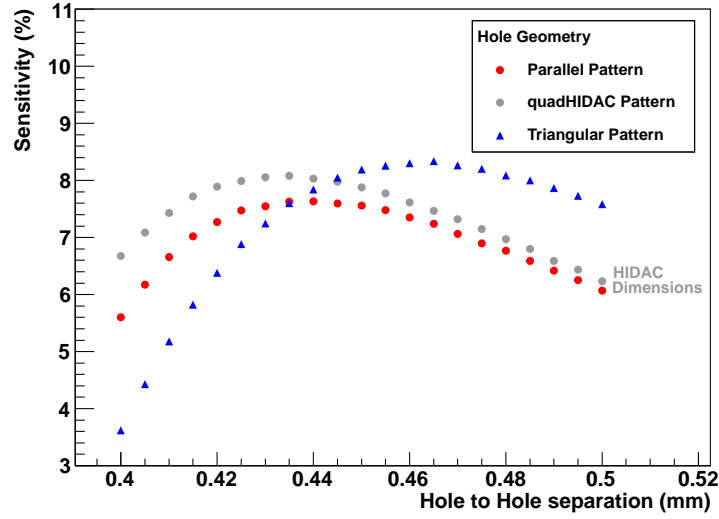


Fig. V.3: Influence of the hole-to-hole separation on the sensitivity for trues and scattered coincidences simulated for different hole patterns. In the analysis, the hole diameter was fixed to $400 \mu\text{m}$.

but having a momentum direction into the solid. Otherwise the amount of the overall lead is decreased for thinner walls leading to the reduced conversion probability for thinner walls. The coincidence sensitivity maximum for the parallel and HIDAC pattern is given for a minimal wall thickness in the range of $35\text{-}40 \mu\text{m}$, resulting in an increase in sensitivity compared to the $100 \mu\text{m}$ wall thickness of 25.9% for the parallel pattern and 29.7% for the HIDAC pattern. The highest sensitivity is reached with the equilaterally triangular pattern, whereby the optimal minimal wall thickness is $65 \mu\text{m}$. Thus, in the case of a realizable configuration, a coincidence sensitivity increase compared to the quadHIDAC design of 33.7% would be possible.

IV.2.1.2 Hole Diameter and Insulator Thickness

A way to optimize the photon conversion probability would be the reduction of the hole size. This would lead to an increase in the overall amount of the holes, and thus an increase in the amount of lead. However, smaller holes are more difficult to produce, and the ionization and transport properties of the holes would be heavily influenced. In first order, these drawbacks will now be neglected. Following the results from the last section, the equilaterally triangular geometry was further investigated and the hole diameters were varied for different thicknesses of the in-

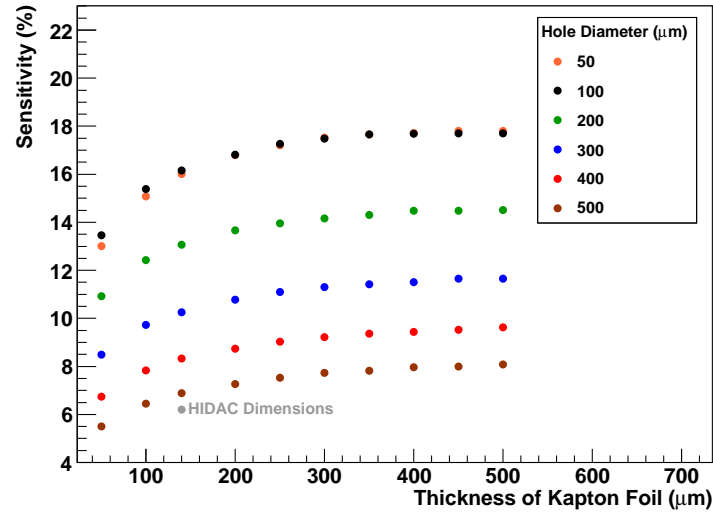
sulation material³, as well as for different hole-to-hole separations. In the case of different insulation thicknesses, the hole-to-hole separation was fixed to hole diameter plus $65 \mu\text{m}$, since good results were obtained for this wall thickness as shown in the previous section. The results are shown in Fig. V.4(a). For the hole-to-hole separation variation, the insulator thickness was fixed to $250 \mu\text{m}$, since the results from Fig. V.4(a) let us assume that the further improvement by thicker insulation material is negligible. In detail, it is assumed that larger depth of the holes caused by thicker insulation foils would definitely result in lower sensitivity. The results of the hole-to-hole separation variation are shown in Fig. V.4(b). It is noticeable that the sensitivity is heavily increased for smaller holes and also a small performance increase could theoretically be achieved with thicker insulation material Fig. V.4(a). Electrons reaching the insulation material have larger mean free paths in the material than in lead, which gives them a higher probability to reach a hole instead of being absorbed in the following lead layer if the insulation material is thicker. Additionally, thicker insulation layers could potentially increase the sensitivity because secondary electrons produced from ionizations induced by the high energy electron in the insulation have a higher probability than in lead to enter hole volumes due to the larger mean free path. Thus, they could cause additional ionizations able to generate or increase signals which would otherwise not be detectable. It should be remarked that the simulation can not recognize those increased signals.

The simulation predicts that the sensitivity increase potentials of thicker insulation materials for a thickness change from $50 \mu\text{m}$ to $500 \mu\text{m}$ vary between 31.6% to 47% for the $100 \mu\text{m}$ diameter and the $500 \mu\text{m}$ diameter holes.

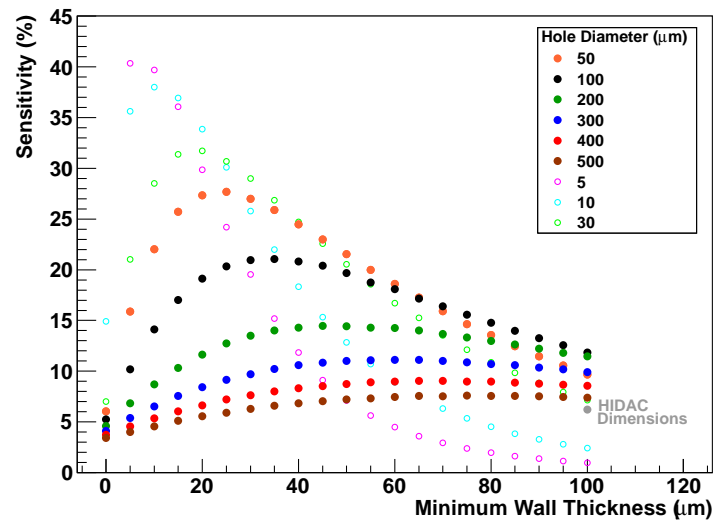
A similar slope for the hole-to-hole distance variation (Fig. V.4(b)) is observed if compared to the results from the setups with the $400 \mu\text{m}$ hole diameters of the last section. But the optimal minimum wall thickness changes from $75 \mu\text{m}$ to $25 \mu\text{m}$ in the case that the diameters are set from $500 \mu\text{m}$ to $50 \mu\text{m}$. The sensitivity increase potential from the $100 \mu\text{m}$ minimum wall thickness to the optimal minimum wall thickness rises from 2.8% to 186% if the hole diameters are changed from $500 \mu\text{m}$ to $50 \mu\text{m}$.

The potential improvements for the residual cases are 5.9%, 12.5%, 26.2%, and 77.8% for the respecting $400 \mu\text{m}$, $300 \mu\text{m}$, $200 \mu\text{m}$, and $100 \mu\text{m}$ hole diameters. As mentioned already above, the optimizations discussed in this section only give an upper

³In the simulations, Kapton is used as insulation material. Kapton® is a polyimide film produced by the company DuPont.



(a)



(b)

Fig. V.4: Simulation of the probability that a single decay is measured as a true or scattered coincidence in dependence on the variation of the hole diameter and insulator thickness. In the analysis, the minimum wall thickness was fixed in (a) to see the influence of different insulator thicknesses and in (b) the insulator thickness was set to 250 μm to see the behavior for variations in the hole-to-hole separation.

limit of the accessible coincidence sensitivity, since the probabilities to ionize gas molecules and to extract drift electrons decline with the hole diameter. Hence, high coincidence sensitivities with hole diameters below $50 \mu\text{m}$ are not expected, even though high conversion probabilities are predicted by the simulations.

IV.2.1.3 Honeycomb Geometry

In all the covered hole geometries so far, no defined wall thickness is given since only the minimum wall thickness between two distinct or arbitrary (dependent on the pattern) holes or the maximum wall thickness in the center of three or four holes can be used for the definition. Hence, it may be of interest to have a honeycomb geometry (Fig. V.5(a)) to achieve a more uniform detection probability over the full detection area⁴. The honeycomb pattern was implemented in `Geant4` by the use of polyhedrons with six edges instead of holes. A visualization of the pattern is shown in Fig. V.5(a). The results of an analysis with a polyhedron to polyhedron separation of $450 \mu\text{m}$ and an insulation material thickness of $140 \mu\text{m}$ is presented in Fig. V.5(b). Since an optimized wall thickness between two polyhedrons was questioned, the results propose the use of thicker walls. Compared to the former results, no sensitivity gain for thinner walls is observed as the overall number of polyhedrons within a module stays the same for every wall thickness. Thus, the gas volume inside the polyhedron becomes smaller for thicker walls, which would have worse electron drift and ionization properties. A simple approximation could be achieved by assuming that the polyhedron volume scales linear with the efficiency of the detector. Hence, the sensitivity was normalized to the polyhedron volume with $50 \mu\text{m}$ thick walls which is shown in Fig. V.5(b) as blue dots. Conclusively, an optimal wall thickness of $70 \mu\text{m}$ should give the highest sensitivity for such a setup. Overall, the accessed sensitivity range is in the same order like the ordinary hole geometries. Therefore, it is not expected that this pattern is superficial to the implemented geometry. Nevertheless, maybe increased electron transport capabilities could be realized with a honeycomb geometry.

⁴Even though equally element-to-element separations are given, full homogeneity can never be reached since the distance to the polyhedron surface always influences the detection probability and nearly no photon interaction probability is given inside the holes.

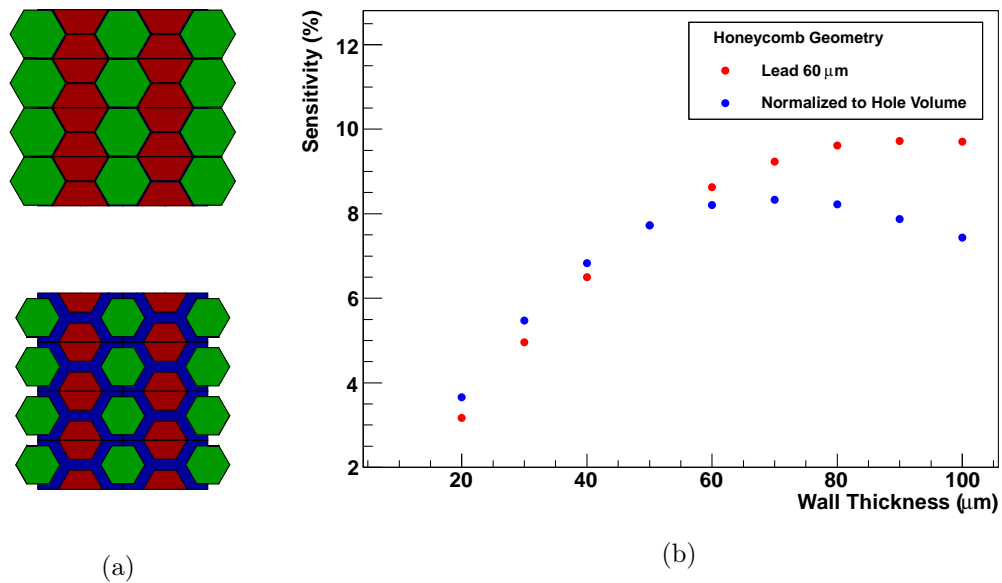


Fig. V.5: Honeycomb geometries as alternative to the hole pattern of the HIDAC converters simulated in `Geant4`. In (a), examples of DAWN visualizations of the converter geometry are presented where wall thicknesses of 10 μm (up) and 100 μm (down) were selected. In (b), the coincidence sensitivity dependence on the wall thickness of a honeycomb geometry is shown. In the study, the insulation thickness was fixed to 140 μm and the polyhedron to polyhedron distance was set to 450 μm .

IV.2.1.4 Cone-Shape Geometry

Another interesting idea for a hole geometry came up during discussions about lead etching, which will be subject of Section V.3.3. It is possible to manufacture hole patterns with etching techniques. If slow liquid etching solvents are used, it is unavoidable that the resulting holes have a cone-shape instead of a cylindrical geometry. This is especially the case when relative thick layers are treated. Depending on the concentration of the solvent, it is possible to manipulate the steepness of the wall sides, whereby the steepest slope is given for the highest concentration. The influence of the different steep wall sides of the standard setup with the 400 μm hole diameter as the maximum hole diameter were analyzed in two different of four possible setup orientations (Fig. V.6(a)) with the presented `Geant4` code in [Ber11]. The analysis was done with 450 μm and 500 μm hole-to-hole separations and 140 μm thick insulation material. The results are presented in Fig. V.6(b). It was observed that steeper wall sides increase the overall system coincidence sensitivity and that the orientation of the structured foils has a minor but observable influence.

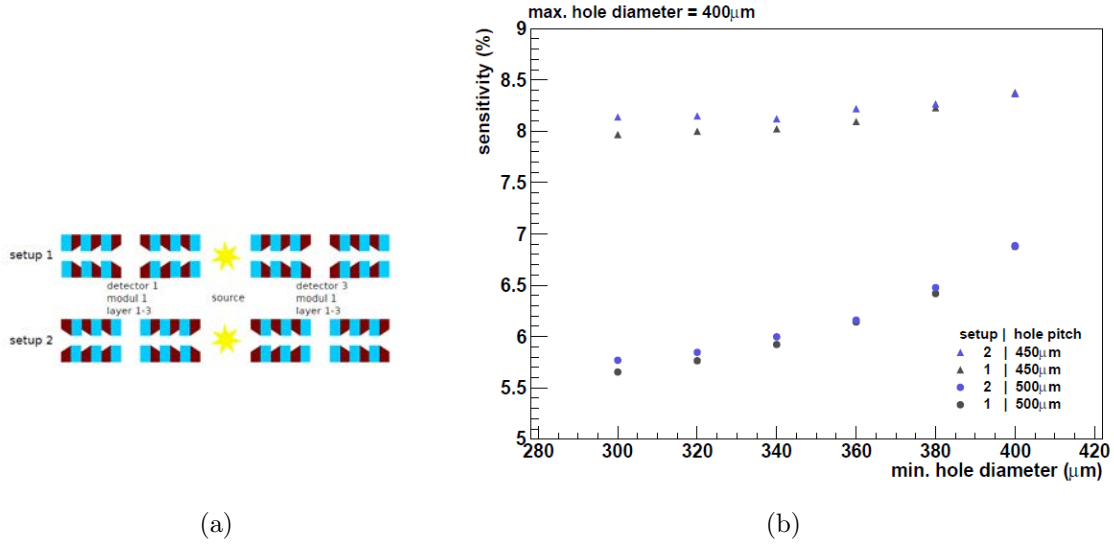


Fig. V.6: Analysis of the influence of cone-shaped holes in the lead layers simulated for two different setup orientations and two different hole-to-hole separations. Sketch of hole orientation in the simulated setups presented in (a) and results of the examination illustrated in (b) [Ber11].

V.2.2 Ionization Induced by Electrons and Their Drift in Gaseous Holes

With the accessed sensitivity of approximately 6% with the `Geant4` simulation for the real HIDAC geometry, the system would already be compatible with modern small animal PET scanners. Unfortunately, the experimental measurements with a freshly manufactured 32 module quadHIDAC system were only able to reach a system coincidence sensitivity of $\sim 2\%$ [SRK⁺05]. Thus, not every converted photon leads to a detectable signal. The electron detection probability p_e can be calculated by [GKV⁺13],

$$p_e = \sqrt{\frac{\epsilon_c^{meas}}{\epsilon_c^{simul}}} = \sqrt{\frac{2\%}{6\%}} = 58\% , \quad (\text{V.1})$$

where ϵ_c^{meas} and ϵ_c^{simul} are the measured and simulated coincidence efficiencies. Since the simulation implementation does not consider the electric fields within the gas volumes and also the differential approach of particle tracking (discussed in Section IV.2.1) would not give precise results even if the field had been modeled, it is necessary to study the electron drift properties which have to be partly responsible for the low electron detection probability (V.1). Thus, it is necessary to maintain

the electron transport and gas amplification separately to explain the reduced p_e and to be able to make predictions on how changes in the converter dimensions and geometry influence p_e . The interaction of electrons with gas molecules comprises many models and theories describing effects like ionization, excitation, electron attachment, drift and transport models, δ -electrons, and many more. A lot of physical constants of the well known phenomenons have been experimentally examined for almost all elementary gases and many gas mixture in a wide energy ranges, or were accessed by theoretical calculations. A popular simulation tool-kit for gaseous detectors is the **Garfield** and **Garfield++** package developed at “Conseil Européen pour la Recherche Nucléaire” (CERN) [Vee98]. It makes use of the various models and theories to predict properties of gas detectors with arbitrary counting gas mixtures and geometries. To calculate the electron transport properties of gas mixtures with arbitrary gas contributions, **Garfield** uses the program **Magboltz** [Bia89]. In the study presented in the following, the goal is to estimate the amount of electrons lost due to diffusion and attachment within the detection process.

Electric Fields in Holes

The **Garfield** program has a default interface with the nearly exact Boundary Element Method (**neBEM**) program [MM06] to calculate the electric fields which are necessary to make any predictions on drift lines, signal time development, diffusion, and so on. Hence, in a first approach the HIDAC converter geometry was implemented in **neBEM**, where the influences of cone-shaped lead holes and their orientation compared to tube-shaped holes on the electron drift lines were presented in [Ber11]. No significant influence of cone-shaped holes on the electric fields was observed. In all simulations, the potential difference was simulated in the realistic design where it is higher in the lower layers and smaller in the upper layers (Section III.1.2). The results showed that there is a focusing effect of the drift electrons in the lower region of the hole due to this potential difference, which increases the overall extraction potential of the drift electrons.

There is a drawback to the **neBEM** simulations, since the electric field has to be calculated at the beginning of each simulation as it is not possible to save the resulting electric field in **Garfield**. Hence, the **neBEM** solver is inflexible for the foreseen application, since the geometry of a single HIDAC hole with its sixteen layers takes approximately half a day to be calculated with **neBEM**. Another option to calculate the electric fields is to use finite element methods (FEM). A software package which

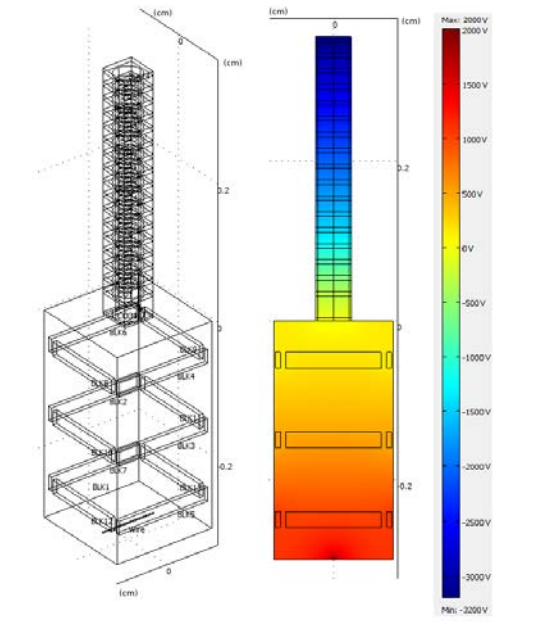


Fig. V.7: Geometry (left) and electric potential (right) of the HIDAC model implemented in `Comsol` from a setup with a $400\ \mu\text{m}$ hole diameter and 16 insulation-lead layers. Extra cathode layer substrate with thicker insulation material, wire, MWPC gas volume, and pusher electrodes are visible.

uses this method to simulate electric fields is `Comsol`. An interface to read the electric field maps with `Garfield` is given for the version `Comsol 3`. The benefit compared to `neBEM` is that the field map can be read by the interface and stored in a binary file. The binary file is quickly read by `Garfield` which is beneficial for the Monte-Carlo based analysis that will be topic of the next section and improves testing capabilities to give different simulation parameters a trial. `Comsol` simulations were made for single hole geometries with different diameters and the standard 16 layer setup. The visualizations of the cell volume definitions for the case of a hole diameter of $400\ \mu\text{m}$ with the according electric field are presented in Fig. V.7 At the bottom of the cell, a single wire with a diameter of $20\ \mu\text{m}$ was simulated. The whole cell was simulated with continuous boundary conditions to mimic the complete converter environment. For each hole diameter, the wall thickness was set to $50\ \mu\text{m}$ to avoid a large number of unrealistic backscatter electrons. This will be discussed in the next section. Furthermore, a large gas drift volume in the MWPC region was selected to prevent electrons from leaving the simulation volume. The vertical dimensions of the gas volume were here $1.1\ \text{mm}$ larger than the hole diameter to reach at comparable results. After a first cycle of the subsequent `Garfield` simulations, the setup was optimized

with three pusher electrode layers with a linear increasing electric potential towards the anode wire to further decrease drift electron escaping.

Generation of Sensitivity Maps using Garfield Simulations

To estimate how many electrons collide with the wall due to diffusion and how many electrons attach to gaseous molecules, the electric fields were read in `Garfield`. The cell geometry was also constructed within `Garfield`, but this was only done for visualization, as the geometry is directly rejected if external fields are read in. As counting gas, the drift properties for an argon-carbon dioxide mixture with a fraction of 10% carbon-dioxide were calculated. The probe used for this analysis is the method `drift_microscopic_electron` offered by `Garfield` to track Monte-Carlo electrons. The hole volume was subdivided in a grid with several radial and axial positions, whereby the center of each element was taken as the initial position of the microscopic electron. On each position, 200 microscopic electrons were liberated and tracked. To generate a sensitivity map in dependence of the liberation positions of the grid, the amount of electrons reaching the wire are counted and divided by the amount of liberated electrons. Additionally, it can be distinguished which fraction of electrons is absorbed by the walls or attached to molecules. The resulting sensitivity map for the standard setup as well as an example of 100 drift tracks for one liberation position are presented in Fig. V.8. It can be seen that in the lower half, the p_e^s ⁵ is between 20-70%, whereas it is only between 5-20% in the upper half. It should also be emphasized that the scaling of the axis is different for y and z, concealing that the hole is much deeper than wide. Regarding the drift plot, the reader may be irritated that the drift lines can enter the solids. As mentioned above, this comes from the rejection of solids. Therefore `Garfield` takes the electric field within the solids from the `Comsol` simulation and assumes that they were traversable for the electrons. This means that `Garfield` simulates everything within a gas volume and does not assign any material to the solids. Fortunately, the direction of the field vectors inside the solids and limited extension of the walls let most of the tracks end very rapidly. Furthermore, there is a probability that a electron reenters the hole and is detected at the wire, which is unrealistic since the electrons would be absorbed by the solid. Luckily there is an inverse effect where electrons move out of the maintained area within the MWPC region. These electrons would, in reality,

⁵The index s denotes that this value gives the detection probability on single electrons instead of clusters which would be produced by the high energetic conversion electrons.

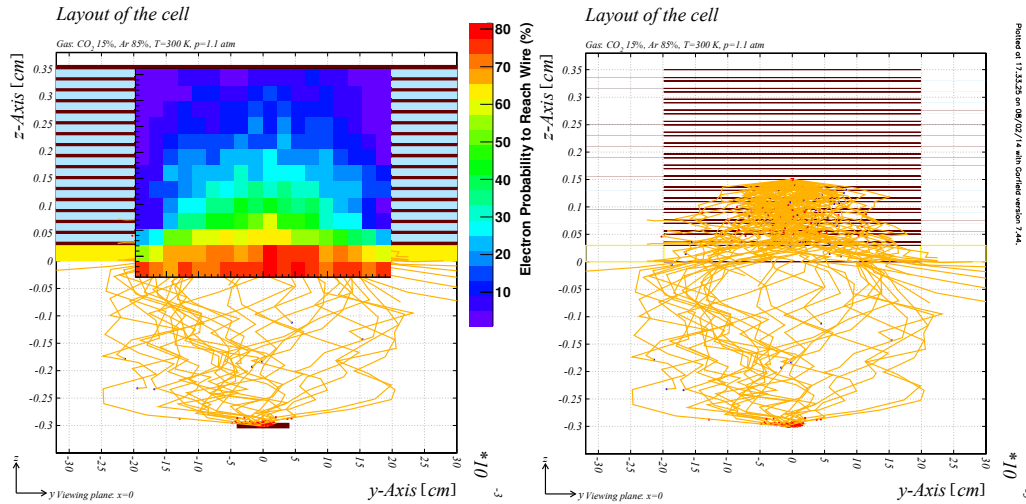


Fig. V.8: Probability map that indicates how likely single electrons reach the vicinity of the sensitive wire (left) in dependence of the radial and axial position of the ionization inside the converter hole volume. The map is overlaid with the `Garfield` drift plot output where 100 microscopic drift electrons were started at position (0, 0, 1.5 mm) and the `neBEM` visualization of the solids (not recognized by `Garfield`). The plain `Garfield` drift plot output is shown in the right figure. Red dots mark ionizations, whereas blue dots mark attachments.

be presumably detected at an adjacent wire. Both effects are hopefully of the same order, which would decrease the overall error.

The plot also conveys that there is gas ionization within the gaseous hole due to the red dots. However, this is not true, as these ionizations take place within the solids which are not visualized. This comes from the fact that from the geometry, only the slice is plotted, whereas the full 3D projection of the microscopic electron tracks is plotted. Following these simulation results, there is no gas amplification inside the holes. In the lower part of the hole there are only electric fields up to 20 kV/cm. This would be high enough to ionize molecules in pure argon, but this is unlikely the case when a quencher gas is added. Hence, the name transition from HDDC to HIDAC is misleading. Nevertheless, it was shown here that interleaving insulator sheets between the lead induces higher conversion electron yields as well as higher drift electron extraction yields due to the improved electric field properties. The last argument leads directly to higher signals which is maybe the reason why gas amplification was assumed.

Nevertheless, `Magboltz` is not able to calculate the cross sections for DIPE. Hence, only isobutane mixtures were studied to observe gas amplification. Therefore, it

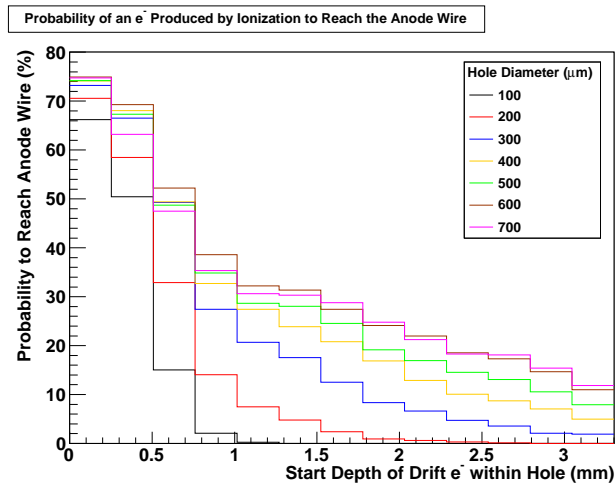


Fig. V.9: Mean probability of drift electrons to reach the amplification wire simulated with **Garfield**. Here, the probability on the y -axis was averaged (Fig. V.8), and only the dependence on the depth of starting position of the microscopic electrons within the hole (z -axis) for different hole diameters is plotted.

cannot be absolutely concluded that there is no gas amplification but it is very unlikely.

The output of the **Garfield** simulations is used for further studies. For simplicity, the single values for the p_e^s were averaged along the y -axis (Fig. V.8) and stored. The resulting distributions for hole diameters ranging from 100 μm to 700 μm are illustrated in Fig. V.9.

V.2.3 Simulation of the Electron Detection Probability

Based on the sensitivity mapping derived above, a small Monte-Carlo based simulation to estimate the overall electron detection probability p_e was established in **ROOT**. As input, the macro needs the passage length of the primary tracked electron within the gas volume and the average axial position. To derive this information, **Geant4** simulations of a perforated single full lead converter layer for each hole diameter size, and the different layer thicknesses of 0.8 mm, 1.6 mm, and 3.2 mm were created. The output for the passage length and the mean axial position of the primary electrons for the hole diameters from 100 μm to 700 μm with a layer thickness of 3.2 mm are presented in Fig. V.10. The decreasing number of events for larger hole diameters is given by the smaller sensitivity, since each histogram is based on the annihilation of 2M positrons placed 8.5 cm far away from the single converter layer.

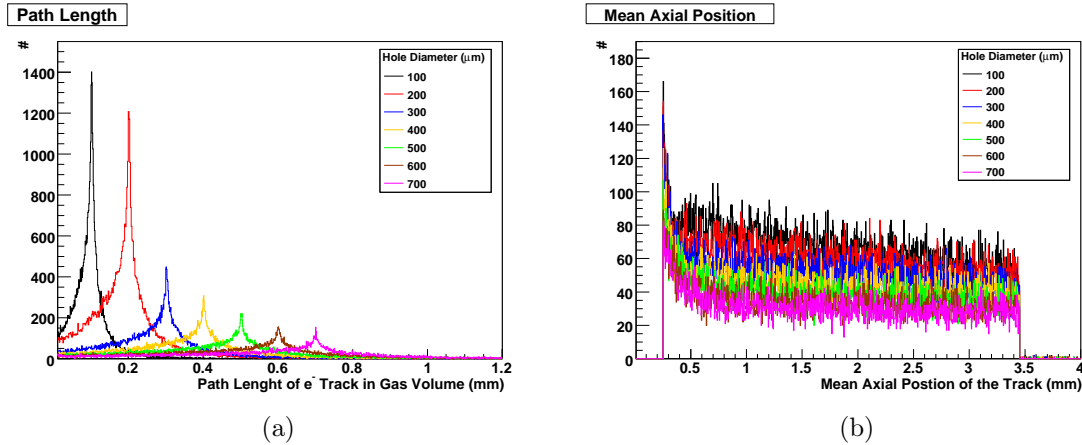


Fig. V.10: Output from Geant4 simulations of a 3.3 mm thick single lead converter layer with hole diameters from 100 μm to 700 μm used to generate electron track information within a “single” hole. Primary electrons enter the gaseous hole at some point and impinge somewhere else back into the hole wall, since the electric field is too low to deflect them. The simulated passage length of these high energetic conversion electron tracks in the gaseous volume is presented in (a) and their average axial position is illustrated in (b).

The new Monte-Carlo simulation is based on two approximations. On the one hand the sensitivity is averaged in the radial direction as described above, and on the other hand, only the mean value of the axial position of the track is taken. Depending on the path length, it is simulated whether the electron is unaffected or lead to one or more ionization clusters. In this case, the cluster size is fixed to four secondary electrons. The resulting number of secondary electrons is multiplied with the sensitivity of the current position. Then it is again simulated on the calculated sensitivity if the event is detected or discarded. For the standard setup with 400 μm hole diameters, the simulation responses an ionization probability of 72% and a p_e of 59%. The value matches very precisely to the result in (V.1), which is surprising since it is just a rough calculation with multiple approximations. A missing factor in the overall consideration is the inefficiency of the readout electronics. It is not known which fraction of the signals is below the trigger value and how many erroneous signals are rejected during the measurement. Additionally, the simulation cannot account for further secondary electrons which can be produced by the primary electron before and after entering the gas volume. Those secondary electrons may also reach the gas volumes and ionize molecules. However, the presented simulation accesses the relative efficiency difference of different hole dimensions and the framework is promising

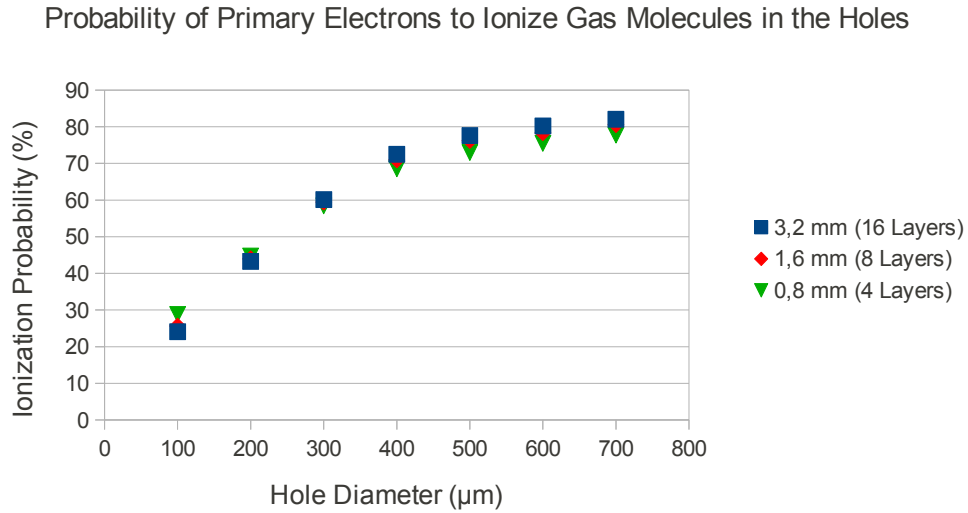


Fig. V.11: Results for the ionization probability generated with the Monte-Carlo simulation approach. Depending on the simulated path length of the electron, the ionization probability is simulated for different hole diameters and hole depths.

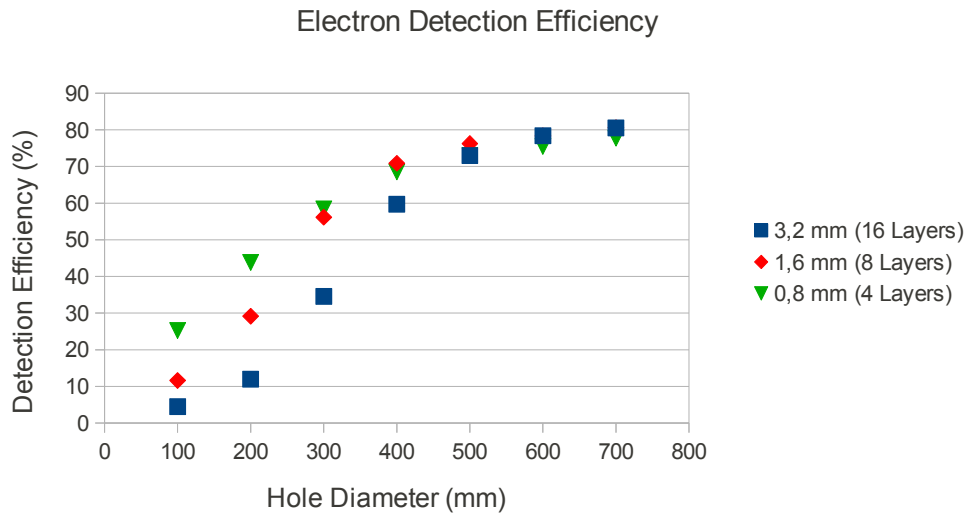


Fig. V.12: Overall electron detection efficiency simulated for holes with different hole diameters and hole depths.

to give reasonable first order estimations on optimized converter geometries.

The presented framework was furthermore used to determine the electron detection efficiency for different hole diameters and hole depths. The results for the ionization probabilities are presented in Fig. V.11, and the overall electron detection probabilities are illustrated in Fig. V.12. The ionization probabilities give the overall limit for the p_e s. Their dependence on the total hole depth is negligible, while a strong decrease for smaller hole diameters is given as presented in Fig. V.11. The overall

electron detection efficiencies p_e in Fig. V.12 show an intense dependence on the total hole depth for hole diameters below 500 μm , whereas nearly no effect is seen for larger hole diameters. For the hole depth of 0.8 mm, the electron detection efficiency converges to the ionization probability for all hole diameters. For deeper holes, the efficiency gets worse and worse for smaller diameters, indicating that a huge amount of potential signal producing electrons are lost in the holes.

V.2.4 Implication on the Overall Coincidence Sensitivity

The electron detection efficiencies p_e and the **Geant4** simulations results (Section V.2.1) can now be used to forecast the overall coincidence sensitivity of potential new scanner designs in the quadHIDAC geometry. The following relations are used to calculate the single photon detection sensitivity s_γ or the coincidence sensitivity s_{co} :

$$s_\gamma = p_e \cdot s_\gamma^{Geant4}, \quad s_{co} = p_e^2 \cdot s_{co}^{Geant4}, \quad (\text{V.2})$$

where s_γ^{Geant4} and s_{co}^{Geant4} are the respective simulated **Geant4** sensitivities. The results of the overall coincidence sensitivity for hole diameters from 100 to 500 μm calculated with the conversion probability derived from the **Geant4** simulations (Fig. V.4), and the electron detection efficiencies from the last section are presented in Fig. V.12. The detection efficiencies p_e s for the thinner holes are hereby translated to scanner systems with 64 and 128 detector modules, since double or four times of the absorbing material is needed to correspond to the conversion probability s_{Geant4} derived with the **Geant4** simulations. The errors are calculated with an uncertainty of 10% for the p_e s.

From these results, it is expected that the best parameter set would be a 64 detector module setup with 1.6 mm thick converters with 400 μm diameter holes. With this setup, including the optimized hole-to-hole separation and inclusion of the error, sensitivities above 5% are possible. This represents a 150% performance enhancement of the current quadHIDAC. For smaller hole diameters, a decline of the sensitivity is observed. Nevertheless, the possibility to increase p_e with thinner converters allows the build up of a high resolution system with 200 μm hole diameters and 128 detectors that would still exceed the current system in sensitivity. If a system with 32 detectors is desired, the results recommend a converter with 500 μm diameter holes.

In these findings, it is difficult to compare systems with more detector modules. An increasing number of modules cause higher costs and require more space for

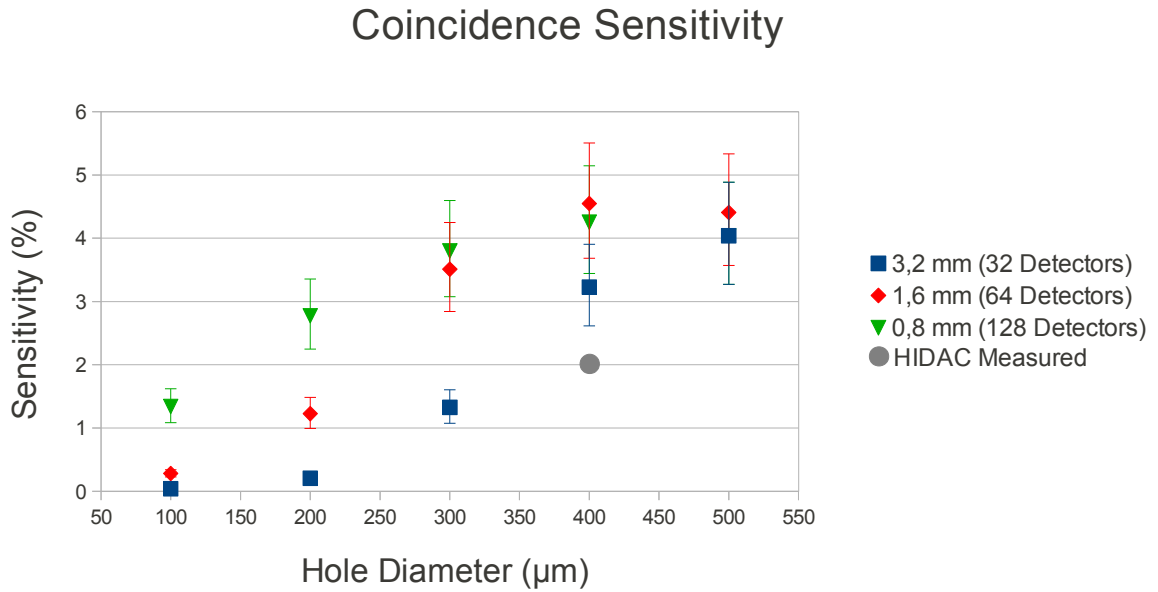


Fig. V.13: Overall coincidence sensitivity calculated from the combined results of the conversion probability (Fig. V.4) and the electron detection efficiency p_e (Fig. V.12) simulations. Errors are given by accounting for an uncertainty of 10% for the electron detection efficiency.

electronic readout. Additionally, the placed question to the simulation completely changes for systems with more detector modules. Hence, new `Geant4` simulations need to be performed to find the perfect parameter sets for highest sensitivity for a, for example, scanner with 64 detector modules. However, this topic will again be discussed partially in Chapter VII.

V.3 Photon Converter Manufacturing

The sensitivity limitations of the quadHIDAC are partly given through manufacturing restrictions. Since desirable optimized converter geometry parameters were derived by simulations in the former sections, it should be now discussed which geometries are obtainable by different manufacturing methods. This section discusses feasibility, advantages, and drawbacks of different alternative manufacturing techniques. Furthermore, the promising techniques for converter production were tested, whereby small produced samples are presented and reviewed here.

V.3.1 Mechanical Perforation

Many different perforation techniques that use mechanical forces for hole production are available on the market. The most obvious technique is needling. The technique is available in rotational and inline operation mode. An example of an inline machine manufacturer is the company RING. The hole diameters of 200-400 μm are quite common, but for single needle stations, only hole-to-hole separations down to 2 mm are realizable. This is due to a substantial amount of material which is needed to hold the needles and the facing holes in a firm and rigid condition. A distinct drawback of the technique is that the material is only ousted instead of rejected. This leads to deformed hole-to-hole bridges. Another method is a rotational stamp



Fig. V.14: Rotating stamp perforation of lead-Kapton samples performed by Schober. The diameter of the holes was 4 mm.

technique. An example of a machine manufacturer is the company Schober. For this technique, the limitations are the same as for the needling techniques, but here the material is removed by a system of male and female stamp heads. An example of a perforated single layer lead-Kapton sandwich is illustrated in Fig. V.22. Unfortunately, Schober only delivered an example for holes with 4 mm diameters. Even though they have 400 μm diameters listed, it is not known how good the quality of the holes would be for the specific material. Both perforation techniques are only able to perforate thin layers. This means that a perforation of a stack of multiple layers is not possible. Thus, an assembly and alignment technique would be necessary. The drawback of the large hole-to-hole spacing could potentially be overcome by a serial application of multiple perforation stations. However, the implementation

would require a lot of effort and be quite costly. The cost of a single perforation station is rather moderate, dependent on the technique, and the throughput would be fantastic but only for single layers with large hole-to-hole separations. Consequently, the results from the simulations concerning the hole-to-hole separations interdict the use of these perforation methods for converter manufacturing.

A further possible mechanical technique would be sand or water beam perforation. Unfortunately it is not possible to operate them in pulsed conditions. Thus, single positions had to be maintained sequentially, which makes the techniques too slow. This means that these methods have more a cutting capability instead of perforation properties.

V.3.2 Drilling

Of course, the best mechanical perforation technique is drilling since it is, up to now, the only production technique used to manufacture complete HIDAC modules. The limitation of drilling is more on the side of the hole-to-hole separations instead of hole diameter. Drilling is possible down to diameters of some microns, but the reachable hole depth is strongly dependent on the hole diameter since thinner drillers have a higher probability of cracking during processing. Therefore, the driller tip has to be replaced more often the thinner it is. An option to have lower drill tip abrasion is to drill in an oil environment. Furthermore, the rotational speed has to be much higher for smaller hole diameters where e.g., 400 μm holes can be drilled with 100,000 rpm⁶, while 200 μm need at least $\sim 300,000$ rpm to deliver acceptable quality. The reachable hole-to-hole separation is dependent on the quality of the PCB drilling machines. The main disturbing influences affecting the positioning system of the drilling tip are vibrations. In high-end machines, a lot of effort has been made to minimize self-induced vibrations and to decouple the system from outer vibrations which allows those machines to operate with high processing speeds. Thus, with state-of-the-art high-end machines, the drilling time for a single HIDAC converter could be reduced from some days to a few hours. But even with high-end machines operating at low speeds to maximize the precision, are not able to reach hole-to-hole separations far below 100 μm for hole diameters of 400 μm .

For the test setup presented in Chapter VI, stacks of six lead and six Kapton layers were glued together, and an area of one square centimeter was drilled at the CERN workshop with a PCB drilling machine from the middle price range. A microscopic

⁶rpm $\hat{=}$ rounds per minute

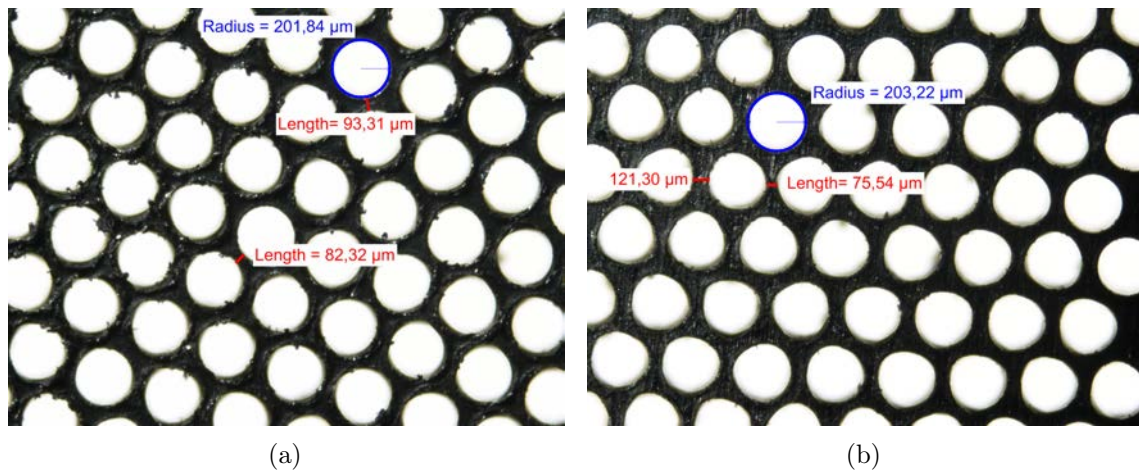


Fig. V.15: Upper (a) and lower (b) face of a drilled converter produced at the CERN workshop. The prototype was drilled in an equilaterally triangular geometry with $400\ \mu\text{m}$ hole diameters. Some measured hole-to-hole separations and hole diameters are indicated.

image from both sides of the drilled prototype converter is illustrated in Fig. V.15. The quality of the drilled samples is very good. The hole diameter approximately matches the desired radius of $200\ \mu\text{m}$. The hole-to-hole separation which was set in the machine parameters to $500\ \mu\text{m}$ varies in the range of $\pm 30\ \mu\text{m}$. It is shown that the improved equilaterally triangular hole geometry, suggested by the simulations in Section V.2.1, can be easily realized with a PCB drilling machine. The main advantage of drilling is that the whole assembled stack can be perforated at the end of the production, whereas all other perforation methods can only aim to perforate one to some few layers. Examples of manufacturers who currently build high-end PCB drilling machines are Hitachi, Pluritec, and Schmoll.

V.3.3 Etching

Another very promising perforation method is etching. In this technique, undesired lead or Kapton material is treated chemically, whereby the treated surfaces can be eluted with solvents afterwards. The structure which should remain on the substrate is protected by a photo resist. In detail, the whole untreated surface is laminated in photo resist and subsequently, a printed screen mask with the desired pattern is mounted above and illuminated. Depending on the photo resist, the screen mask has to be negative or positive. In the one case, the illuminated photo resist can be

eluted with a solvent and in the other case, the illuminated material polymerizes, and the residual photo resist can be eluted.

Single Layer Etching

To test if it is possible to etch single layers of lead in the dimensions needed for the HIDAC converter, the Fraunhofer Institute IPM⁷ in Freiburg etched several samples and geometries. The applied method implies wet etching steps. This means that the chemicals used to treat the surface are liquid. Here the amount of etching medium in the vicinity of the solid determines the speed and efficiency to solve single atoms. Thus, if the goal is to perforate thick layers, like 60 μm lead, liquid etching solvents can only produce cone shaped holes, as was already mentioned in Section VI.7. It is also possible to use gaseous etching solvents that are capable of producing nearly cylindrical holes. However, the IPM does not support the infrastructure for such processes. Images from an example of the etching samples where the holes in the screen mask had a hole diameter of 400 μm and a hole-to-hole separation of 500 μm with the displaced hole geometry of the real HIDAC converters are presented in Fig. V.16(a,c). Another example of a sample with an equilaterally triangular pattern with a hole-to-hole separation of 500 μm and a hole diameter of 300 μm is illustrated in Fig. V.16(b). The samples were glued on a 200 μm thick Kapton foil with a two component epoxy glue. In a first step, the samples were etched with different solvent concentrations and different etching times, whereby the best results are illustrated here. Following the microscopic image, the steepness of the wall is approximately 28°. Despite the wall shape, there are no further limitations to the geometry. The cone shape limits the hole diameter for 60 μm thick foils to approximately 100 μm , and arbitrary separations can be chosen on the upper surface. Single layer etching can be applied in inline processes able to treat large substrate dimensions. The drawback is that there is no glue which can be etched afterwards to get access to the Kapton layer, which on the other side is firm enough to guarantee no outgassing and a firm connection between the insulation and lead at the same time. Thus, it is not possible to perforate also the Kapton layer with this method.

⁷IPM $\hat{=}$ Fraunhofer Institute for Physical Measurement Techniques

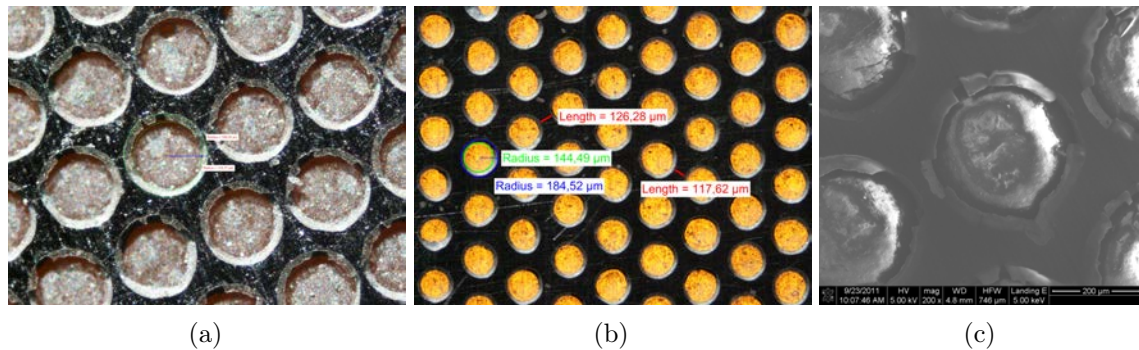


Fig. V.16: Microscopic (a,b) and REM (c) images of an etched sample manufactured at IPM. The geometrical pattern is that of the original HIDAC converters (a),(c) and in an equilaterally triangular pattern with a hole-to-hole separation of $500 \mu\text{m}$ and a hole diameter of $300 \mu\text{m}$ (b). The cone shape holes are visible where on multiple rims the etching solvent has cracked the border in (a),(c). The equilaterally triangular pattern was produced in a second trial delivering stable rims.

Double Layer Etching

To also be able to etch the Kapton layer, copper clad Kapton foil that is commercially available can be used. The lead can be deposited on the copper surfaces by electroplating on both sides at the same time. Conclusively, the lead can be etched from both sides. Afterwards, the thin copper layer should be etched. Finally the Kapton layer can be etched. This is possible since no glue was used. Of course, this procedure is also only possible for single layers, but this technique can also perforate the Kapton layer and results in better hole quality. A drawback of this technique is that it can be applied only to moderate substrate sizes of $\sim 300 \text{ cm}^2$, since it is difficult to align the screen masks precise enough on both sides at the same time. In a first step, two $50 \mu\text{m}$ thick copper clad Kapton foils have been electroplated with lead. The foils have a size of around $15 \times 35 \text{ cm}^2$, and it was observed that the lead thickness steadily decreases from the foil rims with a thickness around $110 \mu\text{m}$ to the foil center with a thickness of around $60 \mu\text{m}$. Microscopic images of two samples are shown in Fig. V.17. The foils have unfortunately not been etched yet.

V.3.4 Laser Perforation

Another good perforation technique is laser drilling. In contrast to a mechanical removal of material, here the material is evaporated by a huge amount of photons. Unfortunately, it is not possible to drill a stack, as the beam intensity to evaporate

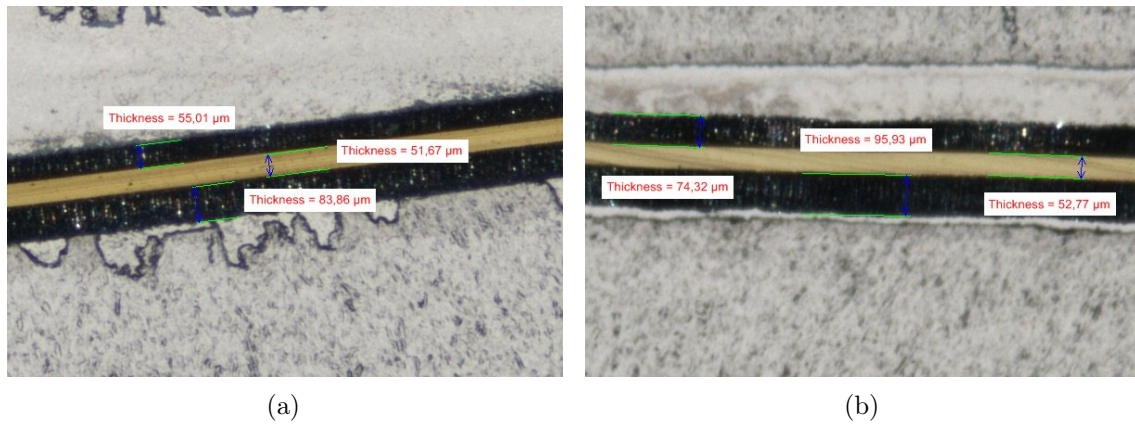


Fig. V.17: Microscopic images of electro plated Kapton-copper-lead samples illustrated in a cross-view. In (a), a sample from the central region is presented and in (b) a sample from the outer region is shown. The lower layer is approximately $20 \mu\text{m}$ thicker than the upper one.

the lead and Kapton must be different. Thus, if a stack were to be drilled, the lead holes would obtain the right size, whereas only the last layer of Kapton would obtain the right size where, more or less, the whole Kapton of the upper layers would be vaporized.

Single Pulse Perforation

It is possible to perforate single layers of the material with many types of lasers. The company ROFIN tested multiple CO_2 and solid state lasers for perforating glued layers of Kapton and lead foils. Many of the different lasers were able to perforate both layers. In all cases, more Kapton was evaporated than lead. Examples are shown in Fig. V.18. It was found that a lot of lasers are able to produce precise hole geometries, but only for single lead or Kapton layers. Since the single sequential positioning of the laser is time consuming, this technique is slow and as these lasers are expensive, the procedure would be too cost extensive.

Mask Perforation

It was shown that single layer etching methods produce satisfactory results. Hence, it was tested whether or not it is possible to reject the remaining glue and Kapton with a broad beam from a CO_2 laser. The laser has an optimized wave length which is primarily absorbed by Kapton. It was observed that a direct laser drilling from

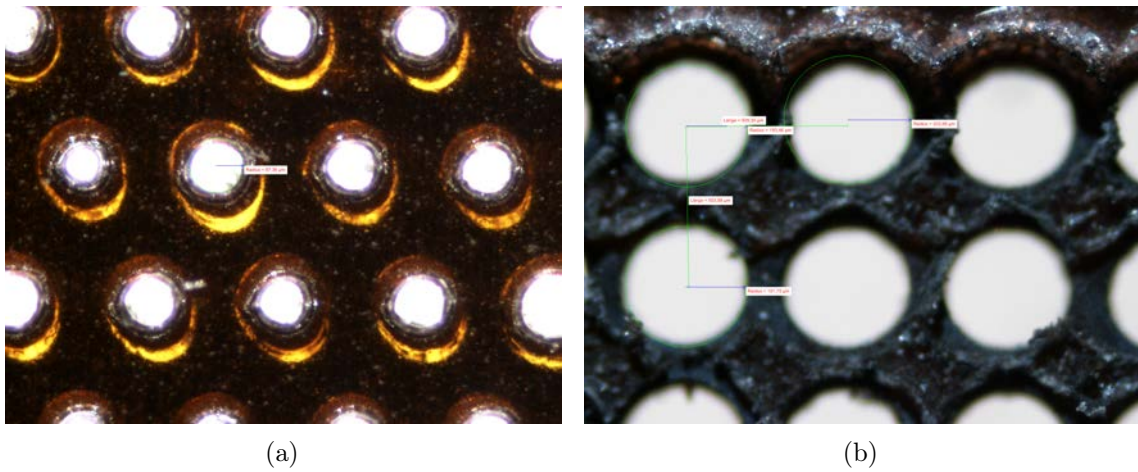


Fig. V.18: Microscopic images from laser treated samples delivered by ROFIN. In (a), a CO₂ laser and in (b) a UV-laser was used. In both cases, the laser beam came from the lead side.

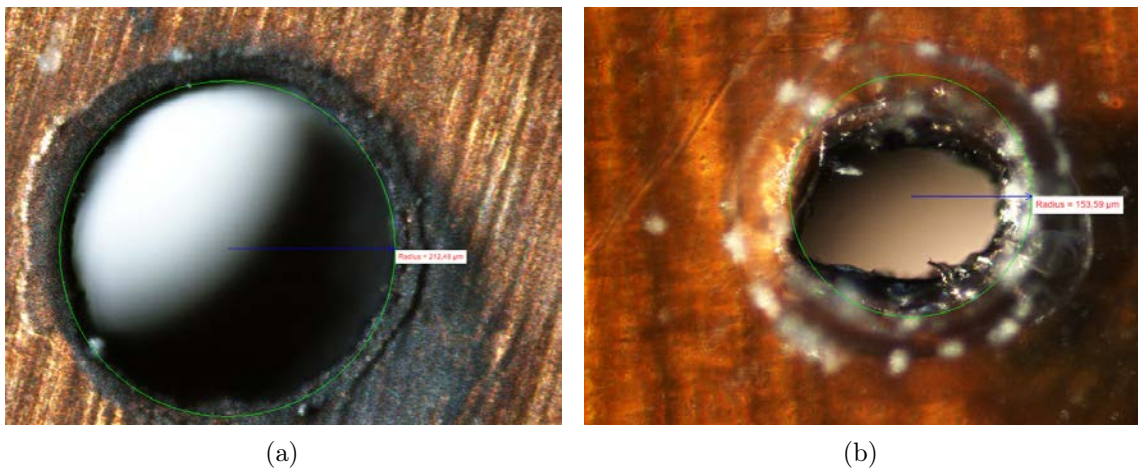


Fig. V.19: A multi stack of Kapton-lead foils perforated with a broad laser beam and a copper protection mask. Images taken from the copper layer side (a) and Kapton layer side (b).

the lead side is not possible since the melting points from lead and Kapton are too close. Hence, it was decided to use structured copper as a mask to laser only the Kapton. To test the principle, single Kapton metal samples were glued, and the metal layer was drilled. Then the samples were aligned under the microscope. The results are shown in Fig. V.19. It was observed that the laser is able to perforate one to three double layers with the copper mask. From the images it is not possible to see if the lead melted and contaminated the Kapton layers. The images show poor quality, which may however be improved with better aligned stacks.

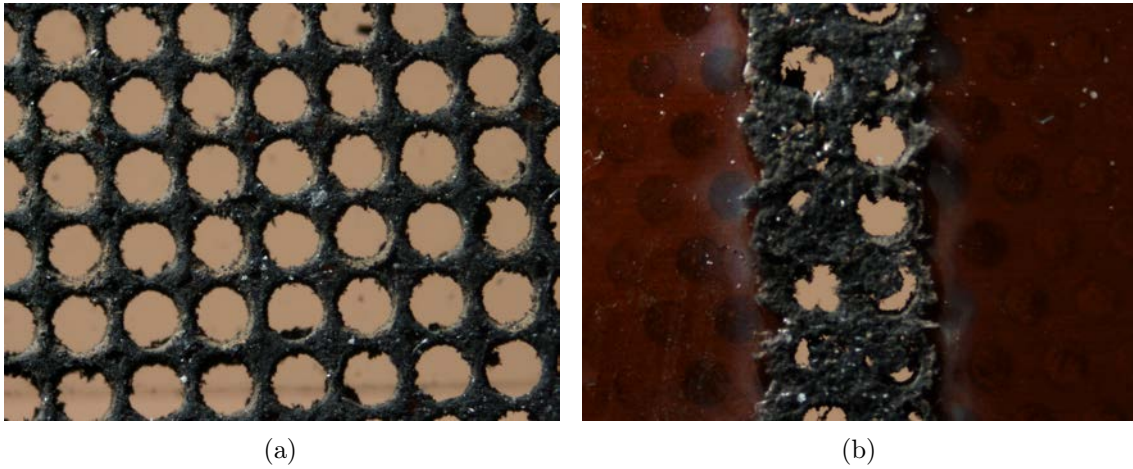


Fig. V.20: Microscopic images of samples from the Kapton side which were perforated with a CO_2 laser through a copper mask. In (a), the sample was irradiated with a scanning speed of 200 mm/s and in (b) the scanning speed was increased to 800 mm/s while the beam intensity was enlarged by a factor of four.

In a second iteration, a sample holder which aligns the samples precisely to the photo mask for the etching process was constructed. The holder was additionally used to produce 50 μm thick copper masks. It was tested in two different setups with different beam intensities and scanning times whether or not the broad beam of the CO_2 laser is able to remove the Kapton in the desired layer. In Fig. V.20, it can be seen that in both setups too much Kapton was evaporated. In both setups, the Kapton completely changes color after irradiation. The lead structure was also affected. Furthermore, high currents were observed even if only some volts were applied in a electrostatic test. Following the results, masked laser perforation does not seem to be an alternative perforation technique for converter manufacturing. However, it is possible that more sufficient hole quality could be reached if the CO_2 lasers are adjusted more precisely.

A more promising approach would be to increase the melting point of the lead to be able to use the lead directly as the mask. To test whether this idea works, a zinc foil with a melting point of 419.5° C which is approximately 100° C higher than for lead was used. The images in Fig. V.21 show that zinc is already usable as a laser shield. An increase of the melting point in the order of 100° C can be reached by using a lead-calcium alloy with only tiny amounts of calcium. The

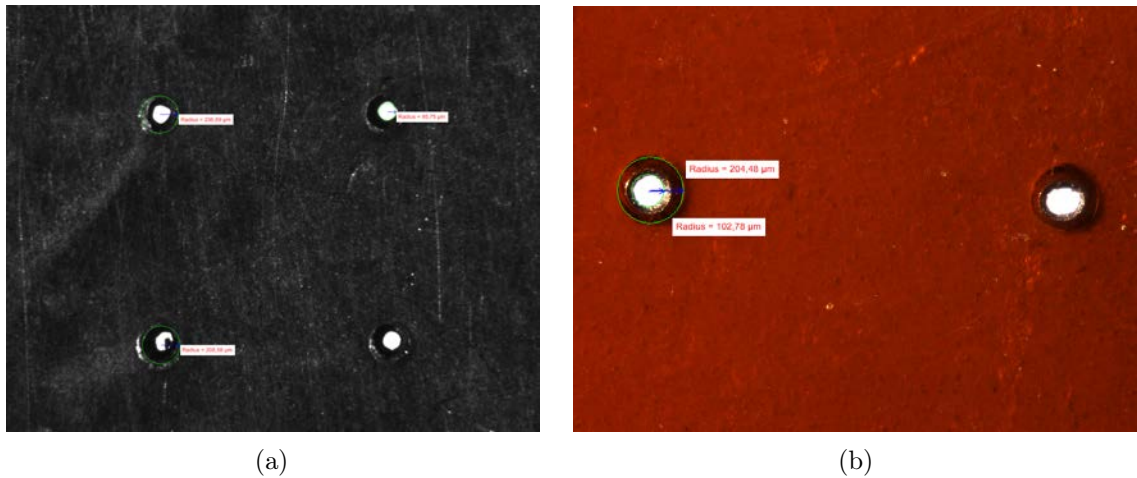


Fig. V.21: A zinc sample perforated with a broad laser beam. Images taken from the zinc layer side (a) and Kapton layer side (b).

calcium changes the rigidity of the metal. Unfortunately, this alloy is currently not processable by common foil manufacturers.

Even though these principles are very exciting, it remains questionable whether or not lasers could be used in advanced converter production.

V.3.5 Powder Metallic Screen Print

Screen print techniques have been widely used in the past to print things such as advertisement posters and signs, traffic plates, textile, bottles, and many more. Today the technique can often be replaced by digital printing techniques. Nevertheless, it is still used in many specific applications.

In the specific case of metals, a fine granulated powder of the material is necessary. This is combined with a binding agent, which is necessary to form a viscose paste which can be pressed through a screen or rather a sieve. The screen commonly consists of a stainless steel mesh with a fine granularity, which is used as the mask. Similar to the etching process, the mesh is laminated with photo resist laquer, which can be developed after irradiation of a printed screen mask. Hence, the metal paste can only be pressed through developed meshes of the screen, which gives the desired pattern. After print and dry, it is often desired that organic compounds given from the binding agent should be removed. This can be provided by sinter processes, whereby a temperature close to the melting point of the metal is applied within an oven or by a laser. The process step is necessary in the case that

the distinct properties like conductivity, rigidity, and others of the elementary metal are needed. To test whether powder metallic screen print is an adequate technique for HIDAC converter geometries, the Fraunhofer Institute IFAM⁸ in Dresden made several tests with lead alloys. After a failed attempt, it was possible to create a printable paste, which was printed on paperboard. Here it was seen that precisions in the order of 30-40 μm can be reached. The paste was also tested in sinter processes. It was shown that the technique is principally applicable for manufacturing HIDAC converters, but it was also seen that the created paste smears out at many positions and that holes within the solids appear after the printing process. This is demonstrated in Fig. V.22. Furthermore, the sinter processes have to be optimized to yield good results. Thus, it was realized that a lot effort has to be done to adjust the lead paste to reach results which are compatible to drilling techniques.

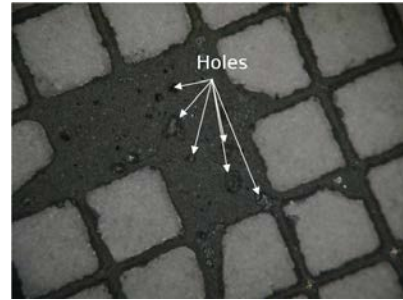


Fig. V.22: Sample of the screen print test of lead performed by IFAM. The print paste, which contains lead, had bad print characteristics that result in print errors, paste smearings, and holes in the solid structures.

Nevertheless, motivated by the mass production capabilities and potential precision of the technique, a screen print machine was purchased by the EIMI, and the upgrade of the machine for the purpose of converter production was the topic of the master thesis by *Konstantin Bolwin* [Bol13a]. A photograph of the upgraded screen print machine is presented in Fig. V.23. The production of photon-electron converters requires the alternating deposition of a high Z material and an isolation material. To obtain high quality prints, it is advisable to dry the printed paste on the sample after each layer deposition. One print cycle commonly produces a 10-30 μm thick layer. For the production of a full lead or insulation layer, thus, around three to six print cycles are required, respectively. Furthermore, a cleaning step for the screen is necessary in the case of lead or insulation paste exchange. Hence, it has to be ensured that the printing sample as well as the screen print mask are always placed in the same position with high precision. This is realized by using four cameras mounted on the machine and two markers on the screen and the sample, each. Additionally, electroluminescent foils are attached behind the markers to optimize the positioning accuracy. In Fig. V.23, the two cameras and markers for the position adjustment of the screen frame are highlighted. For the basis of the printed

⁸IFAM $\hat{=}$ Fraunhofer Institute for Manufacturing Technology and Advanced Materials

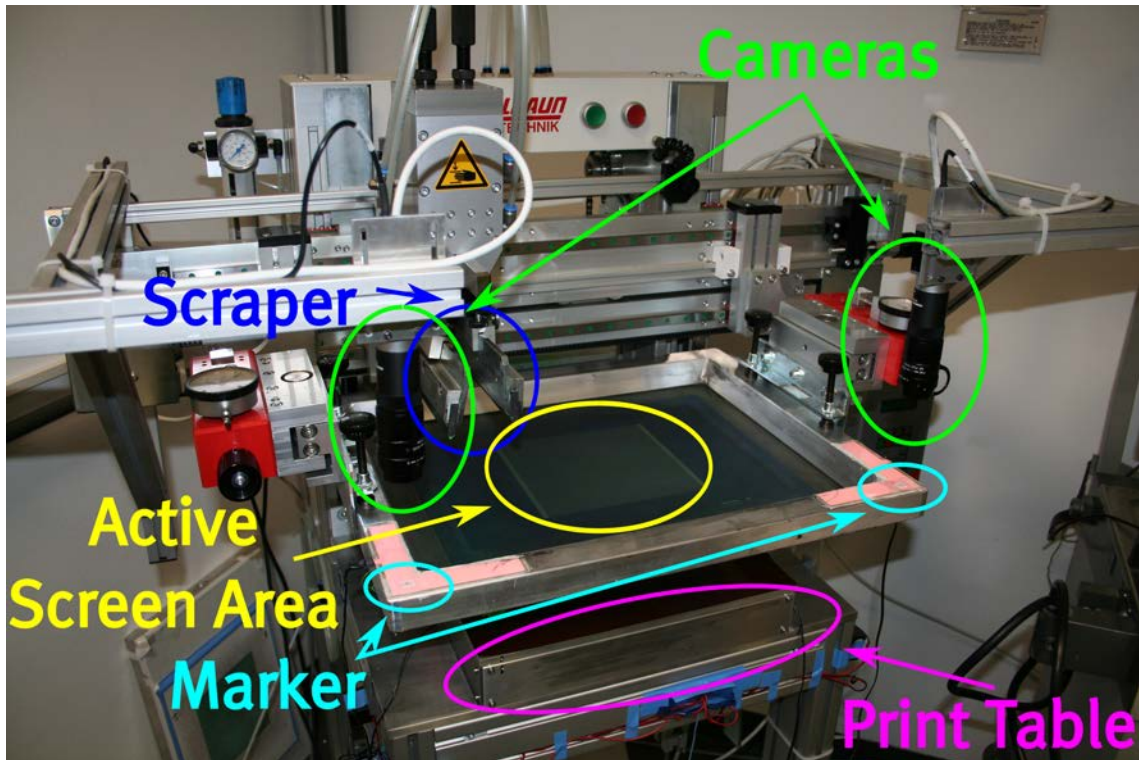


Fig. V.23: Photograph of the screen print machine which was upgraded in the EIMI. The machine uses a scraper to print the paste through the open meshes of the active screen area. To be able to wash the screen in between the overall printing process and to use different meshes, two cameras are installed on the machine frame to track two markers which are fixed on the screen frame. During the printing process, the screen is pressed on the print table where the printed sample is positioned.

converter, currently, a Kapton foil, in which two holes are cut to place the markers, is used. The foil is placed on a vacuum table (Fig. V.24(b)) that guarantees that the foil is positioned flat with respect to the screen mask. Within the table, two bores are made where the two other cameras are placed below. Of course, the bores have the same separation as the markers on the kapton foil.

With this setup and with conventional print pastes, it was possible to print stacks of different pastes with a sufficient precision for HIDAC converter production. In a next step, it is planned to build up a stack of several conductive and isolating layers as well as to examine whether these stacks provide high voltage stability. In long-term perspective, the goal is to find providers for high quality printing pastes that contain high Z materials to produce real HIDAC converters.

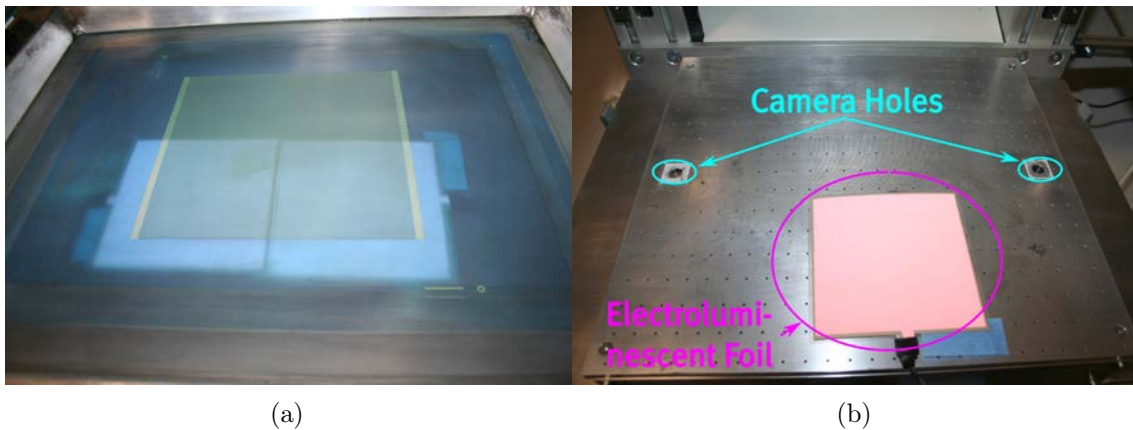


Fig. V.24: The zoomed view on the screen frame shows the screen pattern of a cathode strip pad layout with a honeycomb converter geometry (a). To emphasize the screen pattern, the two electroluminescent foils were hold in the background. In (b), a zoomed view on the print table is shown. The table is drilled with thin holes and connected to a vacuum pump which ensures that positioned samples lay flat with respect to the screen frame. Furthermore, cameras are positioned below the table to track markers, which are fixed on the print samples. Two electroluminescent foils are placed behind the markers to improve the positioning accuracy.

V.3.6 Further Production Techniques

Despite the followed up techniques described above, other techniques are still imaginable. For example, weaving techniques could be used to take thin lead or tungsten wires to form net structures, which could directly be used as the single lead layers of the converters. Similar techniques may be feasible to create high Z , low density materials (to give conversion electrons a large free mean path). These can be placed in homogeneous electric fields, which would be necessary to extract the conversion electrons. It should also be possible to use electro plating techniques to ablate the heavy metal atoms on cathodes, which are directly in the desired pattern.

V.4 Discussion

It was presented on the basis of `Geant4` simulations that a simple change in the drill pattern to equilaterally triangular arranged holes with a hole-to-hole separation of $465 \mu\text{m}$ would substantially increase the system sensitivity by 33.7% (Fig. V.3). This hint for improved sensitivity states the most concrete value in this analysis, since it involves no changes in hole diameter or insulation thickness. All other

geometry considerations heavily intervene in the detection process. For the other sensitivity improving parameters derived in this chapter, it is instead more difficult to judge how well the single models (`Geant4`, `Comsol`, `Garfield`, `neBEM`, own tools) describe the reality. Nevertheless, the individual results show convincing properties which correspond to expected tendencies and magnitudes.

Following the models, the sensitivity has a strong dependence regarding the hole diameter (Section V.2.1.2 and Section V.2.2), wall thickness (Section V.2.1), hole depth (Section V.2.2), a medium dependence on insulator thickness (Section V.2.1.2), and is slightly influenced by production given parameters like cone-shape holes (Section VI.7.3) or alternative honeycomb hole patterns (Section V.2.1.4).

In conclusion, the combined simulation results prospect a sensitivity enhancement of around 150% for a scanner in which only the hole pattern is optimized, the number of modules is doubled, and thinner converters are utilized. Alternatively, a sensitivity enhancement of around 100% can be reached if the hole pattern is optimized and a hole diameter of 500 μm is employed. Nevertheless, it must be considered that this result is only valid in the case that no gas amplification occurs within the converters.

Although the simulations give reasonable results in the first order, it is of certain importance to validate the electron detection efficiency experimentally to confirm whether the prospected sensitivities are really accessible. Furthermore, the optimal hole pattern is strongly dependent on the number of applied modules or layers. Thus, the maximum sensitivity can be further increased by taking thinner walls and more modules. This subject will be resumed in the simulation of single lead layer detectors (section VII.2).

The majority of possible hole manufacturing techniques have been examined for the specific feasibility to produce HIDAC converters. The benefits and drawbacks of each technique have been discussed, whereby each technique has unique advantages in flexibility in the hole geometry variations, processing complexity, or active area size optionality. In conclusion, it was found that in principle, etching techniques are able to produce single lead-Kapton layers, but further work would be necessary to find good processing parameters to reach a reasonable hole quality. Moreover, the problem is that, until now, no smart solution for assembling the single layers to a stack has been found. Indeed, single layers could be stacked in supporting frame structures, but this only allows moderate detector sizes and puts

additional absorbing material into the device. Hence, those production techniques are not too promising for a second HIDAC generation.

The only alternative production method, able to directly produce stacks, is therefore the screen print technique. Regarding the first results of the screen print test, the technique will need a lot of effort to deliver reasonable hole quality. However, the method has a huge potential to produce complete converters quickly and cost-effectively.

Although alternative production processes are possible, the simulation results presented here do not encourage the replacement of the drilling technique. Of course, the desired hole pattern with a hole-to-hole separation of $465 \mu\text{m}$ is hard to reach, but high-end drilling machines should be able at least to deliver stable results with a minimum wall thickness of $80 \mu\text{m}$. By following the simulation results, this is sufficient for hole diameters of $400 \mu\text{m}$ to substantially increase the photon conversion probability.

CHAPTER VI

Converter Test-Bench

A photon converter test-bench to validate the high voltage (HV) stability, investigate count rate and efficiency performance, to test MWPC parameter influences, and to check the foreseen readout electronics was built. This chapter describes the complete setup and shows results from different measurement trials.

VI.1 Setup

The central part of the test-bench consists of the wire frame base and the converter holder. Different types of converters can be mounted in front of the holder by four nylon screws. Washers made with a height of 3 mm were produced to keep the converter at a precise distances from the anode wires. The converter holder is mounted on the wire frame base plate, where two sliding guides with four sliders assure that the converter can be positioned accurately and plainly in front of the wire and cathode planes. The wire frame base carries the cathode readout plane and the wire frame. The converter holder can be carefully positioned to the frame by the use of a threaded spindle. The readout pad carrier, the converter holder, as well as the washers were made of PEEK¹ to assure reasonable insulation to the HV parts. The cathode plane and the wire frame are made of G11, which is a flame resistant composite of fiberglass and epoxy resin, and is a typical PCB material. The wires are made of gold plated tungsten-rhenium and have a diameter of 20 μm .

¹PEEK $\hat{=}$ polyether ether ketone. An organic thermoplastic with good mechanical handling properties as well as chemical and high temperature resistance.

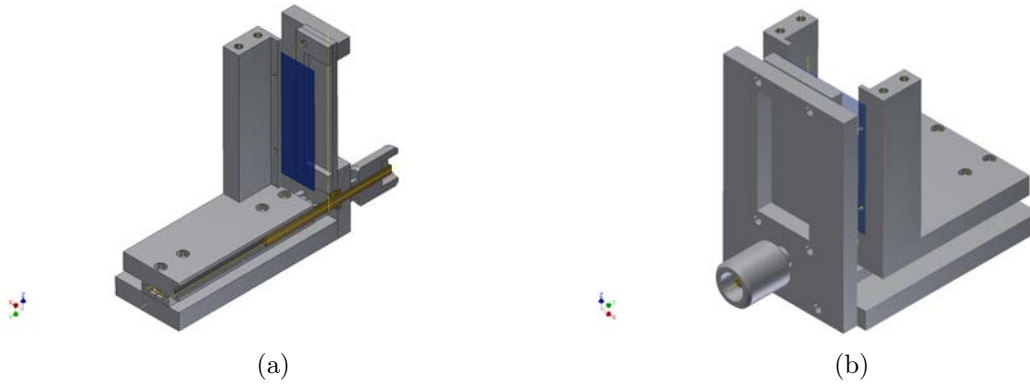


Fig. VI.1: Construction drawing of the converter holder and wire frame base made with Inventor. The wire frame base carries the cathode readout plane and the wire frame. In (a), a half cut-view is shown, whereas (b) gives the full view. Converter sample is highlighted in blue and threaded spindle in yellow [Ber11].

The wires are 8 cm long and separated 1.5 mm. The readout pad plane has eight cathode strips each with a size of 3 cm×3.4 mm and a pad to pad width of 3.8 mm. They are arranged perpendicular to the anode wires and connected to a HARWIN connector, which lies on the side behind the wire frame. The design drawings of the converter holder and the base plate are shown in Fig. VI.1. The wire frame base is fixed on a 20×35 cm² large aluminum plate, which also holds the readout electronics to an appropriate distance to the HARWIN connector of the pad plane. The whole setup is placed in a 22×43×60 cm³ large acrylic glass box. The edges of the box are glued with an epoxy glue from Araldite, whereas the top sealings were made with window gaskets from Tesa and twelve screws to guarantee gas tightness to the environment. The low and HV supply and the data transfer are directed through two flanges. One flange is dedicated for the HV supply with two SHV² feed-throughs to supply the anode wires and converter probes with different voltages. The other flange is equipped with a D-sub vacuum feed-through with 25 pins to supply the low voltage to the readout electronics as well as the USB connection for the data interface. A photograph of the converter holder with the wire frame base and the complete measurement setup is illustrated in Fig. VI.3. The HV power supply is established by the two ISEG modules EHS 8630n-F and EDS F025p for negative and positive voltages and are installed in a Wiener Mpod Mini. It is possible to set arbitrary measurement protocols for the HV control by the use of self-written PEARL scripts and a PC. In the setup, the positive HV is applied only to the wires, whereas its ground is connected to the pad plane and the electronics ground. The negative

²SHV connector $\hat{=}$ safe high voltage connector

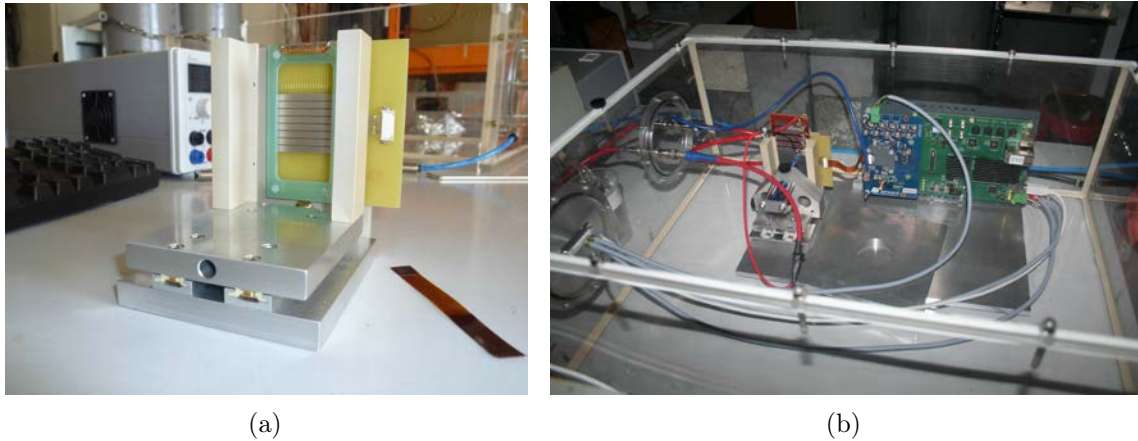


Fig. VI.2: Photograph of the assembled converter holder equipped with the wire frame base (a). In (b), the full setup with the electronics with cabled connections inside the gas tight acrylic glass box is shown.

HV is connected to the rear conductive layer of the converter, whereas the layer facing the wires is connected with its ground. For the low voltage power supply, a HAMEG HM7044 with four channels is used.

The gas supply system with components from MKS is able to support gas mixtures with up to three gases with exact fractions and is described in [Ver10]. In most measurements, the system was run with a constant flow of 10 l/h with an argon-carbondioxide mixture with 15% CO₂. Behind the acrylic glass box at the gas output, a small bubbler filled with DIFFELEN oil is installed, which guarantees a small overpressure inside the box, which assures that no contaminations from the environment get into the system.

VI.2 SPADIC

A possible candidate for the readout electronics of a new HIDAC based scanner system is the self-triggered pulse amplification and digitization ASIC (SPADIC) [AFP10]. It is a specialized readout ASIC³ for the transition radiation detector (TRD) of the CBM experiment [FHK⁺11], which is planned at the upcoming accelerator facility FAIR in Darmstadt. Compared to the current electronics of the HIDAC, the main advantage is the self triggering. The HIDAC electronics use the anode wire signal to trigger the cathode pad read out. This method limits the performance of the system

³ASIC $\hat{=}$ application-specific integrated circuit

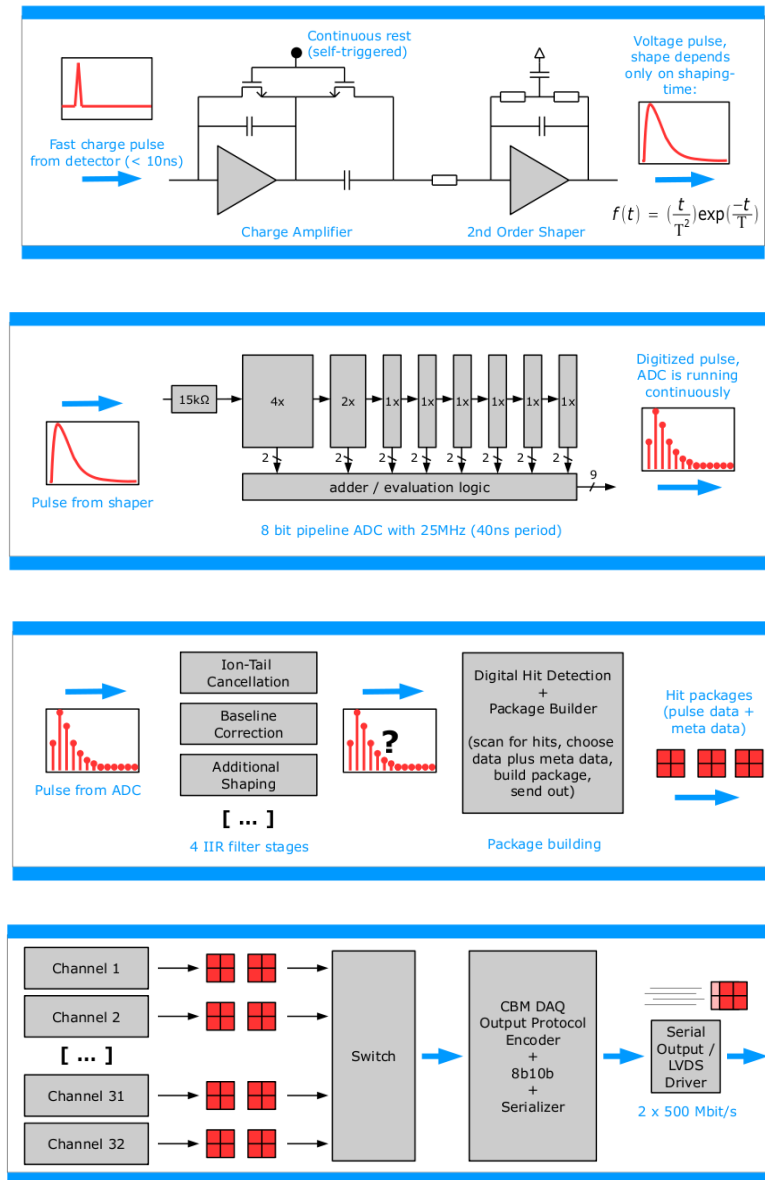


Fig. VI.3: Flow chart from the analog and digital part of the SPADIC illustrates the signal and data processing concept [Arm13].

at high activities, since no time information is given when multiple hits occur on different cathode pads within the time frame of the trigger window. A schematic illustration of the signal and data processing architecture is shown in Fig. VI.3. The merging of amplifiers and pipeline analog-to-digital converters (ADCs) on one ASIC allows a compact design of the front-end electronics and reduces the amount of dead material within the setup. Additionally, digital shaping and filtration are possible on board which optimizes event selection and allows the synchronization of the data with meta data such as timestamps. In contrast to the HIDAC electronics,

the storage of self triggered single events with time stamps allows the application of arbitrary and activity dependent coincidence window widths in post-processing. The SPADIC trigger thresholds can be set separately for each readout channel. This improves the performance as electronic noise, based on the inequality of readout pad shapes and impurities, can be reduced. At least, this should lead to a longer life span of those detector modules which have a localized damage leading to noise only on some wires and channels. Furthermore, digital data processing capabilities of the SPADIC like second order shaper or ion-tail cancellation are able to improve signal quality and higher rate capabilities. The properties of the chip perfectly match the needs for a gas-based PET detector system and can be acquired for low cost when the electronics come to the phase of mass production. Furthermore, the predecessors can be used free of charge since CBM TRD detector prototypes are developed and tested in the “Institut für Kernphysik” (IKP).

The test setup is equipped with the developer version 0.3 of the SPADIC. The chip has eight channels and is read out and configured with a Susibo 2.0 readout board. In this setup, the chip can only trigger on one channel, whereupon the data output of all eight channels is processed to the USB⁴ data output if a trigger occurs. The SPADIC needs a power supply of 5.5 V@ ~ 80 mA and the Susibo of 3.3 V@ ~ 1.2 A. The C++ based software for the chip configuration, online display, and data extraction is called `hitclient`.

VI.3 Validation of the Test-Bench

The test-bench was validated in a first step with measurements of an iron (⁵⁵Fe) source and a sodium (²²Na) source. The ⁵⁵Fe isotopes decay via electron capture. After the decay, the vacancy of the K-shell is filled by another electron and the gained energy is dominantly liberated by the emission of *Auger* electrons with a kinetic energy of 5.2 keV or X-rays with an energy of 5.9 keV. In the test setup, a carbon foil with an ultra-thin silver cover, which was clamped in the converter holder, was used. The conductive and grounded silver cover is needed to transform the setup in a conventional MWPC. It must be very thin, since it must be traversable for the low energetic X-rays of the ⁵⁵Fe source, whereas the *Auger* electrons are absorbed by the foil.

The ²²Na source is a β^+ emitter, and the daughter nucleus ²²Ne often emits a

⁴USB $\hat{=}$ Universal Serial Bus

1275 keV photon while de-exciting in the ground state. The source has a very thin entrance foil so that some positrons are also able to leave the source volume. Otherwise, the two 511 keV annihilation photons leave the source. For the measurements with the ^{22}Na source, a 55 μm thick single-lead-layer-converter glued on a Kapton foil was used.

The quality of the output data is analyzed by generating an integrated pulse height spectrum of the maximum pad and its two adjacent pads and by evaluating the pad response function (PRF) information.

PRF

The PRF relates to the induced charge on a cathode pad from an avalanche on the wire. The function is dependent on the horizontal distance from the pad center to the position of the avalanche $\lambda = x/h$ weighted by the cathode anode gap h .

A single-parameter semi-empirical formulation for the PRF for MWPCs was derived theoretically by *Gatti* [GLOS79] and the charge on a finite cathode pad can be calculated with [KB09]:

$$\int_{\lambda-\frac{W}{2}}^{\lambda+\frac{W}{2}} \Gamma(\lambda) d\lambda = -\frac{1}{2 \arctan \sqrt{K_3}} \left[\arctan \left(\sqrt{K_3} \tanh \left(\pi(-2 + \sqrt{K_3}) \frac{W + 2x}{8h} \right) \right) + \arctan \left(\sqrt{K_3} \tanh \left(\pi(-2 + \sqrt{K_3}) \frac{W - 2x}{8h} \right) \right) \right], \quad (\text{VI.1})$$

where Γ is the cathode charge distribution function, W is the pad width, and K_3 is the empirical parameter, which varies for different MWPC geometries.

The displacement from the center of the pad to the avalanche can be simply derived approximating the PRF with a *Gaussian* distribution:

$$x = \frac{W}{2} \frac{\ln(Q_{i+1}/Q_{i-1})}{\ln(Q_i^2/Q_{i+1}Q_{i-1})}, \quad (\text{VI.2})$$

where Q_i is the induced charge on a pad and Q_{i-1}, Q_{i+1} are the charges on the two adjacent pads.

An overview on the simple derivations of the formula and values for the parameter K_3 are given in [Ver10], whereas a full description of the derivations is described in [BRR08] or [MF84].

Examples of the integrated pulse height spectrum results of the measurements with the ^{55}Fe and the ^{22}Na source are shown in Fig. VI.4(a),(c). For the ^{55}Fe source, the anode voltage was set to 1990 V. It can be seen that two peaks occur in the

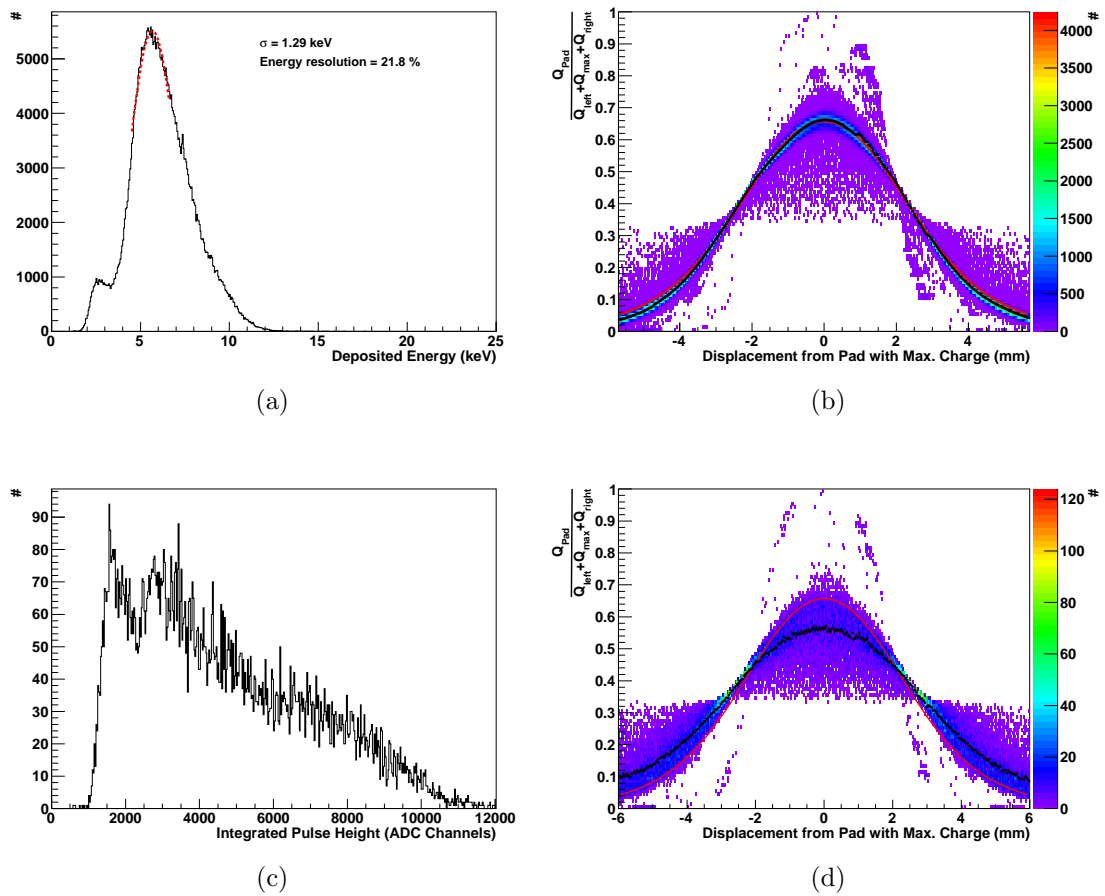


Fig. VI.4: Validation of the converter test-bench performance realized with two different data analysis plots. The upper row presents results from a measurement with the ^{55}Fe source and the lower row results with the ^{22}Na source. Figure (a) and (c) show the integrated pulse height spectrum. For the iron source, the distinct photon energies are known, which can be used to make an energy calibration. The energy resolution of the setup was determined as 21.8%. Figure (b) and (d) show the according pad response functions. For the ^{55}Fe source, the mean values agree well with the theoretical prediction shown in red. The mean values (black dots) do not match to the theoretical distribution for the ^{22}Na source.

spectrum, whereby the main peak comes from the measurement of the full energy of the 5.9 keV photon. Here, the produced photo electron and the subsequent *Auger* electron from the de-excited argon atom are measured. The small peak is the escape peak where the argon atom liberates no *Auger* electron but a X-ray which is able to leave the detection volume. The maximum of the escape peak is approximately at 2.7 keV. Hence, the integrated pulse height spectrum can be calibrated and an

energy resolution can be determined. Regarding all measurements with different anode voltages and a few variations in the CO₂ contributions, it is observed that an energy resolution of the system between 20-25% can be reached with SPADIC readout in the case that advanced data processing after data acquisition is included. In the example of the ²²Na source, the anode voltage was set to 2000 V. The ionizations induced by the ⁵⁵Fe source are localized, whereas the ²²Na source causes electrons in the converter with energies in the order of 511 keV or 1275 keV which are moving more or less on straight lines through the chamber, causing randomly occurring different sized ionization clusters along the track. Thus, the integrated pulse height spectrum shows no characteristic structures. As can be seen in Fig. VI.4(c), it is difficult to set a distinct threshold to register also signals induced by only a few ionizations.

The PRF can be analyzed by plotting the collected charge on a pad to the overall charge on three pads against the displacement of the reconstructed position to the pad center of the pad with the maximum charge by using (VI.2). The results of the measurements with the ⁵⁵Fe and ²²Na source are illustrated in Fig. VI.4(b),(d).

For the ⁵⁵Fe source, the mean values of the charge fractions (black dots) are in very good agreement with the theoretical expectations from (VI.1) (red curve). The spread around the mean values is common for such measurements. It can be seen that the advanced data processing is not able to remove all artifacts from the data. The results from the ²²Na source show that the theoretical expectations only give an upper limit to the resulting charge fractions. The unlocalized input ionizations induce avalanches with a wider spread or even multiple avalanches, resulting in lower charge fractions in the central pad. The spread of the charge fractions around the mean values is already as high as for the ⁵⁵Fe source, whereas only one seventh of the statistics were collected. This demonstrates the worse performance at 511 keV electrons compared to 5.9 keV electrons.

To reach the quality of the presented results, the output data was processed after the data acquisition. In the presented examples, a noise filter, an event based baseline subtraction, and an overflow and multi-hit event rejection were applied.

For comparison, the measurements were redone with older PASA⁵ electronics

⁵PASA $\hat{=}$ pulse amplification and shaping ASIC

from GSI⁶ and a SIS3320 ADC from Struck. This readout chain achieved energy resolutions with the ⁵⁵Fe source in the range from 17-20% for the test setup with different anode voltages. The results for the ²²Na source were very similar to the presented results.

Conclusively, the measurements show that the DAQ system and the test-bench itself are able to produce reliable and reproducible results. Furthermore, it was shown that the SPADIC is able to recognize, amplify, and digitize the upcoming signals. This should be sufficient for the desired PET application.

VI.4 Simulation

The geometry of the test setup was implemented in **Geant4** on the basis of the HIDAC implementation. The simulations of the setup are necessary to make predictions about the expected count rate of the system and to derive estimations on the efficiency of the setup by comparing measurement and simulation. Only geometrical factors are considered in the simulation, whereas events which were not detected due to charge transport in gas or electronic limitations are not considered. Nevertheless, the expected count rates from the simulations should not be several times larger than the measured results. Simulations were made for two differently produced drilled prototype converters. Both converters have four conversion layers either made of bronze or lead. They also differ in the size of the perforated area. A DAWN visualization of the converters together with the implementation of the ²²Na rod source which was used in the measurements is shown in Fig. VI.5. The detailed implementation of the source was necessary since the setup also detects electrons produced from ionizations of the energy loss of positrons, which are able to leave the source volume since the holes of the converters are open to both sides.

As the SPADIC readout is only able to trigger on one single channel, the active gas volume was set to 1 cm width to only consider electrons which pass this volume. The volume was set more broadly than one pad size since the readout also triggers if avalanches occur in the vicinity of the adjacent pads.

In the validation measurements, a large impact on the performance of the system depending on the distance of the sources in relation to the converter was observed. Hereupon, a source holder which fixed the distance from the solid source volume to the converter surface to 7 mm was built. The simulated dependence of the count

⁶GSI $\hat{=}$ Gesellschaft für Schwerionenforschung

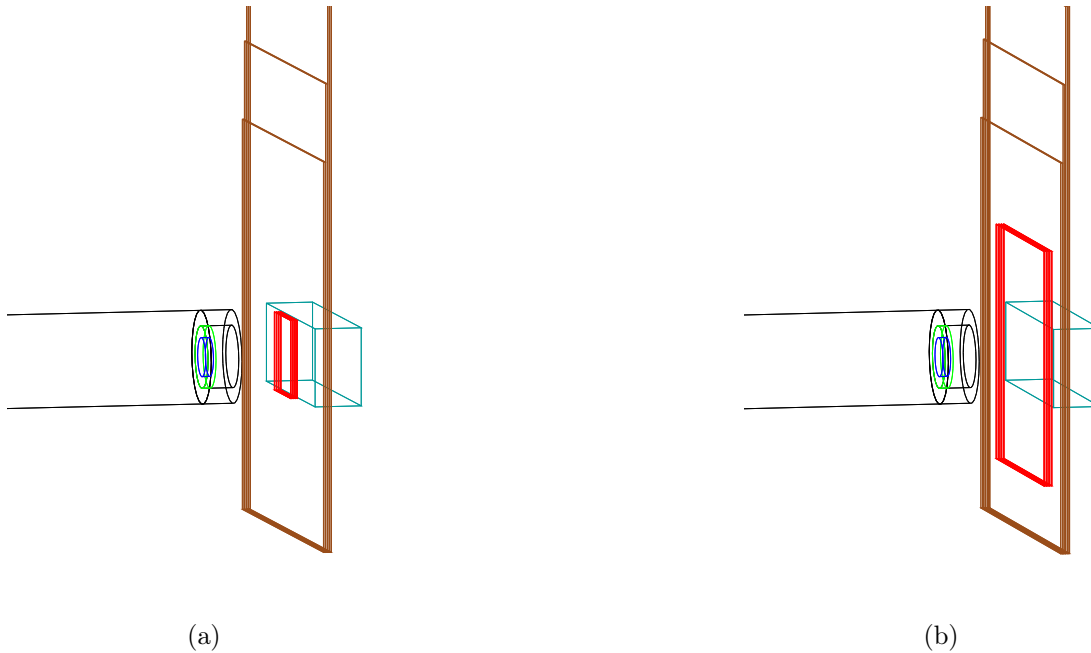


Fig. VI.5: Setup of the test device for two different kinds of converters simulated with `Geant4`. In (a), the lead converter prototype with a perforated area of 1 cm^2 in red is shown. The setup of the bronze converter with a perforated area of 9 cm^2 is presented in (b). The size of the gas volume which defines if a signal is triggered is illustrated in cyan and the insulating material of the converter is colored brown. The used sodium rod source (black) was simulated in detail where the active material is shown in blue.

rate to the distance together with the values for the realized distance of 7 mm are presented in Fig. VI.6. As explained earlier, the simulation does not consider the electric field. Thus, it is only possible to either count only the electrons which are able to reach the large gas volume or to count every electron able to reach any gaseous part of the detector. Transferred to the measurement, this would roughly distinguish the behavior of the test-bench with and without applied HV to the converter.

Even though large efforts were made to mimic the test setup as precisely as possible, some deficiencies are still existing. For example, the source is not aligned to the center of the triggered pad in the measurement. Nevertheless, the simulation gives a rough benchmark for the expectable count rate and is able to predict precisely how geometrical changes within the test setup influence the count rate.

VI.5 Drilled Converter Results

The first HIDAC prototype converter for the test setup was made of four $100 \mu\text{m}$ thick bronze sheets which were glued with a two component epoxy glue on $120 \mu\text{m}$

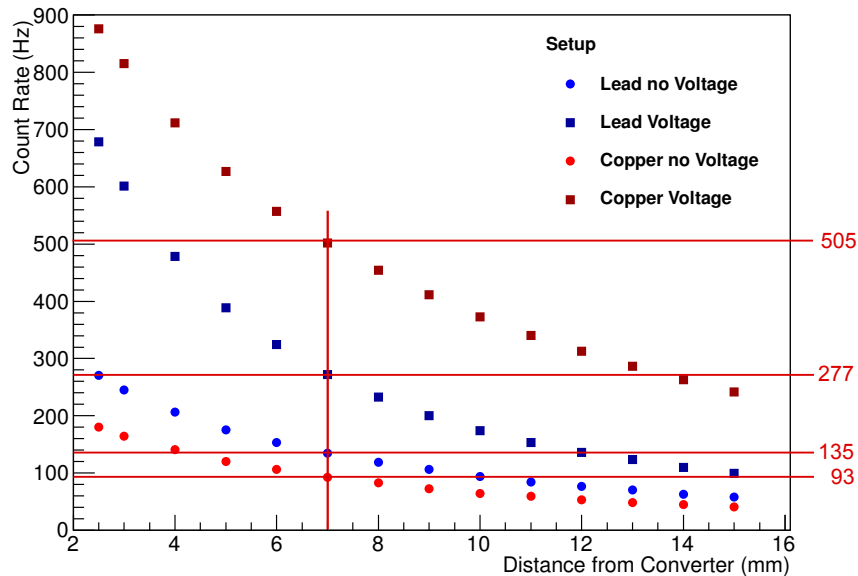


Fig. VI.6: Expected count rates derived from `Geant4` simulations for the different lead and bronze prototype converters with and without applied converter voltage performed for different source distances.

thick Kapton foils. The Kapton foils were larger in size to assure that there is no electrical contact between the bronze layers. The different bronze layers are increased in size to be able to apply different potentials on each layer. All layers are glued together using the same epoxy glue. An active area of $3 \times 3 \text{ cm}^2$ with a triangular shape, a hole diameter of $400 \mu\text{m}$, and a hole-to-hole separation of $500 \mu\text{m}$ were drilled in the IKP workshop with a PCB drilling machine of the lower price segment. Between the single bronze layers, resistors with $1 \text{ M}\Omega$ are soldered to ensure equally distributed potential differences at low currents. The quality of the holes from the resulting converter were rather moderate, but it was possible to use the converter in the test device. The HV stability was quite impressive as converter voltages up to 1350 V were applicable. Results of measurements with this converter are presented in [Bus12].

The second prototype converter was made with $55 \mu\text{m}$ thick lead foils instead of the bronze layers and had the same dimensions as the first prototype converter. Here the holes were drilled with a PCB drilling automate of the medium price segment at the CERN workshop, where an active area of $1 \times 1 \text{ cm}^2$ was perforated. The two prototype converters are illustrated in Fig. VI.7, and the high quality of the holes

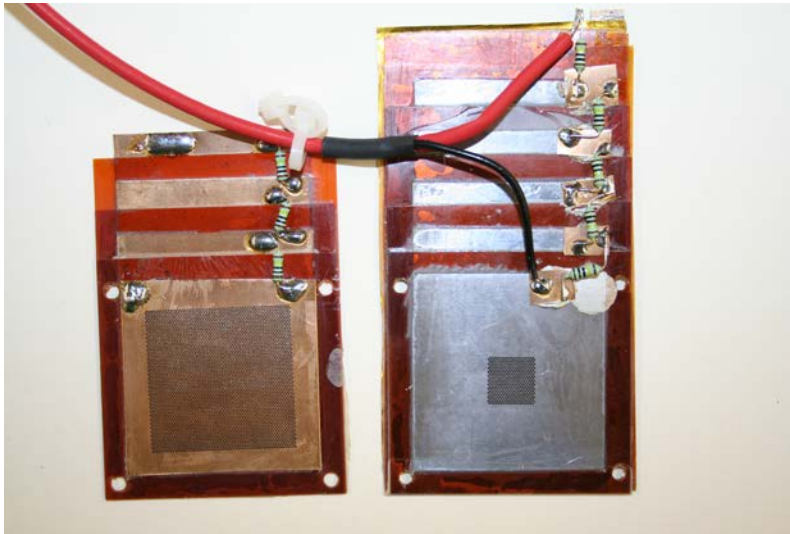


Fig. VI.7: Photograph of the two prototype converters where the left bronze prototype, drilled at the IKP workshop, is compared to the lead converter on the right which was perforated at CERN.

from the lead converter imaged with a microscope can be seen in Fig. V.15.

The prototype converter was tested in the setup where a `PEARL` script was used to automatically apply different anode voltages. Unfortunately, the `hitclient` does not run without breakdowns so that only acquisition times of around 10 hours are possible. Hence, the measurement protocol was set to have a day and a night run, whereby the voltage is raised from 1600 V to 2300 V in 5 V steps. To have a comfortable reset time, in the day run 3 min measurements per step were made, whereas in the night, the count rate was measured for 5 min for each step. Every five seconds, the `hitclient` writes the count rate information to the output stream. In the analysis, a *Gaussian* fit is applied to the count rate distribution, and the mean value with the according standard variation is stored. The results of 39 measurement scans with different applied converter voltages are illustrated in Fig. VI.8. It was observed that the count rate increases exponentially with the applied anode voltage. This comes on the one hand from the fact that with an increased anode voltage, larger signal sensitive volumes are given, i.e., the volumes where the electric field is so low that created electron ion pairs can recombine get smaller. On the other hand, the gain also increases, which means that the electron avalanches get larger. They are therefore able to induce charges to trigger signals on pads which are further away. Both effects lead to increased sensitive volumes. Hence, a constant volume assumed in the simulation is not valid. For voltages above 2200 V, the count rates begin to

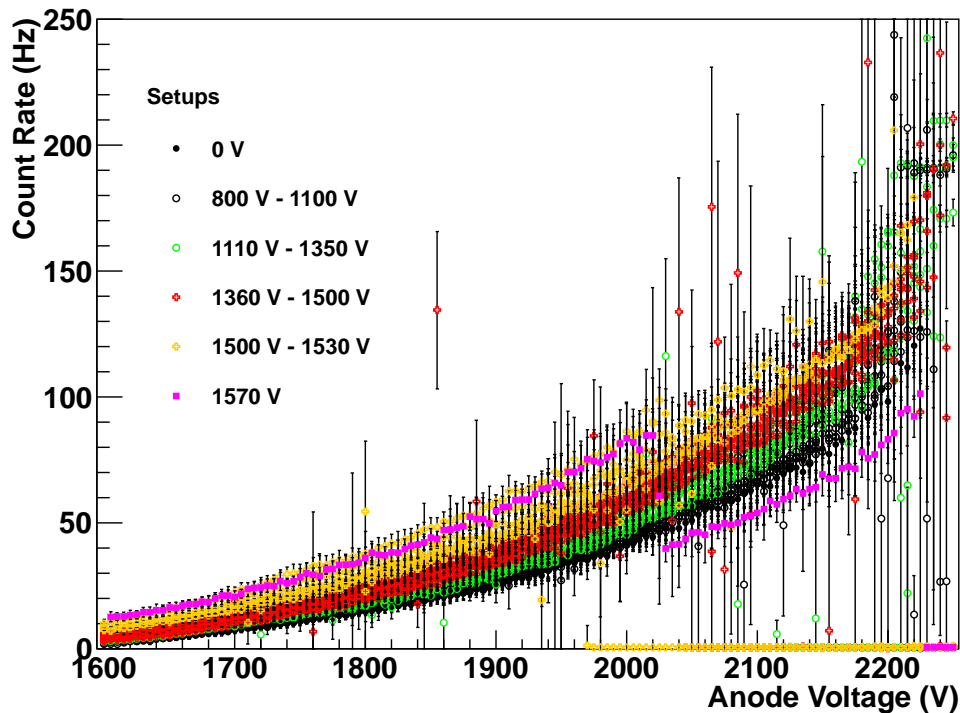


Fig. VI.8: Overlay of 39 count rate measurements made under same conditions with different converter and anode voltages. The measurements were performed with source holder and copper shield. For the measurements with a count rate near 0 Hz, the anode voltage tripped at was set automatically to zero.

diverge and become discontinuous. In this region, the electric fields get so large that so many argon atoms are excited so that some photons from the de-excitation are able to induce further avalanches by liberating electrons at the cathodes.

It is obvious that the count rate rises with increased converter voltage. As in a direct comparison of two measurements, this is not always true. Due to the large errors, the increase can be seen directly by grouping several measurements with adjacent converter voltages. Here, an interesting slope is given for the highest applicable converter voltage of 1570 V (pink). A current trip during the measurement with the anode voltage at 2020 V leads to a turn off of the converter voltage. Thus, in this specific case the second half of the single measurement series correspond to measurements without converter voltage and is in good agreement with the black measurement series.

Overall, the measurements show that the count rate can approximately be doubled for a four layer converter if one applies a converter voltage in the upper range. For

a stable anode voltage at 2100 V, the absolute values for the count rates are approximately 50 Hz without applied voltage and 100 Hz with high converter voltages. Compared to the simulations from Fig. VI.6, the measured values are approximately a factor of 2.7 lower than expected. During the measurements, a 100 μm thick bronze shield was used to assure that no direct positrons or electrons can reach the holes and the measurement triggers only on a single pad whereby it is difficult to determine how many triggered signals correspond to avalanches directly in the front of the pad. Therefore, the size of the assigned sensitive volume in the simulation is very unprecise, which could possibly explain the differences in the observations.

Nevertheless, the results show that the SPADIC electronics and converter production techniques can in principle be used to produce a new HIDAC scanner system.

VI.6 Results from Measurements with a Drift Layer

Following the result from the measured spectrum of the ^{22}Na source in Fig. VI.4(c), one can assume that the test-bench is not able to recognize the smallest electron clusters from primary ionizations of the conversion electrons. To validate if the setup is able to trigger on those small clusters, the setup was extended by a drift frame perpendicularly to the anode wire frame. The drift frame was equipped with 80 μm thick wires consisting of a copper beryllium alloy and placed 3 mm apart from the anode wires. The converter holder was supported with an additional threaded spindle which was conducted through the acrylic glass box. Therefore, the drift volume can be enlarged without opening the box. The drift voltages were adapted to assure a constant drift potential of 100 V/mm. In this domain, the drift velocity is constant, and it is ensured that no ionization is induced by the electrons. The results of measurements with a single layer lead foil with different drift volumes are presented in Fig. VI.9. It was observed that the count rate is neither increased nor decreased when the drift distance was enlarged from 3 mm to 19 mm (Fig. VI.9(a)). For a further checkup, a measurement without applied drift voltage on the same drift setup was repeated. The outcome in Fig. VI.9(b) shows the expected decreasing count rate performance for larger drift distances.

Conclusively, one can derive from these measurements that a substantial part of small ionization clusters can be observed, at least in a 9 mm thick gas volume.

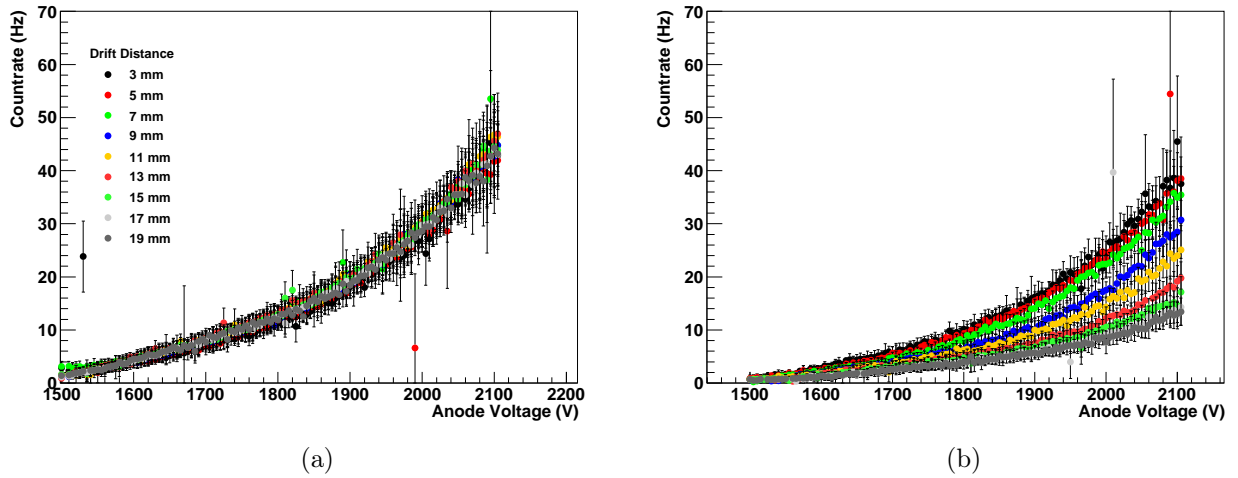


Fig. VI.9: Overlay of 9 count rate measurements performed with a single layer lead converter with different drift distances. The source was fixed in the source holder facilitating a constant distance from the source to the lead converter. In (a), the drift voltage was raised proportionally to the drift distance to have a drift field with a potential difference of 100 V/mm. In (b), the drift voltage was turned off.

VI.7 Cone Shaped Structured Single Layer Design Results

During the simulations of scanner geometries using alternative detector concepts (will be discussed in the next chapter), the idea of using structured lead foils to increase the surface to volume ratio of the converter came up. Considering lead etching techniques, cone shaped holes would be an option for such a structured lead foil. A sketch of the expected layout of such a foil with an optimized choice for the different parameters of the geometry is shown in Fig. VI.10(a). It was assumed that the effect would be very small for a single $55 \mu\text{m}$ thick foil. Hence, simulations for different foil thicknesses, with increasing maximal cone radii to achieve the same geometry, of four single detector modules were performed. The results are shown in Fig. VI.10(c). It was observed that the sensitivity saturates around $60 \mu\text{m}$ for the plain lead foils, whereas the structured foils saturate around $150 \mu\text{m}$. Thus, the comparison of count rate measurements with $200 \mu\text{m}$ thick lead foils should show that the structured converters are able to achieve $\sim 30\%$ higher count rates than the plain converters. Subsequently, four $200 \mu\text{m}$ thick and four $100 \mu\text{m}$ thick lead foils were glued on Kapton foils and were etched by the IPM with the aim to reach the

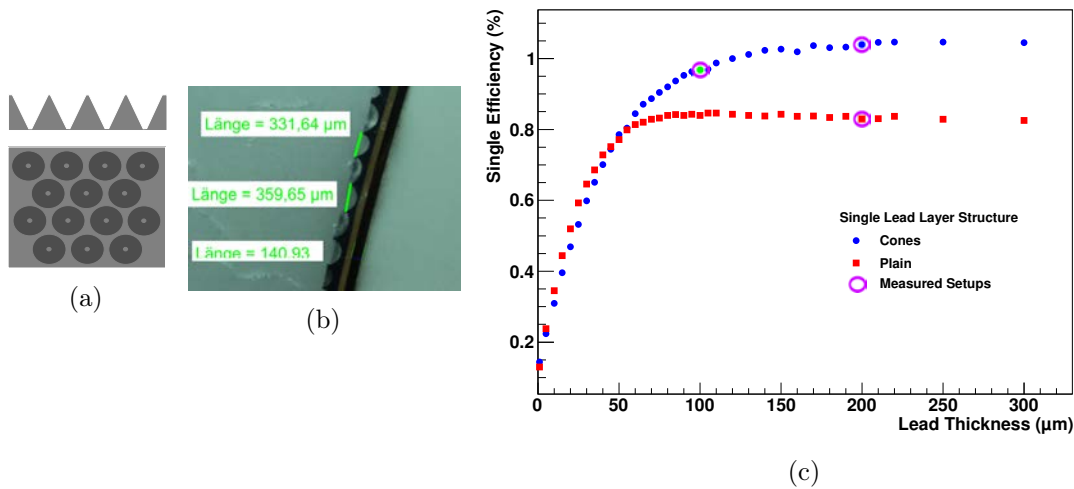


Fig. VI.10: Design of a surface optimized cone structure suggested for a single layer lead converter. The simulated theoretical design of the converter in a cross and top view (a), cross view of a Microtome cut slice of an etched realization of the structured lead converter (b), and the outcome of the simulated single efficiencies of plain and structured single layer lead converters for different lead thicknesses (c) are displayed.

simulated geometry. To obtain a cross view on the etched probes, a small piece of one 200 μm probe was covered with paraffin wax and cut with a Microtome. The resulting image is presented in Fig. VI.10(b). It was found that the holes have more of a bowl geometry than the desired cone shape geometry.

After the construction of the structured lead converters, they were tested in the test-bench. In first measurements without the drift layer, it was seen that the count rate spectra for the different converter prototypes were not comparable. These results are addressed to gain variations induced by the different surfaces of the converters. Subsequently, it was decided to test the converters in the drift layer setup, since this setup always has the same amplification geometry. The derived results from the measurements with this setup with the different converters are shown in Fig. VI.11. Besides one measurement trial, the results are in good agreement with the simulation results shown in Fig. VI.10. The measured count rates of the 200 μm thick structured lead foil are overall approximately 30% larger than the plain 200 μm thick converter, which perfectly matches the simulation outcome. Furthermore, from the simulation it was expected that the 100 μm structured foils should be slightly worse than the 200 μm ones, which was also observed in the measurements (Fig. VI.11). The one measurement trial which did not match to the other measurements (shown in the

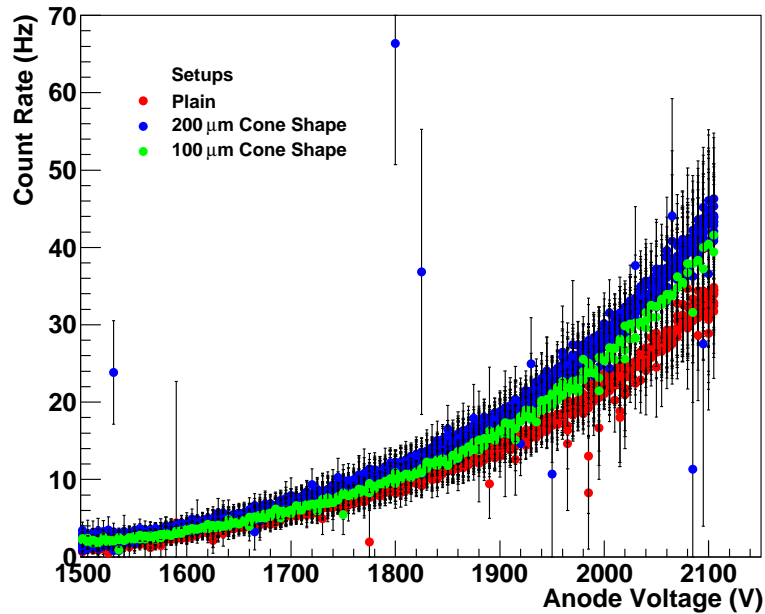


Fig. VI.11: Overlay of 19 count rate measurement series taken out under same conditions with plain and structured single layer lead converters. The test setup was extended by a drift layer whereby a 3 mm thick drift volume with an electric field of 100 V/mm was applied. One measurement trial with the 100 μm structured converter was discarded but is shown in Appendix Fig. A.1.

appendix) was performed after flushing the setup with gas for only one day that maybe caused the mismatch. This indicates that the system has to be operated carefully and that it is susceptible to environmental changes.

VI.8 External Trigger

The converter test-bench was extended by an inorganic BGO⁷ scintillation detector. The $2.5 \times 2.5 \times 7 \text{ cm}^3$ crystal was coupled to a photomultiplier tube (PMT)⁸, wrapped in silicon tape, and sealed with heat shrinkable tubing to prevent the detector from light induced noise. The detector was screwed on a small mounting table with two fixed clamps to guarantee that both detectors are always aligned in the same geometry to the radioactive source. A photograph of the test setup with the mounted scintillation detector is shown in Fig. VI.12. The HV flange was equipped with a

⁷BGO $\hat{=}$ bismuth germanium oxide $\text{Bi}_4\text{Ge}_3\text{O}_{12}$

⁸The PMT is a XP2972 from Photonis

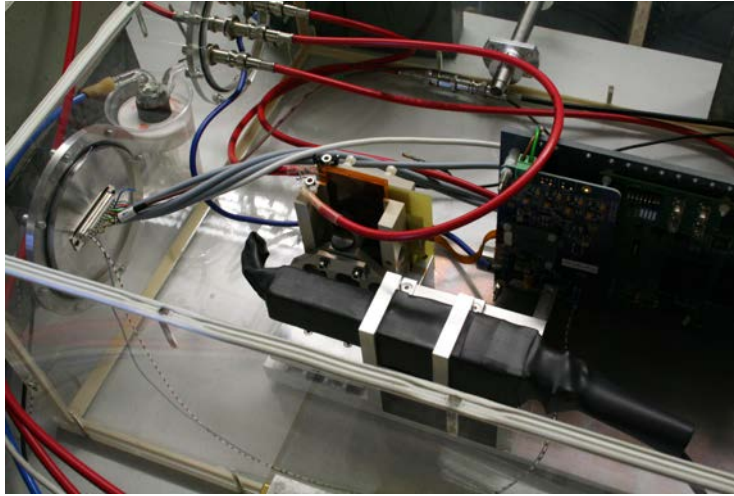


Fig. VI.12: Photograph of the optimized measurement setup equipped with scintillation crystal and shortened sodium source and holder.

third SHV feed-through for the HV support of the PMT. The PMT signal output is transmitted over the D-sub feed-through to a main amplifier⁹, then discriminated¹⁰, converted to a TTL¹¹ signal¹², and subsequently transformed in a LVDS¹³ signal. The final trigger signal is then returned over the D-sub feed-through to the Susibo board inside the acrylic glass box. The scintillator shows a reasonable energy spectrum in the case that the crystal is irradiated with the sodium source at its intended position. The photo-peaks of the 511 keV and the 1275 keV were clearly distinguishable from the *Compton* background of the 511 keV photons. For the subsequent measurements, the discriminator threshold was set to consider only events exceeding the *Compton* background energy. The trigger rate of the established setup was around 600 Hz.

The established setup was used to check whether the external triggering is able to generate spectra with more reliably characteristics to compare different converter prototypes more reliable. Unfortunately, the count rate spectra were very similar to the self-triggered setup. Hence, the setup was only used to again validate the results from the previous section. In the measurements, the three different structured single layer converters were again put 3 mm apart from the cathode drift wire layer and

⁹PNG MA8000

¹⁰CAEN Mod.N842 Discriminator

¹¹TTL $\hat{=}$ transistor-transistor logic

¹²CAEN Mod.N89 NIM-TTL-NIM Adapter (NIM $\hat{=}$ nuclear instrumentation module standard)

¹³LVDS $\hat{=}$ low-voltage differential signaling

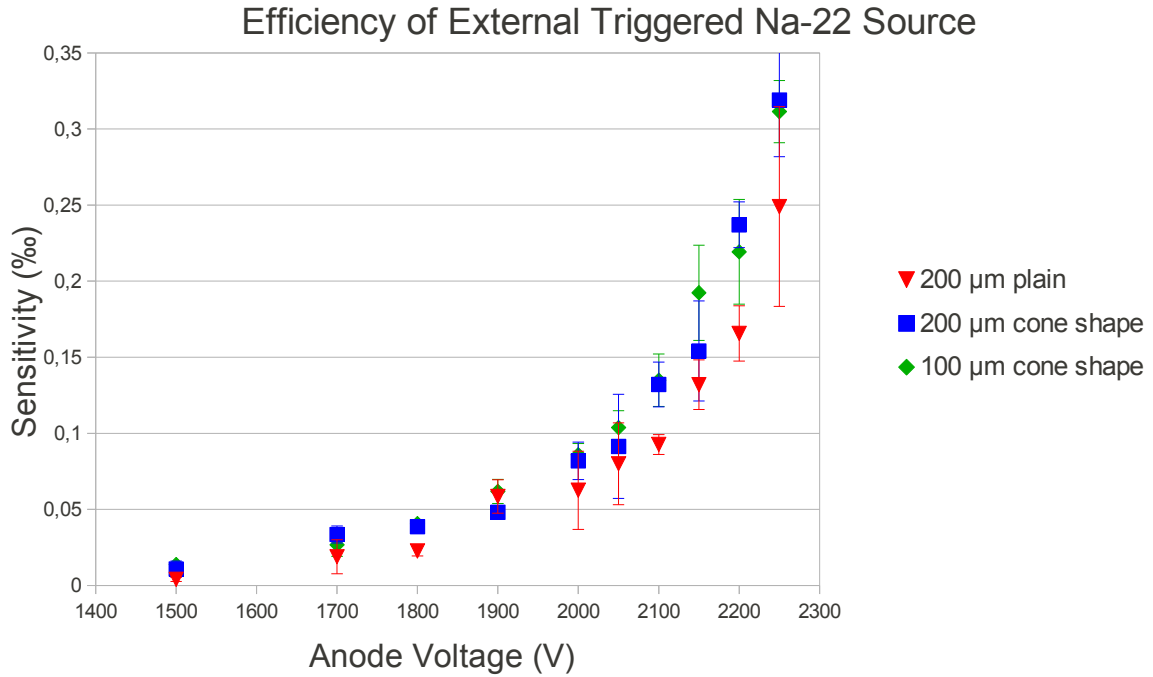


Fig. VI.13: Count rate analysis of three differently structured single-lead-layer-converters measured with an external trigger signal from a scintillation detector.

held on a potential of -300 V each. In the data acquisition, the single runs were stopped when at least 400,000 events were recorded. In the data analysis, all events which have a maximum pulse height above 90 ADC values are accepted. The results for the calculated sensitivities for different anode voltages are presented in Fig. VI.13. Here, each converter was measured three times for every anode voltage, whereby the indicated values in Fig. VI.13 represent the mean value of the measurements, and the error represents the standard deviation. It is visible that the both structured lead converters provide higher count rates than the plain converter. The count rate of the plain converter exceeds the sensitivity of the $200\ \mu\text{m}$ structured converter only for an anode voltage of 1200 V. However, an access for the structured one is still in agreement within the error. A difference in count rate performance between the $100\ \mu\text{m}$ and $200\ \mu\text{m}$ structured converter is not observed in the measurements. Furthermore, the increased count rates of the structured converters is not as prominent as in the results of Section VI.8. Overall, the external setup shows more variations between single measurements, which may be induced by too few statistics. Additionally, it is possible that more precise analyses of the data with better chosen trigger thresholds or applied noise filters would lead to better results. Nevertheless,

the results are to some degree within the expectations from the simulations and the earlier measurements.

VI.9 Discussion

The presented test-bench is able to show whether newly produced converter prototypes are able to operate under stable conditions and to validate if basic performance parameters are fulfilled. One of the goals was to establish a device which is able to reliably determine the efficiency performance difference on variations in the converter geometries. However, it was not possible to build multiple comparable perforated prototypes, and only single layer converters were compared. Following the presented results, it is not expected that the setup is able to distinguish efficiency differences below 10%, and also that converters can only be compared if the test setup is equipped with an additional drift wire frame (Section VI.6). Nevertheless, it was presented that the SPADIC readout ASIC is a well performing option for the electronics of a next generation HIDAC scanner. Although the pulse spectra derived from the sodium source measurements does not show whether all necessary events can be triggered by the ASIC, it was possible to use the measurements with the increasing gas drift layer to validate that, at least with an overall gas thickness of 9 mm, no signals are lost due to too few ionizations in the gas layer (Fig. VI.9(a)).

Regarding the first measurements with the multi layer converter prototypes, it was observed that it is possible to obtain higher count rates in the case that a voltage cascade is applied to the converter. For the five layer lead converter, the count rate can be approximately doubled if the highest possible converter voltage is applied (Fig. VI.8). The same magnitude increase is expected following the **Geant4** simulations (Fig. VI.6). The absolute magnitude of the count rate of the measurement is a factor of around 2.7 lower than in the simulation, but due to the differences between the simulations and measurements described above, the reached count rates still look reliable.

However, it is desirable that the measurements in the same setup are also taken out with the copper converter prototype and that the simulation setup is further improved to more precisely match the real setup. In a broader sense, it is, of course, of special interest to produce prototype converters in the patterns suggested in Section V.2.4 and to compare them in the test-bench, as well as to upgrade the

setup with the newer SPADIC version 1.0 with 32 self-triggered channels.

Furthermore, it was validated in simulation and measurement that it is possible to increase the efficiency of single-lead-layer-converters by applying processes which offer structural patterns inside the lead. In the measurements, two converters with different cone-shape patterns and a plain lead foil were examined and compared. The relative differences expected from the simulations between the plain and structured converters were observed in the setup, including the drift layer, for the self-triggered and external triggered experimental trials. The expectations for the count rate differences between the two different cone-shape geometries were only seen in the self-triggered setup, while in the external triggered setup no remarkable differences were observed.

These first results show that the test setup as well as the **Geant4** implementation deliver qualitative data in the case that it is operated accurately which can be used to predict efficiencies or to check the performance of HIDAC converter prototypes.

CHAPTER VII

Micro Pattern Gas Detector Prototypes

In a first approach, it was planned to construct a low-cost high-resolution small animal PET scanner named MSPET. The design consisted of 400 thin simple MWPCs with single-solid-layer-converters and was evaluated in simulations [Got10] and prototype measurements [Ver10]. This simple concept removes the need for expensive photon-electron converters with holes, but it was shown that the reachable sensitivity of the system would not be competitive with the HIDAC concept. It was also shown that the prototypes detectors did not reach the performance expected from simulations.

Advanced converter geometries have been proposed in Chapter V to overcome the drawback of low sensitivity. However, it should also be possible to reach high sensitivities by remaining on single-solid-layer-converters by using ultra thin micro pattern gas detectors (MPGD). Furthermore, MPGDs could be used as an alternative read-out method for HIDAC like detectors.

These concepts presumably lose the benefit of being low-cost designs but they are, more or less, able to reach any desired spatial resolution. This chapter presents two prototype concepts of such detectors, motivates the concepts from simulations, presents prototypes manufacturing, and first measurement results.

VII.1 Detector Concepts

New developments in the field of MPGDs open the possibility of producing panel detectors with large active areas with fabrication processes which can be applied

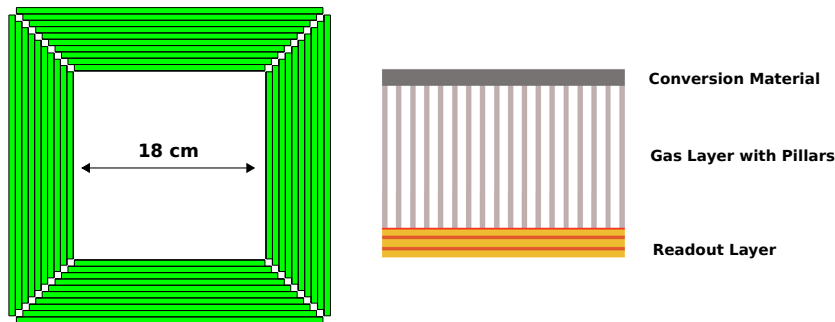


Fig. VII.1: Example of the simulated geometry illustrated with 40 detector modules (left), whereby the modules are 6 mm thick to have a better visualization. A zoomed view on the profile of a principal single module with arbitrary dimensions is presented (right).

by the industry [GOA⁺06]. The most important change compared to the HIDAC concept is that it is now possible to move the x - y cathode readout to one side.

In contrast to the pixel readout for MPGDs that is generally used, new gluing techniques allow one to equip the proposed detectors with thin x - y strips protected by a resistive layer. This reduces the number of readout channels per detection layer and offers the great benefit of using a plain or structured material directly in front of the gas volume to convert annihilation photons into electrons. In other words, this diminishes the absorption of photo- or *Compton*-electrons in material needed for the electric readout and offers a larger surface between converter and gas volume than the HIDAC concept.

As photoelectrons from annihilation photons have an energy of 511 keV, which is near the energy of minimum ionizing particles in gas, an argon filled detector should have at least a 400 μm thick ionization layer to produce at least one secondary electron [A⁺08].

In the following, two possible detector designs are presented. The easiest one would be a gas detector with strip readout. Such a detector would consist of only a grounded readout cathode layer with cathode strips and the converter layer on a negative potential. Both layers should be spaced equally, which can be provided by utilizing small pillars as spacers. In this setup, the gas amplification is the same over the whole gas volume. This causes a high dynamic range since the signal height is dependent on the ionization depth. A sketch of this detector layout is given in Fig. VII.1.

The second design proposal overcomes the problem with the dynamic range of the

signals by dividing the gas volume in a drift and an amplification volume. This can be reached by building a casual micro mesh gas (Micromega) detector with modified strip readout and a converter layer.

For both designs with an ionization layer thickness of $400\ \mu\text{m}$, a spatial resolution of $200\ \mu\text{m}$ should be accessible. The inherent spatial resolution of such detectors is, in principle, possible down to 2-3% of the strip separation if appropriate displacement determination methods are used [BRR08]. For the proposed application, the spatial resolution is constrained by the displacement between the photon interaction position and the position where the primary electron ionizes gas molecules within the detector. It was shown in simulation [Got10] and measurement [Hün07] that the average exit angle of electrons for $60\ \mu\text{m}$ thick lead foils would be around 45° . The spatial resolution of those detectors is therefore constrained to half the thickness of the gas volume. Thus, the spatial resolution can even be improved by using thinner ionization layers filled with xenon gas, but since a smaller amount of readout channels is desirable maybe the spatial resolution should not be pushed to its limit.

VII.2 Simulation

VII.2.1 Environment and Setup

Both detector designs can be treated by a single simulation setup, since the only difference of both concepts is given by a $18\ \mu\text{m}$ thin micro mesh, which can be neglected in first order if the tracking of photons and electrons is considered.

The HIDAC implementation in `Geant4` was adapted to simulate the MPGD based scanner setup. The simulated source is an infinitesimal point source in a water sphere with a diameter of eight millimeters, whereby the positrons are liberated without kinetic energy. The module sizes in x and y are adapted for each module to cover a full angle of 2π in ϕ . The dimension of each module in axial direction is adapted to assure that the whole scanner is covering a constant space angle with an acceptance of 80%. This is necessary to make all the simulations with the different geometries and materials comparable. The separation distance of the closest detector modules is set to 18 cm to match with the HIDAC FOV. An example setup with 40 detector modules (6 mm thick modules for illustration) is shown in Fig. VII.1.

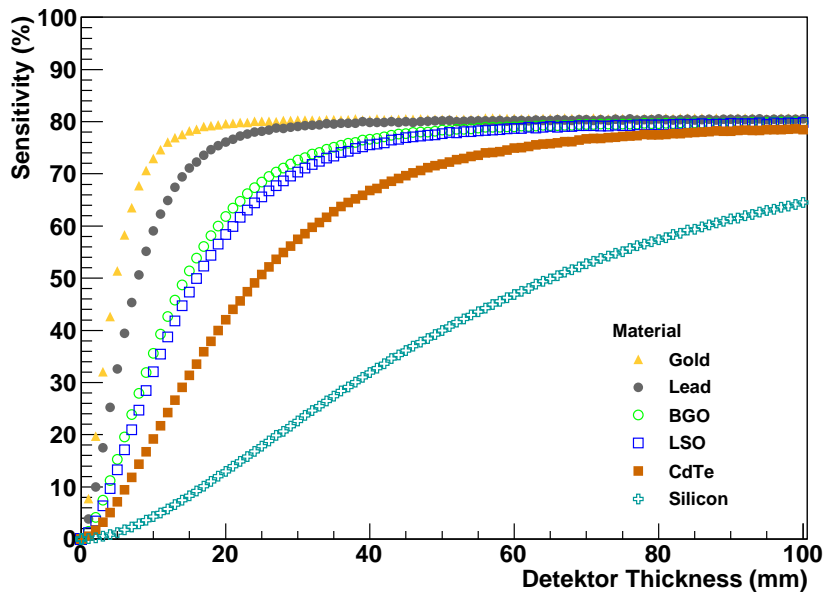


Fig. VII.2: Sensitivities for scanner geometries simulated with different materials under the assumption that the whole detector volume would be sensitive to conversion electrons.

VII.2.2 Sensitivity Predictions for Different Conversion Materials

To emphasize how important the right choice of conversion material inside the converter is and to estimate which overall thickness of conversion material is needed to detect the majority of photons, a simplified artificial detector setup was implemented. In this setup, each module is 1 mm thick and consists completely of a conversion material and flagged as detection volume. Thus, every photon that produces at least one electron within the detection volume is registered in the data. Each simulation is based on one million positron annihilations. The probability for photons to interact with matter is highly dependent on the atomic number of the elements which are utilized in the detection medium. The reachable sensitivities for different materials with different thicknesses, assuming that the conversion material itself would be a detection medium, is illustrated in Fig. VII.2. It has been found that around 90% of the annihilation photons already interact in one centimeter of gold, whereas 1.5 cm of lead is needed to reach the same performance. This is caused mainly by the difference in density of both materials as the difference in atomic number is marginal.

Typical scintillation crystal materials like LSO¹ or BGO need at least 3 cm to be compatible with gold or lead.

A promising alloy to make semiconductor technology accessible for PET is cadmium zinc telluride (CdZnTe) [GMS⁺11]. The simulations show that at least 2-5 cm of this material is necessary to reach sufficient sensitivities, and also indicate why silicon is not the semiconductor material of choice for PET.

With the chosen geometry, the majority of materials saturate at a sensitivity around 80%, which is given by the limitation of covered solid angle.

The results for different materials in manner of sensitivity and thickness are conform to elementary expectations. Therefore, it is verified in first order that there are no serious errors in the simulation implementation.

VII.2.3 MPGD based Scanner Simulations

In the simulations for the new detector setup, each module consists of a plain or structured lead layer, a 400 μm gas volume without pillars, and a 411 μm readout layer (consisting of a 15 μm thick resistive layer, two cathode layers with a thickness of 18 μm each and three 120 μm thick glue layers). The choice of a 400 μm thick gas layer is arbitrary. The gas layer may have to be thicker to reach a sufficient efficiency of the detector, but the gas thickness does not influence the simulation outcome since the covering angle is constant. Nevertheless, the gas thickness should be as thin as possible since the non-collinearity reduces the reachable spatial resolution for increased detector thicknesses.

To accumulate enough statistics, in particular for the structured lead foils, each simulation pursues 5M positron annihilations. For each event, the first electron liberated by the respective annihilation photon that enters a gas volume is stored in the data.

Plain Lead Layer Converters

From previous work [Got10] and [Hün07], it is known that a maximum efficiency for up to 200 detectors with plain lead foils converters is reached with 60 μm thick foils. This means that in thicker foils, *Compton*- or photo-electrons only have an essential chance within the last 60 μm to reach the gas volume. In these deliberations, it was not considered that for a larger number of detection layers, not only the efficiency of a single layer but also the transmission becomes an important factor.

¹LSO $\hat{=}$ lutetium oxyorthosilicate $\text{Lu}_2\text{Si}_3\text{O}_5$

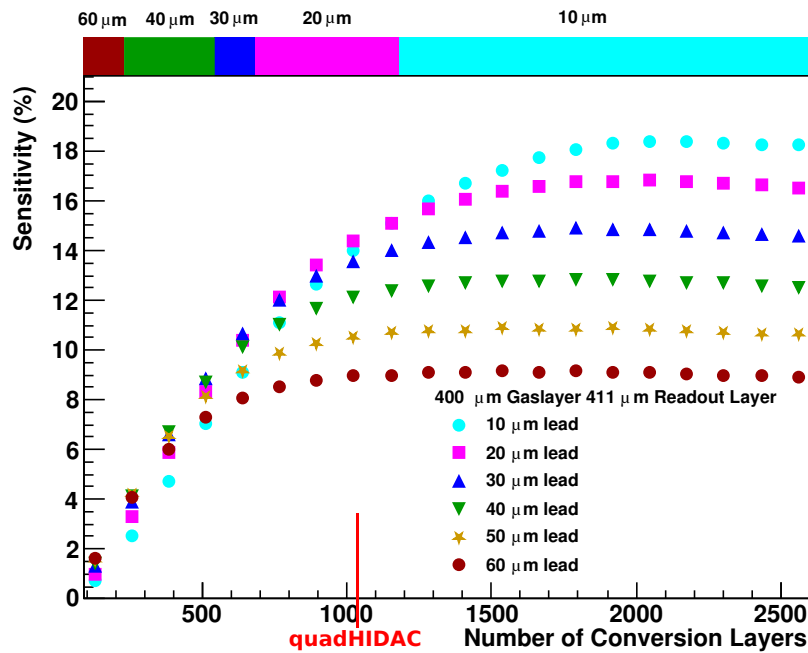


Fig. VII.3: Results of the simulated sensitivity performance of single-lead-layer-detectors arranged in a flat panel setup for various lead layer thicknesses. Upper row indicates which thickness is optimal in a specific range of number of detector modules.

Therefore, the simulations consider up to 2560 detector modules. Here, we started with a lead thickness of $60 \mu\text{m}$, which was then stepwise reduced in $10 \mu\text{m}$ increments. The results of the simulation for plain lead foils are presented in Fig. VII.3. For clarification, the number of conversion layers is the overall number of detector modules which has to be divided by four to get the number of modules per detector head. The best sensitivity of 18.2% is reached at a lead foil thickness of $10 \mu\text{m}$ for 2560 detector modules. It has been found that the optimal converter thickness is dependent on the planned scanner system size. For example, a system consisting of 1024 single-lead-layers like the HIDAC should be equipped with $20 \mu\text{m}$ thick lead foils. Such a system would then reach a sensitivity of 14.4%.

Structured Lead Layer Converters

Perforation of conversion foils has the advantage that the photon transmission is increased and that the surface between gas and conversion material is enlarged. This gives access to higher coincidence sensitivities. The results of simulations for various hole diameters and hole pitches are given in Fig. VII.4. The lead thickness was fixed to $40 \mu\text{m}$ since the best result for plain lead layers for a medium amount of detector layers was reached with $20 \mu\text{m}$, and the volume fraction of the holes for

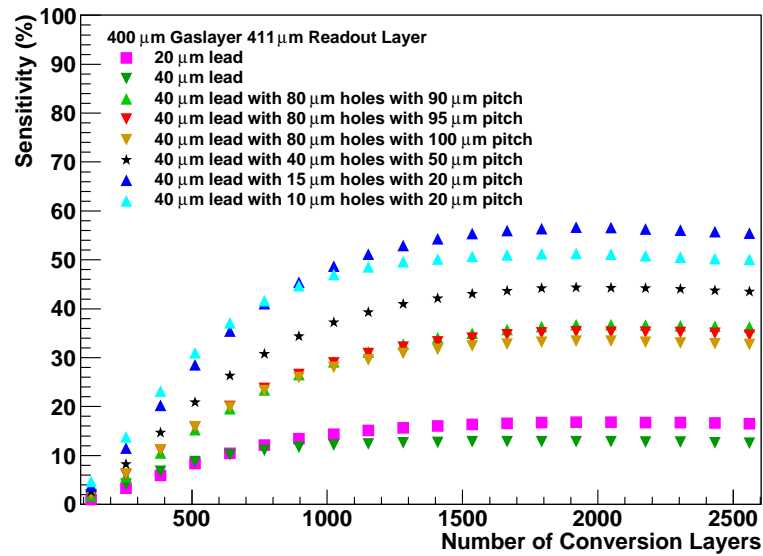


Fig. VII.4: Simulated coincidence sensitivity distribution of single-lead-layer-detectors with perforated lead foils plotted to the number of incorporated detector modules. The single lead foils were simulated with multiple perforation geometries.

the most geometries was chosen to be around 50%.

It is possible to get sensitivities above triple the sensitivity compared to plain conversion layers. The highest sensitivity of $\sim 55\%$ is achieved for a hole pitch of 20 μm and a hole diameter of 15 μm . Since it is unrealistic that this geometry can be manufactured in the near future, the focus shall lie on the 80 μm holes. This is a hole diameter which can approximately accessed in a cone-shape geometry with liquid etching techniques (Section V.3.3).

It must be mentioned that the presented sensitivities are calculated with true and scattered events in the data. The proposed detector concepts have no energy information on the detected photons, and it is therefore impossible to distinguish between scattered and true events. For increased sensitivities, the fraction of detector scatter also grows. Table VII.1 summarizes the best results for potentially realizable geometries where the fraction of scattered events in the data is also listed. As always, these sensitivities only state an upper limit of the sensitivity of a real scanner system. Nevertheless, it should be emphasized that for the proposed detector concepts, these sensitivities should be roughly accessible since electron attachment is suppressed. This is due to the small drift distances

and the fact that wall interactions, which predominantly occur in the HIDAC converters, are unlikely.

TABLE VII.1: Sensitivity and fraction of detector scatter for 2560 detector modules with different geometries for plain and perforated single-lead-layer-converters.

Geometry	Sensitivity (%)	Detector Scatter (%)
60 μm lead	8.9	62.3
10 μm lead	18.2	84.2
80 μm \varnothing 90 μm pitch	36.3	86
15 μm \varnothing 20 μm pitch	50	91.7

VII.3 Experimental Evaluation

VII.3.1 Prototype Manufacturing

The gas detector with strip readout was designed for this specific application, whereas the Micromega is a standard prototype version. Both were manufactured at the CERN workshop. The production processes for the readout layer structure are the same for both detectors where arbitrary readout pad geometries can be designed. Therefore, the different process steps for the first prototype will be described here, and only the parameters of the Micromega prototype dimensions will be given.

The basis of the detector readout is a 75 μm thick copper clad Kapton foil. The copper layers are 18 μm thick. The pad patterns for the x and y readout are etched into the copper layers with photo lithographic processes, as described in Section V.3.3. The structured foil is then stacked together with 75 μm prepreg on top and 200 μm prepreg and 55 μm lead on the bottom and put into a press. The prepreg is a compound of glass fibers and glue which melts in the press and ensures that the single layers become one rigid solid with precise defined thicknesses of the prepreg. The press applies a pressure of around 200 kPa and a temperature of 200° C to the stack for 90 min. The lead converter on the bottom is intended for the

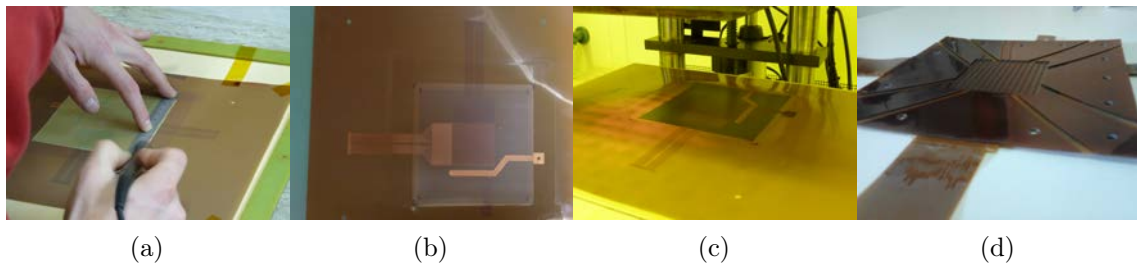


Fig. VII.5: The photographs describe a few production process steps for the prototype detector. The alignment and cutting of the prepreg to the readout structure are shown in (a). Lead, prepreg, and copper cladded Kapton stack after pressing are illustrated in (b). Readout structure positioned under the screen print machine (c) and the finished detector equipped with cooked pillars and gas supply lines (d).

next readout layer for the following detector module. After pressing, the prepreg is gently rejected in a small, specific area to establish a electric connection between the top copper layer and the resistive paste layer, which is subsequently printed onto the top prepreg. The resistive paste is a $1\text{ M}\Omega$ polymer which is printed with a screen print machine (see Section V.3.5) in a precise thickness of $15\text{ }\mu\text{m}$ with the same pattern as the bottom copper readout layer. Electrons which are produced in the avalanches can spread out on the resist much faster than on strip patterns without resist. This makes the detectors faster and gives them much higher rate capabilities. Furthermore, the resist leads to a better high voltage stability of the detector. After drying the paste in the oven, the pillar layer can be produced. This layer consists of photo resist, which is usually used for the etching process. For the prototype detector, a maximum gas thickness is proposed to reach an acceptable electron ionization probability. Therefore, ten layers of cover-lay were stacked on the readout plane which results in a $640\text{ }\mu\text{m}$ thick pillar layer. Thicker layers would lead to bendable pillars. The cover-lay is illuminated with a printed mask with the desired pillar pattern. For the detector, the pillars have a diameter of $700\text{ }\mu\text{m}$ and are separated by 3 mm each. Furthermore, gas supply lines are integrated in the pattern. Afterwards, the cover-lay is developed several times and cooked in the oven to obtain rigid and firm pillars. Photographs of some production steps are illustrated in Fig. VII.5.

Overall, four gas detector prototypes with strip read out and an active area of $4\times 4\text{ cm}^2$ have been produced. The read out strips were 4 cm long, whereby the top strips have $100\text{ }\mu\text{m}$ and the bottom strips have $300\text{ }\mu\text{m}$ wide strips. Both layers have a strip to strip separation of $400\text{ }\mu\text{m}$. The different strip width is chosen to

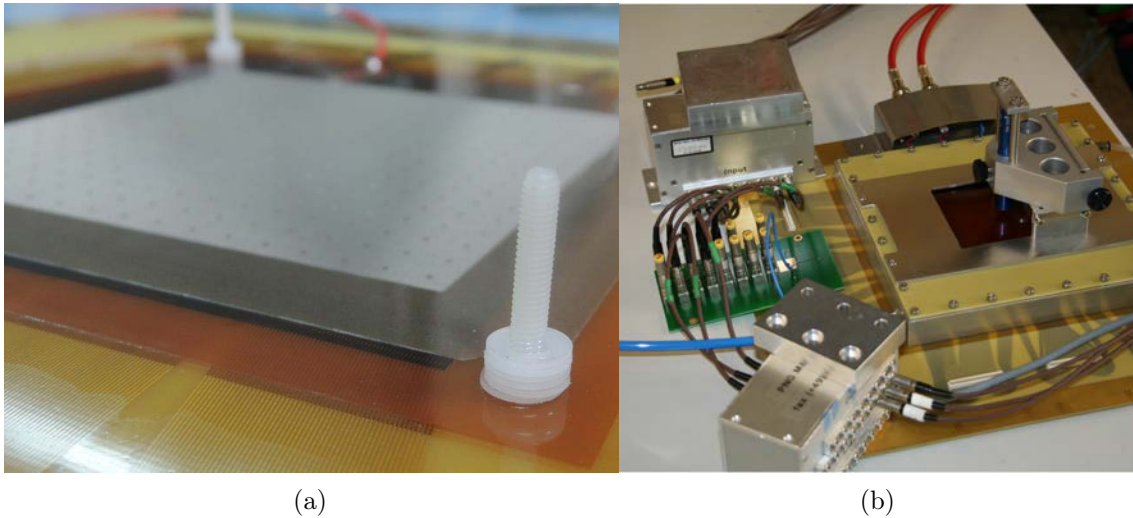


Fig. VII.6: These photographs display the opened Micromegas detector without the second drift mesh (a) and closed image of the connected detector with source holder and readout electronics (b).

have the same amount of charge, which is induced by an avalanche on both pad layers.

The Micromegas prototype is the current standard small version with an active area of $9 \times 9 \text{ cm}^2$ from the CERN workshop. In principle, the readout structure is manufactured with the same process steps like the other prototype detector but instead of pressing the Kapton-prepreg stack on a lead foil, here the stack is pressed onto a 3 mm thick PCB board. The pillar layer is only $128 \mu\text{m}$ thick where a micro mesh with $18 \mu\text{m}$ diameter wires and a mesh size of $45 \mu\text{m}$ is deposited above. The pillars are $300 \mu\text{m}$ thick and are separated 2.5 cm. The mesh divides the gas layer in an amplification and a drift volume where electrons from ionizations are transferred into the amplification region. The strips of the top layer have a width of $80 \mu\text{m}$ and the bottom strips of $200 \mu\text{m}$. Both have a strip to strip separation of $250 \mu\text{m}$. Thus, there are 360 strips which are connected to three Panasonic AXK6SA3677YG header connectors per layer, whereby each connector is equipped with 130 pins. The drift volume is defined by the amplification mesh and a further second drift mesh where the distance of both meshes can be chosen by the user by interleaving plastic washers on four screws between them. Photographs of the opened and closed detector are shown in Fig. VII.6.

VII.3.2 Prototype Measurements

Micro Strip Prototype

Three gas detectors with strip readout were tested in the acrylic glass box of the converter test setup (Section VI) with different argon-carbondioxide mixtures. The detectors were read out with either the GSI PASA readout electronics or CATSA pre-amplifiers from PNG Messel since the intended electronics were not available yet. For all prototypes with a CO₂ fraction of 15% in the range from 1500-1600 V, signals at a rate in the order of 0.1 Hz were observed. Unfortunately, all prototypes break down for higher applied voltages. Furthermore, there was no increase in the signal rate if radioactive sources were mounted in front of the detector. Of course, it is not expected that any signals are observable since the applied field of around 2 kV/cm is not high enough to reach amplification mode.

Micromega

A readout adapter was produced to test and evaluate the Micromega prototype detectors, whereby the adapter connects the detector to the CATSA pre-amplifiers. The adapter combines different numbers of pads to one QLA connector to be able to evaluate the influence of pad multiplexing on the signal noise. In detail, the adapter multiplexes 2×1, 2×2, 2×3, 4×4, 2×5, 6, 8, 10, and 15 pads to one QLA connector.

⁵⁵Fe Measurements

In a first test, the ⁵⁵Fe source was used with a 2 mm aluminum collimator to measure energy spectra. The second drift mesh was positioned 4 mm apart from the amplification mesh. The source was positioned approximately in the middle of the two five pad combinations. For the data acquisition, a Struck SIS3320 ADC that was read out with a modified version of the FPPDAQ software described in [HSMV12] was used. In the data analysis, signals with a maximum charge value on one of the both five pad clusters were triggered, and the charge values of both pads and the neighbored four or six pad cluster were summed to obtain the energy spectrum. The result is shown in Fig. VII.7(a). The resulting energy resolution of 13.9% is quite impressive in regard to the fact that the noise level of the pre-amplifiers is quite large and the source is ~20 mm far away from the drift mesh. By analyzing the 10 and 15 multiplexed pad channels separately, the energy spectrum is still accessible, but the escape peak is more or less hidden in the background. The multiplexed channels

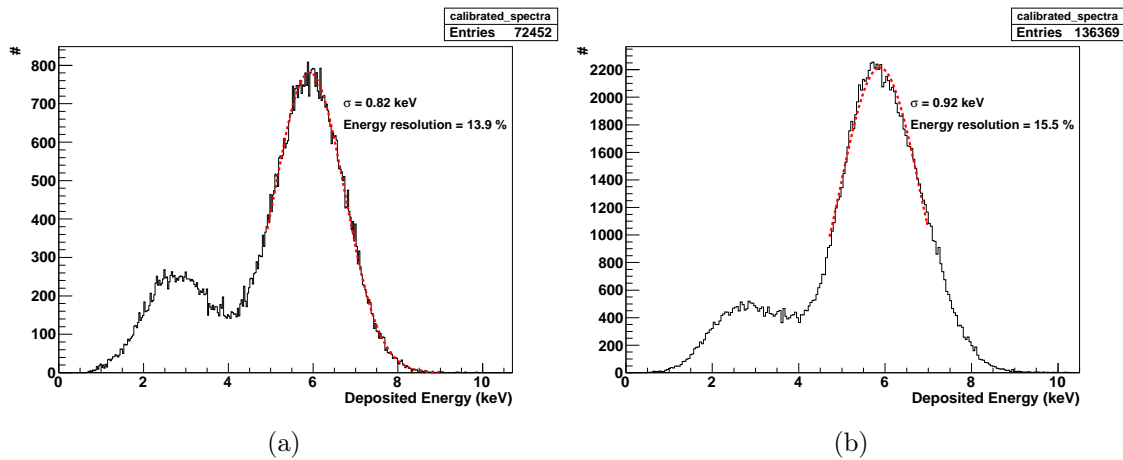


Fig. VII.7: Energy spectra of a ^{55}Fe source measured with the Micromega prototype. In (a), the top strip layer was read out while 15% CO_2 , -980 V drift voltage, and -580 V amplification voltage were applied. In (b), the bottom strip layer was read out while the meshes were set to -959 V drift voltage and -595 V amplification voltage.

with only a few pads were not able to resolve the escape peak as well for applied voltages below 570 V. Furthermore, the spectrum diverges for voltages above 590 V. This first validation of the detector shows that the operational mode of the detector is only in a small voltage range. Nevertheless, excellent performance of the detector was presented and no remarkable artifacts were observed in the spectra. The results show that multiplexing of at least 15 readout pads is not a limit. Furthermore, the ^{55}Fe spectrum was measured with the bottom strip layer. The energy resolution of 15.5% in the measured spectra in Fig. VII.7(b) is only slightly worse than in the top layer but the escape peak is less expressed. The presented result measured at 595 V was the best available measurement. Measurements with other amplification voltages show less expressed escape peaks.

^{22}Na Measurements

Measurements with the ^{22}Na source were made to get an idea of how the ionization probability for conversion electrons from 511 keV photons varies with the drift thickness. The second drift mesh was replaced by a 2 mm thick PCB plate with a 55 μm lead foil glued on one side. Additionally, the setup was equipped with a source holder that places the source for every measurement at the same position. It was ensured that the distance from the source to the converter foil was set on a constant distance. A photograph of the whole measurement setup is illustrated

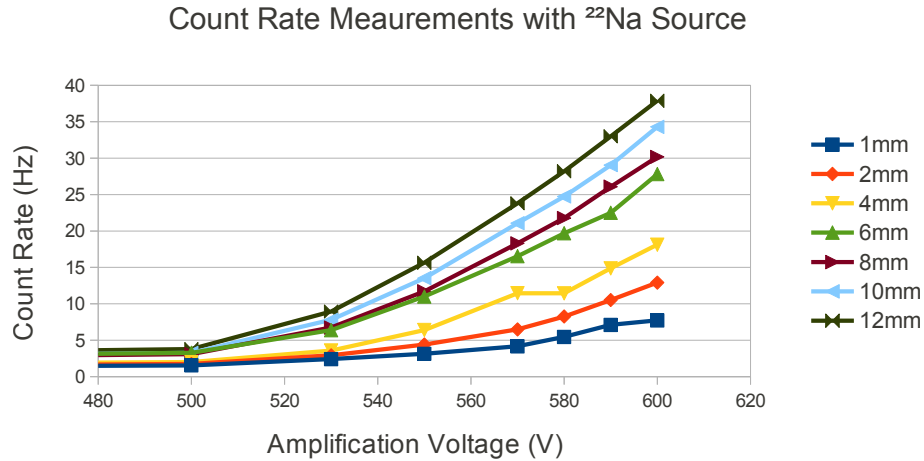


Fig. VII.8: These results for count rate measurements with the Micromesh prototype and a ^{22}Na source were determined for different amplification mesh voltages. The count rate increases with the amplification voltage and for larger drift thicknesses. A slight count rate increase is expected for larger drift thicknesses from simulations (see Fig. VII.10). The strong count rate decrease for thin drift thicknesses indicate that below 4 mm not all ionization clusters are recognized.

in Fig. VII.6(b). The PCB plate with the converter foil was placed on distances varying from 1 mm to 12 mm apart from the amplification mesh. To set a new drift distance, the detector was disassembled in the clean room every time. The results of the measurement trials are given in Fig. VII.8 whereby, as an example, the pulse height spectrum of a channel with five cathode strips is presented in Fig. VII.9. The count rate measurements show that the number of detected events strongly increases with the amplification voltage and with thicker lead-to-mesh separations. To be able to make any statements on the measurements, the setup was simulated in **Geant4**, whereby the resulting count rates are presented in Fig. VII.10. By comparing measurement and simulation, one can notice that the expected count rate of around 30 counts per second is reached for gas thicknesses above 6 mm and amplification voltages above 590 V. This shows that the detector is able to detect a large amount of the conversion electrons. As it is expected to achieve better results with different gas mixtures, one can predict from these first results that for an optimized setup, lead-mesh separations between 4-6 mm would be sufficient to detect the majority of electrons. Nevertheless, for spatial resolutions below 1 mm, lead-mesh separations lower than 2 mm are necessary (see Section VII.1). Therefore, the performance of the system must be improved substantially since currently only up to 33% of the conversion electrons are registered for the 2 mm mesh-lead separation. However, the

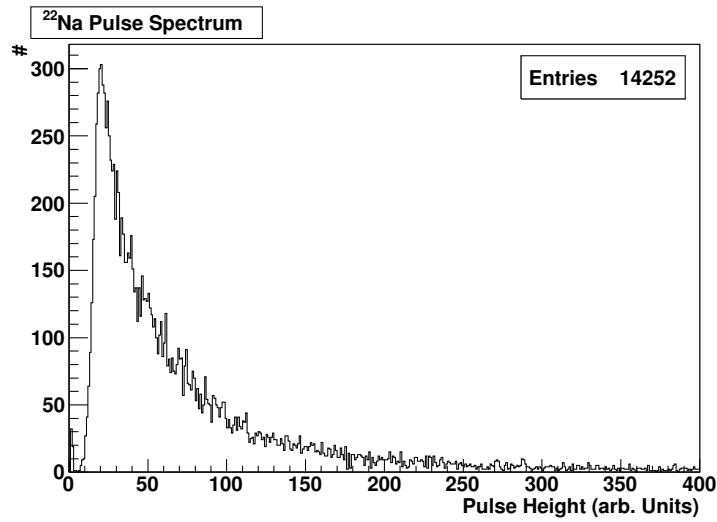


Fig. VII.9: Pulse height spectrum measured with the ^{22}Na source. The spectrum is similar to those obtained from the converter test-bench (see Fig. VI.4(c)).

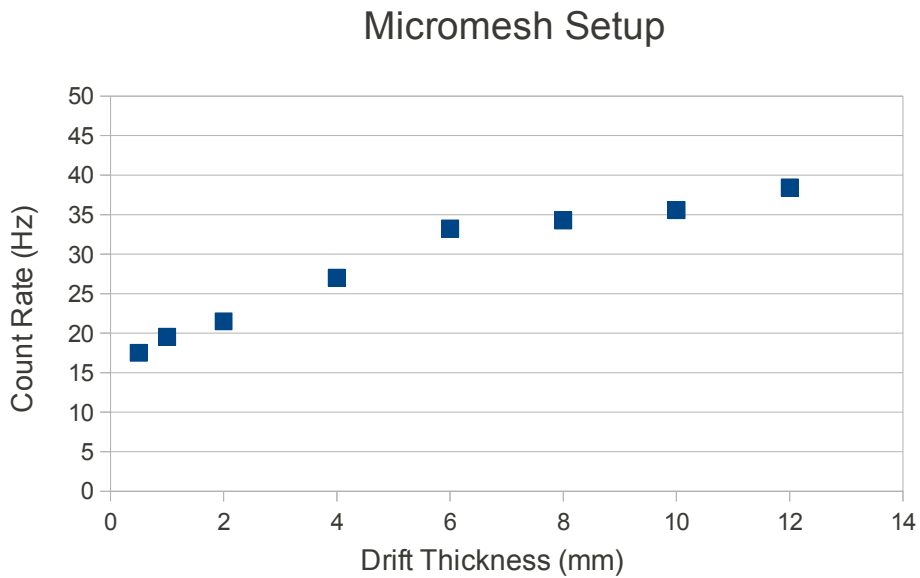


Fig. VII.10: These simulation results for the expected count rate of the Micromesh detector were studied for different mesh-lead separations as response to the sodium source. The simulations were made to interpret the measurement results presented in Fig. VII.8

relative slope of the count rate measurements is validated by the simulation. The absolute count rate predicted by the simulation is only a rough benchmark, as the input parameters still allow a large variance. Therefore, further measurements and simulations are required to make final statements.

VII.3.3 Discussion

An alternative detector concept for a high resolution PET scanner was described, simulated, and examined in first tests with two different prototype detectors. The simulations predict that with an increased number of detector modules and thinner lead converter foils, the sensitivities increase (Fig. VII.3). Moreover, a further substantial sensitivity enhancement can be achieved if structured foils are incorporated instead of plain lead foils (Fig. VII.4). The relative enhancement for this prediction was already observed in first validations, where two different experimental examinations were taken out (Section VI.7 and Section VI.8). Although the absolute sensitivity values from the simulations are quite impressive for a large number of detector modules, the values do not represent the true coincidence sensitivity for a real setup. This is mainly caused by the high fraction of scatter events in the data (Table VII.1), by the impractical layout of the simulated geometry², and limited efficiency for thin gas layers (Section VII.3.2). Following the simulation results shown in Table VII.1, the true coincidence sensitivity for these setups is between 2.87 % and 5.08 %. Hence, it is expected that a scanner with a large number of detectors in a realistic geometry would be able to reach a true coincidence sensitivity of around 4% which is indeed compatible with all commercial preclinical PET scanners, especially, as proposed sensitivity analysis methods by NEMA also include an amount of scattered coincidences in the total or absolute sensitivity values. However, the measurement results show that the full efficiency of a single detector module can currently only be achieved with large mesh-lead separations which would delete the high resolution capabilities of the detector concept.

In conclusion, it was validated that a Micromesh detector with a plain lead converter is able to measure conversion electrons from 511 keV annihilation photons, whereas the simpler detector design showed no feasibility for PET applications. The magnitude of count rate measurements is only moderate for thin gas layers if compared to the simulations for the proposed Micromesh concept, which does not recommend

²The simulated geometry was altered to have a constant covering angle to let the simulations be comparable.

to establish directly a full scanner system. It should be remarked that the presented results are only first measurements and do not provide sufficient grounds for discarding the concept. To give a final quantitative validation, it is necessary to fully read out and test several prototype detectors in a coincidence setup.

However, it is questionable whether single-lead-layer-concepts are more suitable than stacked and perforated converters. If one wishes to design a second generation gas based small animal PET scanner with a focus on high resolution instead of high sensitivity, the best solution is presumably the combination of a finely granulated multi stack converter and a Micromesh detector. The results from Section V.2.4 anticipate the use of 1 mm thin converters with 300 μm diameter holes which, combined with a Micromesh detector, will have a spatial resolution of 300 μm with a sensitivity exceeding the performance of the current HIDAC.

Image Reconstruction

VIII.1 Reconstruction Methods

In PET, image reconstruction intends to deliver an image of the tracer distribution within an imaged object to the physician or the biologist. Image reconstruction techniques are necessary, since only information about measured coincidences is given by the PET scanner system. From the mathematical point of view, the PET image is a description of a density- or intensity-function with a positivity constraint of the form

$$f : \mathbb{R}^N \rightarrow \mathbb{R}^+ \quad N = 2, 3$$

whereby $N = 2$ represents the *tomographic* slice imaging and $N = 3$ the 3D case. The information we obtain about the intensity function is given in detail by the measurement of the number of coincidences g_i along single lines of response (LOR) L_i . Thus, the distinct information which is obtained in a PET scan is roughly an ensemble of single line integrals over the sought-after intensity distribution:

$$\int_{L_i} f(\mathbf{x}) dx_l \approx g_i . \quad (\text{VIII.1})$$

Here, the single measurements of the number of coincidences g_i on L_i can be summarized in a projection vector \mathbf{g} . The approximation in (VIII.1) arises since non-collinearity (Section II.5), scatter or random events (Section II.6), and noise disturb the measurement.

In fact, there are two different approaches to reconstruct the intensity function f out of the measured data \mathbf{g} .

The classical approach is the analytic method, which takes the approximation in (VIII.1) as equal. This method is called the “*Radon inversion problem*” and was solved by *Radon* in 1910 [DJS12]. The procedure used to derive the solution of this approach is the filtered backprojection (FBP) algorithm. Compared to simple backprojection, the measured data is folded with a filter function which accounts for the blurring effect naturally arising during the measurement process, since the activity of a point is smeared to the whole LOR. The solution of the algorithm is exact if the data includes all possible LORs. Unfortunately, this can only be approximately achieved in 2D and is impractical in 3D, as support structures prohibit the measuring of the full solid angle. Nevertheless, the analytical methods are unbeatable concerning processing speed and are mathematically fully described. Therefore, optimal choices of reconstruction parameters can be derived.

A simple introduction to analytical image reconstruction is given in [CD06] and [DJS12].

The other approach of image reconstruction uses algebraic methods. Here, the model in (VIII.1) can be treated more generally by introducing an operator A which transforms the intensity function into data space. Hence, the measurement procedure can be formulated as:

$$\mathbf{g} = Af$$

which equivalently denotes the forward projection of an image f into the projection space. Since A represent a general operator it is not clear at this point whether the inversion A^* of A exists or not. Hence, it is not desired to directly do the operator inversion but to derive a solution in which the forward projection resembles the measured data most probably. This can be achieved by formulating the algebraic description of the inversion problem using the *Bayesian* [Saw11] approach in the form of:

$$\min_{f \geq 0} H_{\mathbf{g}}(Af - \mathbf{g}) + \alpha J(f) , \quad (\text{VIII.2})$$

where $H_{\mathbf{g}}$ denotes a functional which takes the deviation from the condition $\mathbf{g} = Af$ under penalty, $J(f)$ indicates a regularization function where constraints and *a priori* knowledge can be incorporated in the solver, and α is the regularization parameter acting as a relative weight for both terms.

In general, the functional $H_{\mathbf{g}}$ can be derived from any desired model which

incorporates the properties of the underlying physical effects and measurement processes.

Besides the vast number of algebraic reconstruction algorithms, in the following, only the simple expectation maximization (EM) algorithm for ET should be covered, since this is the algorithm which is mainly used in the analysis of the next chapters. For the EM algorithm proposed by Shepp and Vardi [SV82], commonly no prior information or smoothness criteria is used. Therefore, the regularization functional $J(f)$ in (VIII.2) is zero [Mül13]. The functional H_g is derived here by applying the expectation maximization technique with the assumption that the collected data follow *Poisson* distributions. The next section is dedicated to give a rough summarize of the derivation of the algorithm.

Compared to FBP, the algebraic reconstruction methods are much slower, since in algebraic reconstruction methods the A^* operation is usually taken out completely in each iteration that equals the dominant time-consuming factor of the backprojection step in FBP [NW01]. Nowadays, this is often not of significant importance, since computational performance of parallel processors also allow the execution of long calculations in times which are still practical in the clinic. Even though adapted algebraic reconstructions often essentially improve image quality, the user has to apply the algorithms carefully. Measurement statistics and accuracy propose optimized projection binning parameters for the FBP reconstruction, which also fixes the other reconstruction parameters like e.g., cut-off frequency. In algebraic reconstructions instead, these quantities only set part of the reconstruction parameters and other ones, like e.g., iteration length or forward modeling which must be derived in extensive experimental evaluations and do often not allow the fixation of exact error bounds [DJS12]. Hence, both reconstruction methods will coexist in the future and are requested to be further developed. The distinct decision regarding which algorithm (independent whether the algorithm was derived by an analytic or algebraic approach) has to be used is highly dependent on the application and the underlying question.

VIII.2 The EM Image Reconstruction Algorithm for Emission Tomography

VIII.2.1 Generic Concept

The EM framework is not a single algorithm but rather a concept of deriving iterative algorithms. The framework applies an expectation step in which the conditional expected value of the log-likelihood function given the measurement on the current image estimate is calculated. Subsequently, a maximization of the expectation step leads to an image update. Since the detailed formulation of the derivation and convergence proofs need detailed knowledge in probability theory, only a simple derivation with the assumption of a *Poisson* model is given here.

The atomic decay as well as the detection processes are statistically seen *Poisson*-distributed since the occurrence of the decay of a single atom or the interaction with a distinct atom for detection are rare processes. Hence, the likelihood function expresses how likely an intensity function f is resembled by a given projection set \mathbf{g} can be modeled by the product of independent *Poisson*-distributed measurements:

$$p_f(\mathbf{g}) = \prod_{i=1}^I \frac{(Af)_i^{g_i}}{g_i!} e^{-(Af)_i} ,$$

where I is the number of the measured LORs. The number of coincidences observed on each line are summarized in the projection vector \mathbf{g} and $(Af)_i$ is the number of coincidences on LOR_i expected from the model. Now, a maximization of the likelihood function is desired. In a first step, the logarithm is taken to simplify the problem. Since the logarithm is a monotonically increasing function the maximum of the likelihood function is not altered.

$$\log p_f(\mathbf{g}) = \sum_{i=1}^I g_i \log(Af)_i - (Af)_i - \log g_i!$$

Following the Kuhn-Tucker conditions [KT51], the log-likelihood function is maximized if f times the gradient of the likelihood vanishes, i.e.

$$f \nabla \log p_f(\mathbf{g}) = f A^* \frac{\mathbf{g}}{Af} - f A^* \mathbf{1} = \mathbf{0}$$

where $\mathbf{0}$ is a null vector, $\mathbf{1}$ denotes a vector full of ones and A^* is the inversion of the operator A . Here, the division and multiplication are meant component-wise. After solving this condition to f , one can declare the following iterative scheme

$$f^{n+1} = \frac{f^n}{A^* \mathbf{1}} A^* \frac{\mathbf{g}}{A f^n} , \quad (\text{VIII.3})$$

as the well known EM image reconstruction algorithm for emission tomography, where n denotes the n -th iteration. Its application in ET was demonstrated the first time in 1982 by *Shepp and Vardi* [WA04], but it was also derived earlier in another approach for astronomical applications. This derivation became known as the Richardson-Lucy algorithm, which was presented in the 1970s [WA04].

The improvement of the image update in every iteration is given since the log-likelihood function is a convex function and it can be proved that the EM iterations produce a nondecreasing likelihood function [WA04]. This means that the algorithm converges against a maximum of the log-likelihood function but in problems with only a few measurements in bad constellation, several solutions satisfy the measurements. This means that it cannot be verified whether or not the algorithm converges against the sought-after maximum [NW01].

VIII.2.2 Discrete Realization

The formulation of the EM image reconstruction algorithm in (VIII.3) is the general description to calculate a solution of the intensity function f in an iterative way. Until now, it was not distinguished whether the operator A or the intensity function f are given in a discrete or continuous expression. No real device is currently able to display continuous image functions. An image reconstruction algorithm does not have to deliver a discrete or digital image. However, discrete algorithms are generally used since their numerical implementation is much easier to realize. Hence, for our purpose, it is convenient to define the tracer distribution function f as a vector \mathbf{f} with elements f_j , where $j = 1, \dots, J$ signs each pixel (2D) or voxel (3D) element of the sought-after discrete image.

In the discrete case, the projection operator A is a matrix \mathbf{A} of the size $J \times I$, whereby its element a_{ij} represents the probability of an emission from voxel j is being detected along the LOR L_i . Here, the matrix \mathbf{A} is often referred to the “system matrix” of the scanner system, and, as it is a matrix, the existence of the inverse operation is guaranteed and is represented by the transpose matrix \mathbf{A}^T . Following these definitions, (VIII.3) can be transferred to this discrete formulation of the EM algorithm [SV82]:

$$f_j^{n+1} = \frac{f_j^n}{\sum_{i'=1}^I a_{i'j}} \sum_{i=1}^I a_{ij} \frac{g_i}{\sum_{j_s=1}^{J_s} a_{ij_s} f_{j_s}^n}. \quad (\text{VIII.4})$$

Here, the image intensity in voxel j is f_j^n at the n -th iteration.

The algorithm in (VIII.4) is maybe a little bit overloaded for the unexperienced reader. Therefore, a simple scheme that explains each operation of the algorithm in

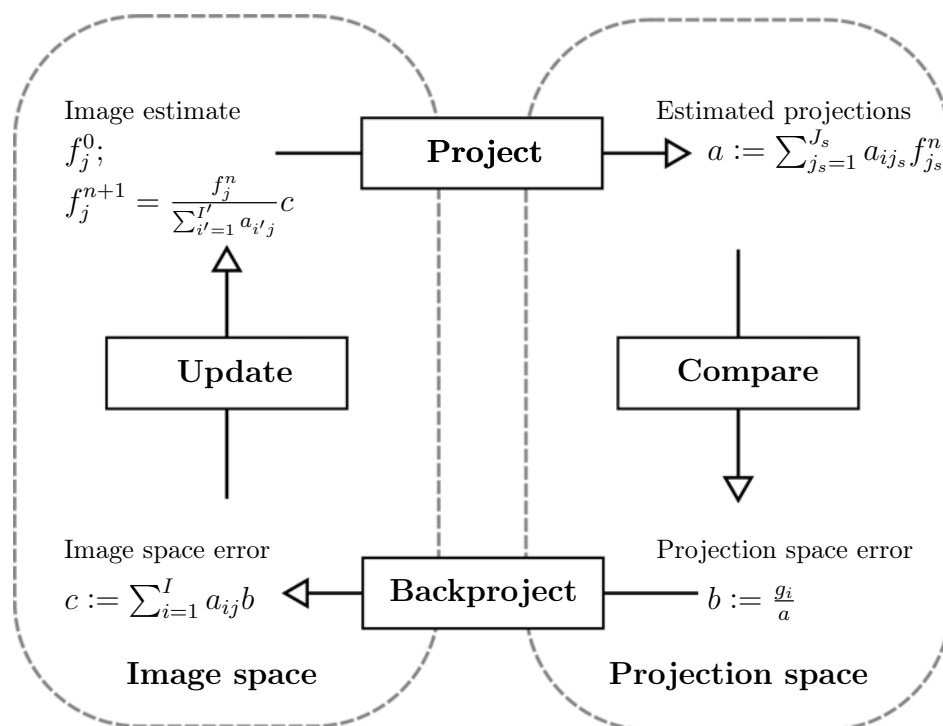


Fig. VIII.1: Flowchart of the EM image reconstruction algorithm for emission tomography, whereby its single mathematical operations and their functional interpretations are displayed. Drawing is inspired by [WA04].

the figurative sense is illustrated in Fig. VIII.1. In fact, the majority of iterative image reconstruction algorithms can be subdivided in the four operations of (1) forward projection of the image estimate into projection space, (2) comparison of the projection to the measurement, (3) backprojection of the difference into image space, and (4) updating the old image estimate.

The following paragraphs makes use of the definitions of a , b , and c , which are declared in Fig. VIII.1. In the formulation of (VIII.4) multiple operation reductions were taken out. In the forward projection a , only matrix elements and image voxels which are effected by the distinct LOR L_i have to be considered, since all other matrix elements are zero. Thus, J_s denotes the number of all effected voxels j_s . A similar procedure accounts for the backprojections in c , whereby in list-mode reconstruction, only the comparisons of the measured projections are taken out. In contrast, the geometric normalization in the first denominator $\sum_{i'=1}^{I'} a_{i'j}$ needs a full treatment of all possible LORs $L_{i'}$ of the system. The number of all possible LORs and their spatial distribution is dependent on the geometrical dimensions of detectors from the PET scanner system. The so called “sensitivity map” \mathbf{s} , with the elements $s_j = \sum_{i'=1}^{I'} a_{i'j}$, is calculated in an extensive calculation outside of the reconstruction framework, whereas the matrix elements a_{ij} for the forward and

backward projection are calculated, on the fly. Here, the direct calculation is often much faster than to load the large data set of a full system matrix into the operation memory. Furthermore, large fine structured scanner systems can cause unmanageable large system matrices. The number of possible LORs for the quadHIDAC with a detector resolution of 0.5 mm for example would be $2 \cdot 10^{13}$. This would lead, for the full FOV with a voxel edge length of 0.4 mm, to a system matrix with around 10^{21} elements.

VIII.3 EMrecon Reconstruction for quadHIDAC Data

The open source reconstruction toolkit **EMrecon**¹ [Kös11] is a framework using expectation maximization (EM) and ordered subset EM (OS-EM) based reconstruction algorithms. It is written in C and allows a user friendly utilization of many different PET or SPECT data from various scanner types to be reconstructed with, up to now, eight different EM based algorithms. This is realized by a modular implementation of data import- and reconstruction-classes. **EMrecon** was partly developed especially for the quadHIDAC geometry. The formulation of the EM image reconstruction algorithm (VIII.4) supposes that the image update is calculated for each voxel. Of course, this procedure is possible, but then the forward projection and the comparison would have to be done then $I \times J$ times. In the **EMrecon** implementation, a ray driven approach is used, where the backprojection of the comparison (b) is stored in an image update vector \mathbf{h} . Here, the single update vectors for each projection bin are summed up which reduces the number of overall forward projections and the number of comparison steps to I steps. Besides the optimized computational speed, only this procedure allows the correct application of the resolution recovery approach which will be explained in Section VIII.3.2.

It is possible to use an appropriate image estimate \mathbf{f}^0 at the beginning of the reconstruction. In the case that no initial estimate is given, the reconstruction starts with an image vector full of ones.

VIII.3.1 List-Mode Reconstruction

The term list-mode data originates from the procedure to store coincidences sequentially in a list, whereby the information of the interaction points of both photons and a time stamp are usually stored in every row. Even though one

¹**EMrecon** $\hat{=}$ expectation-maximization reconstruction

assumes that this is the common way to store data, this is not true. In scintillation based PET scanners, the measured coincidences are commonly stored in a *sinogram* matrix with polar coordinates in the form of $\mathbf{g}(r, \phi)$ (2D) or $\mathbf{g}(r, \phi, \Omega)$ (3D). Here, each element in the sinogram gives the number of measured coincidences along a specific LOR, whereby its position in the sinogram already determines its spatial orientation and position. This type of assignment is obvious for the scintillation cameras, since the spatial extent of the single scintillation crystals and the ring or panel design of the detector heads intuitively leads to this discrete binned data format. The data storage is therefore just done by assigning the combination of two crystals to one sinogram element and counting the coincidences. The advantage of sinogram based data storage is that the amount of data size is smaller compared to list-mode data from long scans. In detail, the file size of the sinogram is independent from the scanning time.

Nowadays, state of the art clinical PET scanners sometimes also use list-mode data acquisition mode, especially if time-of-flight (ToF) information can be provided. In detail, the additional time information is used to constrain the length of the according LOR in the reconstruction. The sequential storage of the event with the time information is convenient since every event has unique time information. However, sinograms with an additional dimension with binned time information are most frequently used.

For the quadHIDAC geometry, only the list-mode data storage is available, since the large panel detectors would lead to large, which were only sparsely filled.

Regarding the EM reconstruction algorithm (VIII.4), each element of the projection data g_i is represented by one element of the sinogram. For list-mode data, each g_i is a 1 given by one measured LOR. This, of course, leads to long calculation times for the reconstruction of list-mode data in the case that the activity is high, and the measurement time is long.

VIII.3.2 System Matrix

In the simplest model of **EMrecon** the elements a_{ij} of the system matrix A are calculated by the *Siddon* algorithm [Sid85]. Here, the assumption in (VIII.1) is replaced by the definition that the left and right hand side are equal. Thus, the probability that the coincidence detected in projection bin g_i is emitted from voxel f_j is estimated by the intersection length of the LOR with the given voxel. The advantage

of this specific algorithm is here the fast calculation time and the algorithm offers a full flexibility in the extent, position, and granularity of the image vector \mathbf{f} with respect to the scanner frame.

Resolution Recovery

A more advanced approach for a more realistic model is the extension the system matrix. Here, the assumption is included that the system matrix can be rewritten by

$\mathbf{A} = \mathbf{X}\mathbf{H}$ like it has been proposed by *Reader* et al. [RAB⁺02], where the matrix \mathbf{X} can again be calculated by the *Siddon* algorithm, and \mathbf{H} is a matrix which accounts for the positron range, the non-collinearity, and the intrinsic resolution of the detectors. Since these contributions are in first approximation position- or respectively shift-invariant for many scanners, this operation can be implemented by a fast and straightforward convolution of the image update vector \mathbf{h} with a simple convolution function. For the quadHIDAC image reconstruction, it was found that a convolution with a *Gaussian* kernel with a FWHM of 1.2 mm gives good results.

VIII.3.3 OS-EM

The ordered subsets EM (OS-EM) strategy is a simple method to accelerate the computational performance of the ordinary EM algorithm. The strategy is to divide the complete projection data set into k subsets, whereby each image update is calculated by (VIII.4) only for the data within one subset. The next image update is then calculated with the subsequent subset. Hence, an iteration is defined in this strategy as the reconstruction of all subsets. This leads to k image updates in one iteration. For list-mode data given from independent radioactive decays, a special order of the LORs is not necessary. For sinogram data instead, the projection bins within the subset need to be re-organized since the algorithm has worse convergence properties if the LORs in a subset are too parallel [DJS12] and gives artifacts if every voxel within the FOV is not affected during a subset [SV82]. It is possible to derive optimized ordering strategies, yet it is often already sufficient to randomly assign the projection bins to a subset.

After n iterations, the resulting image quality is commonly the same as if the image was reconstructed with k times n iterations with the ordinary EM algorithm if the given data set was large enough. The cost of the improved time performance is commonly paid with increased image noise but usually, “*modest acceleration of 8-10 times is possible with very little increase in noise*” [WA04].

VIII.3.4 Geometrical Correction

The sensitivity map introduced in Section VIII.2.2 is calculated with a *brute force* method where all possible LORs are maintained. For a specific detector module pair, all possible coordinate pairings are depicted, whereby the single coordinates are selected stepwise with a position increment of one millimeter. Here, the intersection length of each LOR with each voxel is computed with the *Siddon* algorithm and summed up in the sensitivity vector \mathbf{s} , which has 1 mm^3 large voxels. And subsequently, the single sensitivity maps of the different detector pairs are summed up where only active (physical operating) pairs are maintained. At the end, the map is normalized to the maximum voxel content. In the case that the real image reconstruction is done with another granularity, the voxel elements of the sensitivity map are derived by interpolating the content of the map with the 1 mm^3 voxels.

VIII.3.5 Randoms and Scatter Correction Implementation

To apply a straightforward correction of random and scatter events in the EM algorithm, the randoms and scatter corrected list-mode EM (RS-LMEM) scheme with image non-negativity constraint² suggested in [RCB⁺05] and [RLR⁺04] is used. Explicitly, the EM image reconstruction algorithm with randoms and scatter correction can be written by:

$$f_j^{n+1} = \frac{f_j^n}{\sum_{i'=1}^{I'} a_{i'j}} \sum_{i=1}^I a_{ij} \frac{\delta_i}{\sum_{j_s=1}^{J_s} a_{ij_s} f_{j_s}^n} \quad (\text{VIII.5})$$

with

$$\delta_i = \begin{cases} 1, & \text{if } i \text{ is a prompt event} \\ -1, & \text{if } i \text{ is an estimated random or scatter event.} \end{cases} \quad (\text{VIII.6})$$

Here, the advantage compared to classical ordinary Poisson LMEM (OP-LMEM) methods is that the randoms and scatter estimates can be directly added in list-mode format without an additional step, whereby random and scatter estimates are binned in projection space.

²The non-negativity constraint does not allow the update vector to have negative elements. Thus, negative elements are set to zero.

Randoms and Scatter Correction

Induced by basic differences of the detection principle of gas detectors compared to scintillation detectors, randoms and scatter correction techniques in PET are much more important for the gas detector types according to the missing energy information of the measured photons. This chapter shows how the presented **Geant4** simulation of the quadHIDAC is used to investigate the impact of scatter and random events in the quality of the reconstructed images. Furthermore, the simulation data was reconstructed with **EMrecon** [Kös11] with and without randoms and scatter corrections to validate the correct performance of the corrections. Additionally, results from reconstructions with improved image quality of real measurements are presented where the according randoms and scatters estimates were generated with the **Geant4** simulator. The main results of this chapter have been published in [GKV⁺13].

IX.1 Quantitative Image Reconstruction

In quantitative image reconstruction, it is desired to adequately represent the administered activity of the radio tracer in the amplitudes of the image voxels, which render the single organs of the imaged object. To arrive at quantitative images, it is necessary to apply several corrections which can be applied prior, during, or after the image reconstruction. Calibration measurements are commonly taken out daily with solid sources with known activity to obtain information necessary to correct the reconstructed images. The simplest correction is here to just measure the sensitivity

s of the scanner in the center of the field of view and to multiply every voxel value f_j times $1/s$. Another example for a correction method with solid radioactive sources relies on the use of transmission scans, which are taken out while the imaged object is within the scanner. The transmission scan is used to generate an attenuation map which can be applied during image reconstruction. This is a common method for clinical stand-alone scanners.

In clinical routine, many corrections are typically applied. The single steps are documented in standardized imaging protocols for the single scanners and applications. The main focus, in general, is here on the geometrical correction (Section VIII.3.4), attenuation correction¹, randoms and scatter correction, detector normalization², and dead- and decay-time corrections³ to obtain quantitative correct images. Quantitative image reconstruction is still a missing issue concerning the quadHIDAC, thus, in this chapter, procedures to apply accurate randoms and detector scatter corrections are suggested.

Beside these major degrading effects in the quadHIDAC, it should, of course, be pointed out that object scatter and attenuation corrections are also needed if it is aimed to get quantitative images. Nevertheless, both effects have less impact if compared to clinical PET examinations. Contributions from scatter in humans are quite large (scatter fraction 75% for a 40 cm diameter human-like NEMA phantom), whereas in rodents, the amount of scattered events is rather manageable (15-24% scattered events in rats and 6-10% in mice for an energy window of 350-650 keV,) [Kon10].

Furthermore, it has been shown by *Chow et al.* [CRC05] that photon attenuation is large in humans (correction factor 45 for a 40 cm diameter human) compared to rodents (correction factor of 1.6 for a 5 cm diameter rat versus 1.3 for a 3 cm diameter mouse). Here, the correction factor c_f is defined by $a_r = c_f \cdot a_m$ where a_r and a_m are the corresponding real and measured activity.

¹The attenuation correction accounts for annihilations which are not measured by the scanner because of photon absorption or scatter within the imaged object. This leads to an underestimation of the real activity within the object. In clinical PET, so called “attenuation maps” (μ -maps) are obtained by CT, magnetic resonance imaging (MRI), or transmission scans and applied in image reconstruction. In small objects, like mice, it is often sufficient to apply just a single scaling factor.

²The detector normalization accounts for the position sensitive and angle dependent photon detection efficiency of the detector elements.

³The decay-time correction takes the decline in emission probability of the tracer into account and scales later counts to the initial activity. The dead-time correction instead considers that the scanner is not able to determine each single event if high activities are applied. The dead-time in which the detector is not able to count a further event after a hit is often event type dependent and suppresses the real count rate.

IX.2 Reconstruction including Randoms and Scatter Corrections

The incorporation of the randoms and scatter correction method in **EMrecon** was already described in Section IX.3.1. Now, the focus is more on the technical side, whereby the interlacing of the random and scatter events into the list-mode stream and the appropriate scaling of estimates is considered. It is important to distinguish between corrections on simulated and measured data, whereby both will be presented later on.

In the simulation, no direct random events are generated since the simulator tracks particles and photons on an event base without any time information. Nevertheless, spatial distributions of random events can be estimated for simulated and measured events, which will be discussed in Section IX.3.1. This means that simulated data must be mixed with random events to test the performance of correction techniques and therefore, their amount in the data is precisely known. For measured data, the amount of random events in the list-mode data can be estimated by (II.6), where, in this case, the s_A and s_B are the single count rates of the single modules and the coincidence window Δt_c is 40 ns for the quadHIDAC. The single rates information of each module is reported in the list-mode stream every 2 s by the quadHIDAC.

For scattered coincidences, no direct estimation techniques for the amount or their spatial distribution are available for quadHIDAC measurements. So far, only the simulation based method described here is possible. In simulations, these quantities are directly given since scattered events are flagged. In measurements where no simple source geometries are studied, the spatial scatter distribution can be estimated using the voxelized event generator described in Section IV.2.2. The generator takes images which were reconstructed with **EMrecon** and simulates positron annihilations at the center of a voxel proportionally to the image voxel intensity.

The photons here are produced within the world volume material⁴. Thus, these simulations only account for the detector scatter fraction and neglect the object scatter.

Explicitly, the average fraction of scattered events within the simulation can be

⁴The world volume material is a **Geant4** term which defines the basic material of the simulation which is set to air in the default HIDAC simulations.

directly determined in the output data and is used to scale the number of scattered events to be corrected in the measurement using the following factor

$$\frac{S_s}{T_s} \cdot (T_m - R_m), \quad (\text{IX.1})$$

here S_s is the number of simulated scattered events, $T_{s,m}$ is the amount of total simulated and measurement events and R_m is the number of random events.

The estimated events have to be incorporated into the list-mode stream to be able to apply the randoms and scatter correction with the RS-LMEM scheme in (VIII.5). The converter macro described in Section IV.2.2 was extended to read in the measured list-mode and `ROOT TTree` files with the randoms and scatter estimates, as well as to stream everything into one list-mode output file. It has to be assured that the estimates are scaled correctly, whereby the scatter fraction can be retrieved directly from the simulation and the random fraction has to be calculated from the single rates information. The single events are then inserted randomly into the output to guarantee a fair processing within the reconstruction algorithm, especially, in the case that OS-EM reconstruction is used. If the number of events in the `ROOT TTree` is lower than needed, the successive event is taken again from the beginning of the simulated files. Within the list-mode file, the random and scatter events to be corrected are flagged with a negative angle value.

IX.3 Randoms Correction

IX.3.1 Estimation of the Spatial Distribution from Random Coincidences

In PET, several approaches to estimate the spatial distribution of random events for quantitative image reconstruction have been developed. This is necessary because analytical descriptions are commonly not accessible. Some of these methods to approximate the spatial randoms distribution are listed in the following:

- A good random estimate can be simply obtained if the distinct single rates on each measured LOR can be determined by using (II.6). With this information, the random fraction could be corrected on each LOR. Unfortunately, it is impractical to measure this quantity in systems with a fine detector element granularity as the number of channels where the single rates need to be measured increases dramatically with the system resolution.
- A more common method is to estimate the spatial distribution of randoms is the “delayed coincidences” method. Here, measured detector hits are delayed by a time interval which is substantially larger than the coincidence time window and combined to a coincidence with an un-delayed detector hit. This method is not applicable for every scanner, since it requires special read-out electronics. It has been shown by [BKL⁺05] that for large count rates, this method nicely approximates the randoms distribution. Regardless of its poorer statistics compared to the former method, a big advantage is that it accounts intrinsically for dead time effects.
- Another approach to estimate the random distribution on single hit information is the shuffled singles (SHS) method. Here single hits are randomly combined to approximate the random distribution.
- Determination of the spatial random distribution based on voxelized event generators and Monte-Carlo Simulations.
- A less effective but always realizable method for all list-mode based scanners is the shuffled half-coincidences (SHC) method proposed by *Divoli et*

al. [DED⁺04]. The method uses the two single coordinates of the each measured coincidence and combines them randomly with coordinates from another coincidence to form artificial (random) coincidences.

- An experimental access to obtain randoms distributions of simple source geometries is to use a single-photon emitting source. ¹³⁷Cs point sources are usually used since the photon energy of $E_\gamma = 662$ keV is similar to that of annihilation photons ($E_\gamma = 511$ keV).

Unfortunately, there is no possibility to apply one of the two first methods for quadHIDAC data reconstructions since neither information on single rates or hits nor delayed coincidences data support is given by the system.

Only the SHC and the Monte-Carlo based correction methods are therefore possible for the quadHIDAC image reconstruction. In the presented **Geant4** simulator, the direct estimation of random coincidences is not possible due to the lack of time information. Instead, random events and their spatial distribution are generated post simulation by the SHS or SHC methods with the independent single events or coincidences. For the data analysis, the determined random events are mixed randomly to the true and scattered events and are written in list-mode format. It is assured that no single coordinates from the same annihilation (true events) are mixed together, and that they belong to opposite detector heads.

IX.3.2 Influence of Random Events in Reconstructed Images

The spatial distribution of LORs caused by random coincidences depends on the geometry, size, and position of the radioactive sources within the scanner. The large covering angle of the quadHIDAC modules combined with a large coincidence window of 40 ns may account for large fractions of random events in the measured coincidence data. Nevertheless, given by the large FOV, the number of random events in each voxel remains relatively low. The dependency between the activity of a 80 mm long line source in the center of the FOV and the count rates for the quadHIDAC separated for different types of events was simulated with a dead time model by *Gottschlag* [Got10] and measured by *Schäfers et al.* [SRK⁺05]. The results are shown in Fig. IX.1. The ratio of true events to scattered events remains almost constant, while the fraction of true events to random events is decreasing for higher activities. At around 10 MBq the ratio becomes 2 and gets 1 around 18 to 20 MBq.

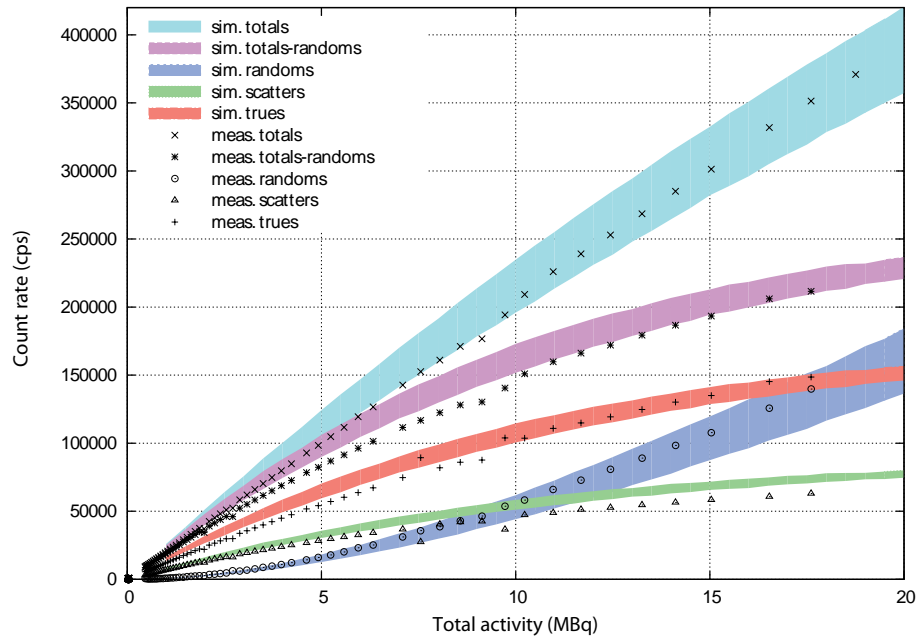


Fig. IX.1: Evaluation of the count rate performance for different event types measured and simulated for a line source. The count rates were obtained with quadHIDAC measurements and dead time model simulations, whereby uncertainties of 10% are assumed. The figure shows the dependence of the count rate on the source activity [GKV⁺13].

In the following, the influence of the random events in reconstructed images should be illustrated and analyzed with simulations of spherical sources with different diameter in the center of the FOV. To create adequate data for the image analysis, the number of simulated positrons Nb_{Data} was here set to a constant value of 160M, where the amount of randoms $Nb_{Randoms}$ is calculated by

$$Nb_{Randoms} = Nb_{Data} \frac{p}{1 - p}$$

where p is the fraction of randoms within the mixed dataset. Thus, the random events can be mixed to the clean data sets in arbitrary fractions. Indeed, in measurements, the random fraction is dependent on the activity and therefore, the simulations give estimations on the impact of randoms dependent on the source size for any activity. With this procedure it is possible to quantify the content of randoms within each voxel by comparing it to the number of events in the associated voxel of the reconstructed image with no random events.

The different diameters are altered from 2 cm to 10 cm. A small ensemble of central transverse slices images from reconstructions of these simulations is presented in

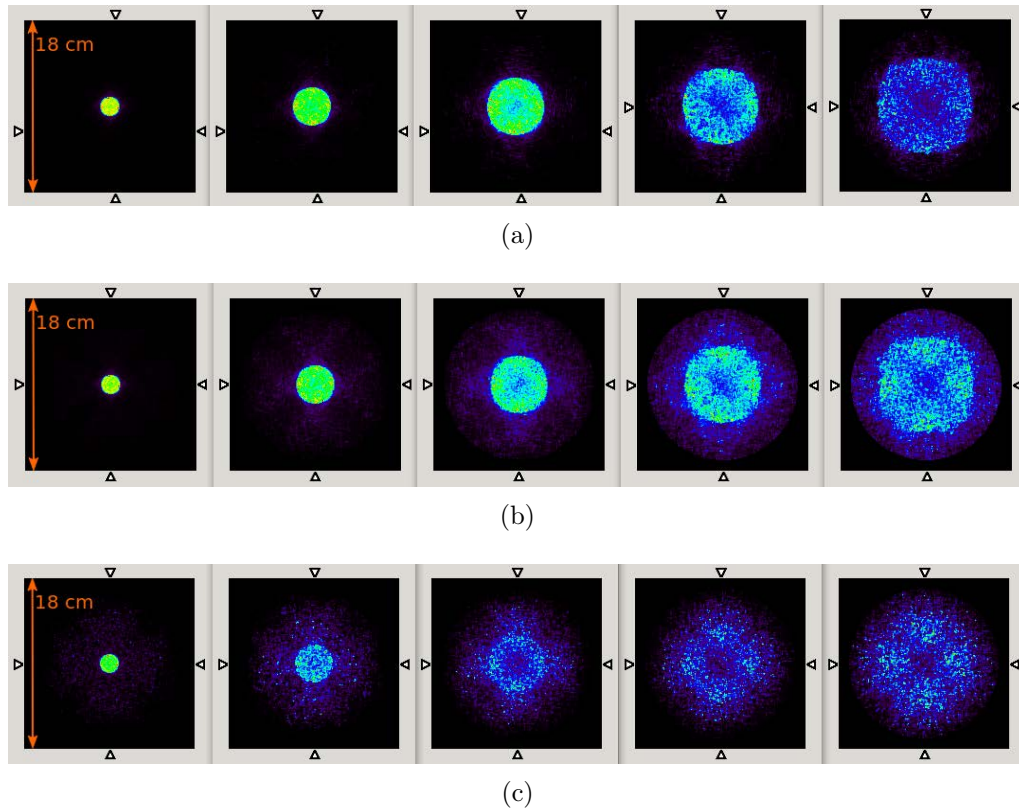


Fig. IX.2: Central transverse slice of reconstructed images are shown from simulations with spherical sources with diameters of 2, 4, 6, 8, and 10 cm. In (a), no randoms were added. In (b) 60% and in (c) 90% of randoms were added to the simulated data.

Fig. IX.2 where the sources with the diameters of 2, 4, 6, 8, and 10 cm with a fraction of 0%(Fig. IX.2(a)), 60%(Fig. IX.2(b)) and 90%(Fig. IX.2(c)) are compared. It is clear that the erroneous image intensities caused by random events increase for larger source volumes as the number of events per voxel is decreasing for larger source volumes. It is also visible that there are distortions on the surfaces for the largest source volumes and that these distortions grow for larger fractions of random events. However, there are also artifacts in the images which are not addressed to random events. On the one hand, there is the cross pattern in the images which is induced by static mode simulation, which means that the detector heads were not rotated. On the other hand, the geometrical correction leads to an over correction in the outer FOV. Thus, in large source volumes the activity in the center is lower than in the peripheral regions.

The quantitative analysis of the full set of simulations is displayed in Fig. IX.3.

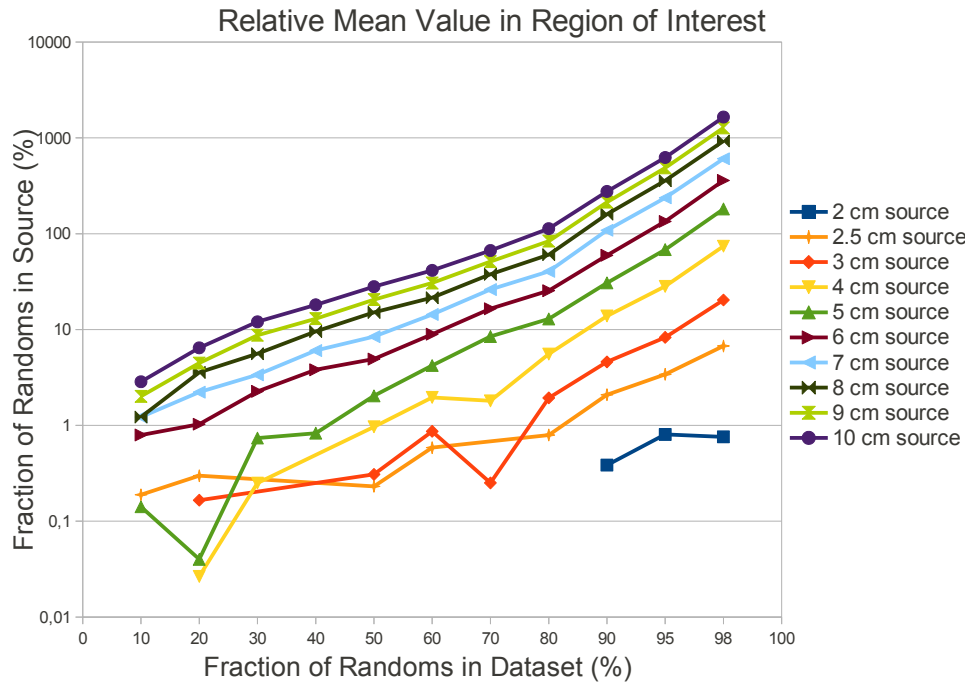


Fig. IX.3: Fraction of random events within the source volume for differently sized source spheres illustrated in dependence of the amount of random events in the data sample. The analysis is based on the images which are partially shown in Fig. IX.2. Here, the fraction of randoms in the source is defined as the ratio of “events in the source volume ROI from the data with randoms” to “events in the ROI without randoms from the clean dataset”.

The images were analyzed with AMIDE⁵ [LG03], with which the mean value of number of events per voxel can be calculated for arbitrary region-of-interests (ROI). A ROI around each source volume, with the according sphere diameter, was here defined for each simulation. Also, the average number of events per voxel within the ROI was determined and divided by the average number of events per voxel for the same ROI from the image without random events. Thus, this ratio determines the relative amount of random events within the source volume. It is visible that the amount increases with the source volume and approximately exponential with the overall amount of randoms in the dataset. It is also important to notice that fractions below 1% are inconsistent for the simulation. This is presumably caused by deviations in the single reconstructions or by the image analysis tool in AMIDE. One should therefore not expect that randoms corrections exceed those limitations. From these results, it can be extracted for measurements with a known activity and determined

⁵AMIDE $\hat{=}$ a medical imaging data examiner

random fraction how large the impact of random events on the reconstructed image activity for a given object size is. In detail, it is possible to predict a random fraction threshold for each object size at which correct random corrections become necessary to reach at quantitative correct images.

IX.3.3 Shortcomings of the Shuffled Half-Coincidence (SHC) Estimation Method

Different methods of deriving the randoms spatial distribution have been introduced in Section IX.3.1. At this point, three different methods should be compared on projection data level. Parallel projections⁶ of random estimations are here generated from point source simulations with the SHS and the SHC methods and compared to measurements with a ^{137}Cs point source. The aim of the comparison is, on the one hand, to validate the appropriateness of the simulation to generate spatial random estimations comparable with measurements and on the other hand, to emphasize the limitations of a SHC based estimation. It is known that spatial distributions of random events obtained with the SHC method yield good estimates if source objects are positioned at the center of the FOV, but the method is inappropriate for objects in off-center positions. The results for four different source positions are presented in Fig. IX.4. In Fig. IX.4(a) it can be seen that the obtained distributions are almost identical for all methods. For the small displacement of 20 mm from the center of the FOV, deviations from the SHC method to the measured distribution up to 20% are observed in the central region ($-30\text{ mm} < x < 30\text{ mm}$), whereas the distribution obtained with the SHS method matches with the measurement as illustrated in Fig. IX.4(b). For larger displacements of up to 50 mm, the SHS method (max. deviation of 10%, Fig. IX.4(d)) is obviously more appropriate than the SHC method (max. deviations of 30%, Fig IX.4(c), and 50%, Fig. IX.4(d)).

It can be summarized that the SHC method proposed by *Divoli et al.* can be used for quantitative image reconstruction with the quadHIDAC in the case of measured objects in the center of the FOV. For large displacements and larger objects, it is more reliable to use randoms distributions obtained from Monte-Carlo simulations.

⁶The parallel projection is a method to bin arbitrary measured LORs into sets of planes which are in approximation perpendicular to the LORs. In detail, this is a transformation of the form: $((x_1, y_1, z_1)(x_2, y_2, z_2)) \rightarrow (x_r, y_r, \Phi, \Theta)$.

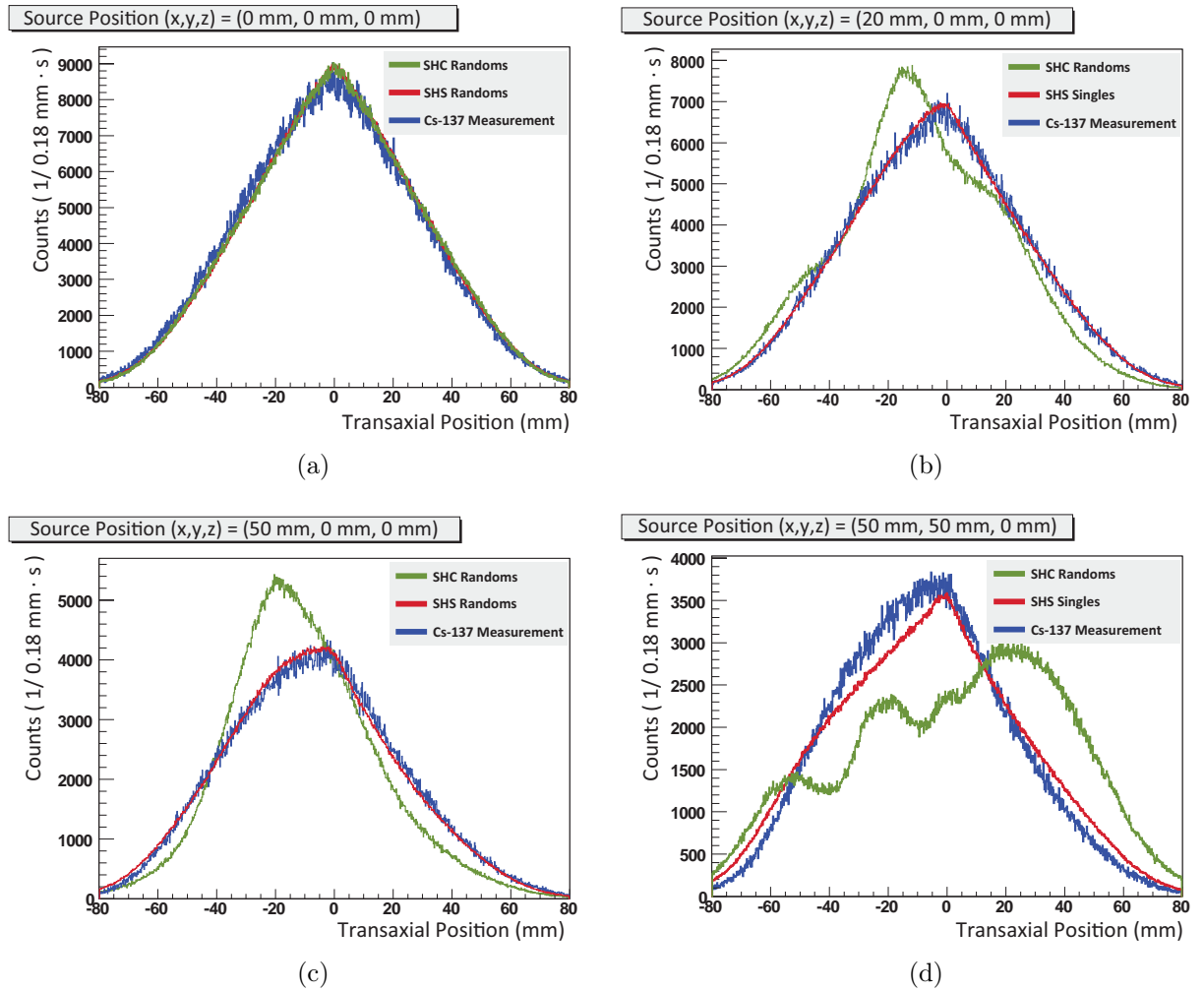


Fig. IX.4: Radial dependencies of the count rates observed in parallel projections where it was integrated over all angles from measurements and simulations of random distributions of point sources. LORs were obtained from combination of arbitrary singles (SHS, red), shuffled half-coincidences (SHC, green) and ^{137}Cs -measurements (blue). The SHC method only gives reasonable estimates for central placed sources. Simulated distribution were normalized to the measurement [GKV⁺13].

IX.3.4 Randoms Correction for Two Simulated Small Spherical Sources

In a first step, random and scatter corrections are compared separately to examine if the derivations of the single estimates are correct and the scaling of each contribution is done properly. Because it is not possible to get a measured data sample without randoms⁷, simulations with spherical sources with different gaps between them were performed to obtain data samples with unbiased true distributions and distributions with added random. The randoms corrections were done using the SHS and the SHC method to demonstrate the performance of the different estimation techniques in the reconstruction. In detail, the impacts caused by random events in reconstructed images have been investigated in two different simulations where in each trial, 400M positron annihilations have been distributed on two point sources with diameters of six millimeters. The sources were positioned with an activity ratio of 2:1 at two different axial distances of 30 mm and 120 mm. They were distributed on the axial axis symmetrically to the center of the FOV.

To resemble measurements with medium activity, an arbitrary random fraction of 30% has been added to the simulation output. The added randoms were here generated with the SHS method. As a correction with an estimate which is equal to the random events in the data is not a realistic and fair situation, a further simulation was made to generate an unbiased random estimate for a proper comparison to the SHC method.

For image visualization, the voxel content was projected on one plane and then summed up in one histogram. Thus, in the results in Fig. IX.5 which show random corrected and uncorrected reconstructions, each bin represents the integral of the voxel content within the corresponding z -plane.

The reconstructed images with performed corrections using the two different SHS estimates perfectly match the image from data without randoms. The results with applied SHC method are not as good but nevertheless, the method is able to reject the major fraction of the random events. The advantage of the SHS compared to the SHC method is demonstrated in particular in the semi-logarithmic view on the sources with larger displacement. The same behavior can also be seen in the enlarged view of the peaks of the point sources (Fig. IX.5, right). The results show that for

⁷Data samples without random events are not obtainable in measurements as a small contribution of background coincidence counts is always measured by the scanner, even though no activity is within the scanner.

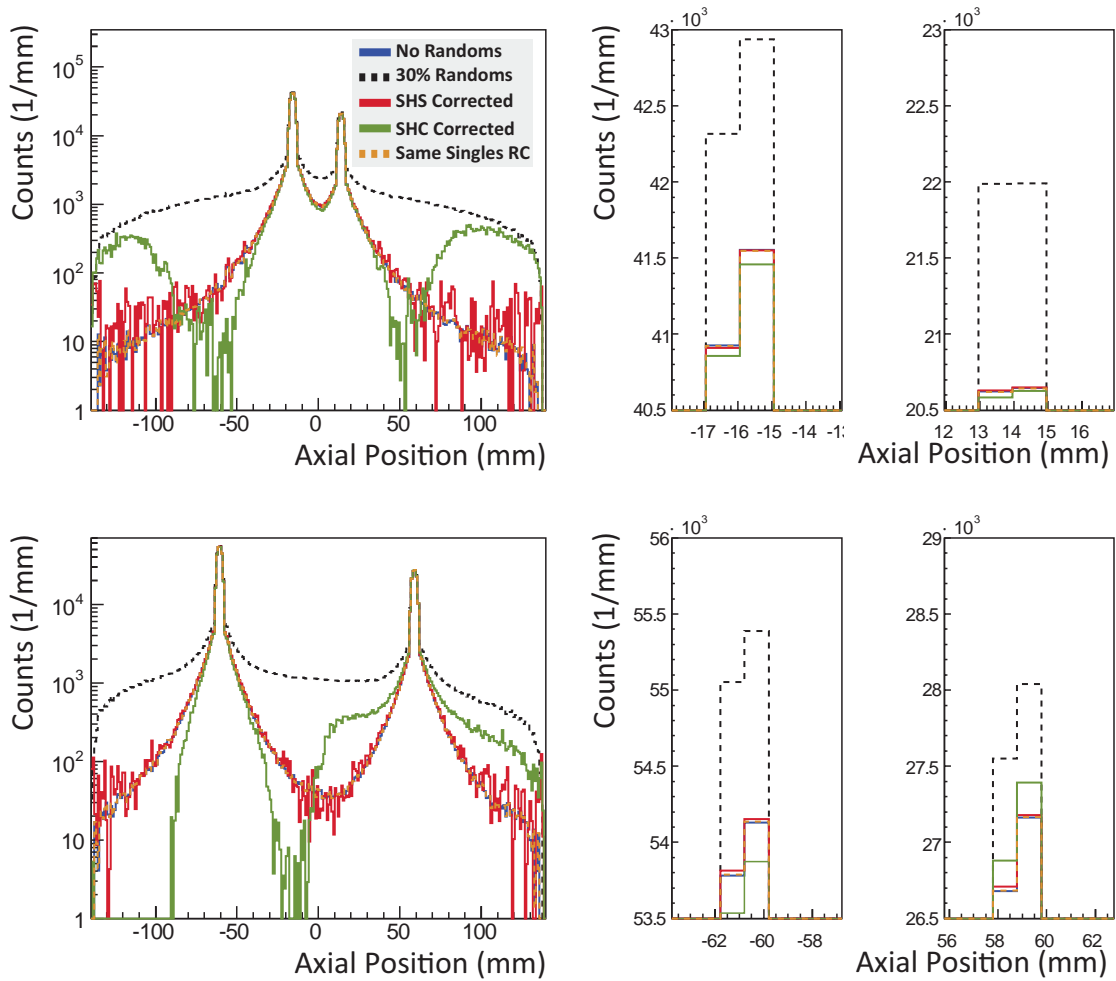


Fig. IX.5: Results of randoms correction based on simulations of two displaced spherical sources. Distributions of integrated counts of the reconstructed images along the axial direction of the scanner are shown, whereby images from data with and without randoms as well as with randoms corrected (RC) were generated. RC was performed using three different randoms estimates. The sources were displaced by 3 cm (upper row) and 12 cm (lower row) respectively with an enlarged view on each peak in the right columns. The RC was performed using (1) the SHS estimate which was added to the simulation (orange) perfectly matching the data without randoms (blue), (2) a SHS estimate from another simulation (red), and (3) a randoms distribution using the SHC method (green).

small separations, common for single mouse scans, only minor deviations between the methods are given where the SHC method slightly over-corrects the images. For the source at 12 cm distance, the SHC method leads to a heavy overestimation of counts in the right source and a strong underestimation of counts in the left source.

In contrast, there are only negligible overestimations if the SHS method is used. As expected, it was demonstrated that for a reliable randoms correction for activities separated by large distances, or if the activity is placed on a large offset, corrections based on simulations are needed since the data based SHC method is not sufficient.

IX.4 Scatter Correction for a Simulated Mouse Phantom

For scatter distributions, no direct estimation techniques are given and therefore, the influence on the offset of sources, like for the random estimates, are not of major interest. Hence, the negative impact on image quality due to scatter events can now be tested and evaluated on a mouse phantom. The phantom, which was also measured with the quadHIDAC, was simulated with the `Geant4` simulator. In detail, the mouse phantom was a bottle phantom with a screw cup filled with FDG⁸. The source was simply simulated by liberating 320M positrons equally within two different sized cylinders which were positioned analogically to the measurement mouse phantom near the center of the scanner. The cylinders were filled with water to account in this case not only for detector scatter, but also for object scatter. The study intends to test whether a scatter correction approach is able to recover sharp edges which otherwise be lost. Additionally, the step between the two cylinders renders a good benchmark for the performance of the applied scatter correction technique. For a fair comparison, the scatter estimate was obtained from the same simulation as well from a separate simulation within the same geometry with comparable statistics. The results of the study are presented in Fig. IX.6 and Fig. IX.7. Apparently, the scatter corrected images with both scatter estimates are able to regain the major activity contributions as well as the geometrical characteristics from the true emission density of the mouse phantom. In the logarithmic-scaled view in Fig. IX.6, a minor deviation of some counts in the outer FOV from the ground truth distribution is observed in the case that the correction with the scatter estimate obtained from the independent and unbiased simulation is used.

⁸Fludeoxyglucose labeled with ¹⁸F is a glucose analog and the most commonly used PET tracer, mainly applied in oncology.

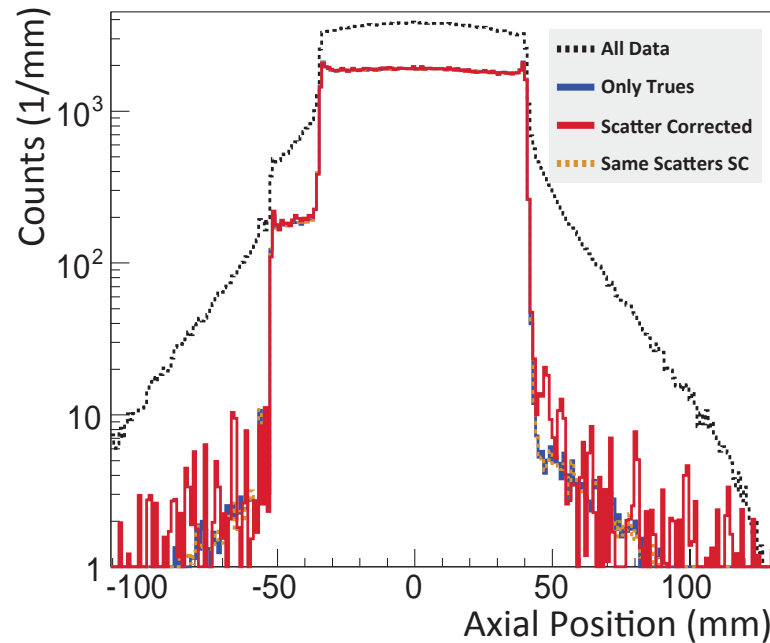


Fig. IX.6: Reconstructed images from scatter corrected and uncorrected simulated mouse phantom data. Distribution of integrated voxel counts along the axial axis of the scanner. The resulting images of reconstructions with scatter corrections where the estimates were obtained (1) from the same simulation (orange) and (2) from another simulation with the same geometry (red) compared to the reconstruction of only ground trues (blue).

Regarding the sagittal central slice images in Fig. IX.7, this even leads to a complete rejection of events outside the object which, on the other hand, exist in the ground truth image due to positron air interactions. Thus, within some offset planes some scatter events still survive. Nevertheless, the results present outstanding rejections of the major fractions of undesired scatter events for both scatter estimates, which renders the `Geant4` simulator to a great tool to generate precise scatter estimates.

IX.5 Randoms and Scatter Correction on Simulated and Measured Mouse Data

To make use of the simulator for randoms and scatter corrections in preclinical routine, the voxelized event generator from GAMOS [ARC⁺08] (Section IV.2.2) was implemented in the code. In the current study, the generator was fed with a recon-

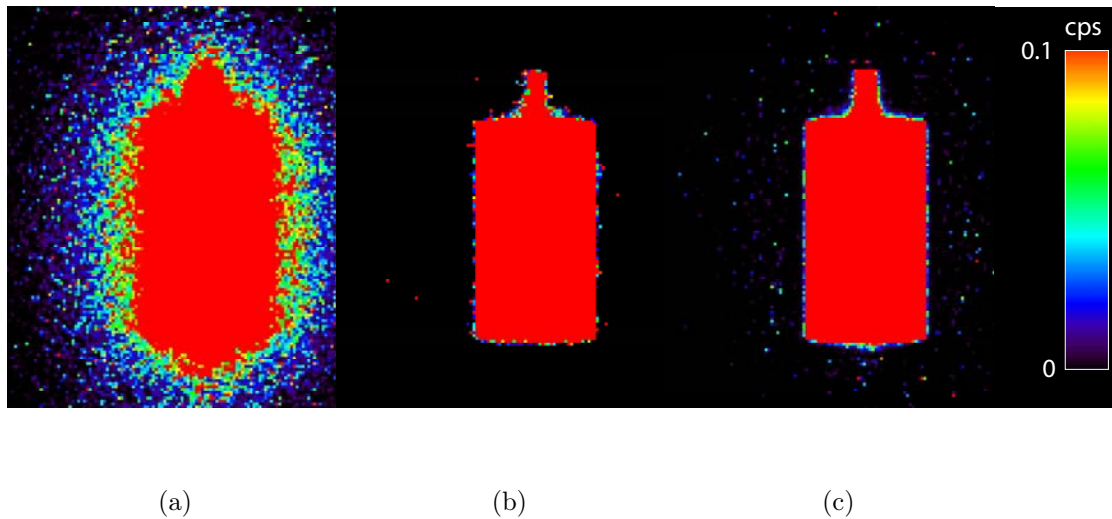


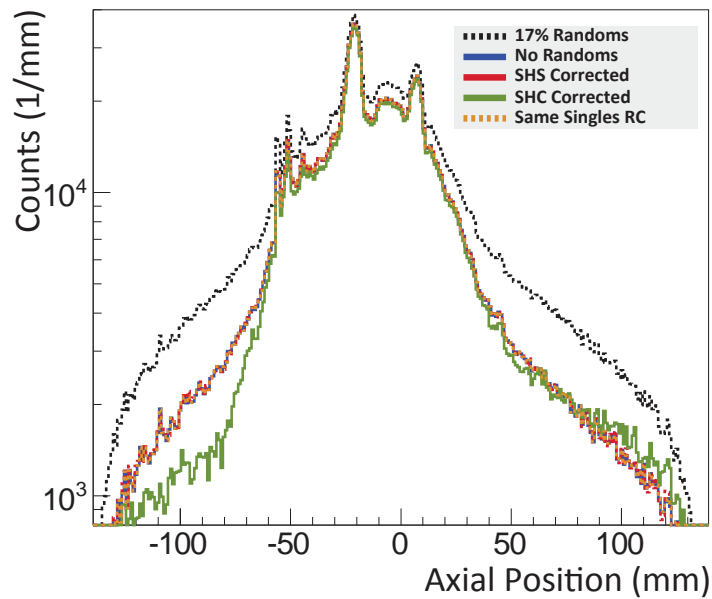
Fig. IX.7: Images from the simulated mouse phantom studied without (a) and with (b) applied scatter correction and the reconstruction of only true coincidences (c). Only the sagittal centered slices are shown in contrast to the full image data in Fig. IX.6. The upper image threshold was lowered to 0.1 counts per second to emphasize the scatter influence.

structed image from data of a real FDG mouse scan to derive randoms and scatter estimates. Conclusively, a second reconstruction was made using the estimates from the simulation.

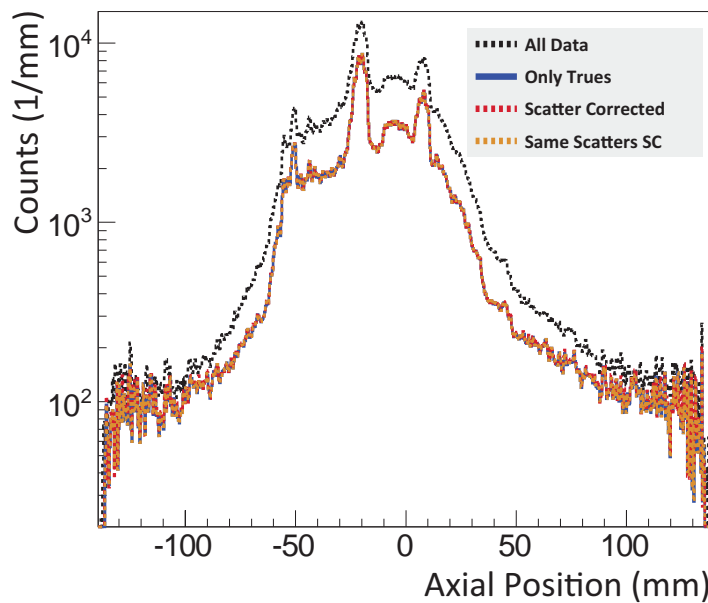
In the quadHIDAC scan, 65M coincidences have been registered in 15 min. Following (II.6), a random fraction of 17% should be within the data. Accordingly, the same amount of randoms derived with the SHS method was mixed to the simulation output. To obtain a comparable amount of coincidences in the simulation, 1G positrons have been liberated with the voxelized event generator.

Verification of Corrections on Simulated Data

The performance of the randoms and scatter corrections on the simulated data output is illustrated in Fig. IX.8 where the impact of the randoms corrections, with estimates obtained with the SHS and SHC method, on the image quality are studied in Fig. IX.8(a) and for the scatter correction in Fig. IX.8(b). In the measured mouse from a FDG scan, a large activity uptake was observed in the heart and the bladder, which are represented by the two main peaks in the histograms. Additionally, the lower uptake within the brain/eyes and the colon are roughly distinguishable.



(a)



(b)

Fig. IX.8: Results from reconstructions of simulated data produced with the voxelized source generator with a reconstructed image of a mouse measurement as input. The figures show the integrated voxel content along the axial plane of the scanner from uncorrected and corrected reconstructed images. For the randoms correction in (a), a fraction of 17% randoms has been added to the data (black) and compared to the data without randoms (blue). Furthermore, the data with randoms was corrected with the SHS (red, orange) and the SHC (green) estimate, where for the SHS method the sample of the given simulation (orange) and a comparable simulation (red) was used. In (b), the simulation output without randoms (black) is compared to the reconstructed ground trues (blue). The output was also scatter corrected with the scatter estimation from the same simulation (orange) and the comparable simulation (red).

For the randoms correction, the SHS method with both data sets generate images which perfectly match to the image without randoms. The performance of the SHC method is also quite impressive, but obviously the activity is slightly underestimated globally and heavily in the front FOV outside the mouse (Fig. IX.8(a)). Nevertheless, the discrepancies are rather small within the mouse, and the SHC method should be still reasonable for typical mouse scans. Apparently, the SHS method for an efficient randoms correction is necessary in studies where large activities are administered in larger species like rabbits and rats or if more than one animal is used in one scan. For the scatter correction (Fig. IX.8(b)), it is shown that both estimates are able to perfectly resemble the truth distribution. It is observed that the scatter correction is able to regain slimmer main source peaks which are slightly broader in the full data reconstruction.

In summary, it is demonstrated that both correction techniques show reliable performance for the given statistics.

Application of the Random and Scatter Estimates on Real Mouse Data

So far, the correct performance of the correction methods and the reliability of the estimates have been proven. Consequently, it is now possible to test them on real mouse data. Of course, an unavoidable issue by using a pre-reconstructed image for random and scatter estimation is that the basic data set in the simulation includes random and scatter events as part of the emission density. Thus, it was also checked if it is possible to obtain more realistic scatter and randoms distributions by performing a further simulation with the corrected image as input. The results of the test with reconstructed images corrected with the original randoms and scatter distributions and with the more realistic distributions obtained from the iterized simulation are compared in Fig. IX.9. For a better comparison, the images of the raw simulation data and the true coincidences of the first simulation have been added to the image. Furthermore, sagittal slices of the images are presented in Fig. IX.10. The analysis results show quantitatively improved images. The performed scatter and randoms corrections have a visible beneficial impact in image contrast, e.g., in cold (colon) and hot (heart) activity regions. The advanced scatter and randoms estimates obtained from the iterated simulation using the pre-corrected image as input show only slight extra improvements in image contrast (Fig. IX.9), which shows that the little improvement does not justify the expense of further simulations.

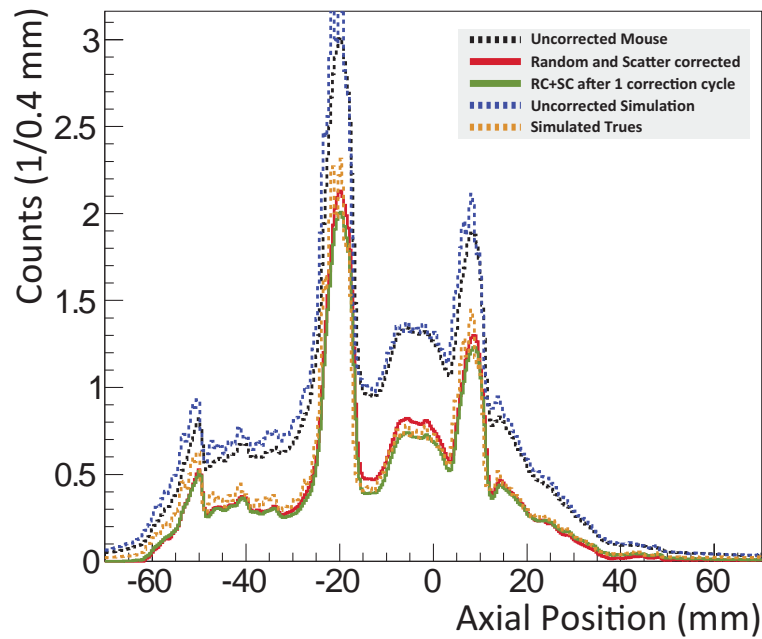
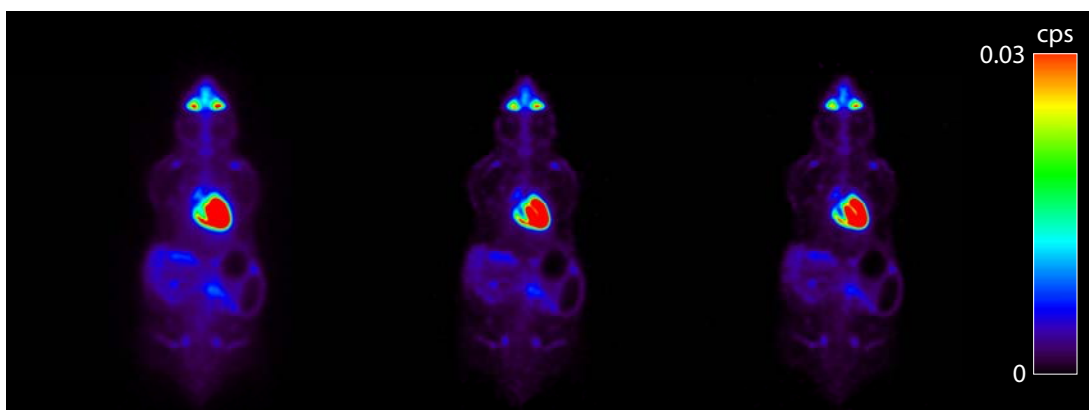


Fig. IX.9: Reconstructed images obtained from measured mouse data and the results from the appropriate randoms and scatter corrections. The measurement output (black) was random corrected with the SHS method and scatter corrected with the estimates obtained from the simulation output (red) shown in Fig. IX.8. Additionally, a further simulation with the corrected image as simulation input was used to generate more advanced scatter and random estimates (green). The results are also compared to the uncorrected simulation output (blue) and the reconstructed true data of the first simulation (orange).



(a)

(b)

(c)

Fig. IX.10: Images from the measured mouse reconstructed without corrections (a), with randoms and scatter correction (b), as well as the applied correction with the advanced random and scatter estimates from a simulation with the corrected image as simulation input (c). Here, only sagittal centered slices are shown compared to the full image data in Fig. IX.9. The image threshold was set down to 0.03 counts per second (cps) to emphasize the image quality improvement.

IX.6 Statistical Analysis

The computational load of simulating random and scatter distributions to arrive at quantitative correct image representations is not insignificant. A kernel of the MAF cluster needs on average one hour to process 60k positron annihilations. This leads to a processing time of $\sim 17,000$ h to simulate the scatter distribution which was used to correct the images shown in Fig. IX.9 and Fig. IX.10. It is therefore of specific interest to evaluate the number of LORs which is necessary to give a sufficient image quality after image reconstruction. This is especially needed to estimate whether or not the procedure can be translated to preclinical routines. The impact of the amount of used scatter events within the scatter correction was studied by adding different amounts of coincidences out of the original scatter estimate. In all corrections, the same scatter fraction is applied, but for lower amounts of scatter coincidences the same coincidences were mixed several times into the list-mode output stream. The results of the different corrections are compared in Fig. IX.11. The upper image threshold was lowered to a very low intensity value of $1 \cdot 10^{-4}$ counts per seconds to see also tiny artifacts and differences in the different corrections. Obviously, the correction where only 3% of the coincidences (this equates to roughly 1M coincidences) were used for the scatter correction in Fig. IX.11(a) has more artifacts where still some scatter events were not rejected. In the case that the correction was done with 10% of the scatter coincidences Fig. IX.11(b), the artifacts are almost gone. However, some differences are still visible if compared to the use of the full scatter estimate in Fig. IX.11(c). For the sake of completeness, all corrections are also compared to the uncorrected image reconstruction Fig. IX.11(c). For a more precise analysis, four different ROIs were defined, whereby a sphere was placed around the heart, the bladder, and the colon, and a cylinder was placed spaciouly around the whole mouse. The comparison of the absolute image intensity by the average voxel values within these volumes calculated with AMIDE is shown in Fig. IX.12. The background in the chart is here defined as the whole image volume subtracted by the mouse cylinder ROI. The quantitative comparison based on these absolute values is illustrated in Fig. IX.13. Here, the relative error is obtained by assuming that the scatter correction in which only one walkthrough the simulated scatter coincidence data set was done (100% scatter; only possible if the simulation statistics is large enough) is correct. By taking the reconstruction with scatter correction of this data set as reference, the relative error to the other reconstructions can be calculated.

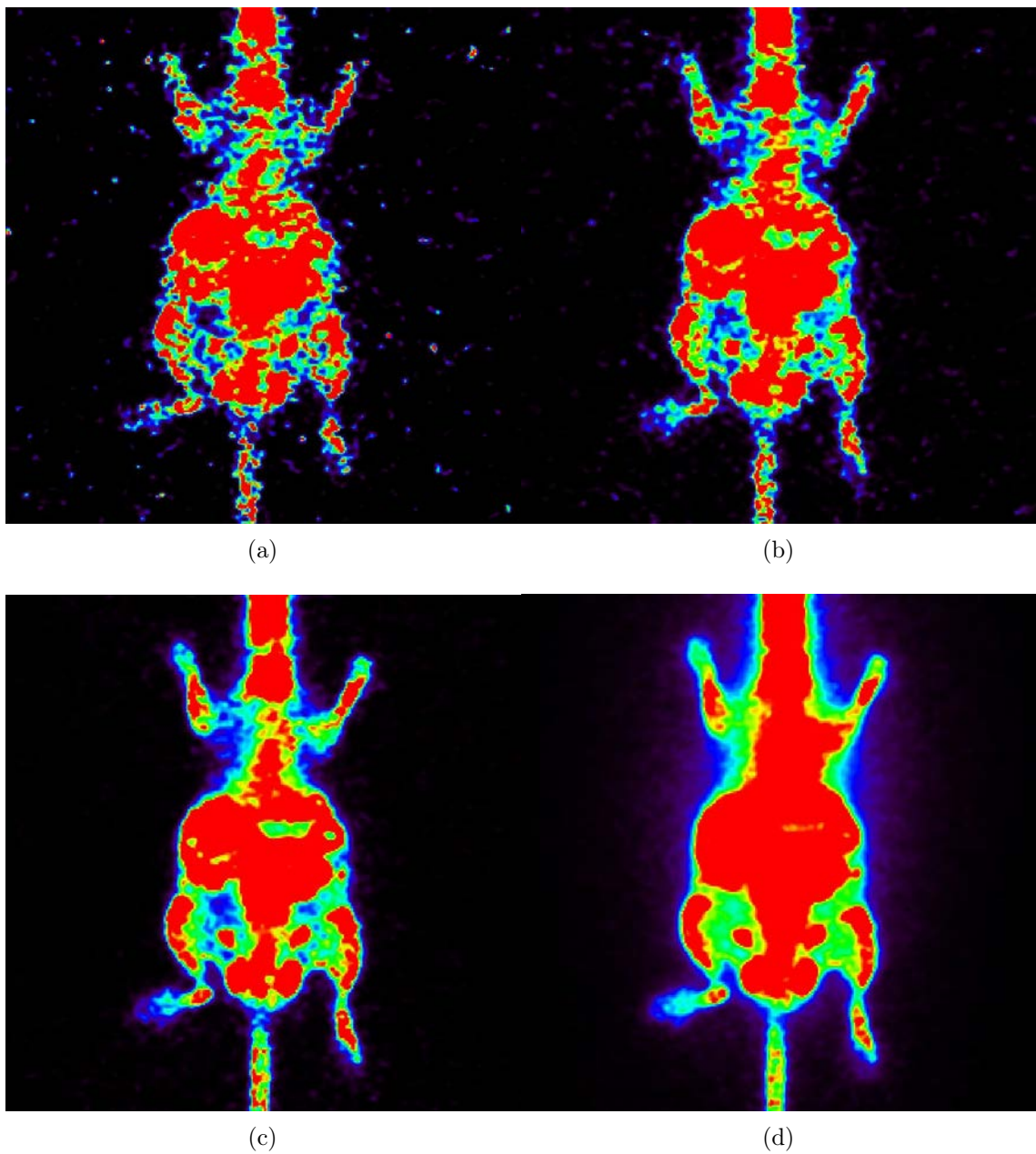


Fig. IX.11: Impact on image quality for the measured mouse scan corrected with different simulation statistics. In (a), 1M independent scattered coincidences (3%) were used, whereas in (b) 3M scattered coincidences (10%) and in (c) 30M scattered coincidences (100%) were used to generate the scatter estimate. All corrected images are compared to the uncorrected one (d).

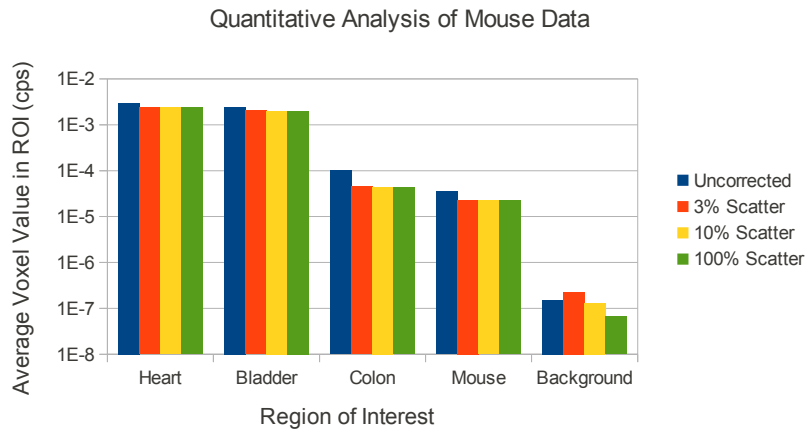


Fig. IX.12: Comparison of the signal intensity obtained within different ROIs of the reconstructed images. All ROIs were spheres within the labeled organs or, in the case of the mouse, a large cylinder. The background ROI is the whole image subtracted by the mouse cylinder. Image intensity is given by the average voxel value within the ROI.

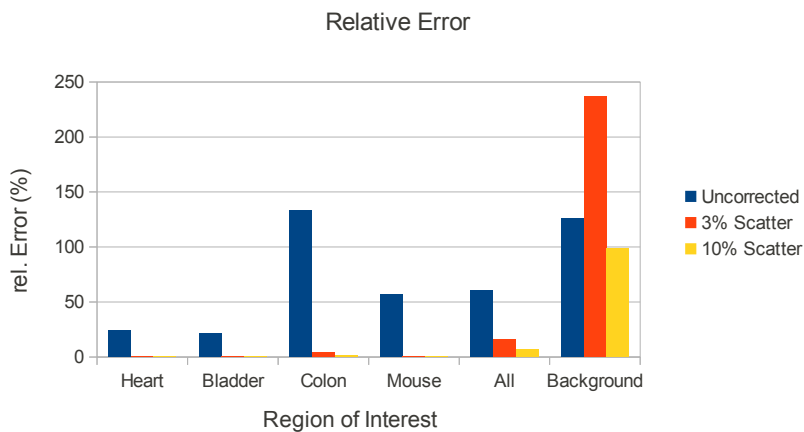


Fig. IX.13: Comparison of the relative error calculated in relation to the corrected image with 100% scatters, i.e., scattered coincidences are only mixed once in the dataset and no repeated walkthrough is necessary. All ROIs were spheres within the labeled organs or, in the case of the mouse, a large cylinder. The background ROI is the whole image subtracted by the mouse cylinder.

It is found that the simulations with 1M and 3M scattered coincidences are already sufficient to correct quantitatively hot regions like the heart or the bladder and even for cold regions the 1M data set only produces an error of 4%. However, the amount of scatter events in the background is very high for both corrections, with an error of 98% and 237% for the 3M and 1M data set, respectively. In comparison to the uncorrected image, the quantitative improvement for both corrections is remarkable.

From this analysis it can be concluded, in first approximation, that for ordinary mouse examinations, 3M simulated scattered coincidences⁹ would give sufficient statistics for a quantitative correction with an acceptable amount of background artifacts, which is very promising for the workload in clinical routine. If possible, corrections should nevertheless always rely on a simulation of comparable statistics to the measurement to reach at highest image quality.

IX.7 Discussion

In this chapter, methods for deriving scatter and random estimates for iterative image reconstruction were presented, and their feasibility was proven on simulated and measured data. The spatial distribution of random events can be obtained either from the measured data or from simulations, whereas the estimation of the spatial distribution from events which have scattered in the quadHIDAC is, so far, only possible with the Monte-Carlo approach presented here. It was observed that the impact of random events on quantitative image reconstruction is negligible for small objects like mice if the measured data is corrupted with moderate amounts of randoms of up to 80% (Fig. IX.3).

The random and scatter correction method introduced in Section VIII.3.5 was validated on several simulated phantoms, and perfect performance was observed on all investigated phantoms. At the end, the presented simulator was used with the voxelized event generator to produce scatter and random estimates for a real mouse scan. The corrected image exhibit a significant increase in signal to background ratio and quantitatively improved activity representations (Fig. IX.10).

In a simple statistical analysis (Section IX.6), it was observed that the scatter correction technique produces artifacts in the case that the number of simulated coincidences in the scatter estimate is too low (Fig. IX.11(a)). For the investigated mouse, it was observed that the amount of artifacts was substantially lowered if more than 3M simulated scattered coincidences were used in the reconstruction. However, the quantitative analysis showed that no remarkable effect is given in the hot regions like heart or bladder. For the cold region, e.g., colon, a quantitative overestimation below 5% was observed, whereas the activity in the background is even with 3M scattered coincidences overestimated by 98%. Thus, it is recommended that at least 3M scattered coincidences should be simulated for any mouse examination, with

⁹3M scattered coincidences correspond to a simulation of around 100M positron annihilations.

an image voxel edge length of 0.4 mm, to have an appropriate background activity representation in the images.

A further necessary quantity which needs to be determined is the number of measured coincidences that must be acquired to produce reliable corrections. It is suggested that for a direct determination of the necessary amount of measured and simulated coincidences, a more precise analysis with an appropriate simulation phantom is made, whereby the relative error induced by the event statistics can be absolutely quantified.

Overall, the `Geant4` simulator and the utilized correction technique show reliable quality for delivering quantitative images. It is possible to use the simulator in daily preclinical service, but the tool is relatively slow and needs detailed experience for erroneous operation. Therefore, a less complex simulation tool is currently under development which will generate the scatter estimates much faster and will be more user-friendly for operators.

Non-collinearity and Spatial Resolution

In this thesis, the commercial small animal PET scanner quadHIDAC, which is, up to now, one of the best preclinical PET scanners in terms of spatial resolution, was discussed in detail. The physical limitations for the spatial resolution were described in Section II.5. As positron range and non-collinearity have been implemented in the simulation code, it is now possible to examine which spatial resolutions the quadHIDAC geometry would be able to achieve with an improved intrinsic resolution of the scanner.

X.1 Simulation Setup

Single point sources are commonly used to investigate the spatial resolution performance of preclinical PET scanners. However, as it is time-consuming and difficult to determine the optimal number of iterations for the lowest FWHM of point sources in iterative image reconstruction, it was decided to examine a two source approach. It is assumed that this approach will pronounce the spatial resolution constraints more clearly and will give a fair comparison of different reconstruction techniques. The experimental setup for the study consists of two infinitesimal point sources which are placed within a water sphere at different distances along the trans-axial axis. The water sphere has a diameter of 2 cm and is positioned in the center of the FOV. The simulation output was processed by the list-mode file converter. This leads to a smearing of the registered interaction points onto 125 μm bins with a DOI resolution of 3.2 mm. In the simulations, 40M positrons were liberated at each source position,

and rotation of the detector heads was enabled. On the one hand, the simulation output was reconstructed with the 3D FBP algorithm, which is implemented in the software of the quadHIDAC terminal computer. On the other hand, the EM reconstruction algorithm from *EMrecon* (Section VIII.3) was used. The FBP applied a ramp filter, and the EM was iterated 400 times without the use of any subsets. The FOV was set in both reconstructions tools to $5 \times 5 \times 5 \text{ mm}^3$ and the edge length of the voxels to 0.1 mm to obtain high resolution images. Examples of the central slice of the reconstructed images are presented in Fig. X.1.

In the presented images, the distance of the sources was enlarged from 0.2 mm to 0.5 mm in 100 μm steps. The EM algorithm was used once without resolution recovery (Fig. X.1(b)) and once with resolution recovery with a *Gaussian* convolution kernel with a FWHM of 0.3 mm (Fig. X.1(c)). From the visual inspection, no reconstruction technique was able to resolve the two sources which were separated by 0.2 mm. For the 0.3 mm source separation, it is difficult to distinguish the sources in the FBP reconstructed image and in the EM reconstructed image without resolution recovery. The EM with resolution recovery is instead able to separate both sources quite well. For larger source distances in all reconstructions, it is possible to separate the two sources by eye (Fig. X.1).

For a further study, the image and voxel size was further reduced when the FOV was set to $3 \times 3 \times 3 \text{ mm}^3$ and a voxel edge length to 0.05 mm was chosen. The comparison of the performance between the EM and FBP reconstructions on the simulation with a source distance of 0.3 mm is shown in Fig. X.2. It was observed that the quality of the EM reconstructed image with the reduced voxel size was improved further (Fig. X.2(a)), while the reconstruction with the FBP algorithm shows only poor results with a lot of artifacts (Fig. X.2(b)). As the FBP method has problems for higher resolutions, most probably given by *Fourier* binning limitations before reconstruction, in the following the former voxel size was retained for the analysis to be compatible with the FBP method. This is also worthwhile since reconstructions with too small voxel sizes require long processing time. However, later on, the influence of the voxel size for some selected setups will also be compared.

X.2 Analysis Method

As the visual inspection of images is a subjective analysis, the intention here is to compare a few systematic approaches. Following the *Rayleigh* criterion [DiM11] for

spatial resolution, two point sources shall be deemed to be resolved if the pixel value in the middle of two sources is below 73% of the maximum value of the two point sources. In the case of 3D images, the definition of a one-dimensional response function, which should fulfill the criteria, enables some freedom of choice for the analyst. In this context, the NEMA NU 4-2008 [NEM08] proposes for the spatial resolution

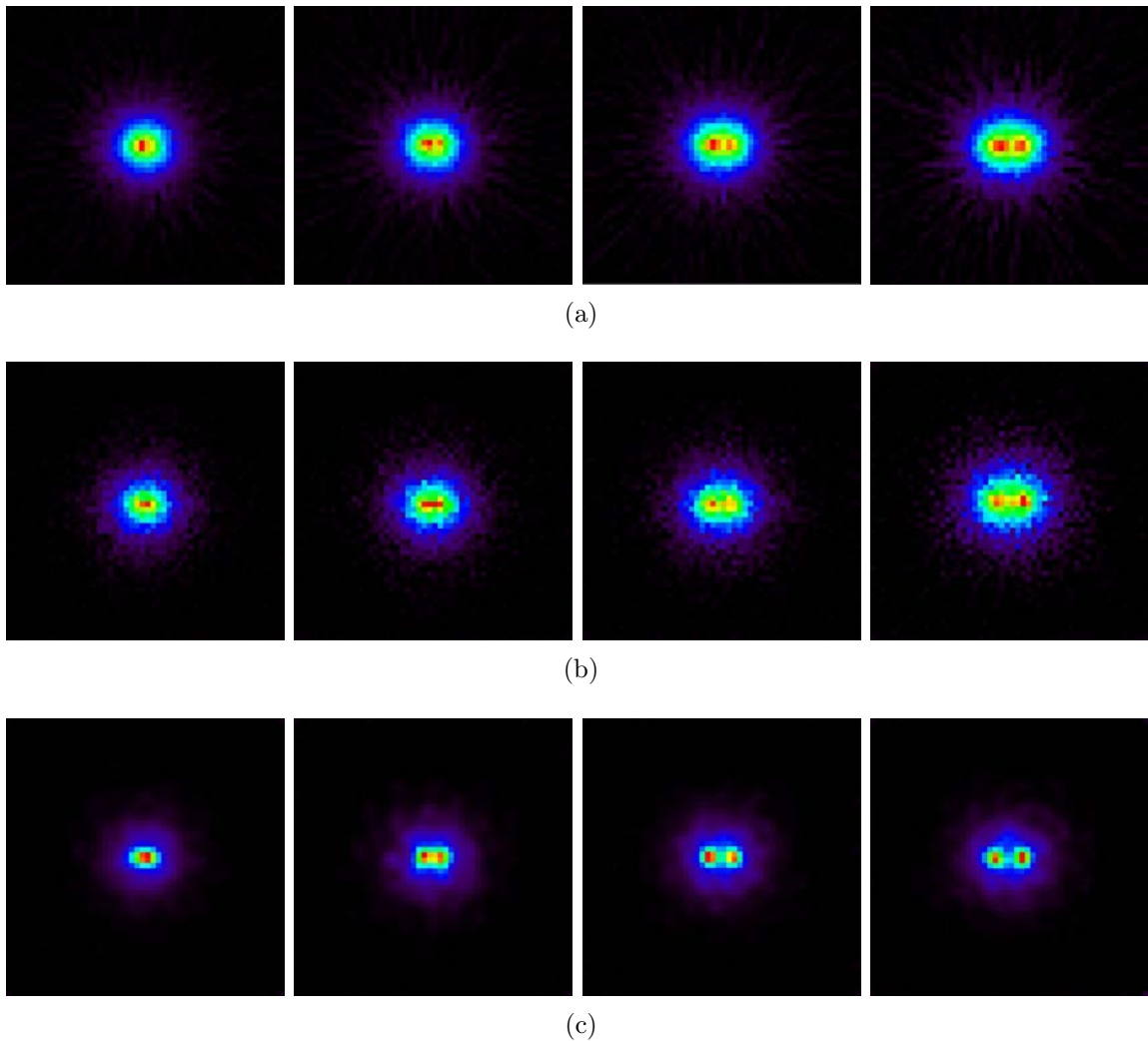


Fig. X.1: Reconstructed images obtained from two simulated infinitesimal ^{18}F point sources including non-collinearity and positron range. The sources are separated by distances from 0.2 mm to 0.5 mm and positioned symmetrically around the center of the FOV. Data are reconstructed by (a) filtered-back-projection, (b) expectation maximization algorithm without resolution recovery, and (c) with the EM algorithm with resolution recovery with a *Gaussian* convolution kernel with a FWHM of 0.3 mm. The edge length of a voxel was set to 0.1 mm and the FOV was reduced to $5 \times 5 \times 5 \text{ mm}^3$.

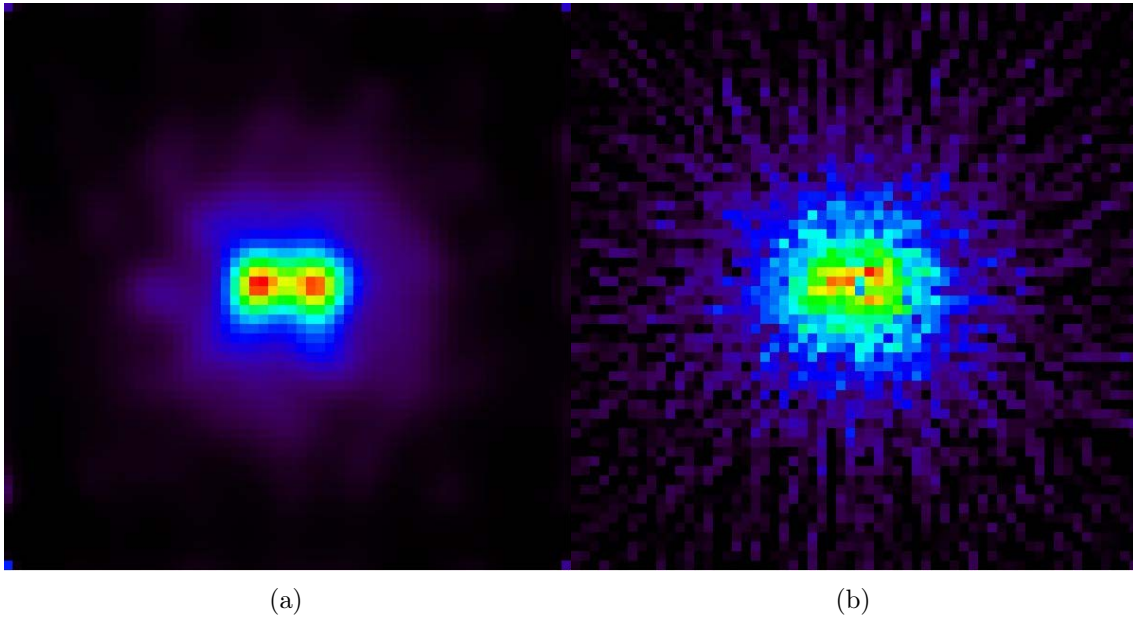


Fig. X.2: Comparison of an EM (a) and a FBP (b) reconstruction performed on the two infinitesimal point source simulation data with a source separation of 0.3 mm. Here, the edge length of a voxel was further reduced to 0.05 mm with a FOV of $3 \times 3 \times 3 \text{ mm}^3$. EM was performed with resolution recovery with a *Gaussian* convolution kernel with a FWHM of 0.3 mm.

analysis to project the pixel content from the central 2D slice image along the respective directions, whereby the projection should include at least two times the reconstructed FWHM of the point source in the direction transaxial to the direction of the measurement. In Fig. X.3, three different methods to generate an one-dimensional response function are compared on the data sets from the simulations with a point source separation of 0.5 mm and 0.8 mm, respectively. The reconstructions were repeated with the FBP, EM, and EM including resolution recovery with a *Gaussian* convolution kernel with a FWHM of 0.3 mm methods. In Fig. X.3(a), the line profile along the radial direction of the central voxels is illustrated. In Fig. X.3(b,c), instead, the radial one-dimensional response functions obtained from the 2D or 3D projections over the full reconstructed FOV of the respective slice or image are displayed. It is found that the resolution performance on the line profiles strongly depends on the chosen position which would produce highest resolution values that are not sufficiently concrete and meaningful in comparison with the different reconstruction methods. Both projection methods offer smoother response functions which are more adequate for a quantitative analysis. Nevertheless, the response functions from the

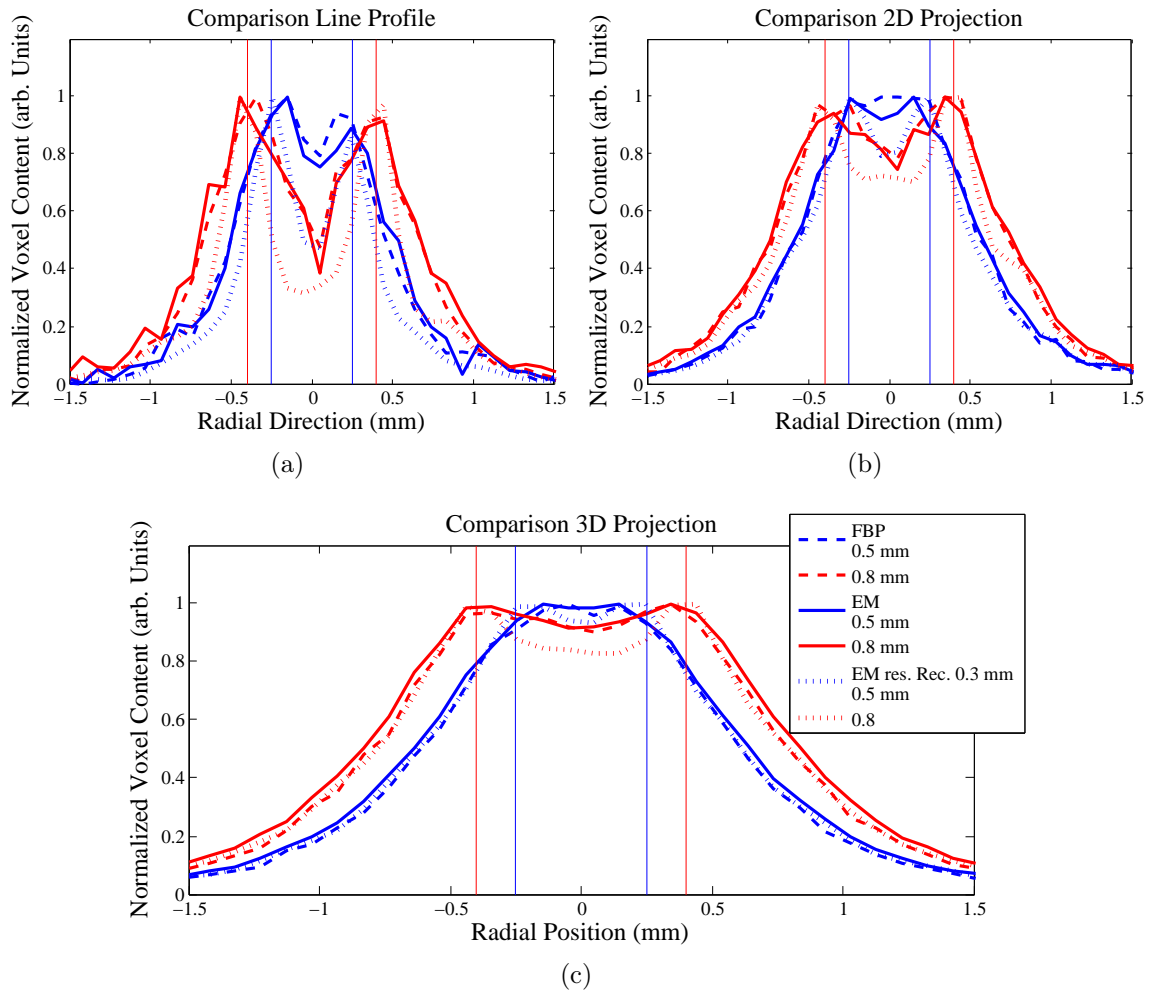


Fig. X.3: Comparison of different display methods of reconstructed images investigated for systematic resolution analysis from the two simulated infinitesimal point sources on 0.5 mm and 0.8 mm separation, respectively. The simulated data was reconstructed with the FBP, EM, and EM including resolution recovery with a *Gaussian* convolution kernel with a FWHM of 0.3 mm algorithms. In (a), the line profile along the x -axis of the central voxel is shown whereas the 2D and 3D projections of the central plane and the full image on the x -axis are displayed in (b) and (c), respectively. The vertical solid lines indicate the position of the simulated source positions.

3D projections presented in Fig. X.3(c) does not fulfill the *Rayleigh* criterion, not even for the source separation of 0.8 mm reconstructed with resolution recovery. Since in Fig. X.1(c) it is clearly visible that resolutions below 0.4 mm are possible, it was concluded that the 3D projection combined with the *Rayleigh* criterion does not provide demonstrative resolution values. Therefore, it was decided to continue the

analysis in the following with the 2D slice projections combined with the *Rayleigh* criterion.

X.3 Non-collinearity Model

In Section IV.2.2, it was mentioned that the quadHIDAC simulator was extended by the non-collinearity model from GATE and how the model is realized (source code Appendix Source Code A.1). In a first step, the data from a point source simulation was compared to a measured source in parallel projections. In the comparison, the distribution of the measurement was broader than the distribution of the simulation due to the higher detector resolution of the simulation (see Appendix Fig. A.2). For a qualitative comparison of the pure non-collinearity model, the simulated and measured data were subsequently analyzed at different radial distances whereby only coincidences were accepted in the case of a hit registrations in the three most inner or outer modules, respectively. The according module selection is displayed in Fig. X.4. Since the spatial resolution degradations given from positron range and



Fig. X.4: Module selection used for the qualitative non-collinearity model comparison. Simulations were made for all modules whereby only coincidences from the highlighted modules (lime-green) were accepted. In detail, only the innermost three or outermost three modules were used.

detector scatter are not dependent on the radial distance of the detector modules, thus, the pure difference induced by the non-collinearity model can be analyzed in the comparison. The result showed that the spatial resolution degradation from the inner to the outer modules in the simulation is around 100-150 μm smaller than in the measurement. Therefore, it was tried to tune the GATE non-collinearity model by double and triple the standard deviation of the 511 keV energy difference of the input generator of the model. The resulting axial projections from the calculated parallel projections of the coincidences for the different simulations and measurements are

presented in Fig. X.5. All the GATE based models show a different behavior compared

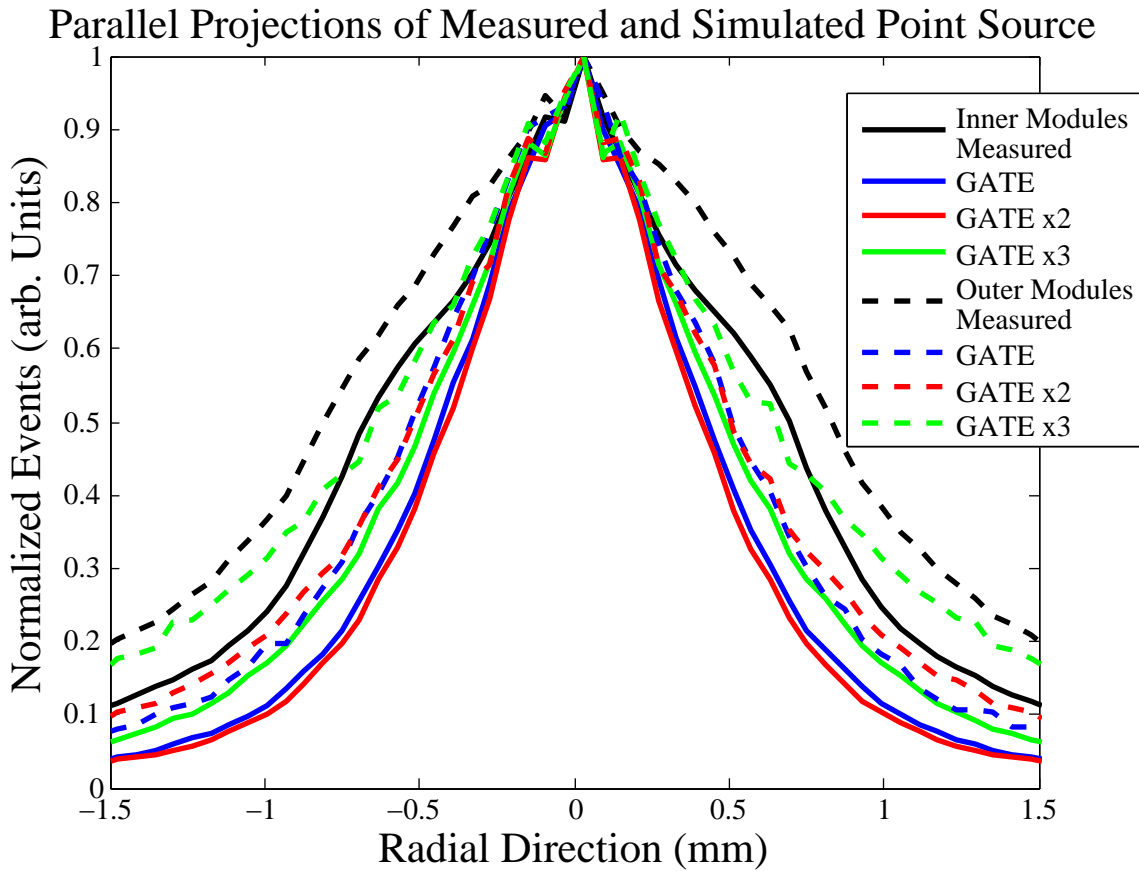


Fig. X.5: Comparison of parallel projections of simulated and measured point sources where on the one hand only the three most inner modules (solid lines), and on the other hand only the most outer modules (dashed lines) were considered. The non-collinearity model of GATE (blue) was tuned by double (red) or triple (green) the standard deviation of used random number generator. In the measurement, a nearly constant broadening of the distributions from the inner to the outer modules is observed whereas for all GATE models the distribution above 70% pixel intensity are approximately identical for both module setups. For lower intensity values, the distributions become larger for the outer modules.

to the measurement. In the measurement, the distribution from the outer modules is all over broader than the distribution from the inner modules, whereby the distribution is around $250 \mu\text{m}$ broader in the upper two thirds. For all the GATE based models no real broadening is observed in the upper third and is constantly growing in the lower two thirds.

From this, it was concluded that the GATE non-collinearity model is not an appropriate model for the examined sodium point source. Therefore, a simple non-collinearity

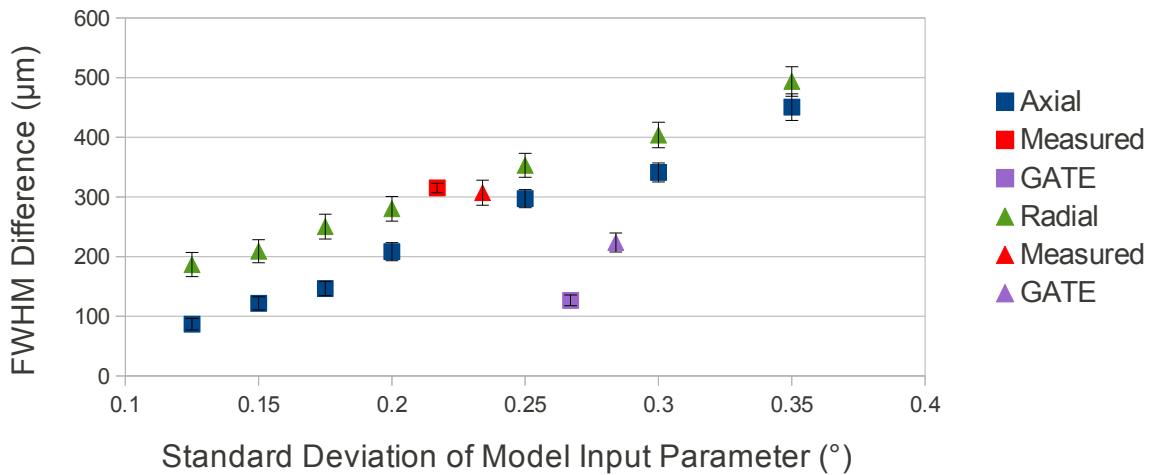


Fig. X.6: Analysis of the *Gaussian* non-collinearity model where the FWHM differences of the parallel projections of the outer and inner detector modules are plotted against the input parameter of the model. The FWHM values of the parallel projections are different for the radial and axial direction. The simulation output is also compared to a measured source and a simulation with the non-collinearity model of *GATE*. Remark: The measurements and the non-collinearity model of *GATE* does, of course, not depend on the input parameter, namely the standard deviation of the alternative model. The entries along the x -axis are thus arbitrary.

model was developed which does not affect the energy of annihilation photons. Instead, just three independent angles are sampled from a *Gaussian* distribution and one of the annihilation photons is turned around each space direction by one of the sampled angles (Appendix Source Code A.2). For a standard deviation of 0.3° , it was observed that the simulation gives qualitative similar results to the measurements. A significant distribution broadening in the upper third for the outer modules was also observed.

To refine the precision of the developed non-collinearity model, simulations with a variation of the input parameter, namely the standard deviation of the *Gaussian* distribution, from 0.125° to 0.2° in 0.025° steps and from 0.2° to 0.35° in 0.05° steps were done. For the data analysis, the simulated data is transformed into parallel projections which are subsequently projected in the radial or axial directions to obtain one-dimensional response functions. The response functions were fitted with *Gaussian* distributions and the resulting FWHMs from the outer three modules were subtracted from the FWHMs of the outer three modules. The outcome of this analysis is illustrated in Fig. X.6 where it is also compared to the standard *GATE* model and the measurement which were analyzed in the same way. It was found that in

the simulations the broadening effect is systematically more dominant in the radial direction with differences from around 30-100 μm whereas in the measurement no remarkable difference for the two different directions is observed. The best agreement between measurement and simulation is given for an input parameter of 0.25° which is, therefore, taken for the further examinations.

X.4 Analysis Results

The spatial resolution analysis was taken out for the FBP and the two EM image reconstruction techniques with the projection approach described in section X.2. The results are listed in Table X.1, whereby the values highlighted in red represent the lowest source separation in which the central value of the one-dimensional response function falls below the 73% limit of the *Rayleigh* criterion. The integration length of the projection orthogonal to the measurement direction was chosen to 2.4 mm, since this is double the spatial resolution reached, as the worst case, for the “new” alternative non-collinearity model with the EM reconstruction without resolution recovery. The FBP and EM without any forward modeling give similar results, whereby resolutions of 0.9 mm for the GATE model and 1.2 mm for the alternative model are reached. These values are similar to the FWHM of single sphere sources, and therefore the analysis method assigns comparable values like the method proposed by the NEMA NU 4-2008 standard (see also Appendix Fig. A.2). Thus, the presented values are very robust as well as a fair indicator for the spatial resolution performance, and it is very beneficial for comparisons that the FBP reconstruction and the EM reconstruction without forward modeling give comparable results. However, for real scanners, such analysis methods are not possible since measurements with infinitesimal point sources are impractical. For the iterative reconstruction with forward modeling, different FWHMs for the convolution kernel were utilized, whereby the best results are shown in Table X.1. Here, the GATE model achieves a spatial resolution of 0.5 mm and the alternative model of 0.8 mm.

It should be remarked that for infinite detector resolution, the EM¹ algorithm with resolution recovery is able to generate images where it is possible to visually resolve source separations even down to around 80 μm if simulated with the GATE model. Nevertheless, intrinsic detector resolutions below 125 μm will

¹The same analysis is not possible with the FBP algorithm since the software only accepts quadHIDAC list-mode data.

probably never be achieved in PET and, furthermore, the GATE model tends to provide too small opening angles. Therefore, it was decided that this topic will not be further evaluated here.

Since the new derived non-collinearity model seems to provide more realistic data, in the following two examinations only the new model was used.

TABLE X.1: Results of the spatial resolution analysis for simulations with different source separations reconstructed with different reconstruction techniques. Here, the GATE non-collinearity model is compared to the “new” alternative model. The last two columns compare the impact of the voxel size on the spatial resolution. The influence on the spatial resolution of further resolution recovery parameters are presented in Appendix TABLE A.1.

Source Separation	FBP		EM		EM Resolution Recovery		EM 0.3 mm Res.Rec. Diff. Voxel Size	
	GATE	New	GATE	New	GATE 0.4 mm Res.Rec.	New 0.8 mm Res.Rec.	GATE 50 ³ μm ³ Voxels	GATE 20 ³ μm ³ Voxels
	0.2 mm	100%	-	97.7%	-	97.6%	-	97.2
0.3 mm	100%	-	98.9%	-	98.6%	-	90.4	89.4%
0.4 mm	100%	-	95.7%	-	83.9%	-	75.1	75.1%
0.5 mm	96.9%	-	92.3%	-	67.7%	-	72.9%	70.8%
0.6 mm	94.2%	100%	87.0%	96.6%	60.2%	100.0%	70.0%	65.9%
0.7 mm	87.8%	98.8%	86.3%	94.8%	49.7%	86.8%	67%	64.4%
0.8 mm	83.3%	94.8%	81.5%	96.3%	53.9%	67.2%	64.7%	62.4%
0.9 mm	65.9%	99.5%	66.1%	98.5%	51.0%	53.2%	58.7%	54.2%
1.0 mm	-	85.9%	-	92.6%	-	40.9%	-	-
1.1 mm	-	77.6%	-	82.0%	-	31.8%	-	-
1.2 mm	-	70.1	-	72.8%	-	24.3%	-	-

X.4.1 Scanner Geometry Variations on the Example of the Zebrafish

In a further examination, the spatial resolution improvement potential for a reduced FOV was analyzed. To visualize the effect of the improved resolution on a practical application, a computer tomography (CT) scan of a zebrafish was taken and the skeleton was segmented. The segmented image was then used as input for the simulation with the voxelmap generator. In a first approach, the upper and lower detector heads of the quadHIDAC were removed, and the separation of the two remaining heads was reduced from 17 cm to 4 cm. Images of the reconstructed data are presented in Fig. X.7. Within the simulation, the rotation of the heads was enabled and 720M positrons were liberated to achieve a high image quality. The simulated data was reconstructed with the EM algorithm including resolution

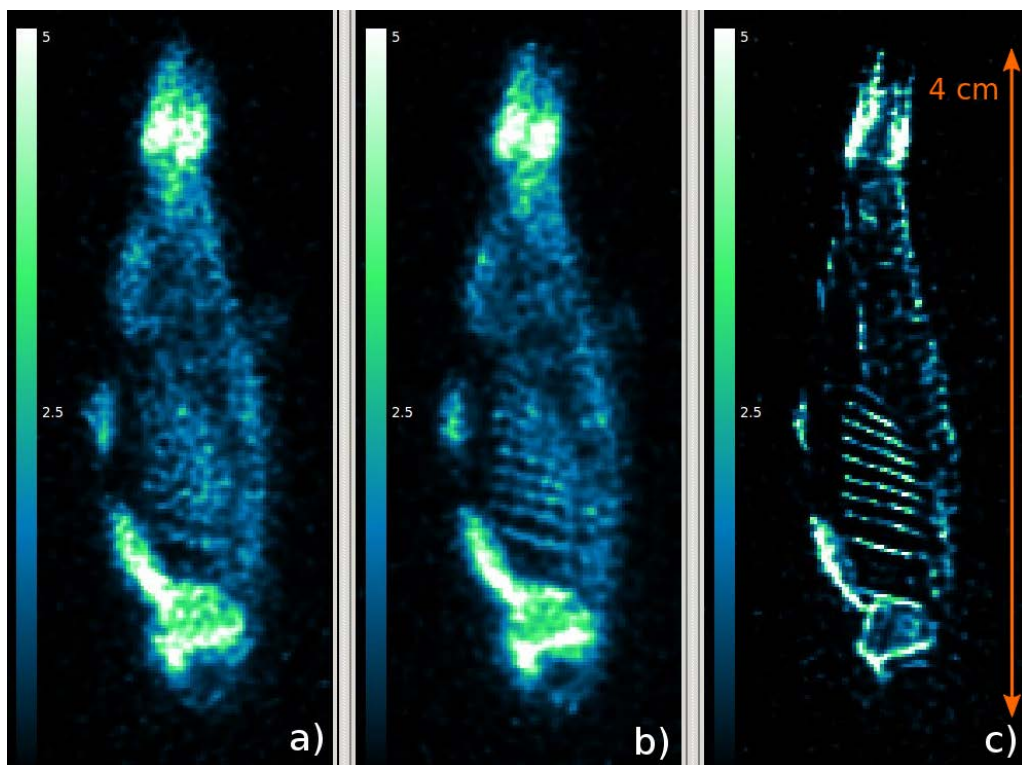


Fig. X.7: Reconstructed images from simulations based on a voxelmap of the segmented skeleton of a zebrafish, obtained from a CT scan. The voxel edge length is $200 \mu\text{m}$. In (a), the default setup of the HIDAC with two detector heads was used, while in (b) the central distance between the two heads was reduced from 17 cm to 4 cm. In the simulations, the derived alternative non-collinearity model and positron energy sampling from a ^{18}F source were enabled whereas they were disabled in (c).

recovery with a FWHM of 0.5 mm, 100 iterations, and a voxel edge length of 200 μm . It was found that the resolution is slightly improved for the smaller FOV whereby, especially, the small structures like the ribs of the zebrafish are distinguishable in the reduced FOV (Fig. X.7(b)) whereas only a noise scatter distribution is observed in the large FOV setup (Fig. X.7(a)). For clarification, the segmented input image was also simulated without the physical degradation factors and compared to the others (Fig. X.7(c)). Additionally, it was observed that the sensitivity of the reduced FOV setup is remarkably increased by 150%. Of course, the same amount of coincidences was used in image reconstruction to offer a fair comparison.

Anyway, the observation of increased sensitivity should motivate the further investigation of two detector head solutions. It is not unlikely that a concept with equally sized very large detector modules is also a promising option to reach high sensitivity. Nevertheless, rotational mode and large scale converter production are still very challenging for engineers and, therefore, precise determination of technical limitations are required.

In parallel projections from a point source simulation, it was observed that the FOV reduction brings a strong resolution improvement in the axial direction, whereas the increase is marginal in the radial direction. As it was expected that this behavior is related to the limited DOI information, the influence of increased DOI information was investigated. For simplicity, the same point source simulation was used and only the list-mode converter macro was adapted to extract only events where the photon interaction position is close to the center of converter positions. It was possible to obtain a radial resolution improvement similar to the axial improvement in the case that DOI information is restricted to 1 mm. Also in the zebrafish simulations, an improvement of the resolution was observed, especially in the head region, which is presented in Fig. X.8. Of course, the majority of coincidences are removed from the data for a strict DOI limitation. Thus, the simulation statistics were increased to 2.6G positron liberations, and all images were reconstructed with 19M coincidences for a fair comparison. These findings also motivate to reduce the converter thickness like it was supposed by the simulations in Section V.2.4 to build up a high sensitivity scanner. Furthermore, the presented results for the increased DOI information do not consider that thinner modules could be packed closer to the object, which would also lead to a smaller resolution degradation from the non-collinearity effect and reduces scattered events.

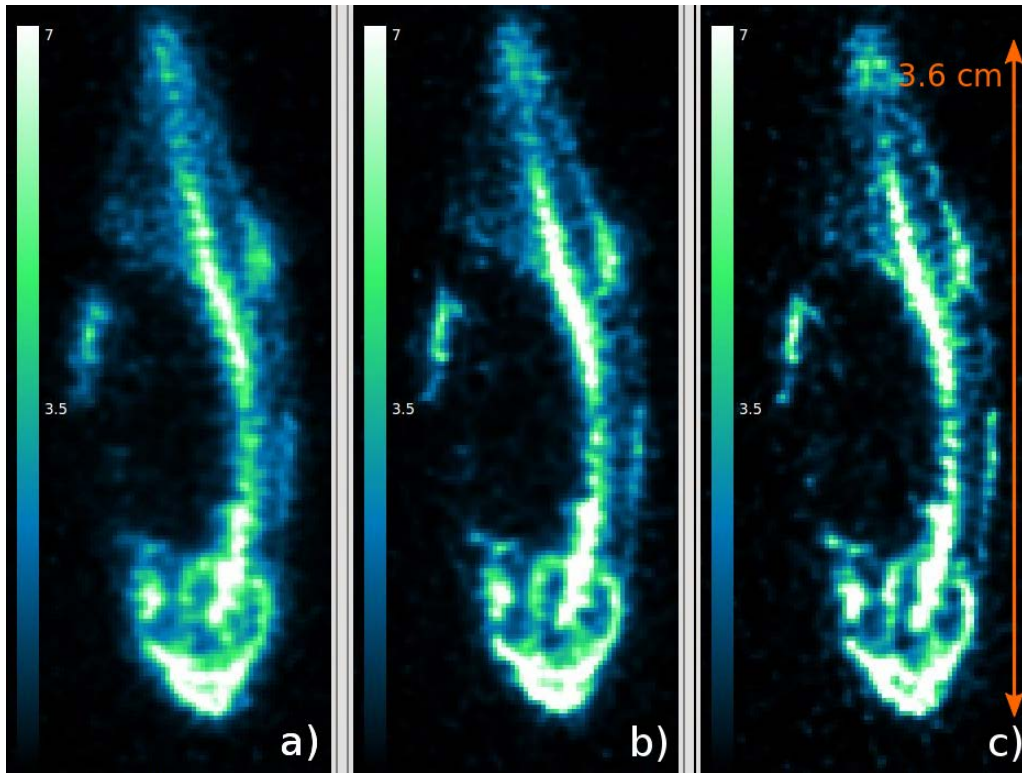


Fig. X.8: Effect of DOI information on reconstructed images from data produced in simulations with the zebrafish's skeleton as source volume. The HIDAC setup was, here, the same as for the reconstruction shown in Fig. X.7(b). Valid coincidences were constraint to have its single photon interactions in the range of 3.2 mm (full, (a)), 2 mm(b), and 1 mm(c) to the center of each converter position which means improved DOI information.

X.5 Discussion

In conclusion, the presented analysis method predicts spatial resolutions of quadHIDAC data, binned on $125 \mu\text{m}$ samples, between 1.2 to 0.5 mm which depends on the used non-collinearity model and the image reconstruction method. Concerning the derived non-collinearity model, it can be concluded that it provides more realistic data for a solid ^{22}Na source than the GATE model. However, if other sources are used, this does not have to be the case. Additionally, the new model gives more uniformly distributed data and represents a great tool to validate advanced image reconstruction strategies for the HIDAC which considers non-collinearity in the forward projection, in the future.

Overall, the analysis shows that spatial resolutions for small animal PET scanners far below 1 mm are realizable in the case that conventional forward modeling is ap-

plied. This motivates the development of scanner concepts, e.g. based on Micromesh detectors, with intrinsic resolutions below $200 \mu\text{m}$ and DOI resolutions of 1 mm. Furthermore, it turned out that no strong influence from scattered events on the spatial resolution is observed, which states that a scatter correction is only necessary to achieve quantitative imaging and not to improve spatial resolution.

At the end, it was also shown that systems with only two detector heads including very large scale HIDAC modules may also be an attractive possibility to establish a high sensitivity system.

CHAPTER XI

Summary

In the context of Molecular Imaging, preclinical PET scanners play an important role in human diagnostics and in improving our understanding of diseases and biological processes. Quantitative determination of tiny amounts of radio-activity within small objects requires high resolution complemented by high sensitivity. The physical background of limiting factors on spatial resolution and coincidence sensitivity were introduced (Chapter II), and details about the first sub-millimeter resolution preclinical PET scanner, the HIDAC, were described in this thesis (Chapter III). As the coincidence sensitivity of the HIDAC is rather moderate, the first subject of investigation was to study the sensitivity optimization potential of the HIDAC converter concept. The HIDAC photon converters consist of a stack of alternating conversion and insulation foils perforated with a dense matrix of holes.

First, photon conversion and detection probabilities for different converter geometries were systematically explored with a **Geant4** model of the HIDAC, which uses the Monte-Carlo methods introduced in Chapter IV. Additionally, new charge transport in gas and detection models were developed, and their results for different hole dimensions were combined with the conversion probability outcomes (Chapter V). It was revealed that with pure geometrical changes, but fixed extent and position of detector modules as well as fixed hole size, the coincidence detection efficiency can be increased by around 34%.

It was known before that smaller hole diameters lead to higher conversion probabilities [Got10], but if ionization and charge transport in gas are also taken into account, the examination demonstrates that a hole diameter reduction will not di-

rectly lead to increased coincidence sensitivity. However, following the predictions of the new models, an increased coincidence sensitivity can still be obtained if more and thinner converters are incorporated into the system. The sensitivity for converters with 500 μm diameter holes in an optimized hole geometry would be increased by 100% for the same amount of modules i.e., 32 modules, whereas an increase of 150% is expected for a system with 400 μm holes, 64 detector modules, and half converter thickness.

In a next step, it was explored whether the optimized converter hole patterns prospected by the simulations can be manufactured. Different production techniques were presented, whereby each technique has specific limitations to reach the desired geometry specifications. In conclusion, currently only etching, screen printing, and drilling are potential methods for producing large-scale converters. However, etching and screen printing still need further research and development to be practical.

Second, a test-bench was established to examine differently produced converter prototypes and to test the performance of newly developed readout electronics for the desired application (Chapter VI). It was possible to verify that the developer version of the SPADIC works well if coupled to a MWPC/HIDAC-converter detector setup. In this combination, the setup was able to detect the majority of ionization clusters. This was validated by exploring the impact of drift thickness on the count rate. Furthermore, it was demonstrated that the test-bench is able to distinguish relative efficiency differences of converter prototypes with a precision of around 10%, if it was equipped with an extra drift layer. Additionally, single-lead-layer-converters were investigated, whereby the relative count rate difference between structured and plain surfaces, predicted by simulations, was observed.

Third, as the production of photon converters is time consuming and expensive, it was investigated whether or not thin gas detectors with single-lead-layer-converters would be an alternative to the HIDAC converter design. Following simulations, those concepts potentially offer impressive coincidence sensitivities up to 24% for plain lead foils and up to 40% for perforated lead foils. This is an increase in performance of ten and 16, respectively, compared to the current HIDAC sensitivity. However, due to high costs for a large amount of detectors, the huge contribution of scatter events, and the inefficiency in first test measurements make these concepts less attractive (Chapter VII). Nevertheless, Micromesh detectors represent a state-of-the-art technology and are an alternative for the applied MWPC readout. The increased spatial resolution and high rate capability of this detector type combined with the potential to decrease the detector thickness is very promising for advanced HIDAC-

based PET imaging.

Fourth, compared to other PET scanner systems, the HIDAC concept suffers from missing energy information. Consequently, a substantial amount of scatter events can be found within the measured data. On the basis of the image reconstruction and correction techniques introduced in Chapter VIII, the influence of random and scatter events and their characteristics on several simulated phantoms were presented in Chapter IX. It was validated with the HIDAC simulator that the applied correction technique results in perfectly corrected images. Moreover, it was shown that the simulator is a credible tool to provide quantitatively improved images.

Fifth, a new model for the non-collinearity of the positronium annihilation was developed, since it was observed that the model implemented in the GATE simulator does not correspond to the measured observation. The input parameter of the new model was trimmed to match to a point source measurement. The influence of both models on the spatial resolution was studied with three different reconstruction methods (Chapter X). Furthermore, it was demonstrated that the reduction of converter depth, proposed for increased sensitivity, also has an advantage on the spatial resolution and that a reduction of the FOV from 17 cm to 4 cm (with only 2 detector heads) results in a remarkable sensitivity increase of 150% and a substantial increase in spatial resolution. The presented simulations for the spatial resolution analysis used an intrinsic detector resolution of $0.125 \times 0.125 \times 3.2 \text{ mm}^3$ and were able to reach fair resolutions down to 0.9-0.5 mm, which is an increase of a factor of around two compared to current commercial systems. This, combined with the further resolution improvement potential found for reduced FOVs and increased DOI information, motivates to further improve the detector resolution of real scanners to reach enhanced PET image quality.

XI.1 Outlook

As a conclusion of this project, building a second generation HIDAC scanner with improved spatial resolution and increased sensitivity is recommended. Following the results of this thesis, these aims can be achieved if thinner converters with $300 \mu\text{m}$ diameter holes are combined with Micromesh readout. In a first step, it would be important to find out which converter-mesh separation is needed for a high detector efficiency and to validate experimentally the presented ionization and transport models. These prerequisites are necessary to design the scanner layout

and to estimate the costs of a second generation HIDAC. Furthermore, it should be figured out which module sizes can be manufactured, e.g., in the screen print approach, and which sizes provide enough mechanical and electric stability for long-time operation and appropriate multiplex readout (i.e., channel reduction).

As the presented simulations showed that a simple FOV reduction with two detector heads leads to significantly improved spatial resolution and sensitivity improvements, this should also be validated experimentally. In the case of success, this would lead to the recommendation to further increase the sensitivity with larger equally-sized detector modules.

Another very promising path for improved high resolution imaging is advanced image reconstruction. It is assumed that appropriate resolution recovery with DOI and impinging angle dependent convolution kernels is able to improve the HIDAC performance. Especially the presented new non-collinearity extensions represent a perfect basis to validate such new concepts.

The work of this thesis was funded by the project B6 of the Sonderforschungsbereich 656 “Molecular Cardiovascular Imaging”. While the project is not being continued, sub-topics, e.g., screen printing and FOV reduction, will be continued by the EIMI and the Sonderforschungsbereich.

Zusammenfassung

In der molekularen Bildgebung spielen Kleintier-Positronen-Emissions-Tomographen eine wichtige Rolle in der Forschung für die menschliche Diagnostik und in der Verbesserung unseres Verständnisses über Krankheiten und biologischen Prozessen. Quantitative Bestimmung von winzigen Mengen an Radioaktivität in kleinen Objekten benötigt hohe Auflösung verbunden mit hoher Photonen-Nachweiswahrscheinlichkeit. Die physikalischen Grundlagen der begrenzenden Faktoren für die räumliche Auflösung und die 2-Photonen-Nachweiswahrscheinlichkeit wurden vorgestellt (Kapitel II) und Einzelheiten über den ersten hochauflösenden präklinischen *PET*-Tomographen mit einer Auflösung von unter einem Millimeter, dem *HIDAC*, wurden in dieser Arbeit beschrieben (Kapitel III). Da die 2-Photonen-Nachweiswahrscheinlichkeit des *HIDAC*s eher moderat ist, war das erste Thema die Erforschung des Potentials des *HIDAC*-Konverterkonzepts für die Optimierung der Photonen-Nachweiswahrscheinlichkeit. Die *HIDAC*-Photonen-Konverter bestehen aus einem Stapel von alternierenden Konversions- und Isolationsfolien, der mit einer dichten Matrix von Löchern perforiert ist.

Erstens: Die Photonen Konversions- und Detektionswahrscheinlichkeiten für verschiedene Konvertergeometrien wurden systematisch mit einem **Geant4** Modell erforscht, welches die Monte-Carlo Methoden benutzt, die in Kapitel IV vorgestellt wurden. Zusätzlich wurden neue Transportmodelle für geladene Teilchen in Gas und Detektionsmodelle entwickelt und ihre Vorhersagen für verschiedene Lochgrößen wurden mit den Ergebnissen für die Konversionswahrscheinlichkeit (Kapitel V) kombiniert. Es wurde festgestellt, dass reine geometrische Veränderungen, allerdings

mit festen Abmessungen und Positionen von den Detektormodulen sowie auch fester Lochgröße, die Koinzidenz-Detektionseffizienz um ungefähr 34% erhöhen können.

Es war bereits bekannt, dass kleinere Lochdurchmesser zu höheren Konversionswahrscheinlichkeiten führen [Got10]. Wenn hingegen Ionisation und Transportmodelle von geladenen Teilchen in Gas auch berücksichtigt werden, zeigt diese Studie, dass eine Durchmesserreduktion nicht direkt zu erhöhter 2-Photonen-Nachweiswahrscheinlichkeit führt. Allerdings kann nach den Vorhersagen des neuen Modells immer noch eine gesteigerte 2-Photonen-Nachweiswahrscheinlichkeit erreicht werden, wenn mehr und dünnere Konverter in das System integriert werden. Die Photon-Nachweiswahrscheinlichkeit für Konverter mit Lochdurchmessern von $500\ \mu\text{m}$ in einer optimierten Geometrie würde um 100% für die gleiche Anzahl von Modulen, d.h. 32 Module, gesteigert werden können, wohingegen eine Steigerung von 150% für ein System mit $400\ \mu\text{m}$ Löchern, 64 Detektormodulen und halber Konverterdicke erwartet wird.

In einem nächsten Schritt wurde erforscht, ob die optimierten Konverter-Lochmuster, empfohlen von den Simulationen, hergestellt werden können. Unterschiedliche Produktionstechniken wurden präsentiert, wobei jede Technik seine spezifischen Begrenzungen für die gewünschten Geometrie-Spezifikationen hat. Zusammenfassend kann man sagen, dass momentan nur das Ätzen, der Siebdruck und das Bohren potenzielle Methoden sind, um großflächige Konverter zu produzieren. Allerdings benötigen das Ätzen und der Siebdruck immer noch weitere Forschungs- und Entwicklungsarbeit um praktikabel zu sein.

Zweitens: Ein Prüfstand wurde errichtet, um unterschiedlich produzierte Konverter Prototypen zu untersuchen und um die Leistungsfähigkeit der neu entwickelten Ausleseelektronik für die gewünschte Anwendung zu testen (Kapitel VI). Es war möglich zu verifizieren, dass die Entwicklerversion des *SPADICs* gut funktioniert, wenn er mit dem Prüfstand für *HIDAC*-Konverter mit *MWPC*-Auslese verbunden ist. In dieser Kombination ist der Aufbau in der Lage die Mehrheit von Ionisationsclustern zu detektieren. Dies wurde validiert, indem der Einfluss von verschiedenen Driftabständen auf die Zählrate untersucht wurde. Des Weiteren wurde demonstriert, dass der Prüfstand in der Lage ist relative Effizienzunterschiede von Konverter-Prototypen mit einer Genauigkeit von ungefähr 10% abzugrenzen, wenn er mit einer extra Driftlage ausgestattet ist. Außerdem wurden Einzel-Blei-Lagen-Konverter untersucht, wobei der relative Zählratenunterschied zwischen strukturierten und glatten Oberflächen, vorhergesagt in Simulationen, beobachtet

werden konnte.

Drittens: Da die Produktion von Photonenkonvertern zeitaufwändig und teuer ist, wurde untersucht ob dünne Gasdetektoren mit Einzel-Blei-Lagen-Konvertern eine Alternative gegenüber dem *HIDAC*-Konverterdesign wäre. Nach Simulationsvorhersagen erlauben solche Konzepte potentiell eine beeindruckende 2-Photonen-Nachweiswahrscheinlichkeit bis zu 24% für glatte Bleifolien und bis zu 40% für perforierte Bleifolien. Das ist eine Leistungssteigerung von vergleichsweise 10 und 16 im Vergleich zu der jetzigen Photonen-Nachweiswahrscheinlichkeit des *HIDAC*s. Allerdings erscheint das Konzept wegen der hohen Kosten für eine große Menge von Detektoren, einem hohen Anteil an gestreuten Ereignissen und der Leistungsschwäche in den ersten Messungen weniger attraktiv (Kapitel VII). Dennoch repräsentieren Micromesh-Detektoren eine hochmoderne Technologie und sind eine Alternative zur verwendeten *DOI*-Auslese. Die verbesserte räumliche Auflösung und die Tauglichkeit für hohe Messraten dieses Detektortypen kombiniert mit dem Potential die Dicke der Detektormodule drastisch zu verringern ist sehr viel versprechend für zukunftsweisende *HIDAC*-basierte *PET*-Bildgebung.

Viertens: Im Vergleich zu anderen *PET*-Systemen, stellt das *HIDAC*-Konzept keine Energieinformation über gemessene Photonen bereit. Demzufolge befindet sich ein substanzieller Anteil an gestreuten Ereignissen in den gemessenen Daten. Auf der Basis von Bildrekonstruktions- und Korrekturmethode, die in Kapitel VIII vorgestellt wurden, wurde der Einfluss von Zufalls- und Streueignissen und ihre Charakteristik in mehreren simulierten Phantomen in Kapitel IX präsentiert. Es wurde mit dem *HIDAC*-Simulator validiert, dass die angewendete Korrekturtechnik perfekt korrigierte Bilder liefert. Darüber hinaus wurde gezeigt, dass der Simulator ein wertvolles Werkzeug ist, um quantitativ verbesserte Bilder zu liefern.

Fünftens: Ein neues Modell für die Nicht-Kollinearität der Positronen-Annihilation wurde entwickelt, da beobachtet wurde, dass das Modell, welches in dem *GATE* Simulator implementiert ist, nicht mit der gemessenen Beobachtung übereinstimmt. Der Eingangsparameter des neuen Modells wurde eingepasst, damit das Modell mit der Punktquellenmessung übereinstimmt. Der Einfluss der beiden Modelle auf die räumliche Auflösung wurde mit drei unterschiedlichen Rekonstruktionsmethoden (Kapitel X) bestimmt. Außerdem wurde demonstriert, dass die Reduzierung der Konverterdicke, vorgeschlagen für erhöhte Photonen-Nachweiswahrscheinlichkeit, auch einen Vorteil für die räumliche Auflösung hat, und dass eine Reduzierung des *FOVs* von 17 cm auf 4 cm (mit nur 2 Detektorköpfen) in einer bemerkenswerten Steigerung der Photonen-Nachweiswahrscheinlichkeit von 150% und einer

substanziellen Erhöhung der räumlichen Auflösung resultiert. Die präsentierten Simulationen für die räumliche Auflösungsanalyse verwendeten eine intrinsische Auflösung von $0.125 \times 0.125 \times 3.2 \text{ mm}^3$ und waren in der Lage gerechte Auflösungen runter bis 0.9-0.5 mm zu erreichen, was eine Verbesserung von einem Faktor von ungefähr zwei im Vergleich zu jetzigen kommerziellen Systemen ist. Dies, kombiniert mit dem weiteren Potential die Auflösung zu verbessern, indem reduzierte *FOVs* benutzt und präzisere Information über die *DOI* bestimmt werden, motiviert die Detektorauflösung von echten Tomographen weiter zu erhöhen, um eine verbesserte *PET*-Bildqualität zu erreichen.

XI.1 Ausblick

Als Fazit dieses Projekts wird der Bau eines *HIDAC*-Tomographen der zweiten Generation mit verbesserter räumlicher Auflösung und erhöhter Photonen-Nachweiswahrscheinlichkeit empfohlen. Folgt man den Ergebnissen dieser Arbeit, können diese Ziele erreicht werden, indem dünnere Konverter mit $300 \mu\text{m}$ Lochdurchmessern mit Micromesh-Auslese kombiniert werden. In einem ersten Schritt wäre es wichtig heraus zu finden, welche Separation von Konverter und Gitter nötig wäre, um eine hohe Detektoreffizienz zu erreichen und die präsentierten Ionisations- und Transportmodelle experimentell zu überprüfen. Diese Vorkehrungen sind notwendig, um den Tomographenaufbau zu konzipieren und um die Kosten für solch einen *HIDAC* der zweiten Generation abzuschätzen. Außerdem sollte ausgearbeitet werden, welche Modulgröße hergestellt werden kann, z.B. mit dem Siebdruckverfahren, und welche Ausmaße genug mechanische und elektrische Stabilität für den Langzeitbetrieb und eine angemessene Multiplexauslese (d.h. Reduktion von Auslesekanälen) liefern.

Da die präsentierten Simulationen zeigten, dass eine einfache Verkleinerung des *FOVs* mit zwei Detektorköpfen zu signifikanten räumlichen Auflösungs- und Nachweisverbesserungen führen, sollte dies auch experimentell bestätigt werden. Im Erfolgsfall wäre es zu empfehlen, die Photonen-Nachweiswahrscheinlichkeit weiter durch größere gleichartige Module zu erhöhen.

Ein weiterer sehr viel versprechender Ansatz für verbesserte hochauflösende Bildgebung ist eine weiterentwickelte Bildrekonstruktion. Es wird vermutet, dass eine angepasste Auflösungs-Wiederherstellung, mit Faltungskernen die von der *DOI* und dem Eintrittswinkel abhängig sind, in der Lage ist, die Ergebnisse des *HIDACs*

zu verbessern. Besonders die präsentierten Erweiterungen der Simulation mit dem Nicht-Kollinearitäts-Modell repräsentieren eine perfekte Basis, um solche neuen Konzepte zu validieren.

Die Arbeiten zu dieser Doktorarbeit wurden von dem Projekt B6 des Sonderforschungsbereich 656 „Molekulare kardiovaskuläre Bildgebung“ finanziert. Während das Projekt selbst nicht weiter gefördert wird, werden Teilprojekte, wie z.B. der Siebdruck und die Verkleinerung des *FOVs*, weiter im *EIMI* und im Sonderforschungsbereich verfolgt.

TABLE XI.1: A collection of some important acronyms:

Acronym	introduced	Explanation
ADC	p. 84	Analog-to-Digital Converter
AMIDE	p. 137	A Medical Imaging Data Examiner (Software)
ASCII	p. 22	American Standard Code for Information Interchange
ASIC	p. 83	Application-Specific Integrated Circuit
BGO	p. 97	Bismuth Germanium Oxide $\text{Bi}_4\text{Ge}_3\text{O}_{12}$
CBM	p. 2	Compressed Baryonic Matter
cdf	p. 37	cumulative distribution function
CdZnTe	p. 107	Cadmium Zinc Telluride
CERN	p. 57	Conseil Européen pour la Recherche Nucléaire
CLHEP	p. 35	A Class Library for High Energy Physics
cps	p. 147	counts per second
CT	p. 163	Computer Tomography
DIPE	p. 22	DIsoPropyl Ether $\text{C}_6\text{H}_{14}\text{O}$
EIMI	p. 15	European Institute for Molecular Imaging
EM	p. 121	Expectation Maximization
EMrecon	p. 125	Expectation-Maximization reconstruction
FBP	p. 25, p. 120	Filtered BackProjection
FDG	p. 142	FluDeoxyGlucose
FEM	p. 57	Finite Element Method
FOV	p. 1	Field-Of-View
FWHM	p. 25	Full Width at Half Maximum
FWTM	p. 25	Full Width at Tenth Maximum
GAMOS	p. 44	Geant4 -based Architecture for Medicine-Oriented Simulations
Garfield	p. 57	Simulation software for charge transport in “gas” within electric “fields”
GATE	p. 44	Geant4 based software for emission tomography

Acronym	Introduced	Explanation
GC	p. 10	Gas Chromatography
Geant4	p. 38	Geometry and tracking (Software)
GSI	p. 89	Gesellschaft für SchwerIonenforschung
HDDC	p. 19	High-Density Drift Chamber
HEP	p. 35	High Energy Physics
HIDAC	p. 1	HIgh-Density Avalanche Chamber
HPLC	p. 10	High Pressure Liquid Chromatography
HV	p. 81	High Voltage
IFAM	p. 76	Fraunhofer Institute for Manufacturing Technology and Advanced Materials
IKP	p. 85	Institut für Kernphysik
IPM	p. 70	Fraunhofer Institute for Physical Measurement Techniques
Kapton	p. 52	Polyimide from DuPont
LOR	p. 24, p. 119	Line-Of-Response
LSO	p. 107	Lutetium OxyorthoSilicate $\text{Lu}_2\text{Si}_3\text{O}_5$
LVDS	p. 98	Low-Voltage Differential Signaling
MAF	p. 46	Münster Analyzing Facility (Grid Cluster)
Micromega	p. 105	Micro mesh gas detector
MIP	p. 19	Minimum Ionizing Particle
MLCG	p. 34	Multiplicative Linear Congruential Generator
MPGD	p. 103	Micro Pattern Gas Detectors
MRD	p. 25	Maximum Ring Difference
MRI	p. 130	Magnetic Resonance Imaging
MWPC	p. 16	Multi-Wire Proportional Chamber
neBEM	p. 57	nearly exact Boundary Element Method (Software)
NEMA	p. 24	National Electrical Manufacturers Association
NIM	p. 98	Nuclear Instrumentation Module standard
OP-LMEM	p. 128	Ordinary Poisson List-Mode Expectation Maximization

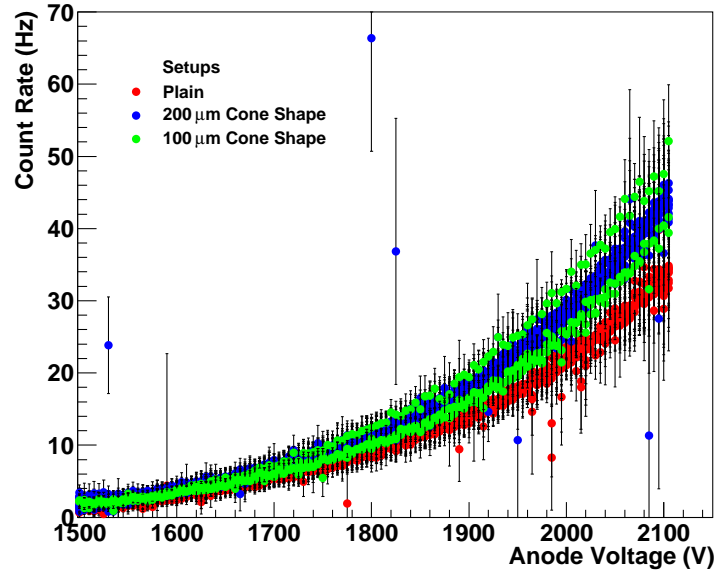
Acronym	Introduced	Explanation
OSEM	p. 125, p. 127	Ordered Subset Expectation Maximization
PASA	p. 88	Pulse Amplification and Sampling Asic
PCB	p. 47	Printed Circuit Board
pdf	p. 37	probability distribution function
PEEK	p. 81	PolyEther Ether Ketone
PET	p. 1	Positron Emission Tomography
PRF	p. 86	Pad Response Function
PRNG	p. 34	PseudoRandom Number Generator
RA	p. 33	Randomized Algorithm
RC	p. 141	Random Corrected
REM	p. 48	Raster Electron Microscope
RNG	p. 33	Random Number Generator
ROI	p. 137	Region-Of-Interest
ROOT	p. 36	Rapid Object-Orientated Technology (Software)
rpm	p. 68	rounds per minute
RS-LMEM	p. 128	Random and Scatter corrected List-Mode Expectation Maximization
sccm	p. 23	standard cubic centimeter per minute
SHC	p. 133	SHuffled half-Coincidences
SHS	p. 133	SHuffled Singles
SHV	p. 82	Safe High Voltage
SPADIC	p. 2	Self-triggered Pulse Amplification and Digitization asIC
ToF	p. 126	Time of Flight
TRD	p. 83	Transition Radiation Detector
TRIC	p. 15	Translational Research Imaging Center
TTL	p. 98	Transistor-Transistor Logic
USB	p. 85	Universal Serial Bus

APPENDIX A

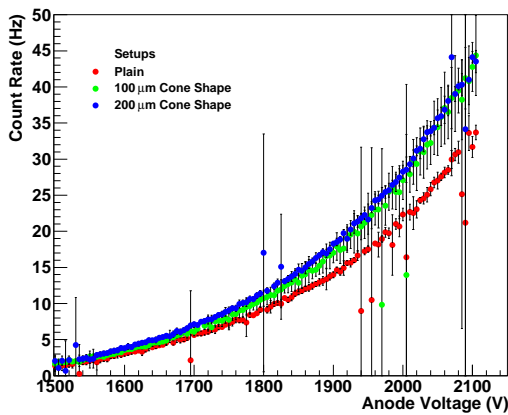
Appendix

TABLE A.1: Further results of the spatial resolution analysis for simulations with different source separations reconstructed with the EM reconstruction algorithm with resolution recovery.

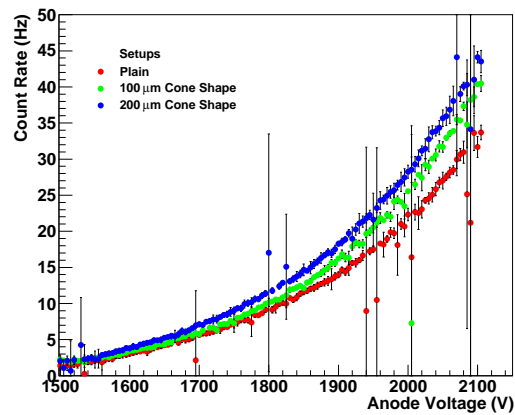
Source Separation	EM Resolution Recovery			
	GATE 0.3 mm Res.Rec.	GATE 0.4 mm Res.Rec.	GATE 0.5 mm Res.Rec.	GATE 0.8 mm Res.Rec.
0.2 mm	94.9%	97.6%	98.8%	99.7%
0.3 mm	95.1%	98.6%	99.1%	99.6%
0.4 mm	78.0%	83.9%	95.4%	100.0%
0.5 mm	78.4%	72.3%	78.5%	100.0%
0.6 mm	78.7%	60.2%	52.0%	88.2%
0.7 mm	70.7%	49.7%	38.9%	53.9%
0.8 mm	71.4%	53.9%	37.8%	28.6%
0.9 mm	62.6%	51.0%	33.2%	15.5%



(a)



(b)



(c)

Fig. A.1: In (a), an overlay of 20 count rate measurement series taken out under same conditions with plain and structured single layer lead converters are shown in which all measurements are shown compared to Fig. VI.11. The test setup was extended by a drift layer whereby a 3 mm thick drift volume with an electric field of 100 V/mm was applied. In (b), the average count rates from all measurements with each single layer converter prototype are presented where the error corresponds the standard deviation. In (c), the same plot is shown whereby the mismatching measurement trial was excluded.

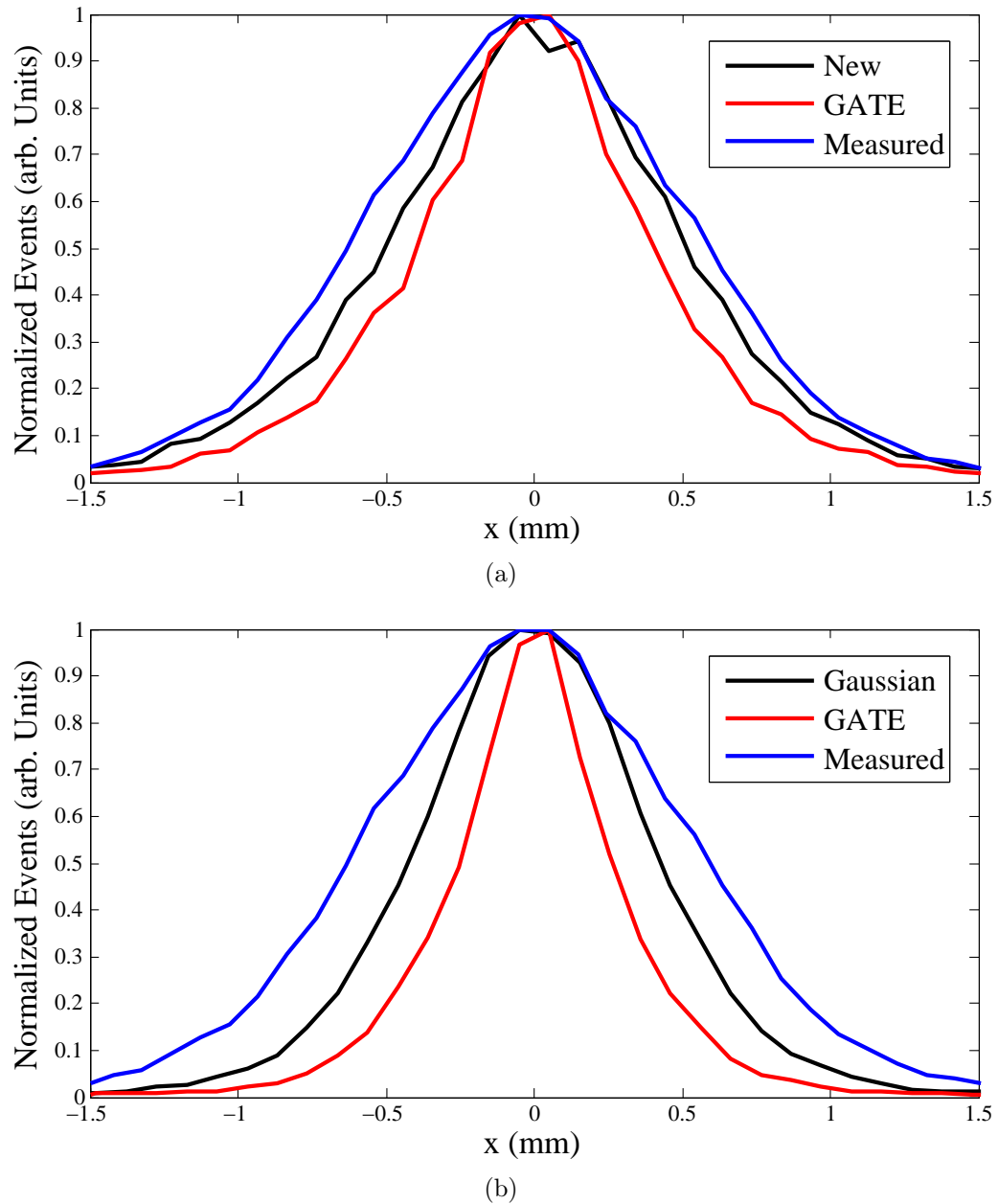


Fig. A.2: 2D slice projections from reconstructed point source simulations and measurements show the influence of the non-collinearity model from GATE and the “new” model developed in this thesis. The simulated data was reconstructed with EMrecon without resolution recovery, 400 iterations, a voxel edge length of $200 \mu\text{m}$, and a FOV of $5 \times 5 \times 5 \text{ mm}^3$. In (a), the measured spherical sodium point source with a diameter of $250 \mu\text{m}$ was modeled within the simulation whereas in (b) only an infinitesimal point source without positron range was simulated to present the pure influence of the non-collinearity.

```

G4VParticleChange* MyeplusAnnihilation::AtRestDoIt(const G4Track& aTrack,
                                                    const G4Step& )
{
  fParticleChange.InitializeForPostStep(aTrack);

  fParticleChange.SetNumberOfSecondaries(2) ;

  G4double r = CLHEP::RandGauss::shoot(0.,0.0011);

  G4double E1 = electron_mass_c2 + r;
  G4double E2 = electron_mass_c2 - r;

  G4double DeltaTeta = 2*r/0.511;

  G4double cosTeta = 2*G4UniformRand()-1. , sinTeta =
sqrt(1.-cosTeta*cosTeta);
  G4double Phi = twopi * G4UniformRand() ;
  G4double Phi1 = (twopi * G4UniformRand())/2. ;
  G4ThreeVector Direction (sinTeta*cos(Phi), sinTeta*sin(Phi), cosTeta);

  G4ThreeVector DirectionPhoton (sin(DeltaTeta)*cos(Phi1),
sin(DeltaTeta)*sin(Phi1),cos(DeltaTeta));
  DirectionPhoton.rotateUz(Direction);

//      G4cout<<"GammaDirection1 " <<DirectionPhoton<<G4endl;
//      G4cout<<"GammaDirection2 " <<Direction<<G4endl;

  fParticleChange.AddSecondary( new G4DynamicParticle (G4Gamma::Gamma(),
                                                    DirectionPhoton, E1) );

  fParticleChange.AddSecondary( new G4DynamicParticle (G4Gamma::Gamma(),
                                                    -Direction, E2) );

  //fParticleChange.ProposeLocalEnergyDeposit(0.);

  // G4double cosdev;
  // G4double dev;

  // Kill the incident positron
  //
  fParticleChange.ProposeTrackStatus(fStopAndKill );

  return &fParticleChange;
}

//....ooo00000ooo.....ooo00000ooo.....ooo00000ooo.....ooo00000ooo....

```

Source Code A.1: Non-colinearity model of GATE

```

G4VParticleChange* MyeplusAnnihilation::AtRestDoIt(const G4Track& aTrack,
                                                    const G4Step& )
{
  fParticleChange.InitializeForPostStep(aTrack);

  fParticleChange.SetNumberOfSecondaries(2);

  G4double cosTeta = 2.*G4UniformRand()-1. , sinTeta = sqrt(1.-cosTeta*cosTeta);
  G4double phi     = twopi * G4UniformRand();
  G4ThreeVector direction (sinTeta*cos(phi), sinTeta*sin(phi), cosTeta);
  //G4cout<<"Gamma Momentum direction angle "<< phi<<G4endl;
  G4double rndm_X = (CLHEP::RandGauss::shoot(0.,0.25)*twopi/(360));
  G4double rndm_Y = (CLHEP::RandGauss::shoot(0.,0.25)*twopi/(360));
  G4double rndm_Z = (CLHEP::RandGauss::shoot(0.,0.25)*twopi/(360));

  fParticleChange.AddSecondary( new G4DynamicParticle (G4Gamma::Gamma(),
                                                       direction, electron_mass_c2) );

  //G4cout<<"Direction1"<<direction<<G4endl;
  direction.rotateX(rndm_X);
  direction.rotateY(rndm_Y);
  direction.rotateZ(rndm_Z);
  fParticleChange.AddSecondary( new G4DynamicParticle (G4Gamma::Gamma(),
                                                       -direction, electron_mass_c2) );

  //G4cout<<"Direction2"<<-direction<<G4endl;
  // Kill the incident positron
  //
  fParticleChange.ProposeTrackStatus(fStopAndKill);
  return &fParticleChange;
}

//....ooo00000ooo.....ooo00000ooo.....ooo00000ooo.....ooo00000ooo....

```

Source Code A.2: "New" non-collinearity model with 0.25° as input parameter

Bibliography

- [A⁺08] Claude Amsler et al. Review of particle physics. *Phys. Lett.*, B667:1, 2008.
- [AA⁺03] S. Agostinelli, J. Allison, et al. Geant4 - a simulation toolkit. *Nuclear Instruments and Methods in Physics Research Section A: Accelerators, Spectrometers, Detectors and Associated Equipment*, 506(3):250–303, 2003.
- [AA⁺13] S. Agostinelli, J. Allison, et al. Geant4 9.2 - physics reference manual, 2013.
- [AFP10] T. Armbruster, P. Fischer, and I. Peric. Spadic - a self-triggered pulse amplification and digitization asic. In *IEEE NSS Conference Record*, pages 1358–1362, Oct 2010.
- [Ams07] Claude Amsler. *Kern- und Teilchenphysik*. UTB Uni-Taschenbücher, Stuttgart, 2007.
- [ARC⁺08] P Arce, P Rato, M Cañadas, JI Lagares, et al. GAMOS: An easy and flexible framework for Geant4 simulations. In *2008 IEEE: Nuclear Science Symposium, Medical Imaging Conference and 16th Room Temperature Semiconductor Detector Workshop, Dresden, Germany*, pages 19–25, 2008.
- [Arm13] T. Armbruster. *SPADIC - a Self-Triggered Detector Readout ASIC with Multi-Channel Amplification and Digitization*. PhD thesis, Ruperto-Carola University of Heidelberg, 2013.
- [Ber11] J. Bersch. Development of small animal pet detectors based on multi-wire proportional chambers. Master’s thesis, Westfälische Wilhelms-Universität Münster, 2011.

- [Bia89] S.F. Biagi. A multiterm boltzmann analysis of drift velocity, diffusion, gain and magnetic-field effects in argon-methane-water-vapour mixtures. *Nuclear Instruments and Methods in Physics Research Section A: Accelerators, Spectrometers, Detectors and Associated Equipment*, 283(3):716 – 722, 1989.
- [BKL⁺05] D. Brasse, P.E. Kinahan, C. Lartizien, C. Comtat, M. Casey, and C. Michel. Correction methods for random coincidences in fully 3d whole-body PET: impact on data and image quality. *Journal of nuclear medicine*, 46(5):859–867, 2005.
- [Bol10] K. Bolwin. Aufbau eines Teststandes zur Evaluierung von Vieldraht-Proportionalkammern einer quadHIDAC PET Kamera in Hinsicht auf Alterung und Wiederherstellung. Master’s thesis, Fachhochschule Münster, 2010.
- [Bol13a] Konstantin Bolwin. Evaluierung eines Siebdruckverfahren zur Herstellung eines Konverters zur Detektion von gamma-Quanten mit einer Vieldraht-Proportionalkammer für die Positronen-Emission-Tomographie. Master’s thesis, FH Steinfurt, 2013.
- [Bol13b] Konstantin Bolwin. Private Communication, 2013.
- [BR97] R. Brun and . Rademakers. ROOT-An Object Oriented Data Analysis Framework. *Nucl. Instr. and Meth.*, A389:81–86, 1997. <http://root.cern.ch/>.
- [BRR08] W. Blum, W. Riegler, and L. Rolandi. *Particle Detection with Drift Chambers*, volume 2nd Edition. Springer, 2008.
- [Bus12] A. Busch. Inbetriebnahme eines Konverterteststandes für die PET. Master’s thesis, WWU Münster, 2012.
- [BWW01] K. Bethge, G. Walter, and B. Wiedemann. *Kernphysik*. Springer-Verlag, 2001.
- [CD06] S.R. Cherry and M. Dahlbom. *PET:Physics, Instrumentation and Scanners*. Springer-Verlag, 2006.
- [CEF⁺84] BE Cooke, AC Evans, EO Fanthome, R Alarie, and AM Sendyk. Performance figure and images from the thescan 3128 positron emission tomograph. *IEEE Trans. Nucl. Sci.*, 31(1):640–644, 1984.

- [Che01] S. R. Cherry. Fundamentals of positron emission tomography and applications in preclinical drug development. *Journal of clinical pharmacology*, 41(5):482–491, May 2001.
- [CRC05] P.L. Chow, F.R. Rannou, and A.F. Chatziioannou. Attenuation correction for small animal PET tomographs. *Phys Med Biol*, 50(8):1837–1850, Apr 2005.
- [DED⁺04] A. Divoli, K. Erlandsson, J. Dickson, M.A Flower, and R. Ott. Estimation of random coincidences from the prompt PET data. In *IEEE NSS Conf. Rec.*, volume 6, pages 3703–3707. IEEE, 2004.
- [Dem11] V. Demchik. Pseudo-random number generators for monte carlo simulations on ati graphics processing units. *Computer Physics Communications*, 182:692–705, 2011.
- [DiM11] Charles A. DiMarzio. *OPTICS for Engineers*. CRC Press Taylor and Francis Group, 2011.
- [DJS12] M. Dawood, X. Jiang, and K. Schäfers. *Correction Techniques in Emission Tomography*. CRC Press Taylor and Francis Group, 2012.
- [FHJ⁺76] N. Ford, Z. Hajduk, A. P. Jeavons, B. Lindberg, and C. Parkman. Two-dimensional proportional chamber readout using digital techniques. *IEEE Trans. Nucl. Sci.*, 23, 1976.
- [FHK⁺11] B. Friman, C. Hoehne, J. Knoll, S. Leupold, J. Randrup, R. Rapp, and P. Senger, editors. *The CBM Physics Book - Compressed Baryonic Matter in Laboratory Experiments*. Springer, 2011.
- [Fro12] Lynn Frohwein. Entwicklung und Optimierung eines 3D-Tracking-Systems zur Untersuchung von freilaufenden Mäusen in der Positronen-Emissions-Tomographie unter Berücksichtigung verhaltensbeeinflussender Faktoren. Master’s thesis, University of Applied Sciences Münster, 2012.
- [GBM⁺12] A.L. Goertzen, Q. Bao, Bergeron M., et al. NEMA NU 4-2008 Comparison of Preclinical PET Imaging Systems. *Jour. of Nucl. Med.*, 53:1300–1309, 2012.

- [GKV⁺13] H. Gottschlag, T. Kösters, D. Vernekohl, K. Reygers, K. Schäfers, F. Wübbeling, and J. Wessels. Towards Quantitative Image Reconstruction Using Monte-Carlo Simulations in Multi-Wire Proportional Chamber-Based Small Animal PET. *IEEE Trans. Nucl. Sci.*, 60:3343–3354, 2013.
- [GLOS79] E. Gatti, A. Longoni, H. Okuno, and P. Semenza. Optimum Geometry for Strip Cathodes or Grids in MWPC for Avalanche Localization along the Anode Wires. *Nucl. Instr. and Meth.*, 163:83–92, 1979.
- [GMS⁺11] Y Gu, J.L Matteson, R.T. Skelton, A.C. Deal, E.A. Stephan, F. Dutweiler, T.M. Gasway, C.S. Levin, et al. Study of high-resolution, 3D positioning cadmium zinc telluride detector for PET. *Phys. Med. Biol.*, 56:1563–1584, 2011.
- [GOA⁺06] Giomataris, Oliveira, Andriamonje, Aune, Charpak, Colas, Giganon, Rebougeard, Salin, et al. Micromegas in a Bulk. *Nucl.Instrum.Meth. A*, 560:405–408, 2006.
- [Got10] H. Gottschlag. *Small Animal Positron Emission Tomography with Multi-Wire Proportional Counters*. Dissertation, Institut für Kernphysik, 2010. <http://d-nb.info/1007715235>.
- [Hei53] W. Heitler. *The Quantum Theory of Radiation*, volume Third Edition. Oxford University Press, 1953.
- [Hol92] E. Holzschuh. Measurement of the neutrino mass from tritium beta-decay. *Reports on Progress in Physics*, 55:1035–1091, 1992. ISBN 0034-4885.
- [HSMV12] V.M. Hannen, S. Streubel, J. Mader, and D. Vernekohl. *MiniPET - Experiment to demonstrate positron-emission-tomography*. WWU Münster, Institut für Kernphysik, May 2012.
- [Hub99] J. H. Hubbell. Review of photon interaction cross section data in the medical and biological context. *Phys. Med. Bio.*, 44:R1–R22, 1999.
- [Hün07] H. Hünteler. Development and Evaluation of a Multiwire Proportional Chamber for a High Resolution Small Animal PET Scanner. Diplomarbeit, Institut für Kernphysik, 2007.

- [Jam90] F. James. A review of pseudorandom number generators. *Computer Physics Communications*, 60(3):329–344, 1990.
- [JB00] A Jeavons and P Bloomfield. Quad-hidac, a next-generation pet camera for small-animal imaging. *IEEE Nuclear Science Symposium Conference Record*, 3, 2000.
- [JCS75] A. P. Jeavons, G. Charpak, and R. J. Stubbs. The high-density multiwire drift chamber. *Nuclear Instruments and Methods*, 124(2):491–503, 1975.
- [JSS⁺04] S Jan, G Santin, D Strul, S Staelens, et al. GATE: a simulation toolkit for PET and SPECT. *Physics in Medicine and Biology*, 49(19):4543, 2004.
- [Kae01] JH Kaempf. *Study of the detection efficiency of the small animal PET camera Quad-HIDAC*. PhD thesis, Diploma Thesis, University of Lausanne, Lausanne, 2001.
- [KB09] M. Klein-Boesing. Development of a Transition Radiation Detector and Reconstruction of Photon Conversions in the CBM Experiment. Dissertation, Institut für Kernphysik, 2009.
- [Kon10] A.B. Konik. *Evaluation of attenuation and scatter correction requirements in small animal PET and SPECT imaging*. PhD thesis, University of Iowa, 2010. <http://ir.uiowa.edu/etd/691>.
- [Kös11] T. Kösters. EMrecon: An Expectation Maximization Based Image Reconstruction Framework for Emission Tomography Data. *NSS/MIC Conference Record, IEEE*, pages 4365–4368, 2011.
- [KP11] F. Kiessling and B.J. Pichler. *Small Animal Imaging - Basics and Practical Guide*. Springer, 2011.
- [KT51] H. W. Kuhn and A. W. Tucker. Nonlinear programming. *Proc. Second Berkeley Symp. on Math. Statist. and Prob.*, pages 481–492, 1951.
- [Leo87] W.R. Leo. *Techniques for Nuclear and Particle Physics Experiments*. Springer-Verlag, 1987.
- [LG03] A.M. Loening and S.S. Gambhir. AMIDE: A Free Software Tool for Multimodality Medical Image Analysis. *Molecular Imaging*, 2(3):131–137, 2003.

- [LH99] C. Levin and J. Hoffmann. Positron range and its effect on the fundamental limit of positron emission tomography system spatial resolution. *Phys. Med. Biol.*, 44:781–799, 1999.
- [Mar68] G. Marsaglia. Random numbers fall mainly in the planes. *Proc. Natl. Acad. Sci.*, 61:25–28, 1968.
- [MF84] E. Mathieson and J.S. Fordon. Cathode Charge Distributions in Multi-wire Chambers. *Nucl. Instr. and Meth.*, 227:267–282, 1984.
- [MK79] T. Mayer-Kuckuk. *Kernphysik*. Teubner Studienbücher, 1979.
- [MM02] E. Zio M. Marseguerra. *Basics of the Monte Carlo Method with Application to System Reliability*. LiLoLe-Verlag, 2002. ISBN 3-934447-06-6.
- [MM06] N. Majumdar and S. Mukhopadhyay. Simulation of three-dimensional electrostatic field configuration in wire chambers: A novel approach. *Nucl. Inst. Meth. Phys. Res. Sec. A*, 566(2):489–494, 2006.
- [Mül13] J. Müller. *Bregmanized (Higher Order) Total Variation and Application in PET*. PhD thesis, WWU Münster, 2013.
- [Mus95] G. Musiol. *Kern- und Elementarteilchenphysik*. Deutsch, 1995.
- [MZH⁺04] J. Missimer, M. Zoltan, M. Honer, et al. Performance evaluation of the 16-module quad-HIDAC small animal PET camera. *Phys. Med. Biol.*, 49:2069–2081, 2004.
- [MZT90] G. Marsaglia, A. Zaman, and W.W. Tsang. Toward a universal random number generator. *Statistics & Probability Letters*, 9(1):35 – 39, 1990.
- [NEM08] National Electric Manufacturers Association NEMA. Standards Publication NU 4-2008:Performance Measurement of Small Animal Positron Emission Tomographs. 2008. Rosslyn, VA: National Electrical Manufacturers Association.
- [NK29] Y. Nishina and O. Klein. Über die Streuung von Strahlung durch freie Elektronen nach der neuen relativistischen quantumelektrodynamik von Dirac. *Phys. Zeit.*, 52:853–868, 1929.
- [NTM⁺13] K. Nagy, M. Tóth, P. Major, et al. Performance Evaluation of the Small-Animal nanoScan PET/MRI System. *Jour. of Nucl. Med.*, 54:1–8, 2013.

- [NW01] F. Natterer and F. Wübbeling. *Mathematical methods in image reconstruction*. SIAM, Mathematical Modeling and Computation, 2001.
- [Obl01] P. Oblozinsky. Charged Particle Cross-Section Database for Medical Radioisotope Production: Diagnostic Radioisotopes and Monitor Reactions. IAEA TECDOC 1211, 2001.
- [RAB⁺02] A.J. Reader, S. Ally, F. Bakatselos, R. Manavaki, R.J. Walledge, A.P. Jeavons, P.J. Julyan, S. Zhao, D.L. Hastings, and J. Zweit. One-pass list-mode em algorithm for high-resolution 3-d PET image reconstruction into large arrays. *Nuclear Science, IEEE Transactions on*, 49(3):693–699, 2002.
- [RCB⁺05] A. Rahmim, J. Cheng, S. Blinder, M. Camborde, and V. Sossi. Statistical dynamic image reconstruction in state-of-the-art high-resolution PET. *Physics in medicine and biology*, 50:4887–4912, 2005.
- [RLR⁺04] A Rahmim, M Lenox, AJ Reader, C Michel, Z Burbar, TJ Ruth, and V Sossi. Statistical list-mode image reconstruction for the high resolution research tomograph. *Physics in medicine and biology*, 49:4239–4258, 2004.
- [Saw11] A. Sawatzky. *(Nonlocal) Total Variation in Medical Imaging*. PhD thesis, WWU Münster, 2011.
- [Sch01] H. Schröer. *Lichtstrom und Beleuchtungsstärke*. Wiss.-und-Technik-Verlag, 2001. Method Description: <http://www.rzuser.uni-heidelberg.de/~c07>.
- [Sch13] Klaus Schäfers. private communication, 2013.
- [SH10] O. Schober and W. Heindel. *PET-CT Hybrid Imaging*. Thieme, 2010.
- [Sid85] R.L. Siddon. Fast calculation of the exact radiological path for a three-dimensional CT array. *Med. Phys.*, vol.12:252–255, 1985.
- [SKLF14] T.J. Spinks, D. Karia, M.O. Leach, and G. Flux. Quantitative PET and SPECT performance characteristics of the Albira Trimodal pre-clinical tomograph. *Physics in Medicine and Biology*, 59:715–731, 2014.
- [SMP11] I. Szanda, J Mackewn, and G. Patay. National Electrical Manufacturers Association NU-4 performance evaluation of the PET component of the

- NanoPET/CT preclinical PET/CT. *Jour. Nucl. Med.*, 52:1741–1747, 2011.
- [SRK⁺05] K. P. Schafers, A. J. Reader, M. Kriens, C. Knoess, O. Schober, and M. Schafers. Performance evaluation of the 32-module quadhidac small-animal pet scanner. *Journal of nuclear medicine*, 46(6):996–1004, Jun 2005.
- [SV82] L.A. Shepp and Y. Vardi. Maximum likelihood reconstruction for emission tomography. *IEEE Trans. Med. Imaging*, 2:113–122, 1982.
- [SV94] J. Stanford and S. Vardeman. *Statistical Methods for Physical Science*, volume 28. 1st edition edition, 1994. ISBN 9780124759732.
- [TRD⁺05] Y.C. Tai, A. Ruangma, Rowland D., et al. Performance evaluation of the microPET Focus: a third-generation microPET scanner dedicated to animal imaging. *Jour. Nucl. Med.*, 46:455–463, 2005.
- [Val03] P. Valk. *Positron emission tomography: basic science and clinical practice*. London ; Springer, 2003.
- [VDB⁺09] E.P. Visser, J.A. Disselhorst, M. Brom, et al. Spatial Resolution and Sensitivity of the Inveon Small-Animal PET Scanner. *Jour. of Nucl. Med.*, 50:139–147, 2009.
- [Vee98] R. Veenhof. Garfield, recent developments. *Nuclear Instruments and Methods in Physics Research Section A: Accelerators, Spectrometers, Detectors and Associated Equipment*, 419(2–3):726–730, 1998.
- [Ver10] D. Vernekohl. Measurements with a multi-wire proportional chamber for small animal position emission tomography. Diploma thesis, Institut für Kernphysik, 2010. <http://qgp.uni-muenster.de/thesisdb/dipl-vern-10.pdf>.
- [WA04] M.N. Wernick and J.N. Aarsvold. *EMISSION TOMOGRAPHY, The Fundamentals of PET and SPECT*. Elsevier Inc., 2004.
- [WSB⁺06] Y. Wang, J. Seidel, Tsui B.M.W., et al. Performance evaluation of the GE Healthcare eXplore VISTA dual-ring small-animal PET scanner. *Jour. Nucl. Med.*, 47:1891–1900, 2006.

Danksagung

Hiermit danke ich vor allem jenen Personen, die die Ausdauer hatten diese Arbeit vom Anfang bis zu diesem Punkt gelesen zu haben und jenen die zum Gelingen dieser Arbeit beigetragen haben.

Insbesondere danke ich Prof. Dr. Johannes P. Wessels und Prof. Dr. Klaus Schäfers für grundlegende Ideen, der Vermittlung zu fachspezifischen Experten und für das Schaffen eines angenehmen Klimas in den Arbeitsgruppen. Auch möchte ich mich dafür bedanken, dass ich an zahlreichen Unternehmungen und Besuchen am CERN und an der GSI teilhaben konnte, an dem FANTOM International Research School Programm und dem EMMI Intensive Programm on PET in Paris/Saclay 2009 teilnehmen durfte und an den Konferenzen „Molecular Imaging School (Rügen 2011)“, „TRDs for the third Millennium (Bari 2011)“, „DPG Frühjahrstagung (Berlin 1012)“ und „IEEE NSS/MIC/RTSD (Anaheim 2012)“ aktiv oder passiv mitwirken durfte.

Desweiteren möchte ich mich bei Dr. Holger Gottschlag, Dr. Thomas Kösters und Dr. Frank Wübbeling für die intensive Betreuung, den zahlreichen Diskussionen und den unverzichtbaren Vorarbeiten danken.

Natürlich möchte ich mich auch herzlich bei meinen Studenten Jennifer Bersch, Annika Busch, Marc-Adrien Mandich, Christopher Rittmeier und Christoph Bors für die „strikte“ Ausführung all meiner Befehle danken.

Konstantin Bolwin, Björn Czekalla, Dr. Mohammad Dawood, Fabian Gigengack, Florian Büter und Michael Fieseler danke ich für die konstruktive Kooperation mit den EIMI Projekten.

Dr. David Emschermann, Dr. Volker Hannen, Dr. Christian Klein-Bösing, Dr. Tom Dietel, Prof. Dr. Alfons Khoukaz danke für die hilfreichen Diskussionen, Kritiken und Ideen.

Desweiteren möchte ich mich bei Cyrano, Jonas, Markus Z., H. und T., Uwe, Linus und Martin K. und W. für das nette Arbeitsklima und die vielen Blödelein in der Arbeitsgruppe und für die vielen nützlichen Hilfen bedanken.

Außerdem will ich mich auch bei Norbert Heine, Roland Berendes, Wolfgang Verhoeven, Vladimir Buglak, Georg Bourichter, Bodo, Robert, Mark und Susanne

für die Fertigung der von mir gewünschten mechanischen und elektrischen Apparaturen und dem Lösen der vielen technischen Probleme bedanken.

Großer Dank gilt auch jenen Mitarbeitern und Kontaktpersonen von Firmen und Instituten, ohne die das Gelingen dieser Arbeit nicht möglich gewesen wäre. Darunter bedanke ich mich vor allem bei Rui de Oliveira und Silvia Franchino für die Fertigung der Micromesh Detektoren und der Konverter Prototypen, Uwe Vetter, Susanne Drost und Dominik Giel für die Ätzarbeiten für Konverter Geometrien, Rainer Patri für die Laserproben und Jörg Hehner für die Hilfe bei der Reparatur von quadHIDAC Modulen.

Ein großer Dank geht auch an alle Mitwirkenden zur Realisierung der Ausleselektronik und des Datenaufnahmesystems. Unter anderen an Tim Armbruster, Michael Krüger, Sergey Linev, Jörn Adamczewski und Andreas Arend.

Meine größte Wertschätzung gilt natürlich den Menschen, die mir das vielfältige Leben neben der Physik verschönern. Meiner Freundin Ines danke ich für die gegenseitige Ermutigung und Durchführung unserer kühnen und chaotischen Plänen und das wir trotz der langen Durststrecken nie unseren Optimismus und Humor verloren haben.

Meinen Eltern und meiner Schwester danke ich für die bedingungslose Unterstützung und der ordentlichen Inobhutnahme meiner mittlerweile drei Nichten und Neffen.

Zuletzt möchte ich noch meinen Freunden dafür danken, dass sie es immer wieder geschafft haben mich von der Physik abzulenken.

Lebenslauf

Name	Don Vernekohl
Geburtsdatum	24.11.1983
Geburtsort	Lünen
Staatsangehörigkeit	Deutsch
Eltern	Wolfgang Vernekohl Ingrid Vernekohl

Schulbildung

1989 - 1993	Grundschule
1993 - 2003	Gymnasium
20.06.2003	Allgemeine Hochschulreife

Zivildienst

2003 - 2004	Hilfskraft im Jugendzentrum
-------------	-----------------------------

Studium

10.2004 - 03.2010	Diplomstudiengang Physik an der WWU Münster
19.9.2006	Diplom-Vorprüfung Diplomarbeit in Experimenteller Kernphysik Titel: Measurements with a Multi-Wire Proportional Chamber for Small-Animal Positron Emission Tomography
8.3.2010	Diplomprüfung

Promotionsstudium

3.5.2010	Beginn der Dissertation am Institut für Kernphysik unter der Betreuung von Prof. Dr. J. P. Wessels
----------	--

Berufstätigkeit

10.2008 - 7.2009

Studentische Hilfskraft am Physikalischen Institut an der
WWU Münster

seit 5.2010

Wissenschaftlicher Mitarbeiter am Institut für Kernphysik
an der WWU Münster

Ort, Datum

Unterschrift